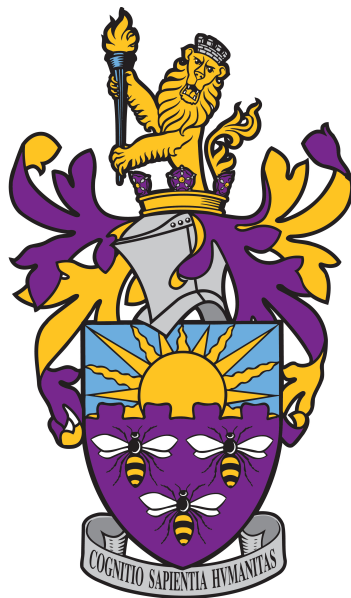


Novel Boosted $\tau_{\text{lep}}\tau_{\text{had}}$ Reconstruction Techniques for TeV-Scale Graviton Search in $HH \rightarrow b\bar{b}\tau_\mu\tau_{\text{had}}$ Channel with the ATLAS Detector



Dong Qichen

董 企宸

Supervisor: Prof. Terry Wyatt FRS

Department of Physics and Astronomy

University of Manchester

This dissertation is submitted for the degree of

Doctor of Philosophy
February 2025

Abstract

In this thesis, I present significant advancements in the reconstruction and identification of highly boosted pairs of tau leptons within the ATLAS experiment, alongside a search for the Graviton in the $HH \rightarrow bb\tau\tau$ decay channel. The development of a muon-removal method for boosted $\tau_\mu\tau_{\text{had}}$ reconstruction has improved the identification efficiency of hadronically decaying taus in the presence of nearby muons. This method recovers τ_{had} identification efficiency to levels expected for isolated decays across all working points, as well as restoring the precision of kinematic measurements for the visible τ_{had} system. Benchmarking with $Z \rightarrow \tau_\mu\tau_{\text{had}}$ samples from the complete Run-2 dataset recorded by the ATLAS detector affirmed the robustness of this method, showing agreement between data and Monte Carlo simulations. Similarly, the electron-removal method for boosted $\tau_e\tau_{\text{had}}$ reconstruction markedly improved the accurate reconstruction of visible decay products of the tau lepton pairs within a single jet by removing the nearby electron contamination. Utilising the muon-removal advancements, we conducted a search for the Graviton in the $HH \rightarrow bb\tau\tau$ channel using the full ATLAS Run-2 dataset collected at $\sqrt{s} = 13\text{TeV}$ with an integrated luminosity of 140 fb^{-1} . Enhanced by a GNN-based bb -jet tagging algorithm and the muon-removal technique, our event selection process achieved high signal efficiency. Results showed good agreement between data and Monte Carlo simulations in the control region, demonstrating negligible QCD background contamination in the signal region. Evaluation of statistical and systematic uncertainties led to the derivation of 95% confidence level limits on the production cross-section $\sigma(pp \rightarrow G \rightarrow HH)$ for mass points ranging from 2 to 5 TeV, significantly surpassing previous ATLAS searches in the $HH \rightarrow bb\tau\tau$ channel. These advancements in tau lepton reconstruction and the subsequent Graviton search highlight the potential to open up a new phase-space, enhancing the sensitivity of the ATLAS experiment for discovering new physics phenomena in the highly boosted di- τ channel.

Declaration

I hereby declare that except where specific reference is made to the work of others, the contents of this dissertation are original and have not been submitted in whole or in part for consideration for any other degree or qualification in this, or any other university. This dissertation is my own work and contains nothing which is the outcome of work done in collaboration with others, except as specified in the text and Acknowledgements.

Dong Qichen

February 2025

Acknowledgements

First and foremost, I would like to express my deepest gratitude to my supervisor, Terry Wyatt, for his unwavering support, guidance, and encouragement throughout the course of my research. His invaluable insights and expertise have been instrumental in the completion of this thesis.

I also extend my heartfelt thanks to the ATLAS collaboration for providing the opportunity to be part of such a prestigious and groundbreaking project. The resources, data, and collaborative environment have significantly contributed to the advancement of my research. Thanks to all the members of the ATLAS collaboration, particularly the TauCP group, for their assistance and for fostering a spirit of scientific inquiry and excellence.

Furthermore, I am immensely grateful to the Manchester ATLAS group for their constant support and camaraderie. The collective knowledge, stimulating discussions, and constructive feedback from the group have greatly enhanced my understanding and have been a source of inspiration throughout my research journey.

Lastly, I would like to acknowledge the support of my family and friends, particularly my loving wife, for her endless patience, understanding, and encouragement during the challenging times.

Thank you all for making this thesis possible!

I dedicate this thesis to my loving wife, **Shang Jiayu**, for her unwavering support and
encouragement throughout this journey...

Table of contents

List of figures	xv
List of tables	xxix
1 Introduction	1
2 Theory framework	5
2.1 The Standard Model of particle physics	5
2.1.1 Symmetry principles	8
2.1.2 Quantum electrodynamics	12
2.1.3 Quantum Chromodynamics	14
2.1.4 Weak force	18
2.1.5 Electroweak unification and the Higgs mechanism	20
2.2 A gravitational extension to the Standard Model	26
2.3 Modelling proton-proton collisions in particle physics	29
2.3.1 Parton Distribution Functions (PDFs)	30
2.3.2 Parton shower, hadronisation, and underlying event	32
3 The ATLAS detector at the LHC	33
3.1 CERN and the Large Hadron Collider (LHC)	33
3.1.1 The operation of the LHC	36

3.1.2 Future LHC upgrades - The High-Luminosity LHC	38
3.1.3 Future collider projects - the Future Circular Collider (FCC)	39
3.2 The ATLAS detector	40
3.2.1 ATLAS Coordinate System and Kinematic Variables	43
3.2.2 Inner Detector	44
3.2.3 Calorimeters	46
3.2.4 Muon Spectrometer	49
3.2.5 Forward Detector	51
3.2.6 TDAQ System	54
3.3 Object reconstruction and identification in ATLAS	57
3.3.1 Reconstruction and identification of electrons and photons	57
3.3.2 Jet reconstruction	61
3.3.3 Missing transverse energy (E_T^{miss}) reconstruction	65
3.3.4 Jet flavour tagging	67
3.3.5 Muon reconstruction and identification	72
3.3.6 τ lepton reconstruction	74
4 The $\tau_{\text{had-vis}}$ reconstruction and identification at ATLAS	77
4.1 $\tau_{\text{had-vis}}$ reconstruction	78
4.1.1 Vertex association	78
4.1.2 Track Association	80
4.1.3 Track Classification	80
4.2 $\tau_{\text{had-vis}}$ Identification and electron-veto	81
4.2.1 RNN-based identification	81
4.2.2 RNN-based electron-veto	83
4.3 $\tau_{\text{had-vis}}$ Energy calibration and resolution	87

5 The muon-removal method for boosted $\tau_\mu \tau_{\text{had}}$ reconstruction	91
5.1 Introduction	91
5.2 Data and simulated samples	92
5.2.1 Simulated samples for development of the method	92
5.2.2 Data and simulated samples for the benchmark analysis	93
5.3 Development of the boosted τ_{had}^μ reconstruction method	95
5.3.1 Muon removal and re-reconstruction of tau lepton candidate	95
5.3.2 Performance of the method	97
5.4 Validation of the τ_{had}^μ method in the $Z \rightarrow \tau_\mu \tau_{\text{had}}$ channel	109
5.4.1 The collinear assumptions and event reconstruction	109
5.4.2 Event-selection	110
5.4.3 Systematic uncertainties	114
5.5 Results	115
5.6 Summary and conclusion	119
6 The electron-removal method for boosted $\tau_e \tau_{\text{had}}$ reconstruction	121
6.1 Introduction	121
6.2 Accretive τ_{had}^e reconstruction method	123
6.3 Energy and spatial resolution of the τ_{had}^e	125
6.4 Benchmark of the τ_{had}^e in the $Z \rightarrow \tau_e \tau_{\text{had}}$ channel	128
6.4.1 Event-selection	129
6.4.2 Results	130
6.5 Summary and outlook	137
7 A search for the Graviton in the $HH \rightarrow b\bar{b}\tau_\mu \tau_{\text{had}}$ channel	139
7.1 Introduction	139
7.2 Data and MC	143
7.3 Event-selection	145

7.3.1 m_{bb} and $m_{\tau\tau}^{\text{col}}$ cuts optimisation	147
7.4 Results	148
7.5 Systematic uncertainties	155
7.6 Interpretation	157
7.7 Conclusion	158
8 Conclusion	161
References	163
Appendix A Investigation for truth 3-prong τ_{had} reconstructed as 2-prong	177

List of figures

2.1	The particles in the Standard Model of Particle Physics, with mass, charge, and spin. Taken from [8].	7
2.2	The running of the strong coupling constant α_s with the energy scale μ in QCD, taken from [9]. The coupling constant decreases as the energy scale increases, demonstrating asymptotic freedom. The experimental measurements of α_s at different energy scales are also shown.	18
2.3	Higgs potential $V(\phi)$ with a minimum at $\phi^\dagger\phi = \frac{v^2}{2}$.	23
2.4	Sketch of how a hadron collision is modelled. In particular, one can notice the initial states, hard scattering, parton shower, hadronisation and the so-called underlying event. From INFN web-page [16].	29
2.5	The NNPDF4.0NNLO parton distribution functions at $Q = 3.2$ GeV and $Q = 100$ GeV [17].	31
3.1	The CERN accelerator complex, including the Large Hadron Collider (LHC) and its experiments, taken from [21]	34
3.2	Cut-away view of the Run 3 configuration of the ATLAS detector indicating the locations of the larger detector sub-systems, taken from [39]	41
3.3	Cut-away view of the ATLAS Inner Detector showing the Pixel Detector, Semiconductor Tracker (SCT), and Transition Radiation Tracker (TRT), taken from [39]	44

3.4 The efficiency to reconstruct charged primary particles in jets with (left) $ \eta < 1.2$ and (right) $ \eta > 1.2$ is shown as a function of the angular distance of the particle from the jet axis for various jet p_T for simulated dijet MC events. These figures are taken from [62].	46
3.5 Cut-away view of the ATLAS calorimeter system showing the Liquid Argon (LAr) calorimeters and the Tile calorimeters, taken from [39].	47
3.6 Cut-away view of the ATLAS Muon Spectrometer, taken from [39].	49
3.7 Resolution of the muon p_T as obtained from simulation after derivation and application of all correction constants. Muons are selected using the High- p_T Working point. The resolution is shown as a function of the true p_T of the muon for a range from 1 GeV to 2.5 TeV, (left) for muons with $ \eta < 1.05$ and (right) for muons with $ \eta > 1.05$. The resolution lines are obtained by interpolating between points sampled in steps of p_T . The continuous lines correspond to the combined momentum, while the dashed lines to that from the ID, and the dotted lines to that of the MS. These figures are taken from [66].	52
3.8 Layout of the forward detectors in the ATLAS experiment, taken from [39]. .	52
3.9 Cumulative integrated luminosity delivered to and recorded by ATLAS between 2015 and 2018 during stable beam pp collision data-taking at $\sqrt{s} = 13$ TeV. This figure is taken from [69].	54
3.10 Schematic of the ATLAS Trigger and Data Acquisition (TDAQ) system, taken from [39].	55
3.11 Identification efficiencies of electrons from $Z \rightarrow ee$ decays as a function of the electron's transverse momentum for the different identification working points. This figure is taken from [72].	58

3.12 (left) The relative jet energy resolution as a function of p_T for fully calibrated PFlow+JES jets. The error bars on points indicate the total uncertainties on the derivation of the relative resolution in dijet events, adding in quadrature statistical and systematic components. The expectation from Monte Carlo simulation is compared with the relative resolution as evaluated in data through the combination of the dijet balance and random cone techniques. (right) Absolute uncertainty on the relative jet energy resolution as a function of jet p_T . Uncertainties from the two in situ measurements and from the data/MC simulation difference are shown separately. These figures are taken from [81].	63
3.13 The p_x^{miss} and p_y^{miss} resolution for different p_T^{miss} working points as a function of interactions per bunch crossing (left) or number of primary vertices (right). PFlow jets are used on SM MC simulations with $Z \rightarrow \mu\mu$ events. These figures are taken from [87].	67
3.14 The GN2 c-jet (left) and light-jet (right) rejections as a function of the b-jet tagging efficiency for jets in the $t\bar{t}$ sample with $20 < p_T < 250$ GeV. The ratio with respect to the performance of the DL1r algorithm is shown in the bottom panels. These figures are taken from [90].	70
3.15 GN2x top and multijet rejections as a function of the $H \rightarrow bb$ efficiency for jets with $p_T > 250$ GeV and mass ($50 \text{ GeV} < m_J < 200 \text{ GeV}$). Performance of the GN2X algorithm is compared to the previous DXbb tagger and variable-radius subjets baselines. These figures are taken from [92].	72
3.16 Muon reconstruction and identification efficiencies for the Loose, Medium, and Tight criteria. It displays the efficiencies measured in $Z \rightarrow \mu\mu$ events as a function of η , for muons with $p_T > 10$ GeV. This figure is taken from [98].	74

4.1	Efficiency to select the correct τ production vertex using TJVA or the default primary vertex in $\gamma^* \rightarrow \tau\tau$ events, as a function of $\langle\mu\rangle$. The left plot shows the efficiency for 1-prong τ_{had} , while the right plot shows the efficiency for 3-prong τ_{had} , taken from [99].	79
4.2	Reconstruction efficiency of the track classifier for 1-prong and 3-prong $\tau_{\text{had-vis}}$ candidates as a function of $\tau_{\text{had-vis}} p_T$ (left) and $\langle\mu\rangle$ (right).	82
4.3	Combined reconstruction and identification efficiency of the $\tau_{\text{had-vis}}$ identification algorithm as a function of $\tau_{\text{had-vis}} p_T$ (left) and $\langle\mu\rangle$ (right), taken from [99]. The decay of the $\tau_{\text{had-vis}}$ efficiency in 3-prong $\tau_{\text{had-vis}}$ candidates at high $\tau_{\text{had-vis}} p_T$ is due to the tracking efficiency in dense environments.	84
4.4	Inverse of the efficiency (rejection) for misidentified 1-prong and 3-prong τ_{had} candidates from dijet background events as a function of the efficiency for truth τ_{had} originating from $\gamma^* \rightarrow \tau\tau$ events, taken from [99].	85
4.5	Efficiency matrix for reconstructing the same τ lepton decay mode as the truth decay mode with DeepSet NN classifier in $\gamma^* \rightarrow \tau\tau$ events, taken from [99]. The labels are in a form of ‘ApBn’, where ‘A’, ‘B’ are the number of prongs (the ‘p’) and neutral pions (the ‘n’) and ‘X’ stands for more than one or more than zero accordingly.	85
4.6	Rejection for misidentified 1-prong and 3-prong $\tau_{\text{had-vis}}$ candidates from $Z \rightarrow ee$ background events with the e-veto algorithm, as a function of the efficiency for truth τ_{had} originating from $\gamma^* \rightarrow \tau\tau$ events, taken from [99].	87
5.1	The distributions of the $\Delta R_{\tau\tau}^{\text{truth,vis}}$ between the truth level $\tau_\mu\tau_{\text{had}}$ pair in the $G \rightarrow HH \rightarrow 4\tau$ with hypothetical Graviton mass ranging from 1000 GeV to 5000 GeV. The distributions are normalised to unity.	96

5.2 The combined reconstruction and identification efficiencies of the standard ATLAS TauID for truth 1-prong (a) and 3-prong (b) $\tau_\mu\tau_{\text{had}}$ pairs in all working points as a function of $\Delta R_{\tau\tau}^{\text{truth,vis}}$; the “Seeding” line (dark cyan) shows the efficiency of a τ_{seed} jet that matches to a truth-level $\tau_\mu\tau_{\text{had}}$ pair being reconstructed; the “ProngCorr” line (black) shows the efficiency of a truth-level τ_{had} being reconstructed with the correct number of associated charged-particle tracks.	96
5.3 The combined reconstruction and TauID efficiencies after the muon removal for truth 1-prong (a) and 3-prong (b) $\tau_\mu\tau_{\text{had}}$ pairs in all working points as a function of $\Delta R_{\tau\tau}^{\text{truth,vis}}$. The extra “MuonRM” line (green) shows the efficiency of a muon being removed from the τ_{seed} . The slight abnormality in the “MuonRM” line between $0.35 < \Delta R_{\tau\tau}^{\text{truth,vis}} < 0.45$ is due to limited detector resolution in the direction of the reconstructed $\tau_{\text{had-vis}}$	98
5.4 The signal efficiencies of the TauID working points as a function of the truth absolute pseudorapidity for truth 1-prong (a) and 3-prong (b) τ_{seed} jets with $\Delta R_{\tau\tau}^{\text{truth,vis}} < 0.4$. The seeding efficiencies and the ratio of the τ_{seed} jets with a muon removed are also shown.	99
5.5 The stability of the signal efficiencies of the TauID working points against the truth transverse momentum (a) (b), and pile-up (c) (d) for truth 1-prong and 3-prong τ_{seed} with reconstructed $\Delta R_{\tau\tau}^{\text{reco}} < 0.4$. The “Seeding” lines indicate the efficiency of a truth-level τ_{had} being reconstructed as τ_{seed} . The “MuonRM” lines show the efficiency of a muon being removed inside the τ_{seed}	101

5.6	The stability of the signal efficiencies of the TauID working points against the truth transverse momentum (a) (b), and pile-up (c) (d) for the truth 1-prong and 3-prong τ_{seed} jets with $\Delta R_{\tau\tau}^{\text{truth,vis}} > 0.45$. In this region, the muon removal should not affect the results. The “Seeding” lines indicate the efficiency of a truth-level τ_{had} being reconstructed as τ_{seed} . The “MuonRM” lines show the efficiency of a muon being removed inside the τ_{seed}	102
5.7	The distributions of the calibrated residuals η (a) (b) and ϕ (c) (d) before (blue) and after (red) muon removal. The left panel shows the 1-prong case; the right panel shows the 3-prong case.	103
5.8	(a) (b): the distributions of the calibrated transverse energy residuals for $\tau_{\text{had-vis}}$ with (red) and without (blue) muon removal. (c) (d): the relative core (68%) and tail (95%) $\tau_{\text{had-vis}}$ E_{T} resolutions as functions of $\tau_{\text{had-vis}}$ $E_{\text{T}}^{\text{truth}}$. The left plots show the 1-prong case and the right plots show the 3-prong case.	104
5.9	The signal rejection ratios for τ_{seed} jets reconstructed from jets originating from semi-muonic bottom decays in $t\bar{t}$ events at medium TauID working point, as functions of the reconstructed p_{T} (a) (b), and pile-up (c) (d). The left panel shows the reconstructed 1-prong case, the right panel shows the 3-prong case.	106
5.10	The receiver operating characteristic (ROC) curves with and without muon removal. (a) shows the reconstructed 1-prong case, (b) shows the 3-prong case.	107

5.11 The signal efficiencies of the TauID working points, as a function of the truth-level Graviton mass, m_G^{truth} , for truth 1-prong (a) and 3-prong (b) τ_{had} with the standard ATLAS TauID; and for truth 1-prong (c) and 3-prong (d) τ_{had} with the τ_{had}^N method. The efficiencies shown correspond to the identification of individual di- τ systems originating from Higgs boson decays. The “Seeding” lines indicate the efficiency of a truth-level τ_{had} being reconstructed as τ_{seed} . the “ProngCorr” line shows the efficiency of a truth-level τ_{had} being reconstructed with the correct number of associated charged-particle tracks. The “MuonRM” lines show the efficiency of a muon being removed inside the τ_{seed}	108
5.12 The distribution of the RNN jet score for τ_{had}^N : (a) in the SR and, (b) in the CR. “Top” represents the predicted contributions from the SM $t\bar{t}$, single-top, and tW processes. “DiBoson” indicates the contributions from WW , WZ , and ZZ processes. “Other” includes the contributions from the $Z \rightarrow ll + \text{jets}$ and $W + \text{jets}$ background processes. “ $Z \rightarrow \tau\tau + \text{jets}$ ” represents the contributions from the signal process. The uncertainties shown include both statistical and systematic uncertainties.	112
5.13 The distribution of $\Delta\phi_{\mu-E_T^{\text{miss}}}^{\text{signed}}$ with all other event-selection criteria applied in the SR is shown in (a); the straight lines indicate the positions of the selection requirements. The same distribution in the CR is shown in (b). “Top” represents the predicted contributions from the SM $t\bar{t}$, single-top, and tW processes. “DiBoson” indicates the contributions from WW , WZ , and ZZ processes. “Other” includes the contributions from the $Z \rightarrow ll + \text{jets}$ and $W + \text{jets}$ background processes. “ $Z \rightarrow \tau\tau + \text{jets}$ ” represents the contributions from the signal process. The uncertainties shown include both statistical and systematic uncertainties.	113

5.14 The distribution of the $m_{\mu-\text{had}}^{\text{col}}$: (a) in the SR, and, (b) in the CR. “Top” represents the predicted contributions from the SM $t\bar{t}$, single-top, and tW processes. “DiBoson” indicates the contributions from WW , WZ , and ZZ processes. “Other” includes the contributions from the $Z \rightarrow ll+\text{jets}$ and $W+\text{jets}$ background processes. “ $Z \rightarrow \tau\tau+\text{jets}$ ” represents the contributions from the signal process. The uncertainties shown include both statistical and systematic uncertainties.	114
5.15 The distribution of the $p_{T\mu-\text{had}}^{\text{col}}$: (a) in the SR, and, (b) in the CR. “Top” represents the predicted contributions from the SM $t\bar{t}$, single-top, and tW processes. “DiBoson” indicates the contributions from WW , WZ , and ZZ processes. “Other” includes the contributions from the $Z \rightarrow ll+\text{jets}$ and $W+\text{jets}$ background processes. “ $Z \rightarrow \tau\tau+\text{jets}$ ” represents the contributions from the signal process. The uncertainties shown include both statistical and systematic uncertainties.	115
5.16 The distribution of the p_T of the τ_{had}^μ : (a) in the SR and, (b) in the CR. “Top” represents the predicted contributions from the SM $t\bar{t}$, single-top, and tW processes. “DiBoson” indicates the contributions from WW , WZ , and ZZ processes. “Other” includes the contributions from the $Z \rightarrow ll+\text{jets}$ and $W+\text{jets}$ background processes. “ $Z \rightarrow \tau\tau+\text{jets}$ ” represents the contributions from the signal process. The uncertainties shown include both statistical and systematic uncertainties.	116

5.17 The distribution of the p_T of the muon removed from the τ_{had}^μ : (a) in the SR and, (b) in the CR. “Top” represents the predicted contributions from the SM $t\bar{t}$, single-top, and tW processes. “DiBoson” indicates the contributions from WW , WZ , and ZZ processes. “Other” includes the contributions from the $Z \rightarrow ll + \text{jets}$ and $W + \text{jets}$ background processes. “ $Z \rightarrow \tau\tau + \text{jets}$ ” represents the contributions from the signal process. The uncertainties shown include both statistical and systematic uncertainties.	117
5.18 The distributions of $m_{\mu-\text{had}}^{\text{col}}$ corresponding to the various signal selections defined in the text: (a) SR, (b) SR^{std} , (c) SR_{tight} , and (d) $\text{SR}_{\text{tight}}^{\text{std}}$. SR, SR_{tight} and CR are with the τ_{had}^μ method, while SR^{std} and $\text{SR}_{\text{tight}}^{\text{std}}$ are with the standard ATLAS TauID.	118
6.1 The combined reconstruction and identification efficiency of the standard TauReco and TauID as a function of the truth-level $\Delta R_{\tau\tau}^{\text{truth},\text{vis}}$. The efficiency is shown for the different working points of the TauID algorithm. In addition, the “Reco” and “ProngCorr” efficiencies are shown, which are the efficiency of the τ_{had} being seeded, and the efficiency of the TauRec algorithm to reconstruct the correct number of tracks in the τ_{had} , respectively.	122
6.2 The combined reconstruction and identification efficiency of the accretive τ_{had}^ℓ reconstruction method as a function of the truth $\Delta R_{\tau\tau}^{\text{truth},\text{vis}}$. The efficiency is shown for every working points of the TauID algorithm. In addition, the “Reco”, “ElecRM”, and “ProngCorr” efficiencies are shown, which is the efficiency of the τ_{had} being seeded, the efficiency of the electron-removal, and the efficiency of the TauRec algorithm reconstructing the correct number of tracks, respectively.	124

6.3 The efficiency of the accretive τ_{had}^k reconstruction method as a function of the truth-level $p_{T\tau}^{\text{truth,vis}}$ (a), and $ \eta ^{\text{truth,vis}}$ (b), where the electron is identified and removed. The efficiency is shown for the different working points of the TauID algorithm for 1-prong and 3-prong. In addition, the “ElecRM”, and “ProngCorr” efficiencies are the efficiency of the electron-removal, and the efficiency of the TauRec algorithm to reconstruct the correct number of tracks in the τ_{had} , respectively.	126
6.4 The distributions of the calibrated transverse energy residuals for $\tau_{\text{had-vis}}$ with τ_{had}^k (red) and τ_{had} (blue) are shown in (a). The relative core (68%) and tail (95%) $\tau_{\text{had-vis}}$ p_T resolutions as functions of $p_{T\tau}^{\text{truth,vis}}$ are shown in (b). The left plots show the 1-prong case and the right plots show the 3-prong case.	127
6.5 The distributions of the ϕ (a) and η (b) residuals for $\tau_{\text{had-vis}}$ with τ_{had}^k (red) and τ_{had} (blue) are shown. The left plots show the 1-prong case and the right plots show the 3-prong case.	128
6.6 The distribution of the $m_{e-\text{had}}^{\text{col}}$: (a) in the SR, and, (b) in the CR. All requirement criteria are applied, except the requirement on the variable being plotted. The vertical line indicates the event-selection requirement on this variable.	131
6.7 The distribution of the $p_{T e-\text{had}}^{\text{col}}$: (a) in the SR, and, (b) in the CR. All requirement criteria are applied, except the requirement on the variable being plotted. The vertical line indicates the event-selection requirement on this variable.	132
6.8 The distribution of the TauID RNN score: (a) in the SR, and, (b) in the CR. All requirement criteria are applied, except the requirement on the variable being plotted. The vertical line indicates the event-selection requirement on this variable.	132

6.9 The distribution of the TauID e-veto RNN score: (a) in the SR, and, (b) in the CR. All requirement criteria are applied, except the requirement on the variable being plotted. The vertical line indicates the event-selection requirement on this variable.	133
6.10 The distribution of the $m_{e\text{-had}}^{\text{col}}$ in the SR: (a) nominal SR, (b) SR ^{std} , (c) SR _{tight} , and, (d) SR _{tight} ^{std} . SR, SR _{tight} and CR are with the τ_{had}^{ℓ} method, while SR ^{std} and SR _{tight} ^{std} are with the standard ATLAS TauID.	134
7.1 Feynman diagram of the gluon–gluon production of the X and G	140
7.2 Predicted cross-section of the $pp \rightarrow G \rightarrow HH$ production at the LHC centre of mass energy of 13 TeV and 13.6 TeV.	140
7.3 The G 3 TeV signal efficiency, background efficiency, and the significance for different cut values on the m_{bb} (a), and $m_{\tau\tau}^{\text{col}}$ (b) distributions.	147
7.4 The distribution of the $ \Delta\phi_{bb-\tau\tau} $ in the SR (a), and CR (b).	149
7.5 The distribution of the $\Delta\phi_{\mu\text{-MET}}^{\text{signed}}$ in the SR (a), and CR (b).	150
7.6 The distribution of the $\Delta R_{\text{fj-jet}}$ in the SR (a), and CR (b).	150
7.7 The distribution of the GN2x _{fj} in the SR (a), and CR (b). The translucent band indicates the cut value of “QCD1.55%” GN2x WP, ranging from 1.6 to 1.7 in the region where the fatjet mass is between 90 and 160 GeV.	151
7.8 The distribution of the m_{bb} in the SR (a), and CR (b).	151
7.9 The distribution of the p_{Tbb} in the SR (a), and CR (b). The p_{Tbb} distribution extends to lower values in the CR than in the SR due to the relaxed $m_{\tau\tau}^{\text{col}}$ and m_{bb} requirements. This is because lower values of $m_{\tau\tau}^{\text{col}}$ and m_{bb} in the CR allow di- τ and $b\bar{b}$ systems at lower p_T to be produced whilst still satisfying the condition $\Delta R < 0.4$	152
7.10 The distribution of the $m_{\tau\tau}^{\text{col}}$ in the SR (a), and CR (b).	152

7.11 The distribution of the $p_{\text{T}}^{\text{col}}$ in the SR (a), and CR (b). The $p_{\text{T}}^{\text{col}}$ distribution extends to lower values in the CR than in the SR due to the relaxed $m_{\tau\tau}^{\text{col}}$ and m_{bb} requirements. This is because lower values of $m_{\tau\tau}^{\text{col}}$ and m_{bb} in the CR allow di- τ and $b\bar{b}$ systems at lower p_{T} to be produced whilst still satisfying the condition $\Delta R < 0.4$	153
7.12 The distribution of the $m_{\text{bb}\tau\tau}^{\text{col}}$ in the SR (a), and CR (b). The $m_{\text{bb}\tau\tau}^{\text{col}}$ distribution extends to lower values in the CR than in the SR due to the relaxed $m_{\tau\tau}^{\text{col}}$ and m_{bb} requirements. This is because lower values of $m_{\tau\tau}^{\text{col}}$ and m_{bb} in the CR allow di- τ and $b\bar{b}$ systems at lower p_{T} to be produced whilst still satisfying the condition $\Delta R < 0.4$	153
7.13 The distribution of the p_{T}^μ in the SR (a), and CR (b).	154
7.14 The distribution of the RNN_τ in the SR (a), and CR (b).	154
7.15 The distribution of the product of the $\tau\tau$ charges in the SR (a), and CR (b).	155
7.16 The expected 95% CL limits on the $\sigma(pp \rightarrow G \rightarrow HH)$ on various mass points. The expected limits are shown as the dotted line. The $\pm 1\sigma$ and $\pm 2\sigma$ bands are shown as the shaded regions around the expected limits. The marked solid lines show the observed limits.	158
A.1 The distribution of the $ \Delta\phi_{\text{bb}-\tau\tau} $ in the SR (a), and CR (b).	179
A.2 The distribution of the $\Delta\phi_{\mu-\text{MET}}^{\text{signed}}$ in the SR (a), and CR (b).	179
A.3 The distribution of the $\Delta R_{\text{fj-jet}}$ in the SR (a), and CR (b).	180
A.4 The distribution of the GN2x_{fj} in the SR (a), and CR (b). The translucent band indicates the cut value of “QCD1.55%” GN2x WP, ranging from 1.6 to 1.7 in the region where the fatjet mass is between 90 and 160 GeV.	180
A.5 The distribution of the m_{bb} in the SR (a), and CR (b).	181
A.6 The distribution of the $m_{\tau\tau}^{\text{col}}$ in the SR (a), and CR (b).	181

A.7 The distribution of the $m_{\text{bb}\tau\tau}^{\text{col}}$ in the SR (a), and CR (b). The $m_{\text{bb}\tau\tau}^{\text{col}}$ distribution extends to lower values in the CR than in the SR due to the relaxed $m_{\tau\tau}^{\text{col}}$ and m_{bb} requirements. This is because lower values of $m_{\tau\tau}^{\text{col}}$ and m_{bb} in the CR allow di- τ and $b\bar{b}$ systems at lower p_{T} to be produced whilst still satisfying the condition $\Delta R < 0.4$	182
A.8 The distribution of the p_{Tbb} in the SR (a), and CR (b). The p_{Tbb} distribution extends to lower values in the CR than in the SR due to the relaxed $m_{\tau\tau}^{\text{col}}$ and m_{bb} requirements. This is because lower values of $m_{\tau\tau}^{\text{col}}$ and m_{bb} in the CR allow di- τ and $b\bar{b}$ systems at lower p_{T} to be produced whilst still satisfying the condition $\Delta R < 0.4$	182
A.9 The distribution of the p_{T}^{μ} in the SR (a), and CR (b).	183
A.10 The distribution of the $p_{\text{T}\tau\tau}^{\text{col}}$ in the SR (a), and CR (b). The $p_{\text{T}\tau\tau}^{\text{col}}$ distribution extends to lower values in the CR than in the SR due to the relaxed $m_{\tau\tau}^{\text{col}}$ and m_{bb} requirements. This is because lower values of $m_{\tau\tau}^{\text{col}}$ and m_{bb} in the CR allow di- τ and $b\bar{b}$ systems at lower p_{T} to be produced whilst still satisfying the condition $\Delta R < 0.4$	183
A.11 The distribution of the RNN_{τ} in the SR (a), and CR (b).	184
A.12 The distribution of the product of the $\tau\tau$ charges in the SR (a), and CR (b).	184
A.13 The expected and observed 95% CL limits on the $\sigma(G \rightarrow HH)$ on various mass points. Limits are obtained with the 2-prong analysis concatenated to the main analysis.	186

List of tables

5.1	Summary of event-selection requirements	111
5.2	Event yields in different event-selections, as defined in the text. SR, SR _{tight} and CR are with the τ_{had}^{μ} method, while SR ^{std} and SR _{tight} ^{std} are with the standard ATLAS TauID. The uncertainties quoted are statistical only. The $Z \rightarrow \tau\tau$ contribution is scaled by +10% to account for the difference between the MC prediction and the data.	117
6.1	Summary of event-selection requirements for the $Z \rightarrow \tau_e \tau_{\text{had}}$ channel.	130
6.2	Event yields in SR and CR. SR, SR _{tight} , SR ^{std} , and SR _{tight} ^{std} are defined mirroring the τ_{had}^{μ} benchmark. CR, CR _{tight} , CR ^{std} , and CR _{tight} ^{std} are defined by requiring the same charge electron- τ_{had} in the SR, SR _{tight} , SR ^{std} , and SR _{tight} ^{std} , respectively. SR, SR _{tight} and CR are with the τ_{had}^{ℓ} method, while SR ^{std} and SR _{tight} ^{std} are with the standard ATLAS TauID. The uncertainties quoted are statistical only.	135
7.1	Summary of the expected and observed 95% CL limits on the production cross-section of the di-higgs ($\sigma(G/X \rightarrow HH)$) set by ATLAS and CMS. Limits are given in fb. The numbers inside and outside the brackets are the observed and the expected limits respectively.	141

7.2	Summary of signal region event-selection criteria. SR events pass at least one trigger listed below. A control region is defined in which events fail any one or more of the cuts marked with *, while passing every other selection. For better CR statistics, the lower bound of $m_{\tau\tau}^{\text{col}}$ and m_{bb} is relaxed to 60 GeV for CR. “fatjet” refers to the large-radius jet clustered with the anti- k_t algorithm with $R = 1.0$	145
7.3	Event yields in the SR and CR regions. The uncertainties are statistical only. The signal yields are shown with fixed cross-sections $\sigma(pp \rightarrow G \rightarrow HH) = 1 \text{ fb}$	146
7.4	The expected and observed 95% CL limits on the $\sigma(G \rightarrow HH)$ on various mass points.	157
A.1	Event yields in the SR 2p and CR 2p regions. Apart from the different selection criteria for prongness and charge, the SR 2p and CR 2p regions are identical to the SR and CR regions in the main analysis. The uncertainties are statistical only. The signal yields are shown with fixed cross-sections $\sigma(pp \rightarrow G \rightarrow HH) = 1 \text{ fb}$	185
A.2	The expected and observed 95% CL limits on the $\sigma(G \rightarrow HH)$ on various mass points. Limits are obtained with the 2-prong analysis concatenated to the main analysis.	186

Chapter 1

Introduction

The field of particle physics is a vibrant and rapidly evolving discipline that seeks to uncover the fundamental constituents of matter and the forces that govern their interactions. At the heart of this endeavour lies the Standard Model (SM) of particle physics [1], a robust theoretical framework that has successfully explained a wide array of experimental results. The SM encompasses the electromagnetic, weak, and strong forces, which are mediated by gauge bosons, and the Higgs mechanism, which imparts mass to these particles. However, despite its successes, the SM is known to be incomplete, prompting the exploration of extensions that can address its limitations.

The Standard Model provides a comprehensive description of the elementary particles and their interactions [2]. It classifies all known fundamental particles into two groups: fermions, which make up matter, and bosons, which mediate the forces between fermions. The fermions include quarks and leptons, while the bosons include the photon, W and Z bosons, and gluons. The Higgs boson, discovered in 2012 at the Large Hadron Collider (LHC) [3], is a pivotal component of the SM, responsible for giving mass to the other fundamental particles through the Higgs mechanism.

Symmetry principles, particularly gauge invariance, underpin the SM. These principles dictate the interactions between particles, leading to the formulation of electroweak theory

for electromagnetic interactions and weak interactions, quantum chromodynamics (QCD) for strong interactions. Both of these theories has been rigorously tested and confirmed through numerous experiments.

Despite its successes, the SM does not include gravity [4], which is described by General Relativity in the classical regime. The quest for a quantum theory of gravity, which would unify all fundamental forces, remains one of the most significant challenges in theoretical physics. Various approaches, such as string theory and loop quantum gravity, aim to address this gap, but a complete and experimentally verified theory is yet to be established. Additionally, the SM does not account for dark matter and dark energy, which constitute approximately 95% of the universe's energy density. The existence of these components is inferred from astrophysical observations, such as the rotation curves of galaxies and the accelerated expansion of the universe. Extensions to the SM, including supersymmetry and theories involving extra dimensions, have been proposed to incorporate these phenomena, but experimental confirmation is still pending.

This thesis is dedicated to exploring the intricacies of the Standard Model and its potential gravitational extensions, as will be introduced in Chapter 2. In the latter part of Chapter 2, the modelling of the proton-proton collisions at the Large Hadron Collider (LHC) will be discussed. Chapter 3 will introduce the ATLAS detector, a sophisticated instrument designed to measure the properties of particles produced in high-energy collisions. The thesis will provide a comprehensive overview of the ATLAS detector's components, including the inner detector, calorimeters, muon spectrometer, and the trigger and data acquisition system. This chapter will also discuss the reconstruction of particles within the ATLAS detector. In Chapter 4, special attention will be given to the reconstruction and identification of tau leptons, which play a crucial role in various searches for new physics. Innovative methods for tau lepton reconstruction, including machine learning techniques such as Recurrent Neural Networks (RNNs), will be discussed.

The thesis will then present the development and performance evaluation of muon- and electron-removal methods in boosted $\tau_{\text{lep}}\tau_{\text{had}}$ lepton-pair reconstruction in Chapter 5 and Chapter 6 respectively, along with benchmarks using $Z \rightarrow \tau_{\text{lep}}\tau_{\text{had}}$ events. To put these new developments to test, in Chapter 7, the thesis will explore searches for heavy resonant particles. In particular, a hypothetical Graviton, in channels involving tau leptons and b-jets. These searches are motivated by theories that extend the SM and aim to provide insights into the nature of gravity. Finally, Chapter 8 will summarise this thesis's key findings and discuss their implications for the field of particle physics. This thesis aims to contribute to the ongoing efforts to understand the fundamental structure of the universe by leveraging the capabilities of the ATLAS experiment and exploring both established and novel aspects of particle physics.

While the theoretical underpinnings presented in Chapter 2 are well-established in the community, and the design and construction of the ATLAS detector described in Chapter 3 were carried out by the broader ATLAS Collaboration, I did not contribute directly to the formulation of these theories nor the detector hardware. My principal contributions begin in Chapter 5 and extend through Chapter 7, where I served as the primary analyst. Specifically, I led the development and performance evaluation of muon- and electron-removal methods for boosted τ -lepton pair reconstruction, benchmarks using $Z \rightarrow \tau_{\text{lep}}\tau_{\text{had}}$ events, and the subsequent searches for heavy resonant particles such as hypothetical gravitons in final states involving τ -leptons and b -jets. These analyses were performed in close collaboration with other members of the ATLAS team. Although I was responsible for designing and executing the primary analyses described in those chapters, the work benefited significantly from the ATLAS software frameworks, simulation tools, and ongoing discussions within the collaboration.

Chapter 2

Theory framework

This chapter provides an overview of the theoretical framework that underpins the research presented in this thesis. The chapter begins with a discussion of the Standard Model of particle physics. The chapter then introduces one possible extension to the Standard Model. To relate the theory to the experiments conducted at the Large Hadron Collider (LHC), the chapter concludes with a brief discussion of the modelling of proton-proton collisions. This chapter is based on review articles of the Standard Model and particle physics [1, 2], and the articles on the Randall-Sundrum model and phenomenology [5–7].

2.1 The Standard Model of particle physics

The Standard Model of particle physics (SM) is a quantum field theory describing the interactions of matter through three of the four fundamental forces in nature: electromagnetic, weak, and strong forces. Formulated from theoretical arguments and experimental evidence, it is one of the most rigorously tested theories in physics. Its core principle is the local gauge symmetry of the gauge group $SU(3)_c \times SU(2)_L \times U(1)$. Here, the non-Abelian $SU(3)_c$ and $SU(2)_L \times U(1)$ groups represent quantum chromodynamics (QCD) and the electroweak sector, respectively.

Figure 2.1 summarise the particles in the Standard Model. Elementary particles in the model fall into two categories based on their spin values: fermions, which have half-integer spin, and bosons, which possess integer spin. The fundamental forces arise from interactions between their corresponding gauge (spin-1) bosons and a subset of fermions. Fermions and bosons are grouped in tables summarising their spin, electric charge, and mass.

Fermions are further classified into two basic types: leptons and quarks. Each group has six particles, arranged into three generations. Every fermion has an associated anti-particle with identical mass but opposite quantum numbers. Leptons include the electron (e), muon (μ), and tau (τ), each paired with a corresponding neutrino (ν). Electrons, muons, and taus are charged and progressively increase in mass, while neutrinos are neutral and have very small masses. Quarks consist of up (u), down (d), strange (s), charm (c), bottom (b), and top (t). They all possess mass and are electrically charged, increasing in mass with each generation. Additionally, quarks contain a colour charge, which determines their interaction through the strong force.

All fermions interact through the weak interaction, charged fermions engage in electromagnetic interactions, and only quarks experience strong interactions. The corresponding gauge bosons mediating these forces include the photon (γ) for the electromagnetic force, gluon (g) for the strong force, and W^+ , W^- , and Z bosons for the weak interaction. The theory also includes a scalar (spin-0) boson, the Higgs boson (H), which provides mass to both bosons and fermions through the mechanism of spontaneous symmetry breaking within the electroweak interaction. The discovery of the Higgs boson stands as a significant confirmation of the predictive power of the SM.

However, the Standard Model remains incomplete as it does not encompass gravity, the fourth and weakest fundamental force, nor does it explain the observed matter-antimatter asymmetry or the indirect evidence of dark matter. Therefore, measuring Standard Model

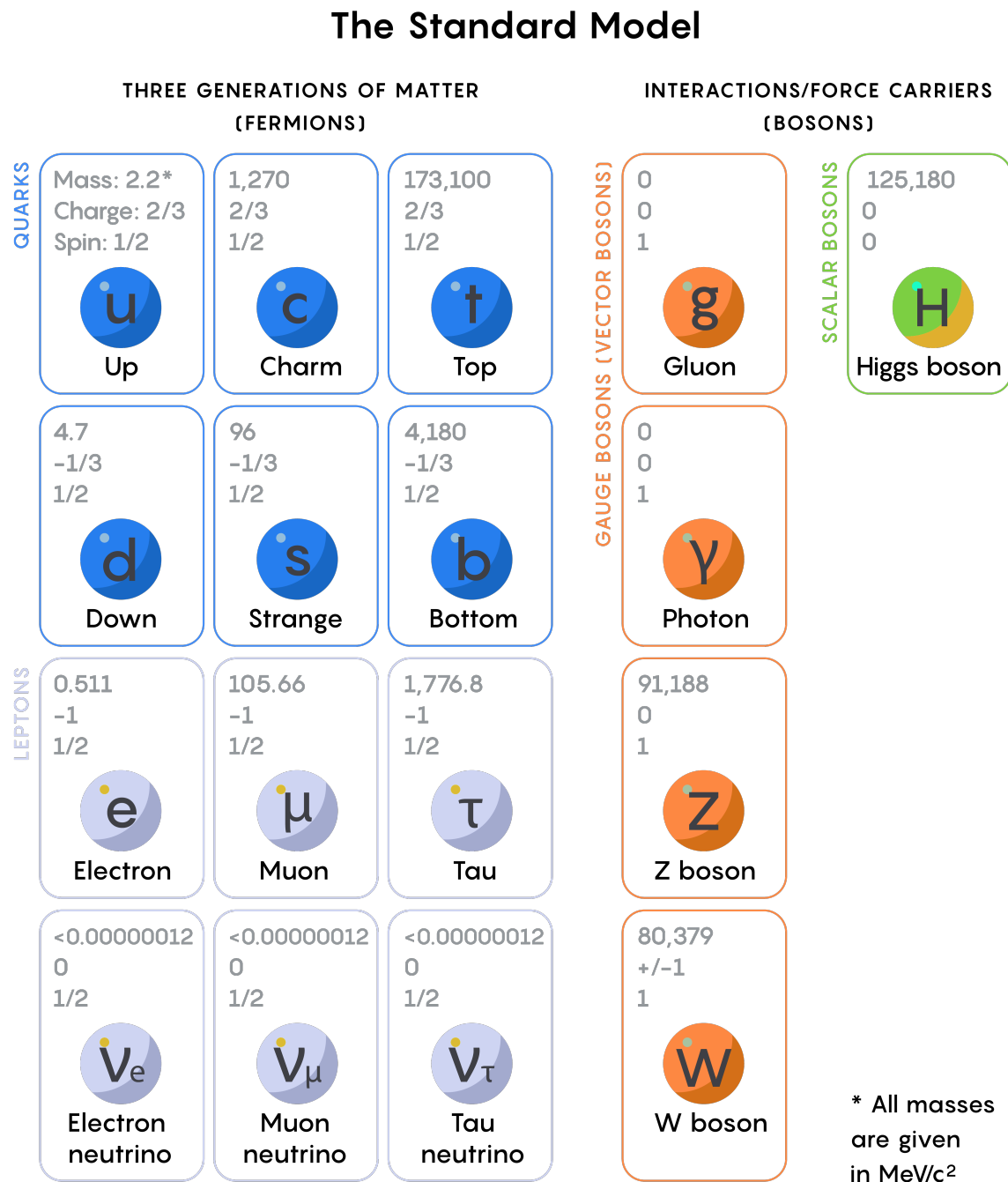


Fig. 2.1 The particles in the Standard Model of Particle Physics, with mass, charge, and spin. Taken from [8].

processes is crucial to uncovering discrepancies between theory and experiment that could address these outstanding issues.

In the following sections, we will discuss the symmetry principles, quantum field theory, the Standard Model of Particle Physics, and the gravitational extension.

2.1.1 Symmetry principles

The concept of symmetry is fundamental to the Standard Model. According to the principle of Lorentz symmetry, the laws of physics remain consistent for observers in different inertial reference frames. This concept, along with quantum mechanics, bridges the gap between classical mechanics and quantum field theories, which is essential for understanding the Standard Model of particle physics.

Lagrangian formulation

In classical mechanics, the Lagrangian is a function of the generalised coordinates $q_i(t)$, generalised velocities $\dot{q}_i(t) = \frac{dq_i}{dt}$, and time t

$$L(q_i, \dot{q}_i) = T(q_i, \dot{q}_i) - V(q_i). \quad (2.1)$$

where T is the kinetic energy, and V is the potential energy of the system. The action S is defined as the integral of the Lagrangian over time

$$S = \int L(q_i, \dot{q}_i) dt. \quad (2.2)$$

The principle of least action states that the action S is minimised along the path of motion of the system. A small perturbation, $q_i(t) \rightarrow q_i(t) + \delta q_i(t)$, should leave the action

unchanged. The change in the action δS under the perturbation can be expressed as:

$$\delta S = 0 = \int_{t_1}^{t_2} \left(\delta q_i \frac{\partial L}{\partial q_i} + \delta \dot{q}_i \frac{\partial L}{\partial \dot{q}_i} \right) dt. \quad (2.3)$$

This can be rearranged using integration by parts:

$$\delta S = 0 = \int_{t_1}^{t_2} \left(\delta q_i \frac{\partial L}{\partial q_i} + \frac{d}{dt} \left(\delta q_i \frac{\partial L}{\partial \dot{q}_i} \right) - \delta q_i \frac{d}{dt} \left(\frac{\partial L}{\partial \dot{q}_i} \right) \right) dt. \quad (2.4)$$

By choosing the perturbation to vanish at the endpoints, the second term vanishes, and the equation simplifies to

$$\frac{\partial L}{\partial q_i} = \frac{d}{dt} \left(\frac{\partial L}{\partial \dot{q}_i} \right). \quad (2.5)$$

This is the Euler-Lagrange equation, which describes the motion of the system.

In field theories, the Lagrangian density, $L[\phi(x), \partial_\mu \phi(x)]$, is used instead of the L . Here, $\phi(x)$ represents a scalar field dependent on the space-time four-vector x , and $\partial_\mu \phi(x)$ is the derivative of the field with respect to the space-time coordinates

$$\partial_\mu \phi(x) = \frac{\partial \phi(x)}{\partial x^\mu}. \quad (2.6)$$

The Lagrangian, as discussed in the previous paragraph, can be obtained by integrating the Lagrangian density over the space volume:

$$L = \int \mathcal{L}[\phi(x), \partial_\mu \phi(x)] d^3 x. \quad (2.7)$$

Additionally, the action S is defined by integrating the Lagrangian density over the entire four-dimensional spacetime:

$$S = \int \mathcal{L}[\phi(x), \partial_\mu \phi(x)], d^4 x. \quad (2.8)$$

Similar to the classical mechanics, the Euler-Lagrange equation for the field $\phi(x)$ can be written as:

$$\partial_\mu \left(\frac{\partial \mathcal{L}}{\partial (\partial_\mu \phi)} \right) - \frac{\partial \mathcal{L}}{\partial \phi} = 0, \quad (2.9)$$

following the same principle of least action. Consider a free particle with mass m , the Lagrangian density can be written as:

$$\mathcal{L} = \frac{1}{2} \partial_\mu \phi(x) \partial^\mu \phi(x) - \frac{1}{2} m^2 \phi^2(x). \quad (2.10)$$

Using the Euler-Lagrange equation, the Klein-Gordon equation can be derived:

$$(\partial_\mu \partial^\mu + m^2) \phi(x) = 0, \quad (2.11)$$

which describes the motion of a free scalar field.

Symmetry and conservation Laws

Conservation laws are a direct consequence of the symmetry of the Lagrangian, not only in field theories but also in classical field theory and even in the classical mechanics of point particles. For instance, symmetry under time translation implies conservation of energy; symmetry under space translation results in the conservation of momentum; and rotational symmetry leads to the conservation of angular momentum. The Noether theorem states that for every symmetry of the Lagrangian there is a corresponding conserved quantity. Or, in field theory, for every symmetry of the Lagrangian density, there is a corresponding conserved current, such that

$$\partial_\mu j^\mu = 0. \quad (2.12)$$

Consider a scalar field ϕ , which undergoes an infinitesimal global transformation $\phi \rightarrow \phi + \delta\phi$. Under such transformation, the Lagrangian density $\mathcal{L}[\phi, \partial_\mu \phi]$ remains invariant

$$\mathcal{L}[\phi, \partial_\mu \phi] \rightarrow \mathcal{L}[\phi, \partial_\mu \phi] + \delta \mathcal{L}(\phi, \partial_\mu \phi) = \mathcal{L}[\phi, \partial_\mu \phi], \quad (2.13)$$

where $\delta \mathcal{L}(\phi, \partial_\mu \phi)$ is by definition zero. Expanding $\delta \mathcal{L}(\phi, \partial_\mu \phi)$ in terms of ϕ and $\partial_\mu \phi$, and using the Euler-Lagrange equation, the conserved current j^μ can be written as:

$$j^\mu = \frac{\partial \mathcal{L}}{\partial (\partial_\mu \phi)} \delta\phi, \quad (2.14)$$

in this case, the conserved current is the Noether current.

Gauge symmetry

In the classical electromagnetic theory, the electric field E and magnetic field B are described by the Maxwell's equations,

$$\nabla \cdot \mathbf{E} = \frac{\rho}{\epsilon_0}, \nabla \cdot \mathbf{B} = 0, \nabla \times \mathbf{E} = -\frac{\partial \mathbf{B}}{\partial t}, \nabla \times \mathbf{B} = \mu_0 \mathbf{J} + \mu_0 \epsilon_0 \frac{\partial \mathbf{E}}{\partial t}, \quad (2.15)$$

where ρ is the charge density, \mathbf{J} is the current density, ϵ_0 is the permittivity of free space, and μ_0 is the permeability of free space. As implied by the Maxwell's equations, the magnetic fields are divergence-free, which implies that the magnetic field can be described by a vector potential \mathbf{A} , such that $\mathbf{B} = \nabla \times \mathbf{A}$. The electric field can be described by a scalar potential ϕ , such that $\mathbf{E} = -\nabla \phi - \frac{\partial \mathbf{A}}{\partial t}$. Both the scalar potential ϕ and the vector potential \mathbf{A} are not unique, as the electric and magnetic fields are invariant under the transformation $\phi \rightarrow \phi - \frac{\partial \Lambda}{\partial t}$, $\mathbf{A} \rightarrow \mathbf{A} + \nabla \Lambda$, where Λ is an arbitrary function of space and time. This is known as the gauge symmetry of the electromagnetic field.

The Maxwell's equations can be re-formulated by introducing the four-potential $A^\mu = (\phi, \mathbf{A})$, such that the electromagnetic field tensor $F^{\mu\nu}$ can be written as $F^{\mu\nu} = \partial^\mu A^\nu - \partial^\nu A^\mu$.

The Maxwell's equations can be written in terms of the field tensor as:

$$\partial_\mu F^{\mu\nu} = \mu_0 J^\nu, \quad \partial_\alpha F_{\beta\gamma} + \partial_\beta F_{\gamma\alpha} + \partial_\gamma F_{\alpha\beta} = 0, \quad (2.16)$$

where $J^\nu = (\rho, \mathbf{J})$ is the four-current. This is known as the covariant form of the Maxwell's equations. The gauge symmetry of the electromagnetic field can be written as $A^\mu \rightarrow A^\mu + \partial^\mu \Lambda$, where Λ is an arbitrary function of space and time.

Using this formalism, the Lagrangian for an electromagnetic field can be expressed as follows:

$$\mathcal{L} = -\frac{1}{4} F^{\mu\nu} F_{\mu\nu} + A_\mu J^\mu, \quad (2.17)$$

The Lagrangian is invariant under gauge transformations, which is fundamental to the formulation of quantum electrodynamics (QED). As we will show in the following chapter, the gauge symmetry invariance leads to the interaction between the electromagnetic field and charged particles, for example, electrons and positrons. This interaction is mediated by the exchange of photons, which are the gauge bosons of the electromagnetic field.

2.1.2 Quantum electrodynamics

In the quest of finding an equation that would not only describe particles correctly and respect the symmetries of the Lorentz transformations, Paul Dirac proposed a first-order linear differential equation, known as the Dirac equation,

$$(i\gamma^\mu \partial_\mu - m)\psi = 0, \quad (2.18)$$

where ψ is the Dirac spinor, γ^μ are the Dirac matrices, and m is the mass of the particle. The γ^μ matrices are defined as follows:

$$\gamma^0 = \begin{pmatrix} I_2 & 0 \\ 0 & -I_2 \end{pmatrix}, \gamma^i = \begin{pmatrix} 0 & \sigma^i \\ -\sigma^i & 0 \end{pmatrix}, \quad (2.19)$$

where I_2 is the identity matrix, and σ^i are the Pauli matrices. The Lagrangian of the Dirac field theory, which is based on the Dirac equation, can be written as:

$$\mathcal{L} = \bar{\psi}(i\gamma^\mu \partial_\mu - m)\psi, \quad (2.20)$$

where $\bar{\psi} = \psi^\dagger \gamma^0$ is the Dirac adjoint. Using the Euler-Lagrange equation, the Dirac equation can be derived from the Lagrangian. Under a global phase transformation $\psi \rightarrow e^{i\alpha}\psi$, the Lagrangian remains invariant, which implies that the Dirac field theory is invariant under global $U(1)$ transformations. However, the Dirac field theory is not invariant under local $U(1)$ transformations, where the phase transformation α is allowed to vary with space and time. To make the theory invariant under local $U(1)$ transformations, like in the classical field theory, a gauge field A_μ is introduced, such that the covariant derivative D_μ can be written as:

$$D_\mu = \partial_\mu - iqA_\mu, \quad (2.21)$$

where q is the charge of the particle. The full Lagrangian of the QED theory can be written as:

$$\mathcal{L}_{QED} = \bar{\psi}(i\gamma^\mu D_\mu - m)\psi - \frac{1}{4}F^{\mu\nu}F_{\mu\nu}, \quad (2.22)$$

Under a local $U(1)$ transformations, the first term of the Lagrangian remains invariant:

$$D_\mu \psi \rightarrow (\partial_\mu - iqA_\mu)e^{iq\alpha}\psi = e^{iq\alpha}D_\mu \psi, \quad (2.23)$$

The second term of the \mathcal{L}_{QED} , $F^{\mu\nu}F_{\mu\nu}$, which describes the the electromagnetic field, is also invariant under local $U(1)$ transformations.

From a physics perspective, the QED theory describes the interaction between charged particles and the electromagnetic field. In the Dirac term in the Lagrangian, the covariant derivative D_μ includes the electromagnetic interaction through the potential A_μ . And the interaction term $i e \bar{\psi} \gamma^\mu A_\mu \psi$ shows how the charge particle field interacts with the electromagnetic field. The photon term in the Lagrangian, $-\frac{1}{4} F^{\mu\nu} F_{\mu\nu}$, describes the quanta of electromagnetic field. The form of the QED Lagrangian also explains the massless nature of the photon, as including the photon mass term would break the gauge invariance of the theory.

The QED theory is a renormalisable theory, to all orders in perturbation theory the divergences in the theory can be absorbed into the redefinition of the mass and charge of the particle.

2.1.3 Quantum Chromodynamics

Quantum Chromodynamics (QCD) is the theory that describes the strong interaction, which binds quarks and gluons into protons, neutrons, and other hadrons. QCD is a type of quantum field theory known as a non-Abelian gauge theory, based on the symmetry group $SU(3)$. The Lagrangian of QCD is given by the Yang-Mills equation:

$$\mathcal{L}_{QCD} = \bar{\psi} (i \gamma^\mu D_\mu - m) \psi - \frac{1}{4} G_{\mu\nu}^a G^{a\mu\nu}. \quad (2.24)$$

Here, ψ represents the quark fields, $D_\mu = \partial_\mu - i g_s A_\mu^a T^a$ is the covariant derivative, A_μ^a are the gluon fields, T^a are the generators of the $SU(3)$ group, g_s is the strong coupling constant, and $G_{\mu\nu}^a = \partial_\mu A_\nu^a - \partial_\nu A_\mu^a + g_s f^{abc} A_\mu^b A_\nu^c$ is the gluon field strength tensor, with f^{abc} being the structure constants of $SU(3)$.

To derive the QCD Lagrangian starting from the SU(3) transformation, we need to follow a few steps. We will begin with the free Dirac Lagrangian and then introduce the SU(3) gauge fields. The free Dirac Lagrangian that describes the motion of quarks is given by

$$\mathcal{L}_{\text{free}} = \bar{\psi}(i\gamma^\mu \partial_\mu - m)\psi, \quad (2.25)$$

where ψ is the quark field, m is the quark mass, and γ^μ are the gamma matrices. The quark field transforms under SU(3) as:

$$\psi \rightarrow U(x)\psi = e^{i\alpha^a(x)T^a}\psi, \quad (2.26)$$

where $U(x)$ is an element of the SU(3) group, with T^a being the generators of SU(3) and $\alpha^a(x)$ being the parameters of the transformation. To maintain local SU(3) gauge invariance, we replace the partial derivative ∂_μ with the covariant derivative D_μ , defined as:

$$D_\mu = \partial_\mu - ig_s A_\mu^a T^a, \quad (2.27)$$

where g_s is the strong coupling constant, A_μ^a are the gluon fields. Similar to the QED, the covariant derivative now transforms as:

$$D_\mu \psi \rightarrow U(x) D_\mu \psi. \quad (2.28)$$

Substitute the covariant derivative into the free Dirac Lagrangian

$$\mathcal{L}_{\text{QCD}} = \bar{\psi}(i\gamma^\mu D_\mu - m)\psi. \quad (2.29)$$

This ensures that the Lagrangian is invariant under local SU(3) transformations.

As we introduced, the kinetic term for the gluon fields is:

$$\mathcal{L}_{\text{gluon}} = -\frac{1}{4}G_{\mu\nu}^a G^{a\mu\nu}. \quad (2.30)$$

Combining the quark and gluon parts, we obtain the full QCD Lagrangian in Equation 2.24

In a non-Abelian group like SU(3), the generators T^a (where $a = 1, 2, \dots, 8$ for SU(3)) do not commute. This means that for any two generators T^a and T^b :

$$[T^a, T^b] = i f^{abc} T^c, \quad f^{abc} \neq 0. \quad (2.31)$$

The form of the QCD Lagrangian is similar to the QED Lagrangian, with the quark fields interacting with the gluon fields by term $g_s \bar{\psi} \gamma^\mu A_\mu^a T^a \psi$. The term $g_s f^{abc} A_\mu^b A_\nu^c$, shows that the gluons interact with each other, unlike the photons in QED, giving rise to the self-interaction of the gluon fields. Physically, quarks come in three types of colour charges, conventionally labelled as red, green, and blue. These colours are purely symbolic and represent the different states of the SU(3) symmetry; anti-quarks carry anti-colours: anti-red, anti-green, and anti-blue. One of the most striking features of QCD is colour confinement, which means that quarks and gluons are never found in isolation; they are always confined within hadrons. The force between quarks does not diminish as they move apart. Instead, it remains strong or even increases, preventing the isolation of individual quarks. At very short distances (high energies), the coupling constant g_s becomes small, and quarks behave as if they are free. This phenomenon is known as asymptotic freedom, and it is one of the key features of QCD. To understand the running of g_s we begin with the renormalisation group equation (RGE), which governs the scale dependence of the coupling constant. The evolution of g_s with respect to the energy scale μ is described by the beta function, $\beta(g_s)$. At one-loop level, the beta function for QCD is

given by:

$$\beta(g_s) = \mu \frac{\partial g_s}{\partial \mu} = -\beta_0 \frac{g_s^3}{16\pi^2}. \quad (2.32)$$

Here, β_0 is a constant that depends on the number of active quark flavours n_f . Specifically, β_0 is expressed as

$$\beta_0 = 11 - \frac{2}{3}n_f \quad (2.33)$$

For the case of QCD with three light quark flavours ($n_f = 3$), we have $\beta_0 = 9$.

To determine how g_s varies with the energy scale μ , we integrate the renormalisation group equation

$$\frac{1}{g_s^2(\mu)} = \frac{1}{g_s^2(\mu_0)} + \frac{\beta_0}{8\pi^2} \ln\left(\frac{\mu}{\mu_0}\right). \quad (2.34)$$

This equation illustrates how the strong coupling constant g_s evolves with the energy scale μ . It explicitly shows that g_s decreases as μ increases, demonstrating the property of asymptotic freedom. It is often convenient to express the running of the coupling constant in terms of the strong coupling parameter α_s , defined as:

$$\alpha_s = \frac{g_s^2}{4\pi} \quad (2.35)$$

Substituting g_s in terms of α_s in the running equation, we obtain:

$$\alpha_s(\mu) = \frac{\alpha_s(\mu_0)}{1 + \frac{\alpha_s(\mu_0)\beta_0}{2\pi} \ln\left(\frac{\mu}{\mu_0}\right)} \quad (2.36)$$

Figure 2.2 shows the running of the strong coupling constant α_s with the energy scale μ , as well as experimental measurements of α_s at different energy scales from various experiments.

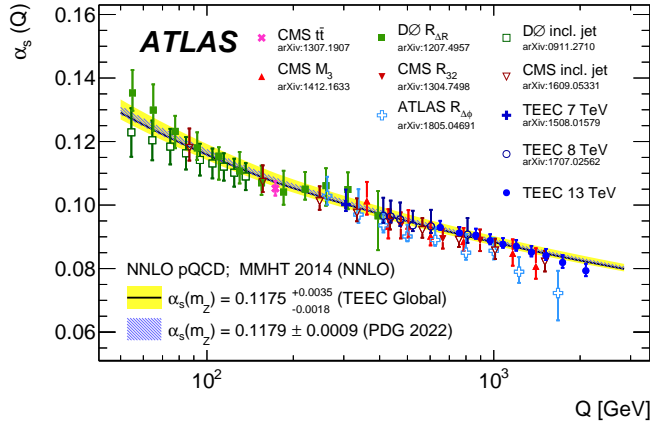


Fig. 2.2 The running of the strong coupling constant α_s with the energy scale μ in QCD, taken from [9]. The coupling constant decreases as the energy scale increases, demonstrating asymptotic freedom. The experimental measurements of α_s at different energy scales are also shown.

2.1.4 Weak force

The concept of the weak force emerged in the early 20th century with the study of radioactive decay. In 1934, Enrico Fermi formulated a theory of beta decay [10] that introduced the idea of a charged current weak interaction, which was responsible for the transformation of a neutron into a proton, an electron, and an antineutrino. This interaction was initially thought to be mediated by a contact force, similar to the classical idea of collisions between billiard balls. The theoretical framework for understanding the weak force significantly advanced in the 1950s and 1960s. The development of gauge theory and the unification of electromagnetic and weak interactions into the electroweak theory, proposed by Sheldon Glashow, Abdus Salam, and Steven Weinberg [11], led to a comprehensive understanding of the weak force. This theory was experimentally confirmed by the discovery of the W and Z bosons in 1983 [12] at the CERN laboratory, for which the Nobel Prize was awarded. Despite its relatively short range and the fact that it is much weaker than both the strong force and electromagnetism, the weak force is responsible for a variety of processes that are fundamental to particle physics and cosmology, such as beta decay, quark flavour change and CP violation.

Chirality refers to the intrinsic property of fermions that distinguishes left-handed (L) from right-handed (R) components. It is defined using the projection operators:

$$P_L = \frac{1}{2}(1 - \gamma_5), \quad P_R = \frac{1}{2}(1 + \gamma_5), \quad (2.37)$$

where $\gamma_5 = i\gamma^0\gamma^1\gamma^2\gamma^3$ is the fifth gamma matrix in the Dirac algebra. Applying these projectors, the left-handed and right-handed components of a fermion field ψ are:

$$\psi_L = P_L\psi = \frac{1}{2}(1 - \gamma_5)\psi, \quad \psi_R = P_R\psi = \frac{1}{2}(1 + \gamma_5)\psi. \quad (2.38)$$

The charged weak interaction exclusively couples to left-handed fermions and right-handed antifermions. This chiral nature of the weak force is a key feature distinguishing it from other fundamental forces.

Isospin symmetry, originally introduced to describe the proton and neutron, can also be applied to leptons within the context of the weak interaction. Leptons, like quarks, can be arranged into doublets under the $SU(2)_L$ symmetry of the weak interaction. Each generation of leptons consists of a left-handed doublet and right-handed singlets. For the first generation:

$$\begin{pmatrix} \nu_e \\ e \end{pmatrix}_L, \quad e_R \quad (2.39)$$

Here, ν_e is the electron neutrino, and e is the electron. The weak isospin (I) and its third component (I_3) are assigned as follows:

- The electron neutrino ν_e and electron e form an isospin doublet with $I = \frac{1}{2}$.
- The third component of weak isospin I_3 for ν_e is $+\frac{1}{2}$, and for e it is $-\frac{1}{2}$.
- Right-handed leptons, such as e_R , are singlets under $SU(2)_L$ and thus have $I = 0$.

The seminal experiment by Chien-Shiung Wu in 1957 [13] demonstrated parity violation in the beta decay of cobalt-60. The electrons emitted in the decay exhibited a preferred direction relative to the spin of the nuclei, indicating a violation of parity symmetry. The weak interaction Lagrangian, incorporating the $SU(2)_L$ gauge fields, is given by:

$$\mathcal{L}_{\text{weak}} = \bar{\psi}_L i\gamma^\mu D_\mu \psi_L, \quad (2.40)$$

where ψ_L represents the left-handed fermion doublets and D_μ is the covariant derivative defined as:

$$D_\mu = \partial_\mu - ig \frac{\sigma^a}{2} W_\mu^a. \quad (2.41)$$

Here, W_μ^a are the gauge fields associated with $SU(2)_L$, g is the coupling constant, and σ^a are the Pauli matrices. The presence of the γ^5 term results in the distinct treatment of left-handed and right-handed components, leading to parity violation. The implications of this phenomenon includes the observation that neutrinos are left-handed and antineutrinos are right-handed.

2.1.5 Electroweak unification and the Higgs mechanism

The electroweak theory in the Standard Model unifies the weak and electromagnetic interactions. The Lagrangian includes terms for the gauge fields, their interactions with fermions, and the Higgs mechanism.

Electroweak unification

The gauge field terms describe the dynamics of the $SU(2)_L$ and $U(1)_Y$ gauge fields:

$$\mathcal{L}_{\text{gauge}} = -\frac{1}{4} W_{\mu\nu}^a W^{a\mu\nu} - \frac{1}{4} B_{\mu\nu} B^{\mu\nu}.$$

$W_{\mu\nu}^a$ is the field strength tensor for the $SU(2)_L$ gauge fields W_μ^a ($a = 1, 2, 3$):

$$W_{\mu\nu}^a = \partial_\mu W_\nu^a - \partial_\nu W_\mu^a + g\epsilon^{abc} W_\mu^b W_\nu^c,$$

where g is the $SU(2)_L$ coupling constant, and ϵ^{abc} are the structure constants of $SU(2)_L$.

$B_{\mu\nu}$ is the field strength tensor for the $U(1)_Y$ gauge field B_μ :

$$B_{\mu\nu} = \partial_\mu B_\nu - \partial_\nu B_\mu.$$

The interaction of fermions with the gauge fields is described by the covariant derivative acting on the fermion fields:

$$\mathcal{L}_{\text{fermion}} = \bar{\psi}_L i\gamma^\mu D_\mu \psi_L + \bar{\psi}_R i\gamma^\mu \partial_\mu \psi_R.$$

ψ_L represents the left-handed fermion doublets:

$$\psi_L = \begin{pmatrix} \nu_e \\ e \end{pmatrix}_L, \quad \begin{pmatrix} u \\ d' \end{pmatrix}_L,$$

where d' is a linear combination of down-type quarks (d, s, b) due to quark mixing. ψ_R represents the right-handed fermion singlets:

$$e_R, \quad u_R, \quad d_R.$$

The covariant derivative D_μ for left-handed fermions is:

$$D_\mu = \partial_\mu - ig \frac{\tau^a}{2} W_\mu^a - ig' \frac{Y}{2} B_\mu,$$

where τ^a are the Pauli matrices, g and g' are the coupling constants for $SU(2)_L$ and $U(1)_Y$, respectively, and Y is the hypercharge.

The Higgs mechanism involves the Higgs field ϕ , which breaks the electroweak symmetry and gives mass to the W and Z bosons:

$$\mathcal{L}_{\text{Higgs}} = (D_\mu \phi)^\dagger (D_\mu \phi) - V(\phi).$$

The covariant derivative $D_\mu \phi$ is:

$$D_\mu \phi = \left(\partial_\mu - ig \frac{\tau^a}{2} W_\mu^a - ig' \frac{Y}{2} B_\mu \right) \phi.$$

The Higgs field ϕ is an $SU(2)_L$ doublet:

$$\phi = \begin{pmatrix} \phi^+ \\ \phi^0 \end{pmatrix}.$$

The Higgs potential $V(\phi)$ is:

$$V(\phi) = \mu^2 \phi^\dagger \phi + \lambda (\phi^\dagger \phi)^2.$$

Higgs mechanism and spontaneous symmetry breaking

The Higgs mechanism explains how the W and Z bosons acquire mass through spontaneous symmetry breaking of the electroweak symmetry. The Higgs field ϕ acquires a non-zero vacuum expectation value (VEV):

$$\langle \phi \rangle = \frac{1}{\sqrt{2}} \begin{pmatrix} 0 \\ v \end{pmatrix},$$

where $v \approx 246$ GeV is the VEV of the Higgs field. The potential $V(\phi)$ has a minimum at $\phi^\dagger\phi = \frac{v^2}{2}$, as shown in Figure 2.3. When the Higgs field takes its VEV, the $SU(2)_L \times U(1)_Y$

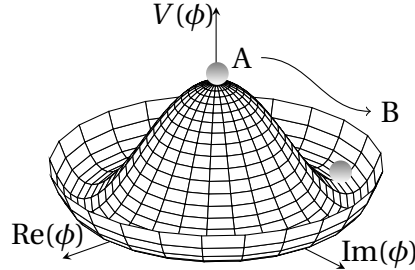


Fig. 2.3 Higgs potential $V(\phi)$ with a minimum at $\phi^\dagger\phi = \frac{v^2}{2}$.

symmetry is spontaneously broken down to $U(1)_{\text{em}}$, the gauge symmetry of electromagnetism. Three of the four degrees of freedom in the Higgs doublet become the longitudinal components of the W and Z bosons, giving them mass. The remaining degree of freedom manifests as the physical Higgs boson.

The masses of the W and Z bosons arise from the interaction between the gauge fields and the Higgs field. The charged W bosons (W^\pm) acquire mass through the term involving the Higgs VEV:

$$(D_\mu \langle \phi \rangle)^\dagger (D_\mu \langle \phi \rangle).$$

Expanding the covariant derivative:

$$D_\mu \langle \phi \rangle = \left(\partial_\mu - ig \frac{\tau^a}{2} W_\mu^a - ig' \frac{Y}{2} B_\mu \right) \frac{1}{\sqrt{2}} \begin{pmatrix} 0 \\ v \end{pmatrix}.$$

The term $\frac{1}{2}g\nu W_\mu^1 - \frac{1}{2}g\nu W_\mu^2$ gives rise to the mass of the W bosons:

$$M_W = \frac{gv}{2}.$$

The neutral Z boson acquires mass similarly, but involves a mixture of W^3 and B :

$$Z_\mu = \cos\theta_W W_\mu^3 - \sin\theta_W B_\mu,$$

where θ_W is the Weinberg angle. The mass of the Z boson is:

$$M_Z = \frac{\sqrt{g^2 + g'^2} v}{2}.$$

The photon remains massless because the corresponding combination of W^3 and B :

$$A_\mu = \sin\theta_W W_\mu^3 + \cos\theta_W B_\mu,$$

does not acquire a mass term from the Higgs mechanism.

Generation of fermion masses

The masses of the fermions (quarks and leptons) in the Standard Model are generated through their interactions with the Higgs field. This mechanism, known as the Yukawa interaction, couples the fermions to the Higgs field, leading to mass terms once the Higgs field acquires a VEV. The Yukawa interactions describe the coupling between the Higgs field and the fermions. The relevant terms in the Lagrangian for a single generation of quarks are:

$$\mathcal{L}_{\text{Yukawa}} = -y_u \bar{Q}_L \tilde{\phi} u_R - y_d \bar{Q}_L \tilde{\phi} d_R + \text{h.c.}$$

Q_L is the left-handed quark doublet:

$$Q_L = \begin{pmatrix} u_L \\ d_L \end{pmatrix}.$$

u_R and d_R are the right-handed up-type and down-type quark singlets, respectively. y_u and y_d are the Yukawa coupling constants for the up-type and down-type quarks, respectively.

Recall the VEV of the Higgs field:

$$\langle \phi \rangle = \frac{1}{\sqrt{2}} \begin{pmatrix} 0 \\ v \end{pmatrix}.$$

Substituting the VEV of the Higgs field into the Yukawa Lagrangian, we obtain the mass terms for the quarks:

$$\mathcal{L}_{\text{Yukawa}} = -y_u \bar{Q}_L \begin{pmatrix} 0 \\ \frac{v}{\sqrt{2}} \end{pmatrix} u_R - y_d \bar{Q}_L \begin{pmatrix} \frac{v}{\sqrt{2}} \\ 0 \end{pmatrix} d_R + \text{h.c.}$$

This simplifies to:

$$\mathcal{L}_{\text{Yukawa}} = -\frac{y_u v}{\sqrt{2}} \bar{u}_L u_R - \frac{y_d v}{\sqrt{2}} \bar{d}_L d_R + \text{h.c.}$$

The terms $\bar{u}_L u_R$ and $\bar{d}_L d_R$ are Dirac mass terms for the up-type and down-type quarks, respectively. Identifying the mass terms, we have:

$$m_u = \frac{y_u v}{\sqrt{2}}, \quad m_d = \frac{y_d v}{\sqrt{2}}.$$

Thus, the masses of the quarks are proportional to their respective Yukawa couplings.

The generation of lepton masses follows a similar process, the Yukawa interactions for the leptons are given by:

$$\mathcal{L}_{\text{Yukawa}} = -y_e \bar{L}_L \phi e_R + \text{h.c.}$$

where L_L is the left-handed lepton doublet:

$$L_L = \begin{pmatrix} \nu_{eL} \\ e_L \end{pmatrix}.$$

where y_e is the Yukawa coupling constant for the electron. Substituting the VEV of the Higgs field into the Yukawa Lagrangian for leptons, we get:

$$\mathcal{L}_{\text{Yukawa}} = -y_e \bar{L}_L \begin{pmatrix} 0 \\ \frac{v}{\sqrt{2}} \end{pmatrix} e_R + \text{h.c.}$$

This simplifies to:

$$\mathcal{L}_{\text{Yukawa}} = -\frac{y_e v}{\sqrt{2}} \bar{e}_L e_R + \text{h.c.}$$

The term $\bar{e}_L e_R$ is a Dirac mass term for the electron (or charged lepton), and the mass of the electron is:

$$m_e = \frac{y_e v}{\sqrt{2}}.$$

Therefore, the mass of the electron (or any charged lepton) is also proportional to its respective Yukawa coupling.

2.2 A gravitational extension to the Standard Model

One potential extension for the SM to describe gravitation is proposed by Lisa Randall and Raman Sundrum [5], exploring the framework of a new higher-dimensional mechanism for solving the hierarchy problem [14]. This model proposes a geometric solution to the hierarchy problem and predicts the existence of Kaluza-Klein (KK) Graviton modes [15]. Detailed explanations of technical aspects discussed briefly below can be found in ref. [5, 14, 15]. The Randall-Sundrum (RS) model provides a geometric interpretation of the hierarchy between the gravitational scale, $M_P \sim 10^{18} \text{ GeV}$, and the weak scale, $M_W \sim 10^2 \text{ GeV}$. In this model, the background geometry is a five-dimensional Anti-de Sitter space (AdS_5), characterised by a constant negative curvature, and is truncated by two four-dimensional Minkowski branes separated by a fixed distance [14]. The model assumes that all relevant parameters arise naturally from various powers of the five-dimensional

fundamental scale, $M_5 \sim M_P$. In the RS framework, the SM fields are confined to one of the four-dimensional boundaries, commonly referred to as the SM brane. The metric induced on this brane generates a physical scale $\Lambda_\pi \sim M_W$ from the five-dimensional fundamental scale M_5 , achieved through an exponential geometric warp factor [14]. This warping effect eliminates the need to introduce large hierarchies, as the exponential factor naturally bridges the gap between the fundamental and electroweak scales. A key prediction of the RS model is the appearance of spin-2 resonances, $G^{(n)}$, which represent the Kaluza-Klein (KK) excitations of the five-dimensional Graviton. The masses and couplings of these resonances are determined by the physical scale Λ_π , making them potentially significant for processes occurring at the weak scale.

The RS model involves a 5D spacetime with the following metric:

$$ds^2 = e^{-2kr_c|\phi|} \eta_{\mu\nu} dx^\mu dx^\nu - r_c^2 d\phi^2,$$

where k is a scale of order the Planck scale. $\eta_{\mu\nu}$ is the 4D Minkowski metric. ϕ is the coordinate of the extra dimension, ranging from $-\pi$ to π . In this space, four-dimensional mass scales are related to five-dimensional mass parameters and the $e^{-2kr_c|\phi|}$, the warp factor. In the RS model, the Graviton field $h_{\mu\nu}(x, \phi)$ can be expanded in terms of KK modes:

$$h_{\mu\nu}(x, \phi) = \sum_{n=0}^{\infty} h_{\mu\nu}^{(n)}(x) \frac{e^{-2kr_c|\phi|} \chi^{(n)}(\phi)}{\sqrt{r_c}},$$

where $h_{\mu\nu}^{(n)}(x)$ are the 4D Graviton modes. $\chi^{(n)}(\phi)$ are the wave-functions of the KK modes that only depend on the extra dimension, ϕ and r_c . $\chi^{(n)}(\phi)$ can be written as:

$$\chi^{(n)}(\phi) \approx \frac{e^{2kr_c|\phi|}}{N_n} J_2\left(\frac{m_n}{k} e^{-kr_c|\phi|}\right),$$

where J_l is the l^{th} order Bessel function. m_n is the mass of the n^{th} KK Graviton, and N_n is a normalisation factor, given by:

$$N_n \approx \frac{e^{kr_c\pi}}{\sqrt{kr_c}} J_2(x_n).$$

The effective 4D Lagrangian for the interaction between KK Gravitons and the SM fields is:

$$\mathcal{L}_{\text{eff}} = -[\frac{1}{M_P} h_{\mu\nu}^{(0)} T^{\mu\nu} - \frac{1}{\Lambda_\pi} \sum_{n=1}^{\infty} h_{\mu\nu}^{(n)}] T^{\mu\nu},$$

where $T^{\mu\nu}$ is the energy-momentum tensor of the SM fields and $\Lambda_\pi = M_P e^{-kr_c\pi}$ is the effective scale on the TeV brane. Studies of the RS model have focused on the \mathcal{L}_{eff} interaction. These interactions are only suppressed by Λ_π . In this thesis, we focus on the Graviton coupling to the SM Higgs boson, with low-TeV masses, the production cross section of the Higgs boson pairs from the KK Graviton resonances is predicted to be significant at the current energy frontier. The 5D action, which describes gravity in the RS model, is:

$$S_G = 2M_5^3 \int d^5x \sqrt{-G} R_5,$$

where M_5 is the 5D Planck scale, G is the determinant of the 5D metric G_{MN} , and R_5 is a 5D scalar. Interactions also occur between the $G^{(n)}$ resonances arising from the S_G . The leading term in this self-coupling, in terms of powers of M_5^{-1} , is the triple Graviton vertex. In four dimensions, this implies that the coupling between three KK Gravitons $\{G^{(l)}, G^{(m)}, G^{(n)}\}$, is governed by powers of Λ_π^{-1} , making it the dominant interaction within the KK Graviton sector.

2.3 Modelling proton-proton collisions in particle physics

Proton-proton collisions, such as those studied at the Large Hadron Collider, are complex processes modelled in several stages: parton distribution functions, hard scattering, parton showering, hadronisation, and underlying events. A typical collision is shown in Figure 2.4.

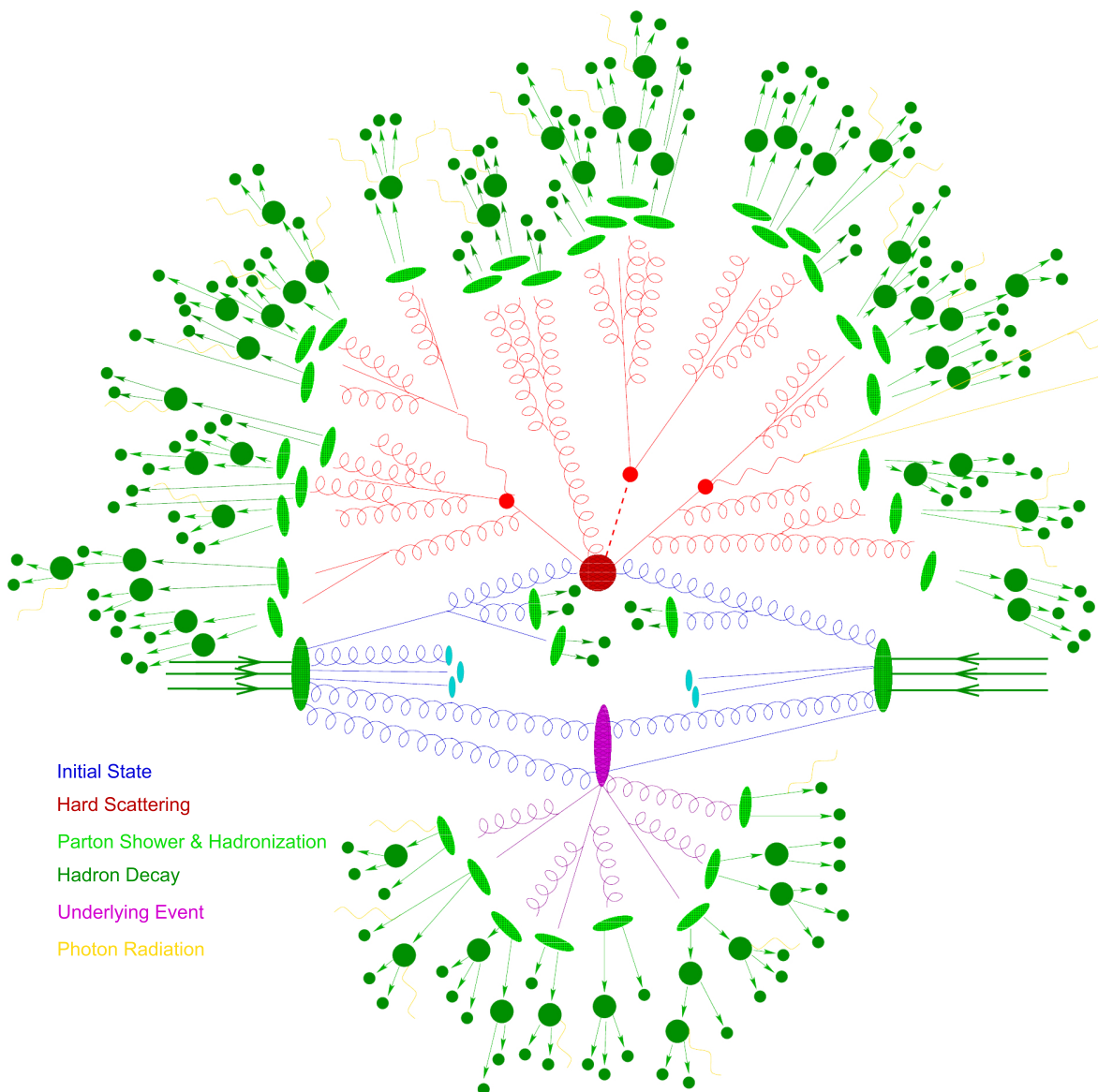


Fig. 2.4 Sketch of how a hadron collision is modelled. In particular, one can notice the initial states, hard scattering, parton shower, hadronisation and the so-called underlying event. From INFN web-page [16].

2.3.1 Parton Distribution Functions (PDFs)

Protons are not fundamental particles; they are bound states of *uud* quarks and gluons, collectively known as partons. The PDF, $f_i(x, Q^2)$, gives the probability density for finding a parton of type i (where i could be u, d, s, c, t, b for quarks and g for gluons) with a momentum fraction x at a scale Q^2 :

$$f_i(x, Q^2) = x q_i(x, Q^2),$$

where $q_i(x, Q^2)$ is the number density of partons of type i . The PDFs are extracted from experimental data and theoretical calculations and are essential for predicting initial states in collisions. The Dokshitzer-Gribov-Lipatov-Altarelli-Parisi (DGLAP) equations describe how PDFs evolve with the energy scale Q^2 :

$$\frac{\partial f_i(x, Q^2)}{\partial \ln Q^2} = \sum_j \int_x^1 \frac{dy}{y} P_{ij} \left(\frac{x}{y}, \alpha_s(Q^2) \right) f_j(y, Q^2),$$

where $P_{ij}(z, \alpha_s)$ are the splitting functions, which describe the probability of a parton j splitting into a parton i with a fraction z of the momentum. And $\alpha_s(Q^2)$ is the strong coupling constant.

The DGLAP equations can be written in a convolution form, showing the relationship between PDFs and splitting functions:

$$\frac{\partial f_i(x, Q^2)}{\partial \ln Q^2} = \sum_j (P_{ij} \otimes f_j)(x, Q^2),$$

where the convolution is defined as:

$$(P_{ij} \otimes f_j)(x, Q^2) = \int_x^1 \frac{dy}{y} P_{ij} \left(\frac{x}{y}, \alpha_s(Q^2) \right) f_j(y, Q^2).$$

In a proton-proton collision, the differential cross-section for a process $pp \rightarrow X$ involving partons i and j can be written as:

$$d\sigma = \sum_{i,j} \int dx_1 dx_2 f_i(x_1, Q^2) f_j(x_2, Q^2) d\hat{\sigma}_{ij \rightarrow X},$$

where $d\hat{\sigma}_{ij \rightarrow X}$ is the partonic cross-section for the subprocess $ij \rightarrow X$. One of the most widely used PDF sets are produced by the NNPDF (NN-based Parton Distribution Function) collaboration, which uses neural networks to parameterise PDFs [17]. The NNPDF4.0NNLO sets are shown in Figure 2.5 for the PDFs at $Q = 3.2$ GeV and $Q = 100$ GeV. This set approximates the PDFs at next-to-next-to-leading order (NNLO) precision. The latest NNPDF releases incorporate QED corrections, marking a significant step

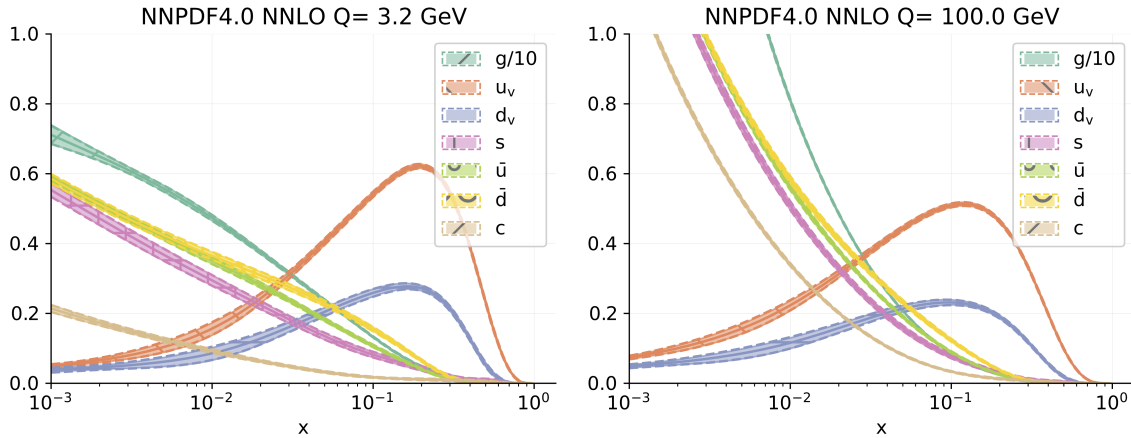


Fig. 2.5 The NNPDF4.0NNLO parton distribution functions at $Q = 3.2$ GeV and $Q = 100$ GeV [17].

forward [18]. They account for the photon parton distribution function, which, although a small correction, impacts the momentum fraction carried by the gluon. The collaboration has made steps towards the next order of precision, approximate N3LO (Next-to-Next-to-Next-to-Leading Order). The N3LO PDFs includes higher-order corrections in the PDFs, the predictions improves. The N3LO PDFs are consistent with NNLO results within uncertainties [19]. A significant milestone achieved by the NNPDF collaboration is the evidence for intrinsic charm quarks within the proton. The intrinsic charm component

was disentangled from charm-anticharm pairs arising from high-energy radiation, with a significance of three standard deviations [20].

2.3.2 Parton shower, hadronisation, and underlying event

After the initial hard scatter, the high-energy partons undergo a cascade of emissions, producing more partons. This process, described by perturbative QCD, includes both initial-state radiation (before the collision) and final-state radiation (after the collision). The parton shower accounts for the sequential splitting of partons, resulting in a multitude of lower-energy partons. As partons cannot exist in isolation due to colour confinement, they must transform into colour-neutral hadrons. Hadronisation is a non-perturbative process where partons combine to form hadrons (e.g., pions, protons). Two common models used to describe hadronisation are the Lund string model and cluster fragmentation. This process occurs over a very short distance and time scale, effectively turning the showered partons into detectable particles. Besides the primary hard scatter, other interactions occur in the collision, collectively known as the underlying event. This includes additional soft parton interactions, beam-beam remnants (particles that do not participate in the hard scatter). The underlying event contributes to the overall activity observed in a collision and must be accurately modelled to distinguish the signal from the background. Together, these processes transform the initial high-energy partons into a rich final state of hadrons that experimental detectors can observe and analyse. Understanding each stage is crucial for accurate simulation and interpretation of collider data.

Chapter 3

The ATLAS detector at the LHC

3.1 CERN and the Large Hadron Collider (LHC)

The European Organisation for Nuclear Research, known as CERN, was founded in 1954 with the aim of establishing a world-class laboratory for particle physics research. Located on the border between France and Switzerland, near Geneva, CERN was established by 12 European countries to promote scientific collaboration in post-war Europe. Its creation marked a significant step in fostering international cooperation in the field of fundamental physics. The modern CERN accelerator complex is shown in Figure 3.1.

CERN's early years were marked by the construction of pioneering accelerators, such as the Synchrocyclotron (SC) [22] in 1957 and the Proton Synchrotron (PS) in 1959 [23]. The SC was CERN's first accelerator, used for nuclear physics experiments, while the PS, with a beam energy of 28 GeV, became instrumental in numerous discoveries, including the observation of neutral currents in 1973. The PS's success laid the groundwork for more advanced facilities and experiments.

In 1976, the Super Proton Synchrotron (SPS) [24] began operations, serving both as a particle accelerator and a storage ring. The SPS played a pivotal role in the discovery of the W and Z bosons in 1983, work that earned Carlo Rubbia and Simon van der Meer

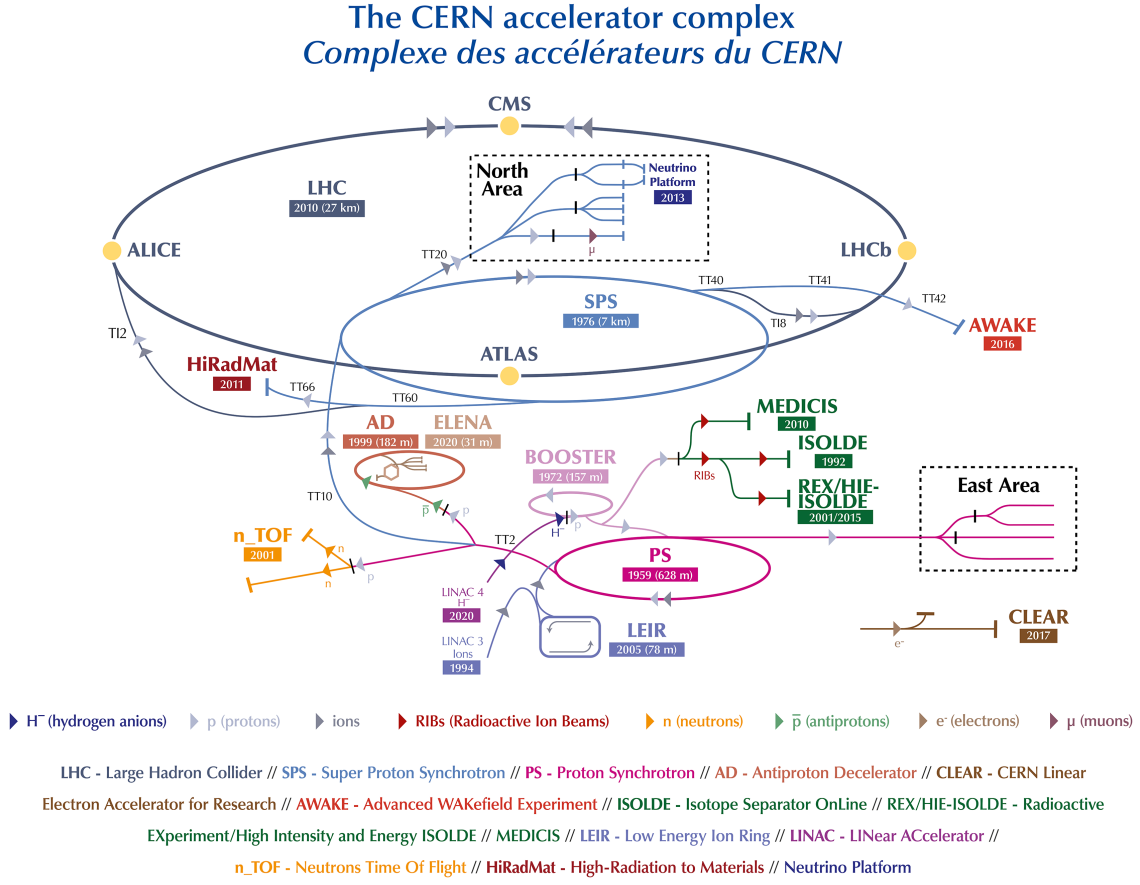


Fig. 3.1 The CERN accelerator complex, including the Large Hadron Collider (LHC) and its experiments, taken from [21]

the Nobel Prize in Physics. These discoveries helped confirm the electroweak theory, a fundamental component of the Standard Model of particle physics.

The Large Electron-Positron Collider (LEP) [25] was a groundbreaking particle accelerator that operated at CERN from 1989 to 2000. Situated in the same 27-kilometre tunnel that now houses the LHC, LEP was designed to collide electrons and positrons at high energies to probe the fundamental constituents of matter. The construction of LEP was a significant engineering and scientific achievement, involving the development of advanced technologies and large-scale international collaboration. One of the notable accomplishments of LEP was its precision measurements of the Z boson [26], which

helped to confirm the electroweak theory. The collider's ability to produce clean and precise collisions of electrons and positrons allowed physicists to explore a wide range of phenomena with unprecedented accuracy. Over its 11 years of operation, LEP produced a wealth of scientific results that significantly enhanced our understanding of particle physics and laid the groundwork for future discoveries.

When LEP was decommissioned in 2000, its tunnel was repurposed for the LHC, which required substantial upgrades to handle the higher energy collisions of protons and heavy ions. The LHC [3], the most ambitious project at CERN, was officially inaugurated on October 21, 2008. It is designed to collide protons at unprecedented centre-of-mass energy levels, reaching up to 13.6 TeV. The LHC's primary objective is to explore the fundamental properties of matter and the forces governing the universe that beyond the Standard Model. The LHC hosts several major experiments, each with specific research goals and sophisticated detection apparatus. ATLAS (A Toroidal LHC ApparatuS) [27] and CMS (Compact Muon Solenoid) [28] are general-purpose detectors. These experiments played a central role in the discovery of the Higgs boson in 2012, a particle essential to the Standard Model as it provides evidence for the mechanism by which other elementary particles acquire mass. The LHCb (Large Hadron Collider beauty) [29] experiment focuses on investigating the differences between matter and antimatter by studying the decays of particles containing b (beauty) quarks. This research aims to understand why the universe is dominated by matter rather than antimatter, despite the expectation that both should have been produced in equal amounts during the Big Bang. ALICE (A Large Ion Collider Experiment) [30] is designed to study the properties of quark-gluon plasma, a state of matter thought to have existed shortly after the Big Bang. By colliding heavy ions, ALICE aims to recreate and analyse this plasma, providing insights into the strong force that binds quarks and gluons together to form protons and neutrons. TOTEM (TOTal Elastic and diffractive cross-section Measurement) [31] and LHCf (Large Hadron Collider

forward) focus on studying forward particles, those that travel close to the beamline, to gain insights into proton structure and the underlying dynamics of particle collisions. TOTEM measures the total cross-section, elastic scattering, and diffraction processes, while LHCf studies particles produced at very small angles to the beam direction.

3.1.1 The operation of the LHC

The LHC's operational phases have significantly advanced particle physics, combining upgrades and high-energy collisions to explore the fundamental aspects of matter and the universe. The ongoing and future upgrades, especially the HL-LHC, promise to further enhance our understanding and potentially lead to groundbreaking discoveries.

Run 1 (2009-2013)

Run 1 of the Large Hadron Collider (LHC) at CERN began in 2009 and continued until early 2013. During this period, the LHC operated at proton-proton (p-p) collision energies of 7 TeV (2010-2011) and 8 TeV (2012-2013), laying the groundwork for significant scientific discoveries and establishing the LHC as the world's most powerful particle accelerator. The most notable achievement of Run 1 was the discovery of the Higgs boson [32, 33] in July 2012 by the ATLAS and CMS experiments. This discovery confirmed the last missing component of the Standard Model of particle physics and garnered the 2013 Nobel Prize in Physics for theorists Francois Englert and Peter Higgs. Run 1 also involved extensive searches for new physics beyond the Standard Model, including searches for supersymmetry (SUSY) and extra dimensions, although no definitive evidence was found. Lead-lead (Pb-Pb) and proton-lead (p-Pb) collisions were also conducted during Run 1. Run 1 marked the successful commissioning of the LHC's complex systems, including its superconducting magnets, cryogenics, and detectors. Significant advancements in data acquisition and analysis techniques were developed, setting the stage for future runs.

Long Shutdown 1 (2013-2015)

Following the successful completion of Run 1, the LHC entered Long Shutdown 1 (LS1) from early 2013 to early 2015. During this period, significant maintenance and upgrades were carried out to prepare the LHC for higher energy collisions and increased luminosity in subsequent runs. LS1 involved enhancements to the accelerator's magnets, cryogenics, and beam instrumentation, ensuring improved performance and reliability.

Run 2 (2015-2018)

The LHC resumed operations in 2015 with Run 2. This phase saw the LHC operate at the higher energy of 13 TeV, leading to further significant discoveries and more precise measurements of the Higgs boson and other Standard Model particles [1]. The increased energy and luminosity provided new opportunities to search for physics beyond the Standard Model, although no new particles were discovered.

Long Shutdown 2 (2019-2021)

Following Run 2, the LHC entered Long Shutdown 2 (LS2) for maintenance and upgrades to prepare for even higher luminosity operations. The upgrades aimed to enhance the performance of the accelerator and detectors [34], ensuring improved data quality and higher collision rates. The COVID-19 pandemic had a notable impact on CERN's LS2. The pandemic necessitated strict health and safety measures, significantly affecting on-site work. CERN implemented remote working protocols and minimised on-site activities to protect staff and contractors. These disruptions caused delays in the planned maintenance and upgrades to the LHC and associated experiments. Despite these challenges, CERN managed to continue essential work, ensuring that critical upgrades were completed, albeit on a postponed schedule.

Run 3 (2022-present)

Run 3 began in 2022, operating at 13.6 TeV with further optimised conditions. This phase focuses on collecting more data to enhance the precision of existing measurements and explore new potential discoveries. Operating at higher energy required extensive calibration and tuning of the accelerator components to handle the increased energy and collision rates effectively. Global supply chain issues delayed the delivery of critical components, hindering technical improvements and maintenance work essential for efficient LHC operation during LS2 [35, 36]. Extensive calibration and validation of upgraded detectors were necessary to ensure accurate and reliable measurements, initially slowing down data collection. Despite these challenges, the LHC has ramped up its performance as technical issues are resolved in 2024. The upgraded systems are fully integrated and optimised. In run 3 the LHC has delivered over 160 fb^{-1} of data to the ATLAS and CMS experiments at the time of writing, with 101 fb^{-1} collected in 2024 alone.

3.1.2 Future LHC upgrades - The High-Luminosity LHC

The High-Luminosity Large Hadron Collider (HL-LHC) [37] is a major upgrade to the current LHC, designed to increase its luminosity by a factor of 5-10. Scheduled to start operations in the late-2020s, the HL-LHC aims to gather approximately 10 times more data than the existing LHC. This significant increase in luminosity will enhance the potential for new discoveries and provide more precise measurements of SM phenomena.

The HL-LHC will feature new, stronger superconducting magnets to better focus the proton beams, increasing the luminosity. Upgraded cryogenic systems will enhance the cooling power of the accelerator, crucial for maintaining the superconducting state of the magnets. The ATLAS, CMS, LHCb, and ALICE detectors will undergo significant enhancements to handle the increased collision rates and data throughput, ensuring they can capture and process the additional information effectively. Components will

be upgraded to withstand the higher levels of radiation expected from the increased luminosity, ensuring the longevity and reliability of the detector systems.

3.1.3 Future collider projects - the Future Circular Collider (FCC)

FCC [38] represents a bold vision for the next generation of particle accelerators, aiming to build upon the discoveries of the HL-LHC. The FCC is a proposed research infrastructure that would significantly extend our understanding of fundamental physics by exploring uncharted energy scales and precision measurements. It is designed to address key questions that remain unanswered in the Standard Model of particle physics and beyond. The FCC project encompasses two main collider configurations: the FCC-ee, a high-luminosity electron-positron collider, and the FCC-hh, a high-energy proton-proton collider. The FCC-ee is envisaged as a first step, providing precise measurements of the Higgs boson, W and Z bosons, and the top quark, while the FCC-hh will follow, offering collisions at energies up to 100 TeV, far exceeding the capabilities of the LHC.

The FCC-ee: A Precision Machine

The FCC-ee collider is designed to operate at various energy stages, initially focusing on Z boson production with centre-of-mass energies around 90 GeV, and subsequently increasing to study the W boson, Higgs boson, and top quark at higher energies. With its unprecedented luminosity and precision, the FCC-ee will provide high-precision measurements of the Higgs boson properties, improved determinations of the W and Z boson masses and couplings, and detailed studies of the top quark. The FCC-ee's exceptional precision will allow physicists to probe for tiny deviations from the SM predictions, potentially revealing new physics.

The FCC-hh: Exploring the Energy Frontier

Following the FCC-ee, the FCC-hh collider aims to push the energy frontier to 100 TeV, offering unprecedented opportunities for discovery. The key objectives of the FCC-hh include probing the nature of dark matter by potentially producing dark matter particles through their interactions with SM particles; exploring the Higgs potential and self-interactions to understand the stability of the Higgs field; searching for new particles and forces that could manifest at higher energy scales, providing insights into physics beyond the SM. To achieve these goals, the FCC-hh will require significant advancements in technology, including the development of stronger superconducting magnets capable of reaching magnetic fields up to 16 T, and sophisticated detectors designed to handle the higher energy and luminosity.

3.2 The ATLAS detector

The ATLAS detector [27], installed at Point 1 of the LHC at CERN, is one of the largest and most complex particle detectors ever constructed. A cut-away view of the ATLAS detector in Run 3 configuration is shown in Figure 3.2. Its diverse array of sophisticated sub-detectors captures and analyses the particles produced in high-energy collisions. The conceptual design of ATLAS began in the early 1990s, with the official Letter of Intent submitted in 1992 [40] and the Technical Proposal in 1994 [41]. Construction commenced in the late 1990s, leading to the installation of the detector in its cavern by 2007. The first proton-proton collisions were recorded in 2009. Over the years, ATLAS has undergone several upgrades to enhance its performance and accommodate increasing collision rates and energies. ATLAS comprises several key components designed to work in concert to achieve comprehensive particle detection and analysis:

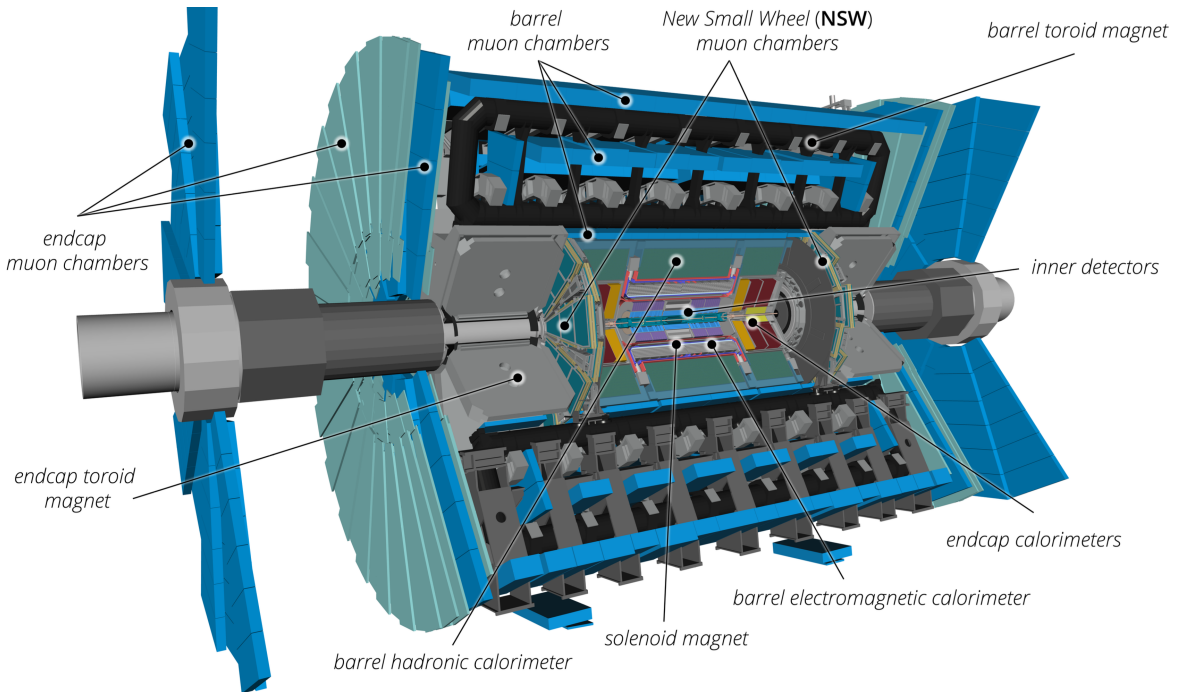


Fig. 3.2 Cut-away view of the Run 3 configuration of the ATLAS detector indicating the locations of the larger detector sub-systems, taken from [39]

- Inner Detector (ID): This component provides precise tracking of charged particle trajectories and interaction points near the collision vertex. It consists of a high-granularity silicon Pixel detector, a Semiconductor Tracker (SCT), and a Transition Radiation Tracker (TRT).
- Calorimeters: These measure the energy of particles by absorbing them. The electromagnetic calorimeter detects electrons and photons, while the hadronic calorimeter measures the energy of hadrons. The ATLAS calorimeters use two sampling technologies: liquid argon (LAr) for the electromagnetic calorimeters and all endcap and forward calorimeters, and scintillating tiles for hadron calorimetry in the central region.
- Muon Spectrometer: Located outside the calorimeters, this system detects and measures muons, which are minimally ionising particles that penetrate the inner

detector and calorimeters. It is based on the magnetic deflection of muon tracks in a large superconducting air-core toroidal magnet system.

- Forward Detectors: Comprised of four sub-detectors, the forward detectors play critical roles in measuring luminosity, studying diffractive events, and characterising the centrality [42] of heavy-ion collisions.
- Trigger and Data Acquisition (TDAQ) System: This system selects events of interest based on distinguishing characteristics and reads them out for further offline processing. It consists of the Level-1 Trigger (L1) and the High-Level Trigger (HLT), along with the Data Acquisition system that transports data from sub-detector electronics to offline processing.

The ATLAS detector has been continuously upgraded to maintain its performance under the increasingly challenging conditions of the LHC. The Phase-I upgrades [43–46], implemented during LS2 from 2019 to 2022, included improvements to the detector subsystems and their electronics to withstand the high interaction rates expected in Run 3 and beyond. These upgrades focused on enhancing the trigger system, increasing precision tracking, and improving calorimetry and muon detection capabilities. In recent years, the LHC has achieved higher collision energies and luminosities, necessitating further upgrades to the ATLAS detector. The Run 3 configuration, for example, includes new LAr Calorimeter digital trigger electronics, an upgraded Muon Spectrometer with new small wheels (NSWs), and enhanced TDAQ systems to handle the increased data rates and complexity. The Phase-II upgrades, planned for the HL-LHC era [47–54], will further enhance the detector’s capabilities to meet the demands of higher luminosities and energies. These upgrades will include improvements in calorimeters for higher granularity and faster readout electronics to handle higher collision rates, a complete replacement of the ID (ITK) that can handle the increased pile-up conditions and radiation dose, upgrades to the TDAQ system that can handle date rates up to 1 MHz at Level-0 and 400 kHz at Level-1,

and an upgraded Muon Spectrometer for better coverage and resolution. In the following sections, we will delve into the key components of the ATLAS detector and their functions in particle detection and analysis.

3.2.1 ATLAS Coordinate System and Kinematic Variables

ATLAS uses a right-handed coordinate system with its origin at the nominal interaction point (IP) in the centre of the detector. The axes are defined as follows: the z-axis points along the beamline. The x-axis points from the IP to the centre of the LHC ring. The y-axis points upwards, perpendicular to the xz-plane. Cylindrical coordinates (r, ϕ) are used in the transverse plane, where r is the radial distance from the z-axis, and ϕ is the azimuthal angle around the z-axis. In hadron-hadron collisions, rapidity (y) and pseudorapidity (η) are used to describe the angle of a particle relative to the beam axis. y is defined as:

$$y = \frac{1}{2} \ln \left(\frac{E + p_z}{E - p_z} \right),$$

where E is the energy of the particle, and p_z is the component of the momentum along the beam axis. y is advantageous because differences in y are invariant under Lorentz boosts along the z-axis, making it a particularly useful variable in hadron collider physics. η is a simplified version of y , used when the particle mass is negligible compared to its momentum. It is defined as:

$$\eta = -\ln \left(\tan \frac{\theta}{2} \right),$$

where θ is the polar angle with respect to the beam axis. η is commonly used in collider experiments to describe the angular distribution of particles because it is a more convenient variable than y due to its simpler form, and the fact that it is approximately equal to y for relativistic particles. The trajectory of a particle is typically described in terms of its transverse momentum (p_T), ϕ , η . p_T is particularly important in collider physics because

it is invariant under boosts along the beam axis, and it is conserved in particle collisions.

It is defined as:

$$p_T = \sqrt{p_x^2 + p_y^2},$$

where p_x and p_y are the momentum components in the transverse plane.

3.2.2 Inner Detector

The Inner Detector (ID) [55–57] of the ATLAS experiment is a sophisticated component designed to provide precise tracking of charged particles originating from the collisions. A cut-away view of the ATLAS Inner Detector is shown in Figure 3.3. The ID is crucial

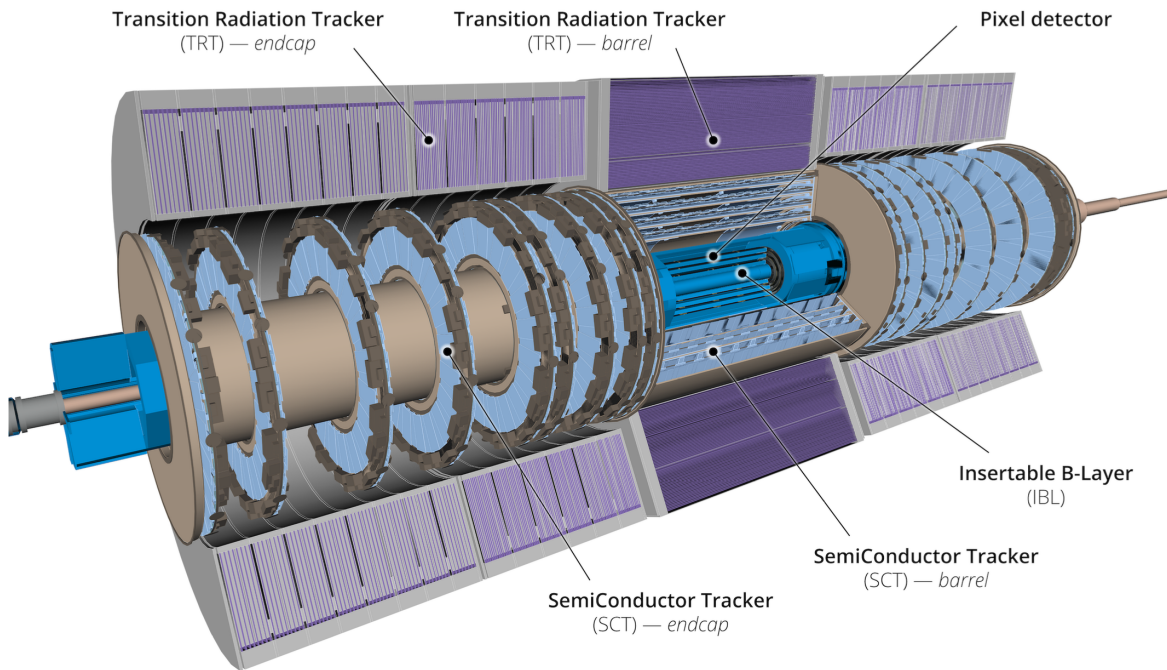


Fig. 3.3 Cut-away view of the ATLAS Inner Detector showing the Pixel Detector, Semiconductor Tracker (SCT), and Transition Radiation Tracker (TRT), taken from [39].

for reconstructing particle trajectories, measuring momenta, and identifying primary and secondary vertices. The design and configuration of the ID have evolved to meet the increasing demands of the LHC. Higher pile-up conditions and radiation levels expected

in Run 2 and Run 3 have necessitated upgrades to the ID to maintain its performance and reliability.

The ID is immersed in a 2 T axial magnetic field generated by a central solenoid, extending over a length of 5.3 meters with a diameter of 2.5 meters [58]. The ID covers the pseudorapidity range $|\eta| < 2.5$ and is composed of three primary sub-systems: the Pixel Detector, the Semiconductor Tracker (SCT), and the Transition Radiation Tracker (TRT).

- **Pixel Detector [59]:** The Pixel Detector provides the highest granularity tracking close to the interaction point. It consists of three barrel layers and three endcap discs on each side, with an additional fourth inner layer known as the Insertable B-Layer (IBL) [60] installed during LS1. The pixels have dimensions of $50 \mu\text{m} \times 400 \mu\text{m}$, with the IBL featuring even finer segmentation at $50 \mu\text{m} \times 250 \mu\text{m}$. This system typically provides four precise position measurements per track, aiding in pattern recognition, accurate vertex reconstruction and b-tagging.
- **Semiconductor Tracker (SCT) [61]:** Surrounding the Pixel Detector, the SCT extends the tracking capabilities further from the interaction point. It consists of four barrel layers and nine endcap discs on each side. The SCT uses silicon microstrip technology, with strips oriented to measure both radial and azimuthal coordinates, providing eight measurements per track. The strip pitch is approximately $80 \mu\text{m}$, allowing for high-resolution tracking over a larger volume than the Pixel Detector.
- **Transition Radiation Tracker (TRT) [57]:** The outermost component of the ID, the TRT, consists of layers of straw tubes interleaved with radiators that induce transition radiation when traversed by high-energy electrons. The TRT covers range $|\eta| < 2.0$, offering additional particle identification capabilities through the measurement of energy deposition in the straws.

Several upgrades and enhancements have been implemented in the ID for Run 3 to handle the increased collision energy of 13.6 TeV and the higher luminosity conditions. These include improvements in detector readout electronics, data acquisition systems, and the integration of new cooling systems to maintain optimal operational conditions under the high-radiation environment anticipated during Run 3. The precision tracking performance of the ID has been pivotal in enabling ATLAS to achieve its broad physics objectives, from detailed studies of the Higgs boson to searches for new physics phenomena.

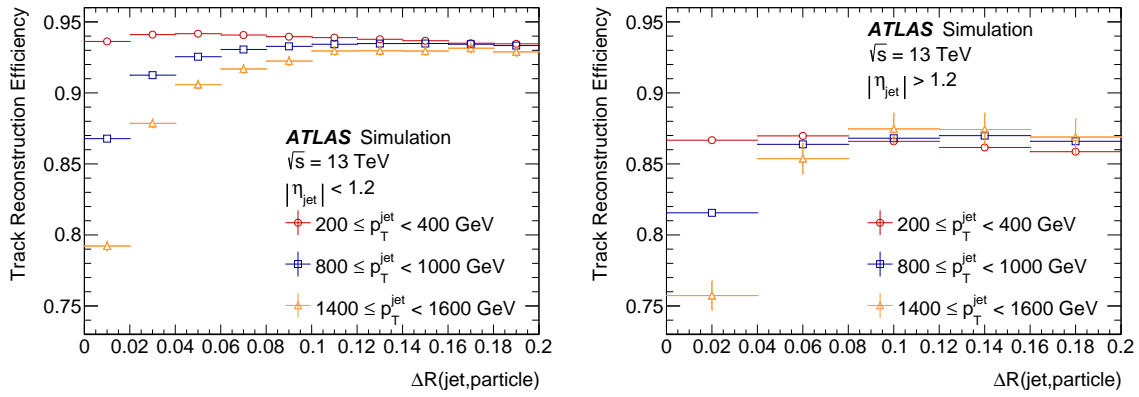


Fig. 3.4 The efficiency to reconstruct charged primary particles in jets with (left) $|\eta| < 1.2$ and (right) $|\eta| > 1.2$ is shown as a function of the angular distance of the particle from the jet axis for various jet p_T for simulated dijet MC events. These figures are taken from [62].

3.2.3 Calorimeters

The ATLAS calorimeter system measures the energies and positions of charged and neutral particles through interleaved absorber and active layers out to $|\eta| < 4.9$. The calorimeter system is divided into two main types of calorimeters: the Liquid Argon (LAr) [63] calorimeters and the Tile calorimeters [64], each optimised for different aspects of calorimetry. A cut-away view of the ATLAS calorimeter system is shown in Figure 3.5.

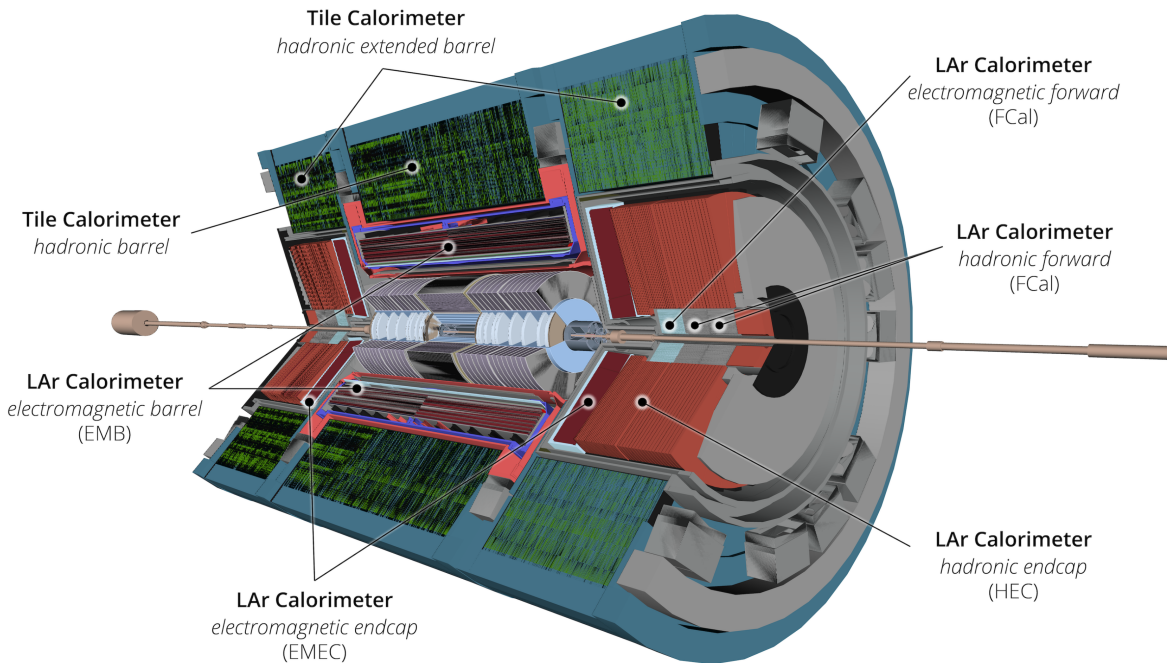


Fig. 3.5 Cut-away view of the ATLAS calorimeter system showing the Liquid Argon (LAr) calorimeters and the Tile calorimeters, taken from [39].

Liquid Argon Calorimeters

The Liquid Argon (LAr) calorimeter systems are responsible for high-precision measurements of the energy deposited by electrons, photons, and hadrons. They employ a sampling technology, where layers of absorbing material are interleaved with active liquid argon layers. This design allows the calorimeters to measure the energy of particles by sampling their energy loss as they pass through the detector. It is divided into several subsystems, each serving a specific purpose:

- LAr Electromagnetic Barrel Calorimeter (EMB): this subsystem covers the central region of the detector and is designed to measure the energy of electrons and photons with high precision. The EMB uses lead absorbers and liquid argon as the active medium.

- LAr Electromagnetic Endcap Calorimeter (EMEC): extending the coverage to the forward regions, the EMEC provides similar functionality to the EMB but for particles emitted at smaller angles relative to the beamline.
- LAr Hadronic Endcap Calorimeter (HEC): located behind the EMEC, the HEC measures the energy of hadrons. It uses copper absorbers and liquid argon, providing complementary measurements to the Tile calorimeters in the central region.
- LAr Forward Calorimeter (FCal): positioned in the very forward regions, the FCal is designed to measure the energy of particles at small angles to the beamline, using a combination of tungsten and liquid argon.

Tile Calorimeters

The Tile calorimeter system is designed to measure the energy of hadrons and jets in the central region of the detector. It consists of steel absorbers interleaved with scintillating tiles. The Tile calorimeter is segmented into three barrel structures. The Central Barrel (CB) covers the central region around the interaction point and the Extended Barrels (EB), positioned on either side of the central barrel to extend the coverage. The Tile calorimeter also uses a sampling technique, with the scintillating tiles producing light when charged particles pass through them. This light is then collected by photomultiplier tubes (PMTs) and converted into electronic signals that are processed to determine the energy of the incident particles.

Calorimeter Upgrades for Run 3

The ATLAS calorimeter system has undergone significant upgrades to enhance its performance for Run 3 [44]. These upgrades include improvements to the readout electronics and the implementation of a new digital trigger system for the LAr calorimeters. These enhancements are aimed at handling the higher collision energy and increased luminosity

expected during Run 3, ensuring that the calorimeter system continues to provide precise measurements under more demanding conditions. The calorimeters are critical for a wide range of physics analyses, including the identification and measurement of electrons, photons, taus, and jets, as well as the calculation of missing transverse energy (E_T^{miss}).

3.2.4 Muon Spectrometer

The ATLAS Muon Spectrometer (MS) [65] forms the large outer part of the ATLAS detector, designed to detect charged particles exiting the barrel and endcap calorimeters in the pseudorapidity range $|\eta| < 2.7$. The primary goal of the MS is to provide precise momentum measurements and trigger capabilities for muons. A cut-away view of the ATLAS Muon Spectrometer is shown in Figure 3.6.

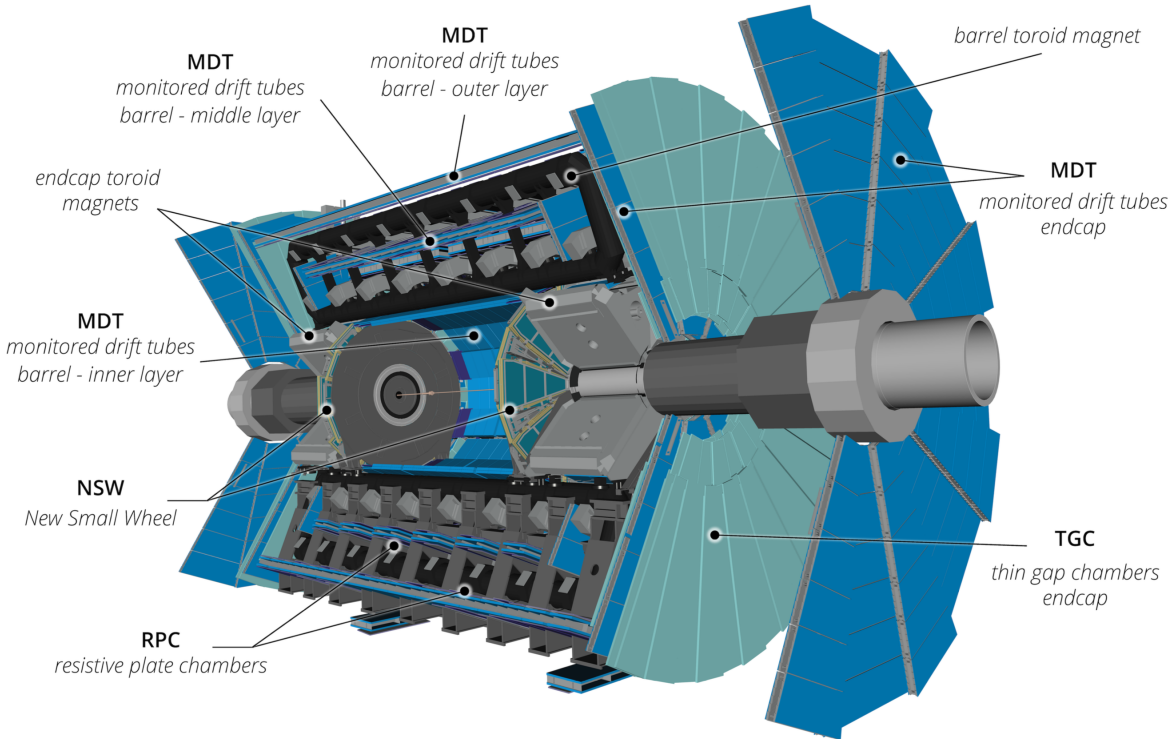


Fig. 3.6 Cut-away view of the ATLAS Muon Spectrometer, taken from [39].

The MS is composed of several layers of different detector technologies, all optimised for tracking muons through the strong magnetic fields generated by the ATLAS toroidal

magnet system. The MS is divided into three main regions: the barrel, the endcaps, and the transition regions between the barrel and endcaps.

- Barrel Region: the barrel region covers the central part of the detector ($|\eta| < 1.0$) and consists of three concentric cylindrical layers known as stations. These stations are equipped with Monitored Drift Tubes (MDTs) for precision tracking and Resistive Plate Chambers (RPCs) for triggering.
- Endcap Regions: the endcaps extend the coverage of the MS to higher pseudorapidities ($1.0 < |\eta| < 2.7$). Each endcap consists of three disc-shaped stations. The precision tracking in the endcaps is provided by MDTs and Cathode Strip Chambers (CSCs), while the triggering is primarily handled by Thin Gap Chambers (TGCs).
- Transition Regions: these regions ($1.0 < |\eta| < 1.4$) require special treatment due to the overlap of the barrel and endcap magnetic fields.
- New Small Wheels (NSWs) [43]: equipped with Small-Strip Thin Gap Chambers (sTGCs) and Micromegas detectors, the NSWs improve the resolution and redundancy in the $1.3 < |\eta| < 2.7$ region.

The MDTs are the primary technology used for precision tracking within the MS. Each MDT chamber contains multiple layers of drift tubes, which measure the time taken for ionisation electrons produced by a traversing muon to reach a central wire. This time measurement allows for precise determination of the muon's trajectory. MDTs cover the entire pseudorapidity range of the MS up to $|\eta| = 2.7$, providing high-resolution tracking data. RPCs are used in the barrel region for fast muon triggering. They consist of two parallel plates with a high voltage applied across them. When a muon passes through the chamber, it ionises the gas between the plates, creating an electrical signal that is detected and used to generate a trigger. RPCs also provide measurements of the azimuthal coordinate of muon tracks, aiding in the overall reconstruction process. TGCs are used in

the endcaps for both triggering and precision tracking. Similar to RPCs, TGCs operate by detecting ionisation events caused by traversing muons. They are designed to handle the high particle fluxes present in the endcap regions and are essential for providing rapid trigger signals to the data acquisition system. CSCs are employed in the innermost endcap layers where particle fluxes are highest. They consist of a plane of wires sandwiched between cathode strips. When a muon passes through the chamber, it ionises the gas, and the resulting electrons are collected by the wires, while the ions induce a signal on the cathode strips. This configuration allows for precise two-dimensional tracking. The NSWs, installed as part of the Phase-I upgrades, are designed to handle the high particle rates and provide improved precision in the forward region. They utilise two types of detectors: sTGCs and Micromegas. The sTGCs offer fast response times for triggering, while the Micromegas provide high spatial resolution for tracking. The combination of these technologies ensures robust performance in the high-radiation environment expected during Run 3 and beyond. The MS aims for a stand-alone transverse momentum resolution better than 15% for 1 TeV tracks, which requires an effective sagitta resolution of about $75\ \mu\text{m}$ over a large detector volume. This precision is achieved through careful design and regular upgrades. For Run 3, the MS has undergone significant enhancements, in addition to NSWs, the MDT readout electronics has been upgraded to handle higher data rates and improve overall performance.

3.2.5 Forward Detector

The forward detector systems of the ATLAS experiment [67] play crucial roles in measuring luminosity, studying diffractive events, and characterising the centrality of heavy-ion collisions. These detectors extend the capabilities of ATLAS by covering the forward regions, providing essential data that complement the central detector systems. Figure 3.8 shows the layout of the forward detectors in the ATLAS experiment.

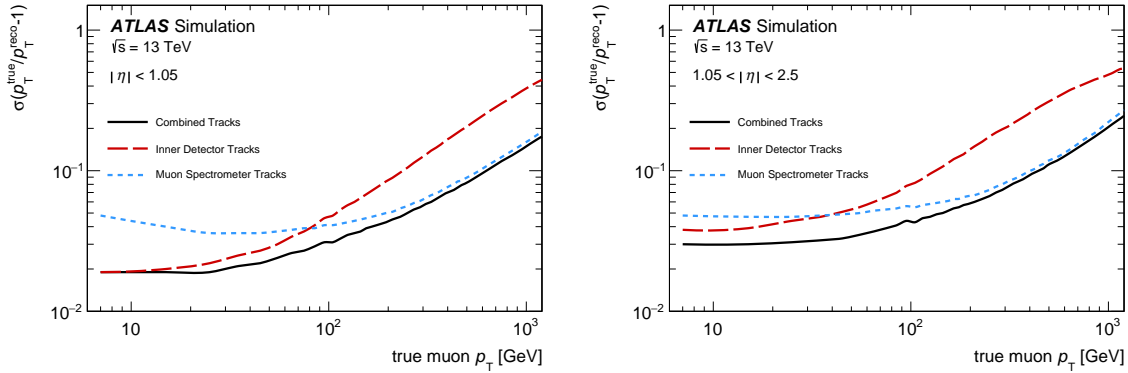


Fig. 3.7 Resolution of the muon p_T as obtained from simulation after derivation and application of all correction constants. Muons are selected using the High- p_T Working point. The resolution is shown as a function of the true p_T of the muon for a range from 1 GeV to 2.5 TeV, (left) for muons with $|\eta| < 1.05$ and (right) for muons with $1.05 < |\eta| < 2.5$. The resolution lines are obtained by interpolating between points sampled in steps of p_T . The continuous lines correspond to the combined momentum, while the dashed lines to that from the ID, and the dotted lines to that of the MS. These figures are taken from [66].

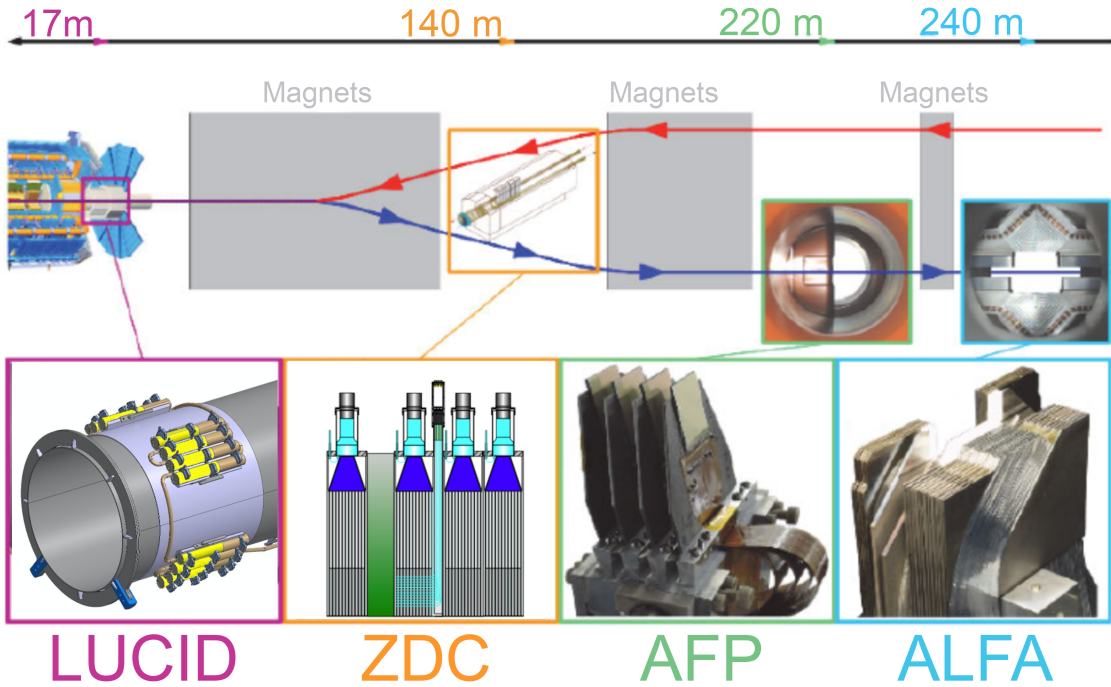


Fig. 3.8 Layout of the forward detectors in the ATLAS experiment, taken from [39].

The LUminosity Cherenkov Integrating Detector (LUCID) [68] is located at a distance of ± 17 meters from the IP. It is primarily designed to monitor the luminosity online and offline by detecting inelastic proton-proton scattering events in the forward direction. LUCID employs Cherenkov tubes filled with C_4F_{10} gas, which emit light when traversed by charged particles produced in collisions. This light is then detected by photomultiplier tubes (PMTs), allowing for precise luminosity measurements.

The Zero Degree Calorimeters (ZDC) are located at ± 140 meters from the IP, just beyond where the common straight-section vacuum pipe splits into two separate beampipes. The ZDC modules consist of alternating layers of tungsten plates and quartz rods, optimised for detecting neutral particles at pseudorapidities $|\eta| \geq 8.2$. The ZDCs play a crucial role in determining the centrality of heavy-ion collisions, providing insights into the collision geometry and the energy deposition of forward-going neutrons and photons.

The Absolute Luminosity for ATLAS (ALFA) Roman Pot detector consists of four stations positioned at ± 240 meters from the IP. Each station includes two scintillating fibre trackers housed in Roman pots, which can approach the LHC beam as close as 1 mm. ALFA is used in dedicated low-luminosity and high- β^* runs to measure the total cross-section for proton-proton interactions through elastic scattering and diffraction studies. In preparation of Run 3, several upgrades were made to ALFA. The aged readout electronics and scintillating fibres were replaced, and additional shielding walls were installed to reduce radiation exposure and extend the operational lifespan of the detectors. The Roman Pot movement system was refurbished, and firmware updates were implemented for the central trigger processor input module to enhance trigger and readout capabilities for ALFA-specific runs.

The ATLAS Forward Proton (AFP) detector, part of the Phase I upgrade, is situated at ± 205 meters (near stations) and ± 217 meters (far stations) from the IP. Each station contains a silicon tracker (SiT) similar to the Insertable B-Layer (IBL) and a Time-of-Flight

(ToF) detector. The SiT provides precise measurements of the proton trajectories, while the ToF detector measures the time difference between protons reaching the detectors, achieving vertex resolution of 3 to 5 mm.

The AFP detector underwent several upgrades during LS2 to prepare for Run 3. These upgrades included:

- replacement of radiation-damaged silicon detectors with new 3D silicon pixel tracker modules.
- redesign of the ToF detector to prevent corona discharge issues in vacuum.
- updates to the trigger and readout electronics to improve timing resolution and data acquisition efficiency.

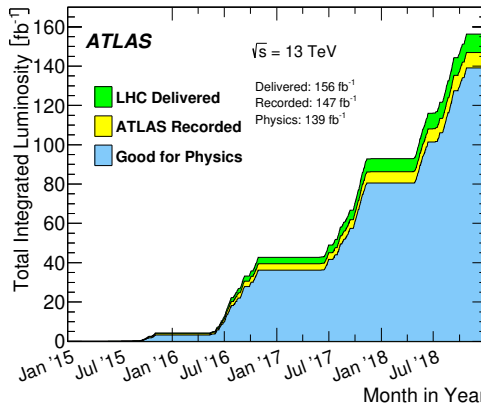


Fig. 3.9 Cumulative integrated luminosity delivered to and recorded by ATLAS between 2015 and 2018 during stable beam pp collision data-taking at $\sqrt{s} = 13$ TeV. This figure is taken from [69].

3.2.6 TDAQ System

The Trigger and Data Acquisition (TDAQ) [70] system of the ATLAS detector is a sophisticated infrastructure designed to manage the immense amount of data generated by particle collisions at the LHC. Its primary function is to select and record the most interesting collision events for detailed analysis, thereby enabling the identification of rare physics

phenomena. A schematic of the ATLAS TDAQ system is shown in Figure 3.10. The ATLAS

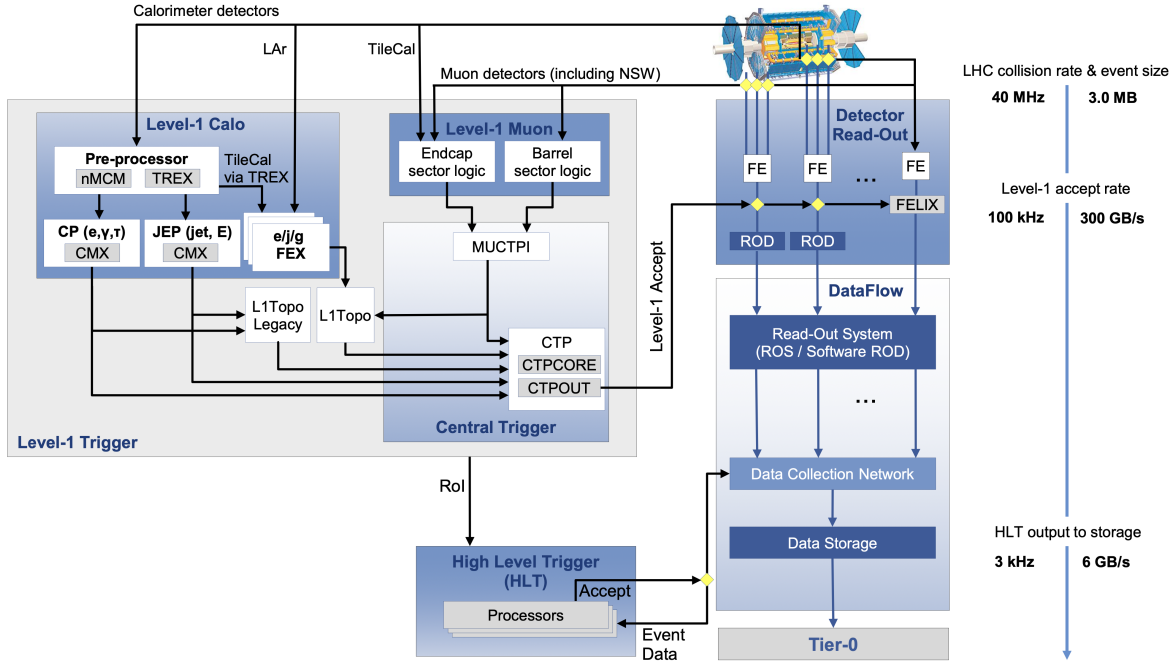


Fig. 3.10 Schematic of the ATLAS Trigger and Data Acquisition (TDAQ) system, taken from [39].

TDAQ system employs a multi-tiered architecture that comprises the Level-1 (L1) Trigger, the High-Level Trigger (HLT), and the Data Acquisition (DAQ) system. This design allows for efficient and rapid data processing, ensuring that only the most relevant events are stored for further analysis.

The L1 Trigger is the first stage in the event-selection process. It operates directly on the raw data from the detector, using custom-built hardware to analyse data with reduced granularity. The L1 Trigger must make decisions within a strict latency of 2.5 microseconds to reduce the event rate from the 40 MHz bunch crossing rate of the LHC to a maximum of 100 kHz. The L1 Trigger comprises the L1 calorimeter triggers and the L1 muon triggers. Both subsystems generate Region of Interest (RoI) signals that guide the HLT in its more detailed analysis. The HLT is a software-based system implemented on commercial processors. It performs detailed event reconstruction using the full detector data, significantly refining the initial L1 selection. The HLT reduces the event rate from

the L1's 100 kHz to about 3 kHz for storage. Guided by RoIs from the L1 Trigger, the HLT performs localised and full-event reconstruction. For Run 3, the HLT uses the AthenaMT software framework, which allows for parallel processing and more efficient resource use. Sophisticated algorithms, including those for track reconstruction and particle identification, enhance the precision and efficiency of event-selection. The DAQ system is responsible for managing data flow from the detector front-end electronics to permanent storage. It ensures that data from accepted events are properly formatted, transported, and recorded. Key components of the DAQ system include:

- Readout System (ROS): The ROS collects data from sub-detectors following an L1 accept and buffers it for HLT processing.
- Data Collection Network: This high-bandwidth network facilitates data transfer from the ROS to the HLT processing farm.
- Data Storage: Events accepted by the HLT are transferred to permanent storage for offline analysis. The system is designed to handle an average output of 3 kHz, corresponding to a data throughput of 6 GB/s.

Several upgrades have been implemented in the TDAQ system for Run 3 [45] to cope with higher luminosities and increased data rates. Upgraded L1 Trigger electronics and algorithms provide finer granularity and improved selectivity, allowing for better background rejection and more efficient event-selection. Level-2 (L2) and event filter (EF) systems used in the previous runs have been integrated into a single HLT framework, streamlining the data processing pipeline and improving resource utilisation. The computational resources of the TDAQ systems have been expanded to handle the increased data volume and complexity, ensuring that event reconstruction and selection can be performed with high efficiency. Enhancements in data management and storage infra-

structure ensure that the system can handle the increased data volume and maintain data integrity.

3.3 Object reconstruction and identification in ATLAS

3.3.1 Reconstruction and identification of electrons and photons

Egamma reconstruction

The reconstruction of electrons and photons (collectively known as Egamma) [71, 72] in the ATLAS detector is a multi-step process that involves the collection of energy deposits in the electromagnetic calorimeter and matching these deposits to tracks reconstructed in the ID. The energy of electron and photon candidates is reconstructed by clustering the energy deposits in the cells of the EM calorimeter. The algorithm used is optimised to handle the different shower shapes and energy distributions of electrons and photons. Superclusters are formed by combining clusters from the presampler and multiple calorimeter layers, using a boosted-decision-tree (BDT) regression algorithm to optimise the energy measurement. This approach accounts for variations in the particle's incident angle and position within the detector. For electrons, the energy clusters are matched to tracks reconstructed in the ID. The matching is based on the consistency between the cluster position and the extrapolated track position at the calorimeter. A combination of criteria, including the ratio of the track momentum to the cluster energy (E/p) and the shower shape, is used to enhance the identification efficiency and purity. This matching process helps distinguish electrons from hadronic background and photon conversions. Photons are identified through their characteristic energy deposits in the EM calorimeter. Unconverted photons, which do not interact in the ID, are identified purely based on the calorimeter information. Converted photons, which produce an electron-positron pair in the ID, require reconstruction of the conversion vertex and matching of the resulting

tracks to the calorimeter clusters. The photon identification criteria involve isolation requirements and shower shape variables to reduce background from neutral hadrons and jets.

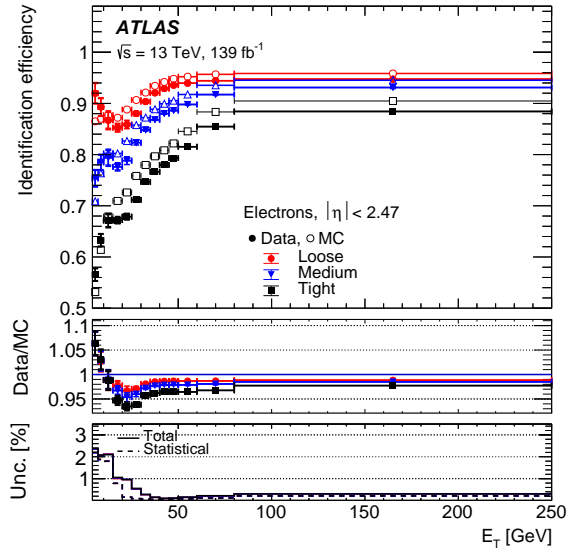


Fig. 3.11 Identification efficiencies of electrons from $Z \rightarrow ee$ decays as a function of the electron's transverse momentum for the different identification working points. This figure is taken from [72].

Egamma calibration

The calibration of electron and photon energies [73] is crucial for achieving precise measurements required for ATLAS physics analyses. The calibration procedure involves several steps to correct for detector response variations and ensure consistency between data and simulation. The EM calorimeter is segmented into longitudinal layers, each of which responds differently to incident particles. The first step in the calibration process involves correcting the energy response of each layer to account for these variations. This is achieved using detailed simulations and data-driven techniques to ensure accurate energy measurements across the detector. A simulation-based BDT regression algorithm is used to combine the energy deposits from different calorimeter layers and the presampler. This algorithm is trained to optimise the energy measurement separately for electrons,

converted photons, and unconverted photons, considering the particle's position and angle of incidence. The simulation-based calibration is applied uniformly to data and simulated events. Several corrections are applied to account for residual differences between data and simulation. These include adjustments for non-uniformities in the detector response, variations in the high-voltage settings, and corrections for biases introduced by the liquid-argon calorimeter electronics. The stability of the calorimeter response over time and across different detector regions is also monitored and corrected as necessary. The final calibration step involves adjusting the global energy scale using samples of $Z \rightarrow ee$ events. The peak of the reconstructed Z boson mass is aligned between data and simulation to ensure consistency. This step also includes smearing the energy resolution in the simulation to match that observed in the data, thereby correcting for any discrepancies in the detector's energy response. Photon-specific calibration steps are needed to account for differences in the lateral development of electron and photon showers. Corrections are derived from studies of out-of-cluster energy leakage and the modelling of photon reconstruction efficiencies. These corrections ensure that the energy measurements for photons are as precise as those for electrons.

The calibrated energy measurements are validated using independent data samples, such as $J/\psi \rightarrow ee$ and $Z \rightarrow ll\gamma$ events. The systematic uncertainties associated with the calibration are thoroughly evaluated, accounting for factors such as the passive material model, the electronic noise, and the pile-up conditions.

Neural Network (NN) based electron identification

Two significant developments in this area are the use of Deep Neural Networks (DNNs) [74] and Convolutional Neural Networks (CNNs) [75] for electron identification. The DNN-based electron identification algorithm leverages high-level discriminating variables derived from the reconstructed electron track and calorimeter energy deposits. The DNN

algorithm enhances electron identification performance by optimising the correlations between input features, which are often neglected in traditional likelihood-based approaches. By performing multinomial classification, the DNN can categorise electron backgrounds into several classes, such as electrons from heavy-flavour decays or light-flavour hadrons, enabling targeted background rejection. This approach has demonstrated a significant increase in combined background rejection, with improvements ranging from 1.7 to 5.5 times compared to previous methods for a fixed signal efficiency. The CNN-based algorithm further refines electron identification by processing low-level detector information, such as calorimeter cell energy deposits, which are treated as images. The CNN architecture is specialised in image recognition, allowing it to effectively analyse the spatial patterns of energy deposits. This algorithm integrates high-level features used in DNNs and additional tracks matched to electron candidates, which enhances its performance. The CNN has shown remarkable improvements in background rejection, particularly for light-flavour hadrons and electrons from photon conversions. For instance, it achieves background rejection factors up to five times better than the likelihood-based method for charged hadrons faking electron signatures. The CNN's ability to output a vector of probabilities for different electron classes further enhances its flexibility and accuracy in various analyses.

These advancements are crucial for enhancing the precision of physics analyses conducted at the ATLAS experiment, particularly those involving multiple leptons or requiring stringent electron background rejection. In the future, these neural network-based approaches will continue to evolve, potentially incorporating real data for training to overcome simulation biases and improve generalisation to actual collision events. Adversarial training techniques might also be employed to mitigate differences between simulated and real data, further refining the performance of electron identification algorithms in ATLAS.

3.3.2 Jet reconstruction

Jets are collimated streams of particles that result from the hadronisation of quarks and gluons produced in high-energy processes. As a direct consequence of the running of the strong coupling constant, and the QCD colour confinement, when quarks and gluons are produced in a collision, they cannot exist freely. Instead, they fragment into a cascade of hadrons, predominantly pions and kaons, which cluster together to form jets. The ATLAS experiment employs sophisticated jet reconstruction techniques to accurately identify and measure jets. The reconstruction processes have evolved to utilise both calorimetric and tracking information, enhancing the precision and robustness of jet measurements. The two primary methods are based on calorimeter information and the particle flow (PFlow) algorithm [76], both of which use the anti- kt algorithm [77] with a radius parameter $R = 0.4$. A larger radius parameter ($R = 1.0$) is used for large-radius jets optimised for boosted object identification [78].

Calorimeter-based jet reconstruction

In the calorimeter-based method, jets are reconstructed using three-dimensional topological clusters (topo-clusters) [79, 80] of calorimeter cells. These cells are grouped together based on their energy depositions and spatial proximity using a nearest-neighbour algorithm. The energy of these clusters is initially calibrated to the electromagnetic (EM) energy scale, which is suitable for measuring energy depositions from electromagnetic showers. Only positive-energy topo-clusters are used as inputs to the jet reconstruction. An origin correction is applied to each topo-cluster to account for the position of the primary vertex, ensuring that the jet's energy and direction are accurately determined with respect to the event's primary vertex.

EMtopo jets, reconstructed using origin-corrected EM scale topo-clusters, were the primary jet definition used in ATLAS physics analyses conducted in Run 2. These jets

exhibited robust energy scale and resolution characteristics across a wide kinematic range and were independent of other reconstruction algorithms such as tracking at the jet-building stage [81].

Particle Flow (PFlow) algorithm

The particle flow algorithm aims to improve jet reconstruction by combining measurements from both the tracking and calorimeter systems [81]. This approach reconstructs individual particles by replacing the energy deposited in the calorimeter by charged particles with the momenta of tracks matched to those deposits. The PFlow algorithm uses the following steps:

- Track Selection: Tracks are selected based on quality criteria, such as a transverse momentum (p_T) threshold of 500 MeV and a distance of closest approach to the primary vertex along the z-axis less than 2 mm. This selection helps to suppress pile-up contributions by rejecting tracks not associated with the primary vertex.
- Energy Subtraction: The energy deposited by charged particles in the calorimeter is subtracted, and the corresponding track momenta are used instead. This subtraction is carefully managed to avoid removing energy deposited by other particles.
- Topo-Cluster Adjustment: The η and ϕ coordinates of topo-clusters are recomputed with respect to the primary vertex position. This adjustment ensures that the reconstructed jets are aligned correctly with the hard-scatter interaction.

PFlow jets, formed from these combined signals, exhibit improved energy and angular resolution, reconstruction efficiency, and stability against pile-up effects compared to jets reconstructed using calorimeter information alone.

Jet calibration and performance

Calibration of the reconstructed jets involves several steps to ensure their energy scale matches the particle level [81, 82]. Firstly, pile-up corrections remove excess energy due to additional proton-proton interactions within the same or nearby bunch crossings. They consist of a jet area-based correction and a residual correction derived from Monte Carlo (MC) simulations. The second step is the absolute energy scale calibration, this step corrects the jet energy and direction to match those of particle-level truth jets. It is typically derived from dijet MC events. Then, the global sequential calibration process reduces the dependence of the reconstructed jet response on tracking, calorimeter, and muon chamber information, further refining the energy resolution and reducing systematic uncertainties. Finally, the in situ calibration corrects any remaining differences between data and MC simulation using well-measured reference objects such as photons, Z bosons, and calibrated jets. The final step is applied to data only. These methods ensure that ATLAS can precisely reconstruct and measure jets.

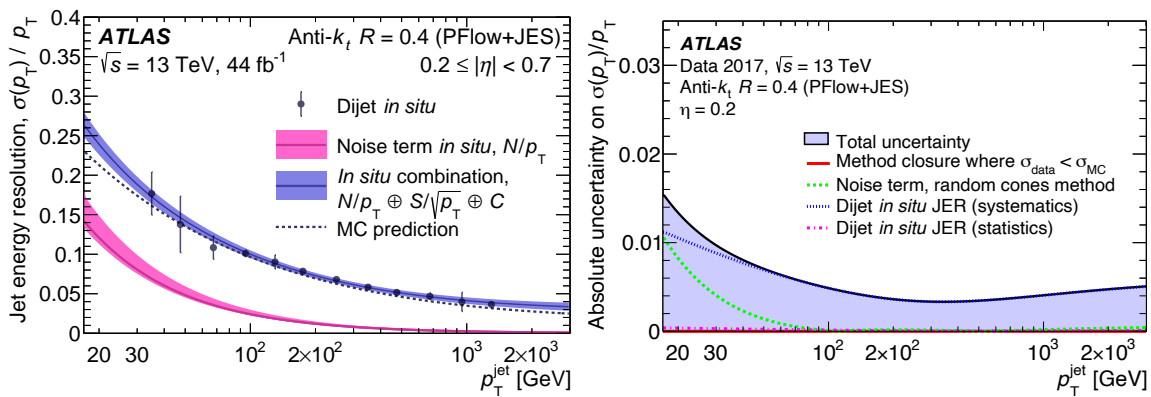


Fig. 3.12 (left) The relative jet energy resolution as a function of p_T for fully calibrated PFlow+JES jets. The error bars on points indicate the total uncertainties on the derivation of the relative resolution in dijet events, adding in quadrature statistical and systematic components. The expectation from Monte Carlo simulation is compared with the relative resolution as evaluated in data through the combination of the dijet balance and random cone techniques. (right) Absolute uncertainty on the relative jet energy resolution as a function of jet p_T . Uncertainties from the two in situ measurements and from the data/MC simulation difference are shown separately. These figures are taken from [81].

Large-radius jets

Large-radius jets are specifically optimised to identify highly boosted topologies, particularly those involving boosted objects such as W , Z , and Higgs bosons, as well as top quarks [83]. These jets are typically reconstructed using the anti- k_t algorithm with a large radius parameter ($R = 1.0$). The substantial radius allows the jet to capture more of the radiation and decay products from highly boosted massive particles, thus providing a clearer insight into their substructure. In Run 2 and Run 3, the unified flow objects (UFOs) [84, 85] have been developed to address the need for a jet input object that combines desirable aspects of PFlow and Track-CalorClusters (TCC) [84] reconstruction. This integration aims to further optimise performance metrics, such as jet energy resolution and pile-up stability, across the full kinematic range. The UFO reconstruction process begins with the standard ATLAS PFlow algorithm. Charged PFlow objects (PFOs) matched to pile-up vertices are removed, ensuring that only relevant tracks from the primary vertex are considered. The remaining PFOs are categorised into three categories: neutral PFOs, charged PFOs used for subtracting energy from a topocluster, and charged PFOs in dense environments. In these dense environments, charged particles produced in regions is very high, the detector may encounter challenges in isolating individual particle signals, and as a result, no energy subtraction is performed for these PFOs. Jet-input-level pile-up mitigation algorithms, such as Constituent Subtraction (CS) and SoftKiller (SK) [86], are applied to neutral PFOs to further reduce pile-up effects. A modified version of the TCC splitting algorithm is then applied, using only tracks from the primary vertex to avoid pile-up instabilities. Tracks used for PFlow subtraction are excluded from this step, as their contributions have already been subtracted. UFOs demonstrate improved tagging performance across both low and high p_T ranges, showing superiority over TCC jets at high p_T and becoming comparable to PFlow jets at lower p_T . Due to the inclusion of only charged-particle tracks matched to the primary vertex, UFOs exhibit natural stability against pile-up, similar to the PFlow

algorithm. Additional stability is provided by input-level pile-up mitigation algorithms applied to neutral particles. UFOs offer an improved jet mass resolution compared to existing large- R jet definitions, with up to a 45% improvement at high p_T for signal jets. However, the calibration process for UFOs is more complex due to the need to account for various factors such as the pile-up contribution and the energy scale of different components [78].

3.3.3 Missing transverse energy (E_T^{miss}) reconstruction

Missing transverse energy, also referred to as missing transverse momentum, serves as a proxy for the transverse momentum carried by undetected particles, which can be indicative of phenomena such as neutrino production within the SM or potential new physics scenarios like dark matter. The reconstruction of E_T^{miss} [87] involves the combination of multiple detector inputs, including calibrated electrons, muons, photons, hadronically decaying τ -leptons, hadronic jets, and soft activity from remaining tracks. This process is inherently complex due to the need to avoid double-counting of momentum and to accurately represent the event's transverse momentum balance.

E_T^{miss} reconstruction

The reconstruction process of E_T^{miss} in ATLAS is divided into two main components:

- Hard Term (p_T^{hard}): This includes signals from well-reconstructed and calibrated hard objects such as electrons, photons, τ -leptons, muons, and jets. Each of these objects is carefully selected and calibrated to ensure accurate measurement.
- Soft Term (p_T^{soft}): This consists of contributions from tracks associated with the primary interaction vertex but not associated with any hard object. The soft term helps capture the residual transverse momentum in the event that is not accounted for by the hard objects.

To form the E_T^{miss} vector, these components are combined as follows:

$$\vec{E}_T^{\text{miss}} = - \left(\sum \vec{E}_T^{\text{hard}} + \sum \vec{E}_T^{\text{soft}} \right)$$

where the sums run over all selected hard objects and soft tracks, respectively. One of the key challenges in E_T^{miss} reconstruction is avoiding double counting of detector signals. This is managed through a signal ambiguity resolution procedure that ensures each detector signal contributes to only one hard object. The procedure prioritizes signals by a set of criteria, detailed in [88]

E_T^{miss} calibration

ATLAS has defined several E_T^{miss} working points, each with varying levels of stringency on jet selections to manage pile-up and other sources of fake E_T^{miss} . These working points range from loose to tenacious, with the latter offering the highest resilience to pile-up by applying more stringent requirements on jets, particularly in the forward region of the detector. The performance of E_T^{miss} reconstruction is evaluated using both real data and MC simulations. The key metrics for performance include the resolution of E_T^{miss} and its systematic uncertainties. The resolution is typically assessed in events with well-known kinematic properties, such as $Z \rightarrow \ell^+ \ell^-$ decays, which provide a clean sample with no true E_T^{miss} . The adoption of a particle flow algorithm, which combines calorimeter and tracking information, improves the resolution of jets. This, in turn, facilitates dynamic E_T^{miss} reconstruction that adapts based on the chosen hard objects in an analysis. Systematic uncertainties are thoroughly evaluated for both the hard and soft components of E_T^{miss} . Recent studies have shown significant reductions in scale and resolution uncertainties, thanks to improved calibration techniques and better handling of pile-up effects.

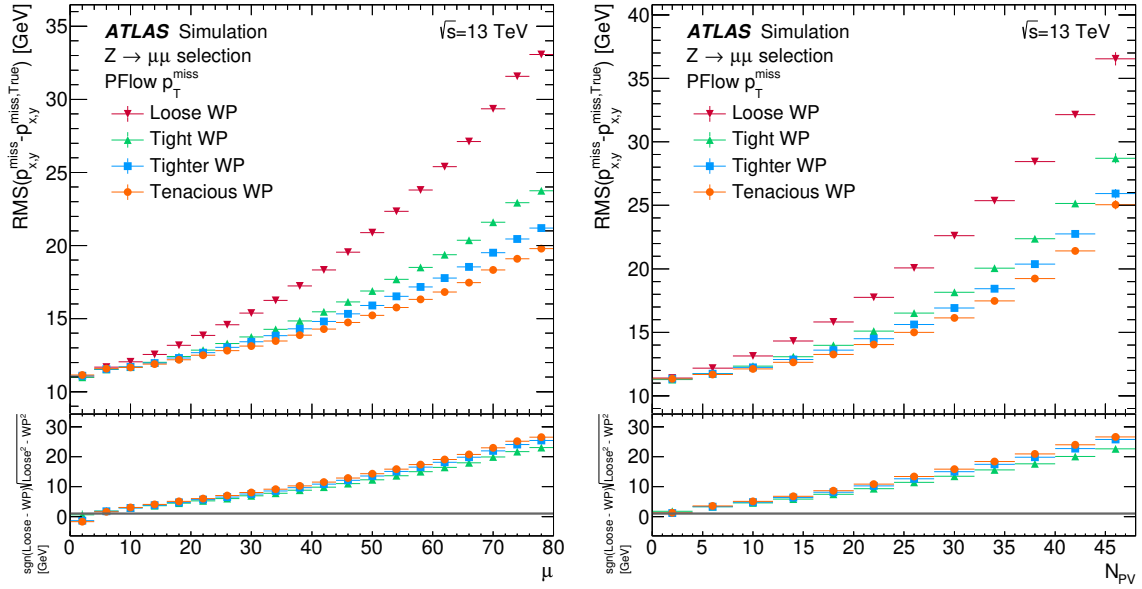


Fig. 3.13 The p_x^{miss} and p_y^{miss} resolution for different p_T^{miss} working points as a function of interactions per bunch crossing (left) or number of primary vertices (right). PFlow jets are used on SM MC simulations with $Z \rightarrow \mu\mu$ events. These figures are taken from [87].

3.3.4 Jet flavour tagging

The ATLAS experiment employs a sophisticated array of algorithms for identifying jets containing b -hadrons (b -jets) and c -hadrons (c -jets), commonly referred to as flavour-tagging algorithms [89, 90]. The core of these algorithms lies in exploiting the unique characteristics of b - and c -hadrons, such as their long lifetimes, high masses, and complex decay patterns, to distinguish them from jets originating from lighter quarks. Specialised flavour tagging is also designed to identify large-radius jets originating from boosted Higgs bosons decaying into pairs of bottom quarks ($H \rightarrow b\bar{b}$) and charm quarks ($H \rightarrow c\bar{c}$) [91, 92]. The latest developments in jet flavour tagging employ Graph Neural Networks to enhance performance [90, 92].

DL1r taggers

The Run 2 flavour-tagging strategy of ATLAS is based on a two-stage approach. The first stage involves low-level taggers that reconstruct specific features of heavy-flavour jets

using two complementary methods: track-based and vertex-based approaches. Track-based algorithms analyse the properties of individual charged-particle tracks associated with a hadronic jet, while vertex-based algorithms focus on reconstructing displaced vertices from these tracks. Key low-level taggers include:

- Impact Parameter Algorithms (IP2D, IP3D) [93]: These algorithms utilise the impact parameters of tracks, which are the distances of closest approach of tracks to the primary vertex. IP2D and IP3D calculate likelihood ratios from the track impact parameter significances, with IP3D additionally considering the 3D impact parameter.
- Secondary Vertex Finder (SV1) [94]: This algorithm reconstructs secondary vertices within the jet by combining tracks that originate from a common point away from the primary collision vertex. It enhances pile-up rejection and overall performance at high jet p_T through advanced track-cleaning and vertexing techniques.
- JetFitter [95]: This algorithm aims to reconstruct the entire decay chain of b -hadrons within the jet by employing a topological vertex finding approach. It identifies multiple vertices and uses a Kalman filter to improve vertex reconstruction.
- RNNIP: A track-based Recurrent Neural Network (RNN) that utilises the sequential nature of track hits to improve the identification of b - and c -jets.

The outputs of the low-level taggers are then fed into high-level taggers, which are multivariate classifiers designed to maximise flavour-tagging performance. The primary high-level tagger used during Run 2 is the DL1 [93] algorithm series, which employs deep learning techniques. DL1 Combines the outputs of IP2D, IP3D, SV1, and JetFitter using a feed-forward neural network. DL1r [93] is an enhanced version of DL1 that also incorporates the RNNIP outputs. DL1r significantly improves the tagging performance by leveraging the low correlation of RNNIP outputs with other taggers. The performance of

flavour-tagging algorithms is evaluated in terms of their efficiency to correctly identify b -jets (ϵ_b) and their ability to reject light-flavour jets and c -jets. The DL1d tagger achieves a light-flavour jet rejection factor of 170 and a charm-jet rejection factor of 5 at a b -jet identification efficiency of 77%. For charm-jet identification, DL1r achieves a light-flavour jet rejection factor of 70 and a b -jet rejection factor of 9 at a charm-jet efficiency of 30%. The flavour-tagging performance is further assessed across various jet p_T and $|\eta|$ ranges, and by ensuring robustness against pile-up interactions. The algorithms maintain consistent performance even with increased pile-up, showing minimal variation in b -tagging efficiency and background rejection factors across different collision environments.

GNN-based tagger

In Run-3, ATLAS will implement a novel jet tagger using a Graph Neural Network (GNN) architecture known as GN1 [90, 92]. This advanced method represents a significant departure from traditional flavour tagging approaches, relying on its ability to process information from a variable number of charged particle tracks within a jet without intermediate low-level algorithms. Here, we detail the architecture, implementation, and performance of the GNN-based taggers.

GN1 utilises a sophisticated GNN layer combined with auxiliary training objectives. The primary goal is jet flavour classification, identifying whether jets originate from b - or c -quarks. GN1 employs a fully connected graph where each node represents a track within the jet. These nodes are characterised by feature vectors derived from a per-track initialisation network, which then interact within the graph to predict jet flavour, track origins, and vertex groupings. GN1 demonstrates superior performance compared to the current DL1r tagger across various metrics. For jets within the $t\bar{t}$ sample with transverse momentum (p_T) between 20 and 250 GeV, GN1 improves light-jet and c -jet rejection by factors of approximately 1.8 and 2.1, respectively, at a 70% b -jet tagging efficiency. In the

higher p_T range ($250 < p_T < 5000$ GeV) from the Z' sample, these improvements rise to factors of around 6 for light-jet rejection and 2.8 for c -jet rejection at a b -jet efficiency of 30%. This method's inclusive reconstruction efficiency in b -jets reaches approximately 80%, indicating its robust capability to identify displaced vertices from b -hadron decays. GN1 represents a significant advancement in jet flavour tagging for the ATLAS experiment, offering improved performance and flexibility. By eliminating the dependence on low-level algorithms and employing a unified GNN approach, GN1 not only enhances the efficiency of b - and c -jet identification but also simplifies the optimisation process for various tagging applications.

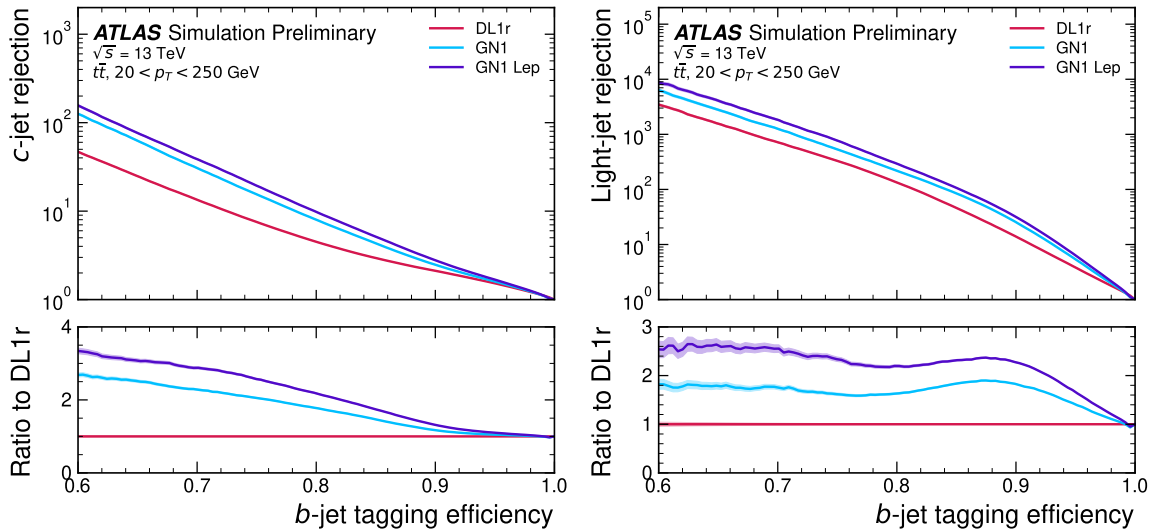


Fig. 3.14 The GN2 c -jet (left) and light-jet (right) rejections as a function of the b -jet tagging efficiency for jets in the $t\bar{t}$ sample with $20 < p_T < 250$ GeV. The ratio with respect to the performance of the DL1r algorithm is shown in the bottom panels. These figures are taken from [90].

GNN-based flavour tagging for large-R jets

In Run 3, ATLAS advanced its flavour tagging capabilities with the development of the GN2X [92] algorithm, designed to identify large-radius jets originating from boosted Higgs bosons decaying into pairs of bottom quarks ($H \rightarrow b\bar{b}$) and charm quarks ($H \rightarrow c\bar{c}$). The GN2X algorithm leverages recent advancements in GNNs and transformer architectures,

providing significant improvements in background rejection and tagging efficiency compared to previous methods.

The base GN2X model takes three large-radius jet variables and 20 track variables as inputs. Up to 100 tracks per jet are considered, sorted by decreasing transverse impact parameter significance to prioritise tracks from displaced vertices. The GN2X architecture utilises a transformer network with multiple encoder blocks and attention heads [96, 97] to process the track representations. This setup allows the model to capture complex relationships among tracks and derive a global jet representation for classification. In addition to the primary jet classification task, GN2X includes auxiliary training objectives for track origin classification and vertex grouping, enhancing the model’s ability to identify displaced vertices and improve tagging performance. GN2X achieves significant improvements in background rejection compared to previous taggers in $H \rightarrow b\bar{b}$ tagging. At a 50% $H(b\bar{b})$ tagging efficiency, GN2X provides a background rejection factor of 40 for jets from top quark decays and 300 for multijet events. This represents a factor of 1.6 improvement in top jet rejection and a factor of 2.5 improvement in multijet rejection compared to the baseline tagger D_{xbb} [89]. For $H(c\bar{c})$ tagging, GN2X offers substantial enhancements in rejecting background jets, including those from $H(b\bar{b})$ decays. At a 50% $H(c\bar{c})$ tagging efficiency, GN2X achieves a factor of 3 improvement in top jet rejection, a factor of 5 improvement in multijet rejection, and a factor of 6 improvement in $H(b\bar{b})$ rejection. GN2X maintains stable tagging efficiency across the entire transverse momentum (p_T) spectrum of the jets. At a 50% $H(b\bar{b})$ efficiency working point, GN2X shows consistent performance, significantly outperforming the baseline taggers across all p_T ranges. The algorithm exhibits less efficiency drop-off at high p_T compared to previous methods, ensuring reliable performance even for high-energy jets.

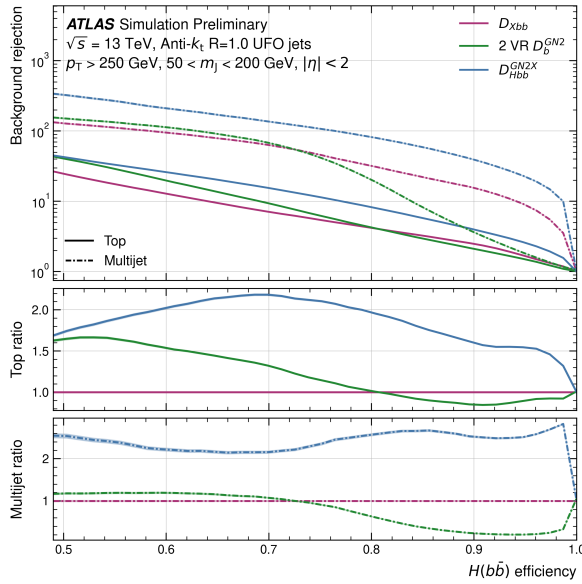


Fig. 3.15 GN2X top and multijet rejections as a function of the $H \rightarrow b\bar{b}$ efficiency for jets with $p_T > 250$ GeV and mass ($50 \text{ GeV} < m_J < 200 \text{ GeV}$). Performance of the GN2X algorithm is compared to the previous DXbb tagger and variable-radius subjets baselines. These figures are taken from [92].

3.3.5 Muon reconstruction and identification

The muon reconstruction and identification process [98] involves several sophisticated techniques that use the capabilities of the ATLAS detector's subsystems, including the Inner Detector (ID), Muon Spectrometer (MS), and calorimeters.

Muon reconstruction

Muon reconstruction in ATLAS primarily exploits the characteristics of minimum-ionising particles. This involves the identification of tracks within the MS or through specific energy deposits in the calorimeters. The reconstruction process utilises data from both the ID and MS tracking detectors, with calorimeter information contributing to track parameter determination and tagging of muon candidates independently from the MS.

The MS Stand-Alone Reconstruction process starts by identifying short straight-line segments from hits in individual MS stations using a Hough transform. These segments are combined into track candidates, taking into account the initial pointing constraint and the

parabolic trajectory of the muon bending in the magnetic field. A global χ^2 fit of the muon trajectory is then performed, which considers possible interactions with detector material and misalignments between detector chambers. Outliers are removed, and missing hits are added to refine the track fit. The final track is extrapolated back to the beam line, with its p_T expressed at the interaction point (IP). Global Muon Reconstruction involves a combination of information from the ID, MS, and calorimeters. The process follows five main strategies, resulting in different types of muons: Combined (CB), Inside-Out (IO), Muon-Spectrometer Extrapolated (ME), Segment-Tagged (ST), and Calorimeter-Tagged (CT) [98]. Each type has its reconstruction pathway, which includes matching MS tracks to ID tracks, extrapolating ID tracks to the MS, or using calorimeter data to tag muons.

Muon identification

Different WPs are defined based on the required efficiency, resolution, and background rejection. These criteria are applied to hits in the ID and MS, track fit properties, and compatibility variables between detector measurements. The WPs are tailored to optimise performance for various physics analyses, targeting prompt-muon identification, momentum resolution, and non-prompt muon rejection. The tag-and-probe method uses dimuon pairs from $Z \rightarrow \mu^+ \mu^-$ decays to measure reconstruction and identification efficiencies. One muon (the tag) must satisfy stringent criteria and trigger the event-selection, while the other (the probe) tests the efficiency of specific algorithms. Several probe types (ID, MS, CT, ST) are used to measure various efficiencies, and a matching requirement of $\Delta R < 0.05$ is applied to ensure accurate efficiency measurements. Efficiency scale factors are derived to correct simulation data to match real detector performance.

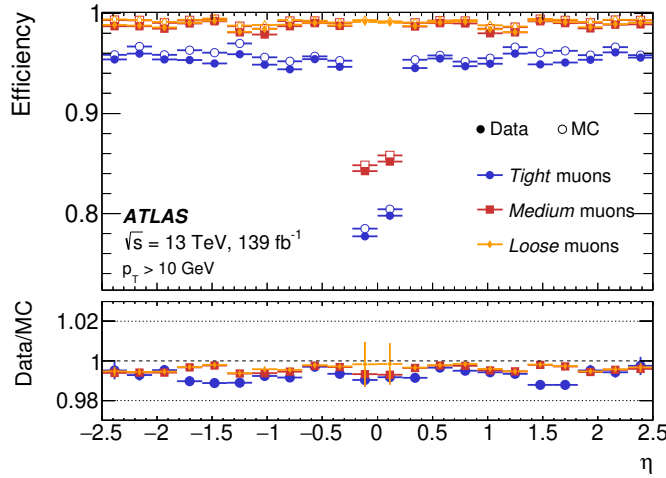


Fig. 3.16 Muon reconstruction and identification efficiencies for the Loose, Medium, and Tight criteria. It displays the efficiencies measured in $Z \rightarrow \mu\mu$ events as a function of η , for muons with $p_T > 10 \text{ GeV}$. This figure is taken from [98].

Muon calibration

Muon momentum calibration [66] is critical for achieving precise measurements, especially given the complexities of the detector geometry and alignment. Biases introduced by residual misalignments in the detector are corrected using a charge-dependent momentum calibration technique. This method involves analysing the mass of the dimuon system from $Z \rightarrow \mu^+ \mu^-$ decays to estimate and correct biases in the muon momentum scale. The calibration procedure is validated using independent samples of $J/\psi \rightarrow \mu^+ \mu^-$ and $\Upsilon \rightarrow \mu^+ \mu^-$ decays. These procedures include detailed studies of detector response, alignment system uncertainties, and the development of correction factors for both the ID and MS. The ultimate goal is to minimise the systematic uncertainties and achieve the highest possible precision in momentum measurement.

3.3.6 τ lepton reconstruction

A τ lepton has a 35% probability of decaying leptonically to a lighter lepton (τ_e or τ_μ) and two neutrinos. In the remaining 65% of cases a τ lepton decays hadronically (τ_{had})

to one or more charged hadrons, zero or more neutral hadrons, plus one neutrino. The leptonically decaying τ leptons are reconstructed as prompt electrons or muons in the ATLAS detector with non-zero impact parameters. The visible part of the hadronically decaying τ leptons ($\tau_{\text{had-vis}}$) are reconstructed and identified using a combination of tracking and calorimetric information.

A significant portion of this thesis is dedicated to the detailed reconstruction and identification of $\tau_{\text{had-vis}}$. This constitutes a major part of the research I have been worked on. The next chapter will delve deeply into this topic, providing comprehensive insights and methodologies.

Chapter 4

The $\tau_{\text{had-vis}}$ reconstruction and identification at ATLAS

This chapter describes the reconstruction (TauReco) and identification (TauID) of hadronically decaying tau leptons ($\tau_{\text{had-vis}}$), largely based on the “Reconstruction, Identification, and Calibration of hadronically decaying tau leptons with the ATLAS detector for the LHC Run 3 and reprocessed Run 2 data” [99]. Over the years, TauReco and TauID has been significantly improved, starting from a cut-based approach adopted during early Run 1 [100], to a boosted decision tree (BDT) algorithm from the end of Run 1 [101], and finally to a recurrent neural network (RNN) algorithm during Run 2 and Run 3 [99]. In the future, TauID will be further improved by incorporating more advanced machine learning techniques such as graph neural networks (GNNs) and transformers. Early results from the GNN-based TauID have shown promising performance, with the potential to further enhance the signal-to-background separation in the $\tau_{\text{had-vis}}$ identification.

4.1 $\tau_{\text{had-vis}}$ reconstruction

The candidates for $\tau_{\text{had-vis}}$ are initially seeded by jets formed using the anti- k_T algorithm, which has a radius parameter of $R = 0.4$. The TopoClusters are calibrated using a local hadronic calibration (LC). Jets that seed $\tau_{\text{had-vis}}$ candidates must have p_{T} greater than 5 GeV and $|\eta| < 2.5$. The p_{T} requirement is applied to the LC energy of the jet, prior to any JES corrections.

4.1.1 Vertex association

During p-p collisions at the LHC, multiple simultaneous interactions occur, resulting in the reconstruction of several interaction vertices. Typically, particles are assumed to originate from the primary vertex, which is defined as the vertex with the highest sum of the squared transverse momenta of the associated tracks ($\sum p_T^2$). However, since tau leptons decay away from the primary vertex, a dedicated tau vertex association algorithm (TJVA) is used to identify the correct production vertex for each $\tau_{\text{had-vis}}$ candidate. This production vertex is then used for $\tau_{\text{had-vis}}$ reconstruction instead of the primary vertex.

The tau production vertex is crucial for calculating quantities such as the impact parameter and determining which tracks are associated with the $\tau_{\text{had-vis}}$ candidate. Parameters of the associated tracks are recalculated relative to the tau production vertex.

For Run 3, the vertexing algorithm has been updated to handle the high pile-up environment, necessitating a re-tuning of the TJVA. The method is based on the p_{T} fraction of a given vertex $f_{p_{\text{T}}}$:

$$f_{p_{\text{T}}} = \frac{\sum p_{\text{T}}(\text{tracks associated with the vertex})}{\sum p_{\text{T}}(\text{all tracks})}$$

where all tracks within (ΔR) of less than 0.2 from the seed jet are considered. The vertex with the highest $f_{p_{\text{T}}}$ fraction is chosen as the tau production vertex and is used for de-

terminating the $\tau_{\text{had-vis}}$ direction, associating tracks, and building the coordinate system for calculating identification variables.

The efficiency of selecting the correct tau production vertex compared to the primary vertex is evaluated as a function of the $\tau_{\text{had-vis}} p_{\text{T}}$ and the average number of simultaneous proton-proton collisions ($\langle \mu \rangle$). The tau production vertex consistently shows better efficiency, especially at low p_{T} .

The $\tau_{\text{had-vis}}$ four-momentum is calculated by first computing η and ϕ of the barycentre of the TopoClusters of the seed jet, calibrated at the LC scale, assuming a mass of zero for each constituent. The four-momenta of all clusters in the region $\Delta R < 0.2$ around the barycentre are recalculated using the tau production vertex coordinate system and summed, providing the momentum magnitude and direction of the $\tau_{\text{had-vis}}$. Figure 4.1 shows the efficiency to select the correct τ production vertex using TJVA or the default primary vertex in $\gamma^* \rightarrow \tau\tau$ events, as a function of $\langle \mu \rangle$, taken from [99].

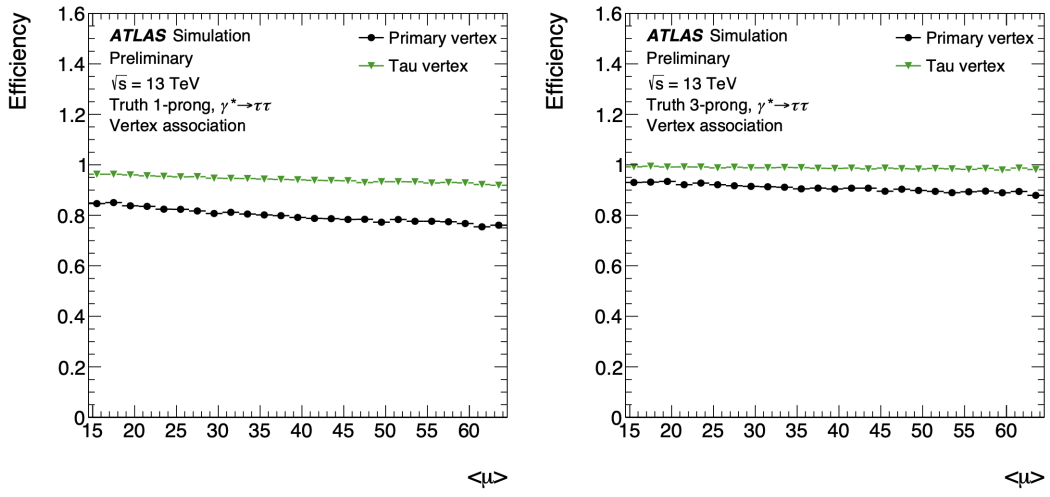


Fig. 4.1 Efficiency to select the correct τ production vertex using TJVA or the default primary vertex in $\gamma^* \rightarrow \tau\tau$ events, as a function of $\langle \mu \rangle$. The left plot shows the efficiency for 1-prong τ_{had} , while the right plot shows the efficiency for 3-prong τ_{had} , taken from [99].

4.1.2 Track Association

Tracks are associated with the $\tau_{\text{had-vis}}$ candidate if they are within a core region ($\Delta R < 0.25$) around the $\tau_{\text{had-vis}}$ direction and meet the following criteria:

- p_T greater than 1 GeV,
- at least two associated hits in the pixel layers of the inner detector,
- at least seven hits in total in the pixel and SCT layers.

Additionally, association requirements are imposed on the distance of closest approach of the track to the tau production vertex in the transverse plane ($|d_0^{\text{TJVA}}| < 1.0$ mm) and longitudinally ($|z_0^{\text{TJVA}} \sin \theta| < 1.5$ mm). Tracks in the region $0.25 < \Delta R < 0.4$ are also associated with the $\tau_{\text{had-vis}}$ if either:

- they are matched to the τ_{seed} jet by a ghost-particle association technique, or
- the closest jet to the track in terms of ΔR distance is the $\tau_{\text{had-vis}}$ seeding jet.

4.1.3 Track Classification

To correctly establish the charge and the number of charged decay products of a tau lepton, the tracks that are associated with the tau decay need to be correctly distinguished from the other tracks associated with the τ_{seed} . Using a track classifier, tracks that have passed the TJVA requirements are classified into four categories:

- tau tracks (TT): tracks originating from charged tau lepton decay products.
- conversion tracks (CT): tracks from electrons and positrons that are created from photon conversion in the detector.
- isolation tracks (IT): tracks likely originating from quark or gluon jets arising from the remnants of the hard scattering interactions.

- fake tracks (FT): tracks that do not belong to the previous categories, mainly mis-reconstructed tracks and pile-up tracks.

A novel approach for the tau lepton track classification using a recurrent neural network (RNN) [102] has been developed, replacing the previous BDT-based method used during Run 2. RNNs are specifically chosen for their ability to use bidirectional long short-term memory (BLSTM) cells, allowing information to be back-propagated, exploiting forward and backward correlations in sequences of tracks belonging to tau decays.

The network is trained using Keras [103] and TensorFlow [104], applied to sequences of p_T -ordered tracks associated with each $\tau_{\text{had-vis}}$ candidate. The training data includes signal candidates from simulated $\gamma^* \rightarrow \tau\tau$ events and background candidates from dijet events, with each sample divided into subsets for training, validation, and performance evaluation. Input variables for the RNN include kinematic, geometric, and detector hit distribution information for the tracks. The primary measure to evaluate the performance of the track classifier are the reconstruction efficiency. The reconstruction efficiency is the efficiency to correctly classify 1- or 3-tracks originating from truth 1-prong and 3-prong τ leptons. The reconstruction efficiency evaluated as a function of the $\tau_{\text{had-vis}}$ pT and $\langle\mu\rangle$ is shown in Figure 4.2.

4.2 $\tau_{\text{had-vis}}$ Identification and electron-veto

4.2.1 RNN-based identification

During Run 2, a novel $\tau_{\text{had-vis}}$ identification algorithm (TauID) was introduced to separate true $\tau_{\text{had-vis}}$ candidates from those misidentified as originating from quark- and gluon-initiated jets. This algorithm, based on a RNN, utilises information from reconstructed charged-particle tracks and clusters of energy in the calorimeter associated with $\tau_{\text{had-vis}}$ candidates, along with high-level discriminating variables. Compared to the BDT iden-

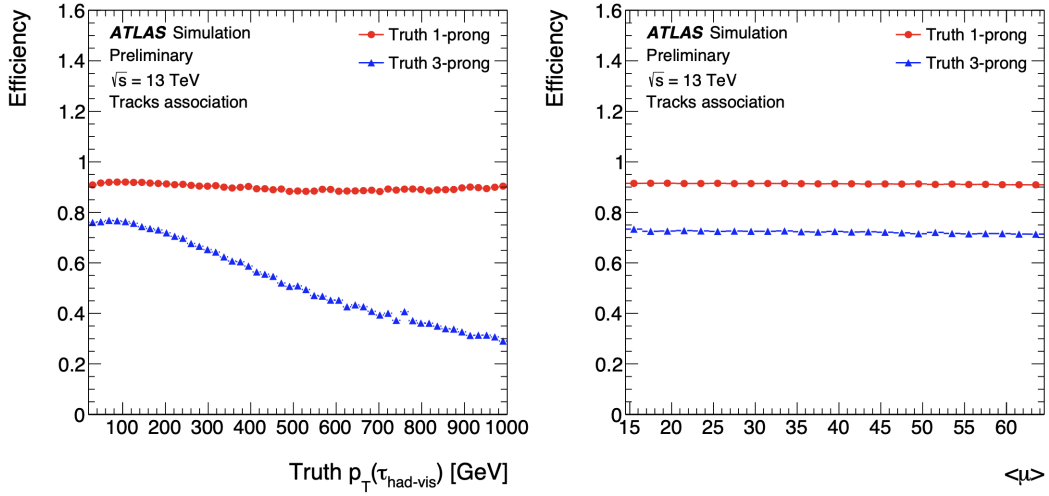


Fig. 4.2 Reconstruction efficiency of the track classifier for 1-prong and 3-prong $\tau_{\text{had-vis}}$ candidates as a function of $\tau_{\text{had-vis}} p_T$ (left) and $\langle \mu \rangle$ (right).

tification algorithm used at the beginning of Run 2, the RNN algorithm improved the rejection of misidentified $\tau_{\text{had-vis}}$ candidates by 75-100%, depending on the $\tau_{\text{had-vis}} p_T$ and the number of tracks.

The RNN architecture used for $\tau_{\text{had-vis}}$ identification consists of three input branches.

- Track Variables: this branch processes information related to the tracks associated with the $\tau_{\text{had-vis}}$ candidate.
- Cluster Variables: this branch processes information related to the energy clusters in the calorimeter.
- High-Level Jet Variables: this branch processes high-level observables calculated from track and calorimeter quantities.

The RNN's internal state allows it to process sequences of unknown length, making it suitable for the variable-length input data associated with $\tau_{\text{had-vis}}$ candidates. Each branch feeds into the RNN, which is trained using simulated samples of $\tau_{\text{had-vis}}$ candidates. The signal sample consists of $\tau_{\text{had-vis}}$ candidates from $\gamma^* \rightarrow \tau\tau$ events, while the background sample consists of candidates from simulated QCD di-jet events. Reconstructed $\tau_{\text{had-vis}}$

candidates from $\gamma^* \rightarrow \tau\tau$ events are required to be geometrically matched to $\tau_{\text{had-vis}}$ at the truth level and correctly reconstructed as 1- or 3-prong decays. Reconstructed $\tau_{\text{had-vis}}$ candidates from simulated di-jet samples are required to be reconstructed as 1- or 3-prong $\tau_{\text{had-vis}}$ candidates.

The performance of the RNN-based $\tau_{\text{had-vis}}$ identification algorithm is evaluated on independent test samples of signal and background events. The efficiency of $\tau_{\text{had-vis}}$ identification is measured as a function of $\tau_{\text{had-vis}} p_{\text{T}}$ and $\langle \mu \rangle$.

The identification algorithm defines several working points (Very Loose, Loose, Medium, Tight) based on the transformed (flattened) RNN score, which ensures that the τ_{had} efficiency does not depend on the reconstructed $\tau_{\text{had-vis}} p_{\text{T}}$ and $\langle \mu \rangle$. The rejection of misidentified $\tau_{\text{had-vis}}$ candidates, defined as the inverse of the background selection efficiency, is evaluated for each working point. The combined reconstruction and identification efficiency of the $\tau_{\text{had-vis}}$ identification algorithm is shown in Figure 4.3. Inverse of the efficiency (rejection) for misidentified 1-prong and 3-prong τ_{had} candidates from dijet background events as a function of the efficiency for truth τ_{had} originating from $\gamma^* \rightarrow \tau\tau$ events is shown in Figure 4.4. Both figures are taken from [99].

The τ_{had} candidates are further classified into five primary decay modes by a DeepSet Neural Network (DSNN) [105] algorithm. This method identifies the number of charged and neutral hadrons from τ decays. The efficiency matrix for reconstructing the same τ lepton decay mode as the truth decay mode with DeepSet NN classifier in $\gamma^* \rightarrow \tau\tau$ events is shown in Figure 4.5.

4.2.2 RNN-based electron-veto

Electrons can be misidentified as $\tau_{\text{had-vis}}$ candidates. In some analyses, electrons represent a significant background contribution even after the suppression of jet-related backgrounds through kinematic, topological, and tau identification criteria. Despite the

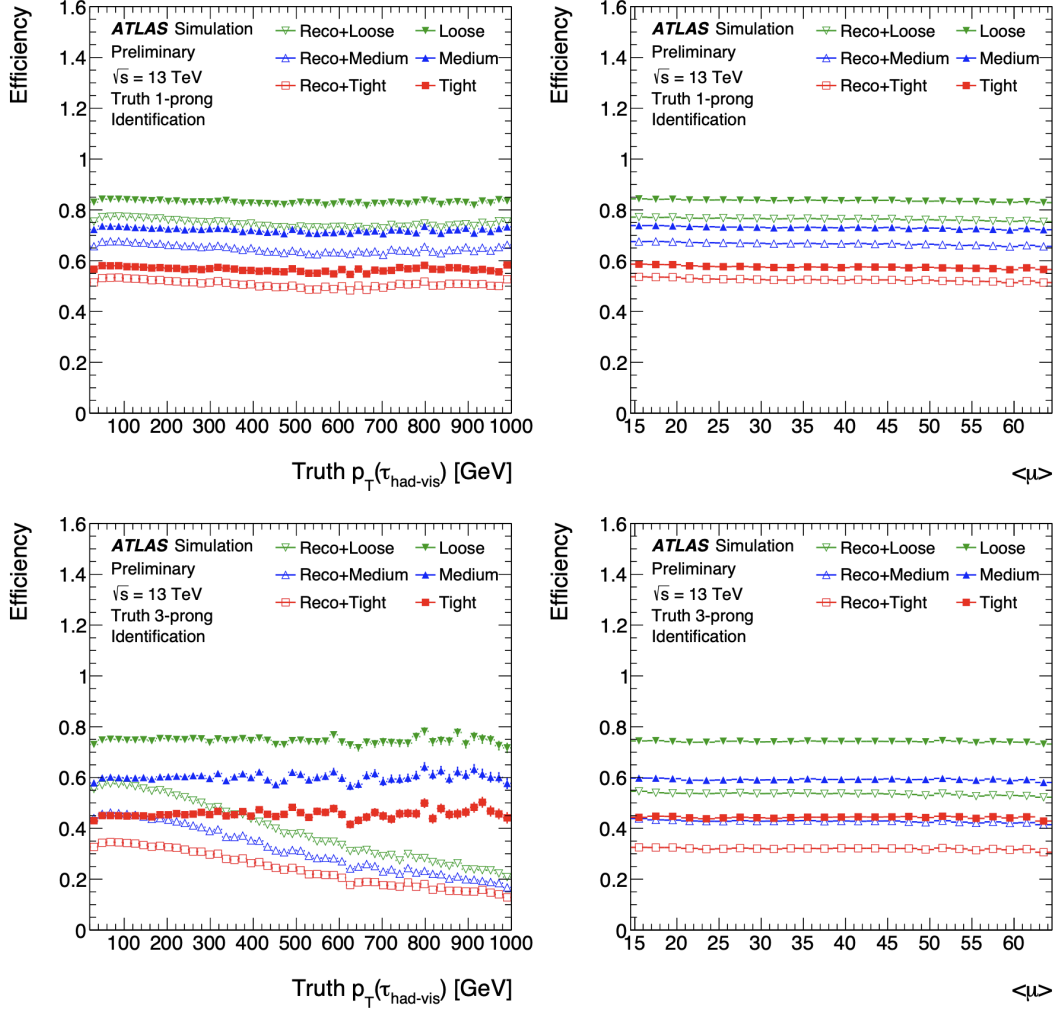


Fig. 4.3 Combined reconstruction and identification efficiency of the $\tau_{\text{had-vis}}$ identification algorithm as a function of $\tau_{\text{had-vis}} p_T$ (left) and $\langle \mu \rangle$ (right), taken from [99]. The decay of the $\tau_{\text{had-vis}}$ efficiency in 3-prong $\tau_{\text{had-vis}}$ candidates at high $\tau_{\text{had-vis}} p_T$ is due to the tracking efficiency in dense environments.

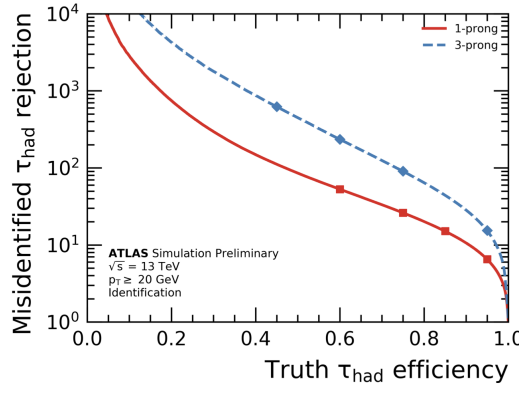


Fig. 4.4 Inverse of the efficiency (rejection) for misidentified 1-prong and 3-prong τ_{had} candidates from dijet background events as a function of the efficiency for truth τ_{had} originating from $\gamma^* \rightarrow \tau\tau$ events, taken from [99].

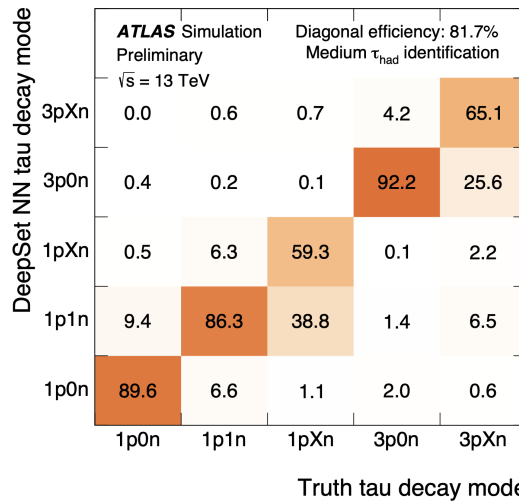


Fig. 4.5 Efficiency matrix for reconstructing the same τ lepton decay mode as the truth decay mode with DeepSet NN classifier in $\gamma^* \rightarrow \tau\tau$ events, taken from [99]. The labels are in a form of 'ApBn', where 'A' 'B' are the number of prongs (the 'p') and neutral pions (the 'n') and 'X' stands for more than one or more than zero accordingly.

similarities between electron signatures and 1-prong $\tau_{\text{had-vis}}$, there are distinctive properties that can be exploited for discrimination. Electrons are highly relativistic particles that emit transition radiation when traversing the radiator material surrounding the straws of the TRT detector. This property, along with the shape of the calorimetric energy deposits in combination with the track information, provides a basis for discriminating electrons from $\tau_{\text{had-vis}}$. The ATLAS overlap removal procedure ensures that identified electrons are not double-counted as $\tau_{\text{had-vis}}$ candidates. However the electron identification is not perfect, and some electrons may fail the electron identification and still be misidentified as $\tau_{\text{had-vis}}$.

The BDT-based e-veto algorithm used during Run 2 has been replaced by a novel approach based on RNN. The updated RNN e-veto offers multiple working points for different levels of discrimination. The e-veto algorithm is trained using simulated samples of signal and background candidates. The signal sample is the same as that used for the TauID algorithm, while the background sample consists of reconstructed $\tau_{\text{had-vis}}$ candidates from $Z \rightarrow ee$ processes, required to pass the Medium $\tau_{\text{had-vis}}$ identification working point.

Dedicated neural networks are trained separately for 1-prong and 3-prong $\tau_{\text{had-vis}}$ cases. The reconstructed p_{T} of the $\tau_{\text{had-vis}}$ is used to re-weight the samples, ensuring no p_{T} -dependent bias in the trained classifier. The training minimises the binary cross-entropy loss function [106] using stochastic gradient descent (SGD) [107] with momentum and a step-wise reduction of the optimiser’s learning rate.

The e-veto algorithm’s output score is transformed to provide a uniform efficiency with respect to p_{T} and η of the true $\tau_{\text{had-vis}}$. The algorithm defines three working points (Loose, Medium, Tight) for different levels of electron rejection efficiency. The performance of the e-veto algorithm is evaluated on independent test samples, measuring the $\tau_{\text{had-vis}}$ efficiency and electron rejection factor as functions of $\langle\mu\rangle$ and the p_{T} of 1-prong and

3-prong $\tau_{\text{had-vis}}$ candidates. Figure 4.6 shows the rejection for misidentified 1-prong and 3-prong $\tau_{\text{had-vis}}$ candidates from $Z \rightarrow ee$ background events as a function of the efficiency for truth τ_{had} originating from $\gamma^* \rightarrow \tau\tau$ events.

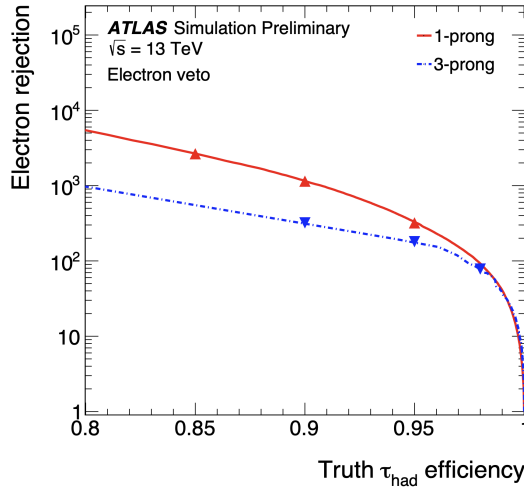


Fig. 4.6 Rejection for misidentified 1-prong and 3-prong $\tau_{\text{had-vis}}$ candidates from $Z \rightarrow ee$ background events with the e-veto algorithm, as a function of the efficiency for truth τ_{had} originating from $\gamma^* \rightarrow \tau\tau$ events, taken from [99].

4.3 $\tau_{\text{had-vis}}$ Energy calibration and resolution

The energy calibration of τ_{had} involves several steps to ensure accurate measurement of the visible energy.

- Pre-calibration: initial energy estimates are obtained from the seed jets.
- MC-based corrections: corrections derived from MC simulations are applied to account for detector response and other systematic effects.
- Boosted regression tree (BRT) refinement: the boosted regression tree algorithm refines the energy estimates using additional input variables and sequential data from the RNNs.

- Data-driven corrections: final adjustments are made using data-driven techniques, comparing MC predictions with actual data to ensure consistency and accuracy.

Pre-calibration

Pre-calibration is the initial step in the energy calibration process for $\tau_{\text{had-vis}}$. This step involves obtaining preliminary energy estimates from the visible decay products of the tau leptons, utilising data from the calorimeter and tracking systems of the detector. After the reconstruction of $\tau_{\text{had-vis}}$ candidates, the four-momentum of the $\tau_{\text{had-vis}}$ candidate is calculated by summing the momenta of all associated clusters and tracks. This preliminary four-momentum estimate provides the initial energy scale for the tau candidates.

MC-based corrections

The MC-based corrections are derived from detailed simulations that model the interactions of particles within the detector, accounting for various physical processes and detector effects. The goal of MC-based corrections is to adjust the initial energy estimates obtained during pre-calibration to more accurately reflect the true energy of the tau leptons.

The energy scale correction adjusts the measured energy to account for systematic biases in the calorimeter and tracking systems. This ensures that the average measured energy matches the true energy over a wide range of tau energies. The resolution correction accounts for the smearing of the energy measurement due to detector resolution effects. It ensures that the distribution of measured energies around the true energy is correctly modelled.

The MC-based corrections are derived by comparing the true energy of tau leptons in the simulation with the energy measured by the detector. This comparison is done as a function of key variables like p_T , $|\eta|$, and decay mode. The derived correction factors are

applied to the initial energy estimates of τ_{had} candidates. The corrected energy measurements are validated by comparing key distributions (e.g., invariant mass of tau pairs) in data and simulation.

BRT refinement

BRT refinement is a sophisticated technique used to enhance the accuracy and precision of the energy estimates of τ_{had} . This method applies machine learning to correct residual biases and improve the resolution of the energy measurements beyond what is achieved by MC-based corrections alone.

At the core of BRT are decision trees, which are simple predictive models that split data into subsets based on feature values. Each split is chosen to minimise the error in predicting the target variable, in this case, the tau energy. Boosting is an ensemble technique that combines the predictions of multiple weak learners (individual decision trees) to form a stronger predictive model. Trees are built sequentially, with each tree correcting the errors of its predecessors.

The energy estimates obtained from pre-calibration and MC-based corrections serve as the starting point for BRT refinement. The BRT model is trained using the simulated samples, where the input features (calorimeter and tracking variables) are used to predict the true tau energy. The model learns to correct systematic biases and improve the precision of the energy estimates. Once trained, the BRT model is applied to the actual data. The model takes the MC-based energy estimates and the same set of input features to produce refined energy predictions for $\tau_{\text{had-vis}}$ candidates. The performance of the BRT refinement is validated using independent test samples. Key metrics such as the energy resolution and scale are evaluated to ensure the model's predictions are accurate and unbiased.

Data-driven corrections

The data-driven method is the final step in the calibration process for τ_{had} . It involves using actual collision data to further refine and validate the energy calibration obtained from MC-based corrections and BRT refinement. This approach helps to correct any discrepancies between simulation and real data, ensuring that the final energy measurements are as accurate and unbiased as possible [108].

The data-driven method relies on reference processes to calibrate the energy measurements of $\tau_{\text{had-vis}}$ candidates. Reference processes, such as well-understood physics decays like $Z \rightarrow \tau_\mu \tau_{\text{had}}$ are used as benchmarks to compare data and simulation. The method exploits the fact that the distribution of the reconstructed visible mass of the $\tau_{\text{had-vis}}$ and muon system, m_{vis} , in $Z \rightarrow \tau_\mu \tau_{\text{had}}$ events is sensitive to the differences in energy scale of the $\tau_{\text{had-vis}}$ candidates between data and simulation.

The τ energy scale (TES) correction is parameterised as $p_{\text{T}} \rightarrow (1 + \alpha)p_{\text{T}}$ for $\tau_{\text{had-vis}}$ candidates, where α is the TES correction factor. The muon energy scale is measured with high precision with independent methods. In Run 2, the TES correction factor is determined by minimising the difference between the m_{vis} distribution in data and simulation. Specifically, α is determined by minimising

$$\chi^2(\alpha, f) = \sum_i \frac{(N_i^{\text{data}} - f N_i^{\text{sig}}(\alpha) - N_i^{\text{bkg}})^2}{N_i^{\text{data}} + f^2 (\Delta N_i^{\text{sig}}(\alpha))^2 + (\Delta N_i^{\text{bkg}})^2},$$

where $N_i^{\text{data/sig/bkg}}$ is the number of events in the i -th bin of the m_{vis} distribution in data, signal, or background; ΔN_i^{sig} is the uncertainty in the number of signal events in the i -th bin; and f is a normalisation factor that accounts for the difference in the total number of events between data and simulation.

Chapter 5

The muon-removal method for boosted $\tau_\mu\tau_{\text{had}}$ reconstruction

5.1 Introduction

The standard ATLAS TauID algorithm is efficient unless activity from other particles is found inside the τ_{seed} jet. One of these cases is when a pair of τ leptons originates from a highly boosted resonance and the decay products of the two τ leptons are reconstructed within the radius of a single τ_{seed} jet. The reconstruction and identification of boosted systems in which both τ leptons decay hadronically is achieved by searching for hadronic τ -like substructure using a boosted decision tree within a large radius seed jet [109]. In this chapter, the decay in the $\tau_\mu\tau_{\text{had}}$ final state is considered.

The minimum ionising nature of the muon and the fact that the muon reconstruction is independent of its isolation [98] prompt the idea of removing the track and clusters produced by the muon from the τ_{seed} jet produced by a boosted $\tau_\mu\tau_{\text{had}}$ system. The kinematic variables that are subsequently supplied to the TauID algorithm are re-calculated without the interference of the muon. The τ_{had} reconstructed with this method is denoted as τ_{had}^μ .

The τ_{had}^μ method was developed using Monte Carlo (MC) simulated events corresponding to the beyond the standard model (BSM), high-mass Graviton [5] decaying into two Higgs boson process as signal. However, before using this technique in future searches for BSM physics, it is important to demonstrate its performance considering a standard model process. As a benchmark for the new method, the production of two τ leptons originating from a highly boosted Z boson decay is used. This process is denoted as $Z \rightarrow \tau_\mu\tau_{\text{had}}$.

This chapter is organised as follows. The data and MC samples are described in Section 5.2. The development of the boosted τ_{had}^μ method is described in Section 5.3. The analysis methods for the $Z \rightarrow \tau_\mu\tau_{\text{had}}$ benchmark are described in Section 5.4. The results of the $Z \rightarrow \tau_\mu\tau_{\text{had}}$ benchmark analysis are described in Section 5.5. The summary and conclusions are given in Section 5.6.

5.2 Data and simulated samples

5.2.1 Simulated samples for development of the method

MC simulated event samples are used to model the signal and the background to develop the τ_{had}^μ method and to evaluate the τ identification efficiency and background rejection power. The signal sample consists of BSM Gravitons [5] decaying to a pair of Higgs bosons, with the hypothetical Graviton mass ranging from 1000 GeV to 5000 GeV. To maximise the signal statistics, the Higgs boson is constrained to decay to a pair of τ leptons. The signal process is denoted by $G \rightarrow HH \rightarrow 4\tau$.

A high- p_T , semi-leptonically decaying heavy flavour hadron may produce a detector signature that has some similarities with the signal sample of boosted $\tau_\mu\tau_{\text{had}}$ pair systems, since the invariant mass of the charmed hadron produced in the semi-leptonic decay of a

B hadron is comparable to that of the τ lepton. The $t\bar{t}$ process is used to model this type of background.

The $G \rightarrow HH \rightarrow 4\tau$ signal samples are generated using the MADGRAPH 5 [110] matrix element (ME) generator. The production of $t\bar{t}$ events is modelled using the POWHEG BOX v2 [111–114] generator at NLO with the NNPDF3.0NLO [115] PDF set and the h_{damp} parameter¹ set to 1.5 m_{top} [116].

PYTHIA [117] with the A14 [118] tuned parameters and NNPDF2.3LO [119] PDF is used for the simulation of the parton showering and hadronisation for both the $G \rightarrow HH \rightarrow 4\tau$ samples and the $t\bar{t}$ samples. The decays of bottom and charm hadrons were performed by EVTGEN 1.6.0 [120]. The effect of multiple interactions in the same and neighbouring bunch crossings (pile-up) was modelled by overlaying the original hard-scattering event with simulated inelastic events generated by PYTHIA 8.186 [117] with the A3 tune [121] and the MSTW2008LO PDF set [122]. The MC samples were re-weighted so that the pile-up distribution matches the one observed in the data. All MC samples are passed through the ATLAS detector simulation based on GEANT 4 [123].

5.2.2 Data and simulated samples for the benchmark analysis

For the $Z \rightarrow \tau_\mu \tau_{\text{had}}$ benchmark analysis, the full Run 2 dataset collected in pp collisions at the LHC [3] with a centre-of-mass energy of 13 TeV and a 25 ns bunch crossing interval is utilised. The integrated luminosity of the dataset recorded while all relevant components of the ATLAS detector were operated in their nominal operating conditions corresponds to 140 fb^{-1} [124].

Simulated samples provide predictions for both signal and background processes. As in Section 5.2.1, the simulation includes the effect of multiple pp interactions per bunch

¹The h_{damp} parameter is a resummation damping factor and one of the parameters that controls the matching of POWHEG matrix elements to the parton shower and thus effectively regulates the high- p_{T} radiation against which the $t\bar{t}$ system recoils.

crossing, as well as the impact on the detector response due to interactions from bunch crossings before or after the one containing the hard interaction. All MC samples undergo detector simulation, calibration, and corrections to match the performance in data. For all simulated samples, the next-to-next-to-leading-order (NNLO) PDF is employed for ME calculations. The decays of bottom and charm hadrons were performed by EVTGEN [120]. The rest of this section gives details of the specific MC samples used in this study.

The dominant production channel of the boosted $Z \rightarrow \tau_\mu\tau_{\text{had}}$ final state, a Z boson produced in association with jets was modelled using the SHERPA 2.2.14 [125] MC generator in the $Z \rightarrow \tau\tau$ channel; while the SHERPA 2.2.11 MC generator was used in the $Z \rightarrow ll$ ($l = e, \mu$) channels. The ME calculations range from next-to-leading order (NLO) for final states with up to two additional parton emissions to leading order (LO) for up to five additional parton emissions. The matrix elements were merged with the SHERPA parton shower following the MEPS@LO [126] prescription and using the NNPDF3.0NNLO set of PDFs [115]. The production of W boson with jets, and the production of WW , WZ , and ZZ boson pairs, was simulated with the SHERPA 2.2.11 with similar configurations as the Z +jets sample. For Z boson production, particularly for events with $p_T^Z > 100$ GeV, comparing with the measurements of Z -boson p_T^Z and ϕ_η^* using light-lepton pair events at 13 TeV [127], the cross-section for Z boson events with high p_T^Z modelled by SHERPA 2.2.11 is approximately 10% lower than in data [128]. The simulation of initial state QCD radiation is expected to be similar in the SHERPA 2.2.14 sample used in this study. A 10% correction is applied to the predicted numbers for $Z \rightarrow \tau\tau$ events, with the full size of this correction quoted as a systematic uncertainty.

The production of $t\bar{t}$ events was modelled using the same configuration as the one used for the method development.

Single-top t -channel production was modelled using the POWHEG BOX v2 [112–114, 129] generator at NLO in QCD using the four-flavour scheme and the corresponding

NNPDF3.0NLO set of PDFs [115]. The events were interfaced with PYTHIA 8.230 [117] using the A14 tune [118] and the NNPDF2.3LO set of PDFs [119].

The associated production of top quarks with W bosons (tW) was modelled by the POWHEG BOX v2 [112–114, 130] generator at NLO in QCD using the five-flavour scheme and the NNPDF3.0NLO set of PDFs [115]. The diagram removal scheme [131] was used to remove interference and overlap with $t\bar{t}$ production. The events were interfaced to PYTHIA 8.230 [117] using the A14 tune [118] and the NNPDF2.3LO set of PDFs [119].

5.3 Development of the boosted τ_{had}^{μ} reconstruction method

5.3.1 Muon removal and re-reconstruction of tau lepton candidate

The proximity between the $\tau_{\text{had-vis}}$ and the muon is represented by $\Delta R_{\tau\tau}^{\text{truth,vis}}$, the ΔR between the MC truth-level visible decay products of the two τ leptons. In Figure 5.1, the $\Delta R_{\tau\tau}^{\text{truth,vis}}$ distributions of the $\tau_{\mu}\tau_{\text{had}}$ pairs in the $G \rightarrow HH \rightarrow 4\tau$ samples are presented. If the $\Delta R_{\tau\tau}^{\text{truth,vis}} < 0.4$, it is likely that the muon will be reconstructed inside the τ_{seed} jet.

For the purposes of this study, MC truth information is used to match truth-level $\tau_{\mu}\tau_{\text{had}}$ pairs with their reconstructed counterparts. This facilitates focusing on only τ_{seed} jets originating from the boosted $\tau_{\mu}\tau_{\text{had}}$ pair and allows other τ_{seed} jets associated with QCD jets to be neglected. The MC truth-level visible τ decay products are required to satisfy the requirements $p_T > 20$ GeV and $|\eta| < 2.5$, to ensure that the τ_{seed} jets are within the tracking acceptance of the ATLAS detector.

The loss of performance of the standard TauID algorithm in the low $\Delta R_{\tau\tau}^{\text{truth,vis}}$ region is illustrated in Figure 5.2, which shows the combined reconstruction and identification efficiencies of the standard ATLAS τ_{had} reconstruction algorithm and TauID algorithm as a function of $\Delta R_{\tau\tau}^{\text{truth,vis}}$ for truth “1-prong” and “3-prong” $\tau_{\mu}\tau_{\text{had}}$ pairs. Here the “n-prong” denotes the number of charged hadrons that originate from the τ_{had} decay. The

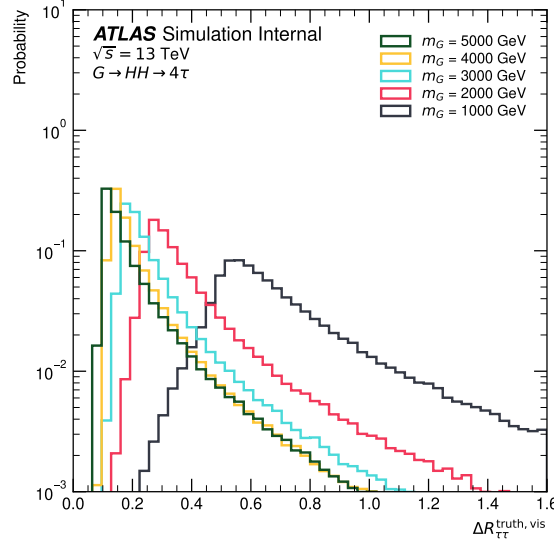


Fig. 5.1 The distributions of the $\Delta R_{\tau\tau}^{\text{truth,vis}}$ between the truth level $\tau_\mu \tau_{\text{had}}$ pair in the $G \rightarrow HH \rightarrow 4\tau$ with hypothetical Graviton mass ranging from 1000 GeV to 5000 GeV. The distributions are normalised to unity.

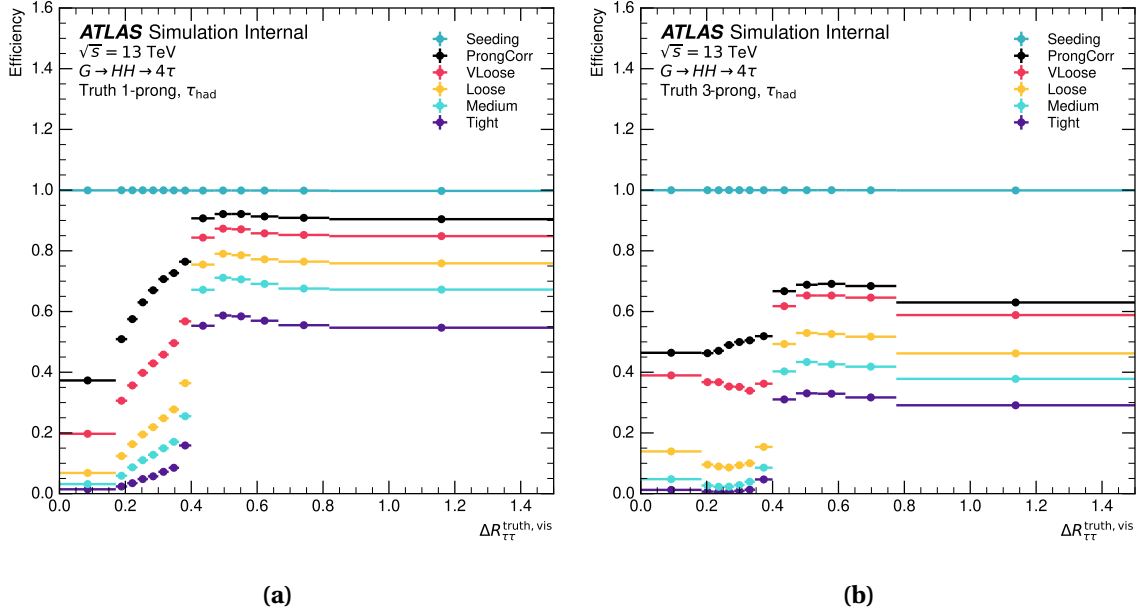


Fig. 5.2 The combined reconstruction and identification efficiencies of the standard ATLAS TauID for truth 1-prong (a) and 3-prong (b) $\tau_\mu \tau_{\text{had}}$ pairs in all working points as a function of $\Delta R_{\tau\tau}^{\text{truth,vis}}$; the “Seeding” line (dark cyan) shows the efficiency of a τ_{seed} jet that matches to a truth-level $\tau_\mu \tau_{\text{had}}$ pair being reconstructed; the “ProngCorr” line (black) shows the efficiency of a truth-level τ_{had} being reconstructed with the correct number of associated charged-particle tracks.

efficiency for a τ_{seed} jet to be reconstructed from a truth-level $\tau_{\mu}\tau_{\text{had}}$ pair remains high for all values of $\Delta R_{\tau\tau}^{\text{truth},\text{vis}}$. However, the efficiencies for all standard TauID working points drop significantly in both “1-prong” and “3-prong” cases when $\Delta R_{\tau\tau}^{\text{truth},\text{vis}} < 0.4$. The tighter the working point, the greater the fractional loss in efficiency due to the presence of the nearby muon. The performance of the standard TauID algorithm is set as a baseline in this study.

The muon’s nature as a minimum ionising particle, combined with the fact that its reconstruction is independent of its isolation [98], provides a motivation for excluding the inner detector track and calorimeter clusters associated with any nearby muon from the standard ATLAS τ_{had} reconstruction algorithm. By removing these contributions, the τ_{seed} jet would better represent only the hadronically decaying τ , improving the accuracy of TauID. Specifically, the inner detector track and clusters associated with a reconstructed muon that satisfies the “Medium” muon ID working point [98] is removed if the track or cluster is found within the reconstructed τ_{seed} jet. After the muon removal, the standard hadronic tau reconstruction algorithm is re-run on the τ_{seed} jet. In this way, the relevant ID variables for the hadronically decaying τ can be calculated without the muon component.

5.3.2 Performance of the method

Figure 5.3 shows the combined reconstruction and identification efficiencies after muon removal as a function of $\Delta R_{\tau\tau}^{\text{truth},\text{vis}}$ for truth 1-prong and 3-prong $\tau_{\mu}\tau_{\text{had}}$ pairs in all working points. The reconstruction and identification efficiencies after muon removal show a considerable improvement compared to those shown in Figure 5.2. The signal efficiency is recovered almost completely in every working point for both 1-prong and 3-prong τ_{had} . For 3-prong cases, the efficiency of TauID is limited by the accurate reconstruction of the correct number of tracks associated with the highly boosted τ_{had} (referred to as “ProngCorr”).

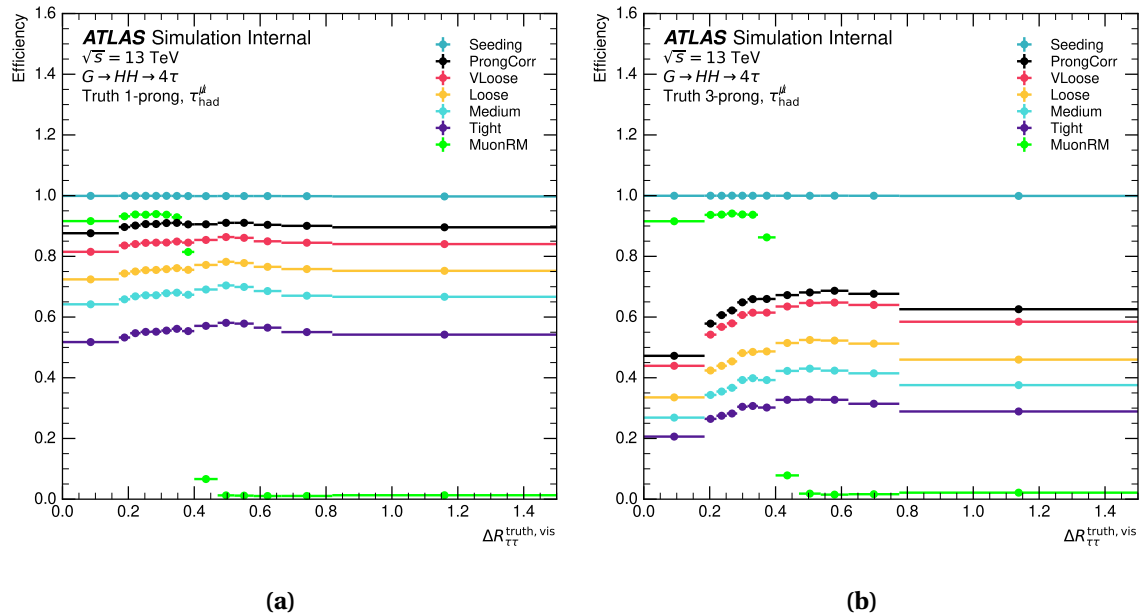


Fig. 5.3 The combined reconstruction and TauID efficiencies after the muon removal for truth 1-prong (a) and 3-prong (b) $\tau_\mu \tau_{\text{had}}$ pairs in all working points as a function of $\Delta R_{\tau\tau}^{\text{truth},\text{vis}}$. The extra “MuonRM” line (green) shows the efficiency of a muon being removed from the τ_{seed} . The slight abnormality in the “MuonRM” line between $0.35 < \Delta R_{\tau\tau}^{\text{truth},\text{vis}} < 0.45$ is due to limited detector resolution in the direction of the reconstructed $\tau_{\text{had-vis}}$.

Roughly 95% of the τ_{seed} jets have a muon removed in the region where $\Delta R_{\tau\tau}^{\text{truth,vis}} < 0.4$. This can be expected given the 97% efficiency of the “Medium” muon ID working point, with a dip below 90% in the region $|\eta|^{\text{truth,vis}} < 0.1$. This is illustrated in Figure 5.4, which shows the signal efficiencies of the TauID working points after muon removal as a function of the $|\eta|^{\text{truth,vis}}$ for truth 1-prong and 3-prong τ_{seed} jets with $\Delta R_{\tau\tau}^{\text{truth,vis}} < 0.4$.

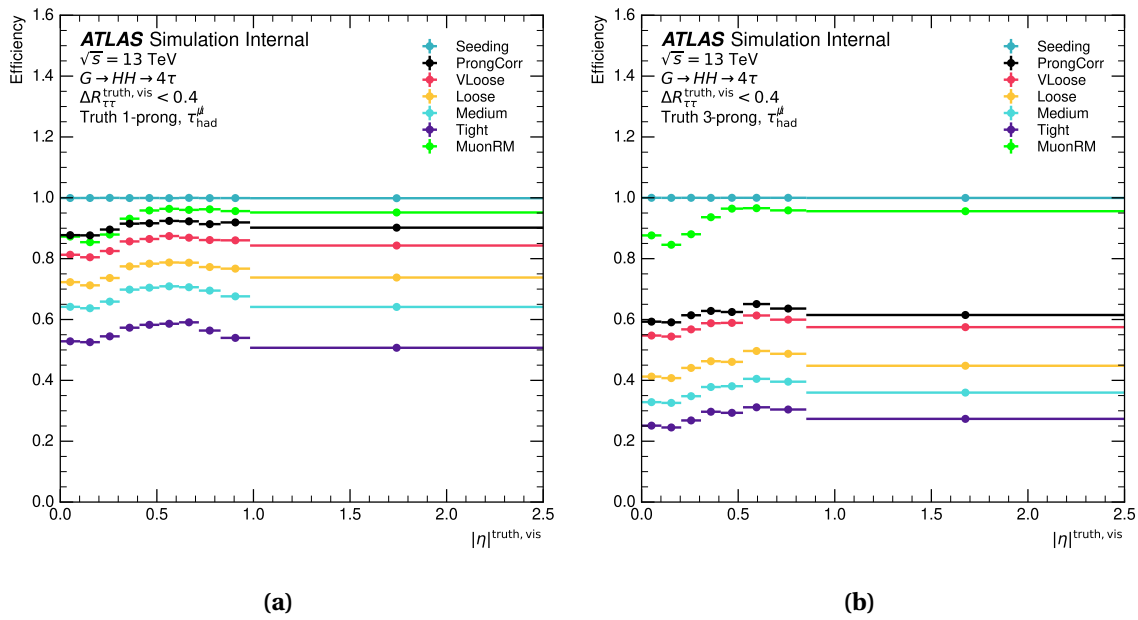


Fig. 5.4 The signal efficiencies of the TauID working points as a function of the truth absolute pseudorapidity for truth 1-prong (a) and 3-prong (b) τ_{seed} jets with $\Delta R_{\tau\tau}^{\text{truth,vis}} < 0.4$. The seeding efficiencies and the ratio of the τ_{seed} jets with a muon removed are also shown.

The signal identification efficiencies in all working points of the standard ATLAS TauID are tuned to show minimum dependency on the $p_{\text{T}\tau}^{\text{truth,vis}}$ and pile-up [132]. The stability of the TauID working point efficiencies after muon removal against these variables is shown in Figure 5.5. To focus on the objects of interest, only truth $\tau_{\mu}\tau_{\text{had}}$ pairs with the ΔR between the reconstructed muon and τ_{had} , $\Delta R_{\tau\tau}^{\text{reco}} < 0.4$ are included in the plots. For comparison, the TauID working point efficiencies as a function of the same variables for τ_{seed} objects in which muon removal is not required ($\Delta R_{\tau\tau}^{\text{truth,vis}} > 0.45$) are shown in Figure 5.6. Similar behaviour is observed in figures 5.5 and 5.6. The improved performance

and good stabilities across different working points demonstrate that, after muon removal, the TauID RNN sees the signal τ_{seed} jet as if it were a τ_{had} that is free from interference of surrounding particles (isolated τ_{had}).

After the removal of the overlapping muon, the precision with which the four-momentum of the τ_{seed} jet is reconstructed improves significantly. Figure 5.7 shows the distributions of the difference between the truth-level and reconstructed variable (residuals) in η and ϕ before and after muon removal. Compared to the performance before muon removal, the root mean square (RMS) widths of the η residuals that correspond to the 68% percentile (core resolution) improves by a factor of 15 for 1-prong τ_{had} , and by a factor of 20 for 3-prong τ_{had} . The core resolution in ϕ improves also by a factor of 15 times for 1-prong τ_{had} and by a factor of 20 for 3-prong τ_{had} . The distributions of the $\tau_{\text{had-vis}}$ transverse energy (E_{T}) residuals and the relative core (68%) and tail (95%) E_{T} resolutions as functions of $\tau_{\text{had-vis}} E_{\text{T}}^{\text{truth}}$ are shown in Figure 5.8. These results align nicely with those reported for isolated τ_{had} in ref. [133], demonstrating further the effectiveness of the muon-removal technique.

Having demonstrated that the reconstruction and identification efficiencies are significantly improved by the τ_{had}^μ method, the background rejection power is now illustrated. The production of $t\bar{t}$ pairs is considered as a source of high p_{T} heavy-flavour jets, which represents an example background to the τ_{had}^μ signal. The background rejection ratios at the medium TauID working point, which are defined as the inverted ratios of a mis-reconstructed τ_{seed} jet being classified as a genuine τ_{had} are shown in Figure 5.9, as functions of the reconstructed τ_{had} p_{T} , $\tau_{\text{had}} |\eta|$ and pile-up. For the background rejection plots, and the following receiver operating characteristic (ROC) plots, event-selections are mostly based on the reconstructed properties instead of the truth-level information. A τ_{seed} jet reconstructed in the background sample is required to have $20 \text{ GeV} < p_{\text{T}} < 300 \text{ GeV}$, $|\eta| < 2.5$, and to not be truth-matched to a τ_{had} lepton from the

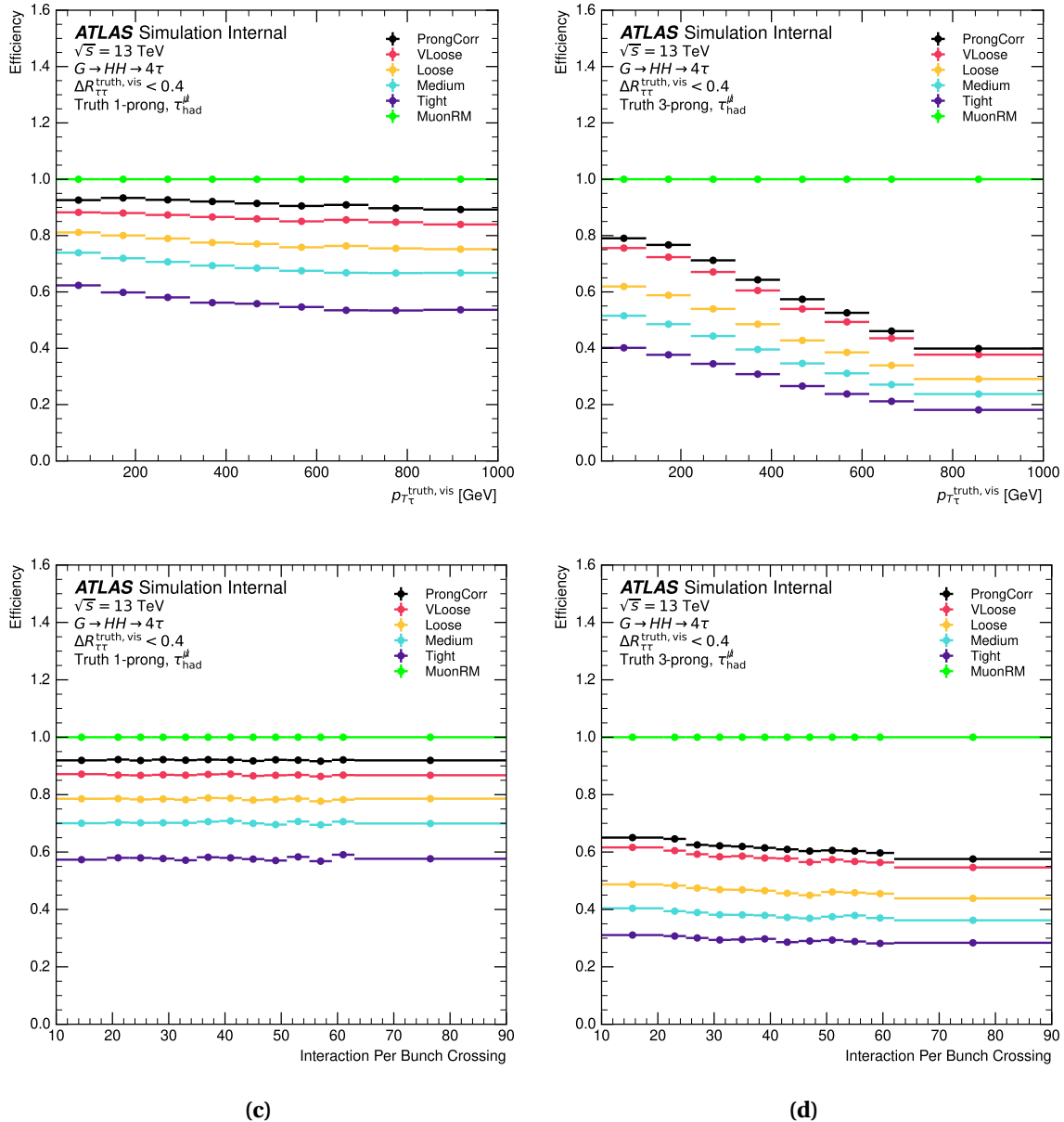


Fig. 5.5 The stability of the signal efficiencies of the TauID working points against the truth transverse momentum (a) (b), and pile-up (c) (d) for truth 1-prong and 3-prong τ_{seed} with reconstructed $\Delta R_{\tau\tau}^{\text{reco}} < 0.4$. The “Seeding” lines indicate the efficiency of a truth-level τ_{had} being reconstructed as τ_{seed} . The “MuonRM” lines show the efficiency of a muon being removed inside the τ_{seed} .

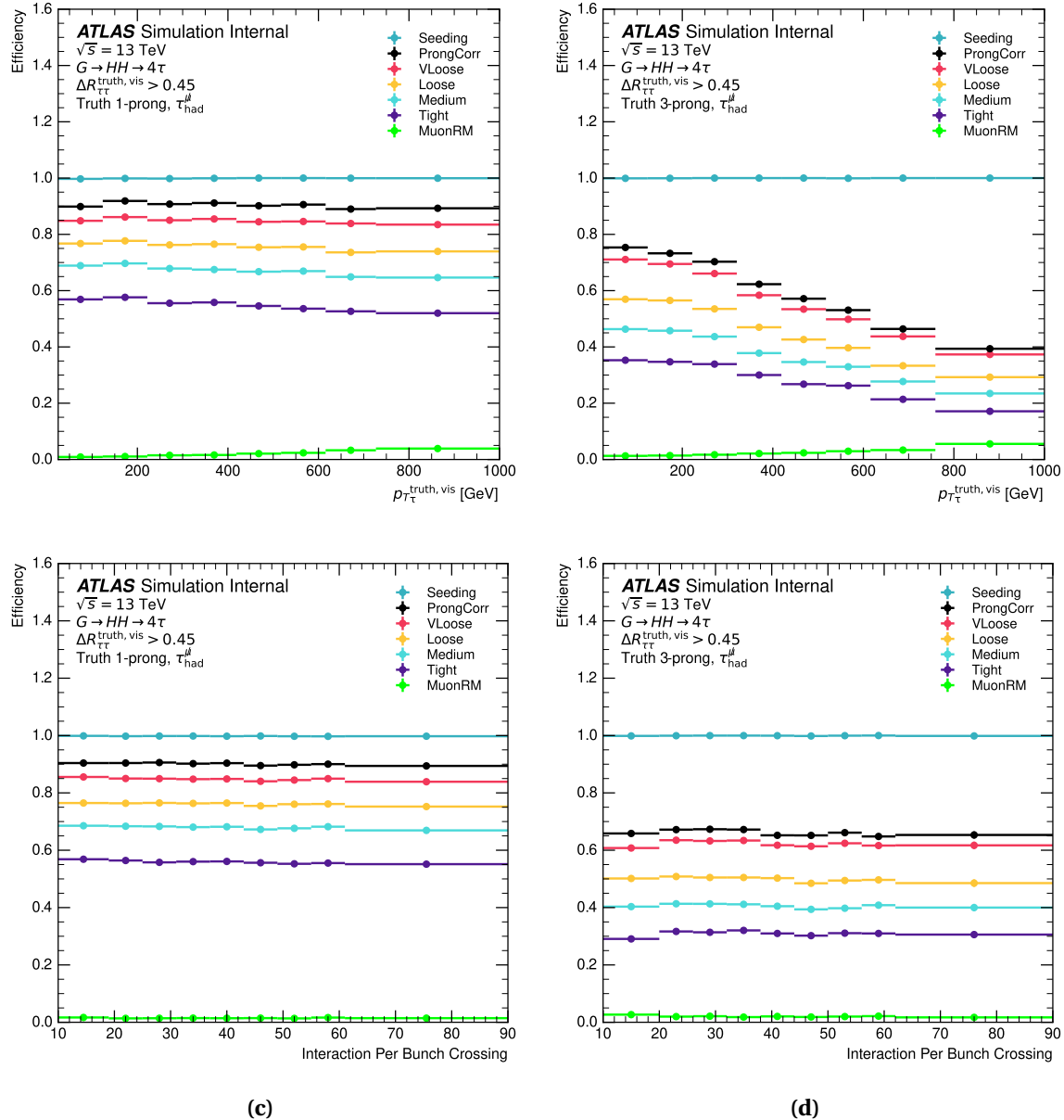


Fig. 5.6 The stability of the signal efficiencies of the TauID working points against the truth transverse momentum (a) (b), and pile-up (c) (d) for the truth 1-prong and 3-prong τ_{seed} jets with $\Delta R_{\tau\tau}^{\text{truth,vis}} > 0.45$. In this region, the muon removal should not affect the results. The “Seeding” lines indicate the efficiency of a truth-level τ_{had} being reconstructed as τ_{seed} . The “MuonRM” lines show the efficiency of a muon being removed inside the τ_{seed} .

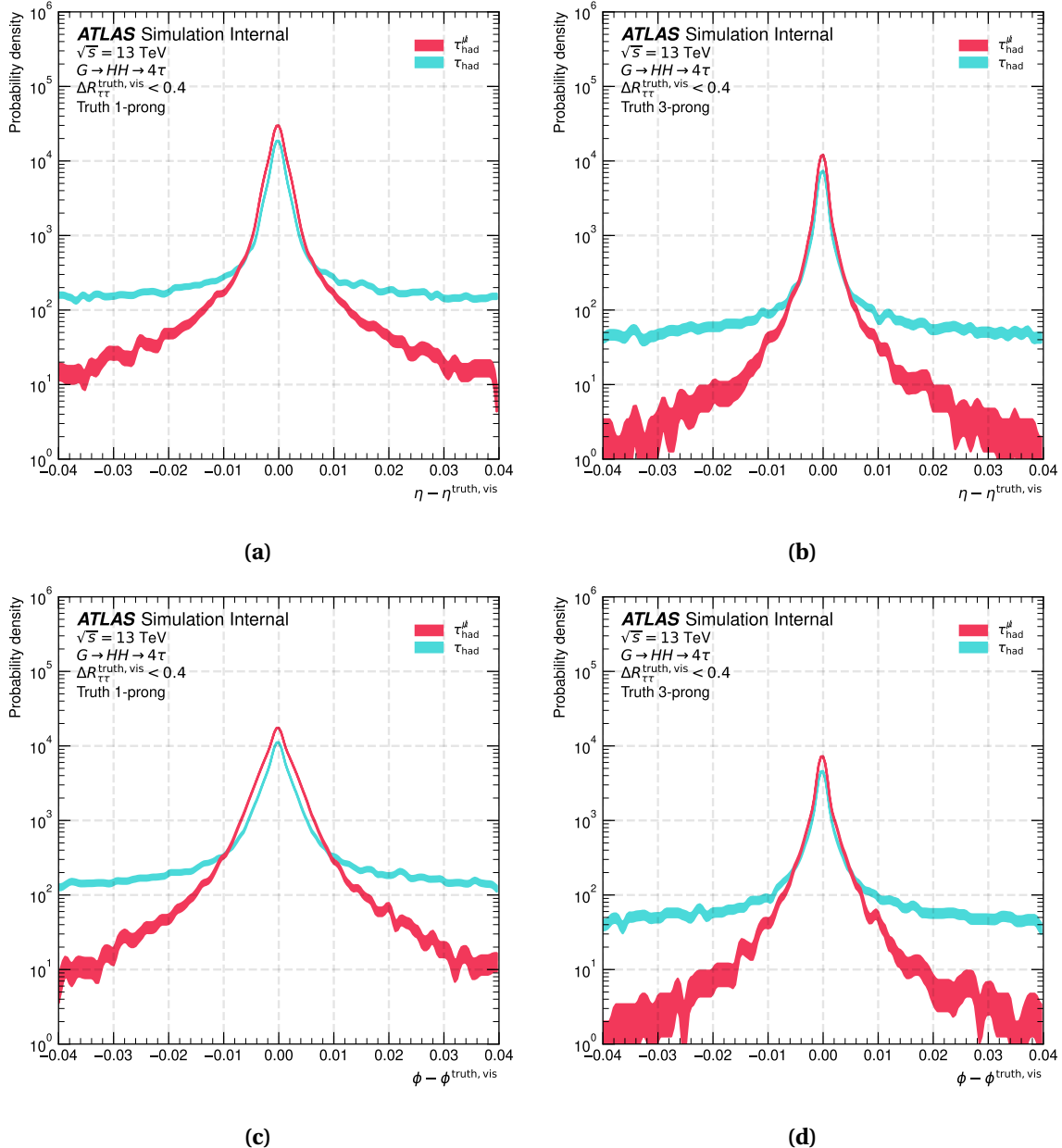


Fig. 5.7 The distributions of the calibrated residuals η (a) (b) and ϕ (c) (d) before (blue) and after (red) muon removal. The left panel shows the 1-prong case; the right panel shows the 3-prong case.

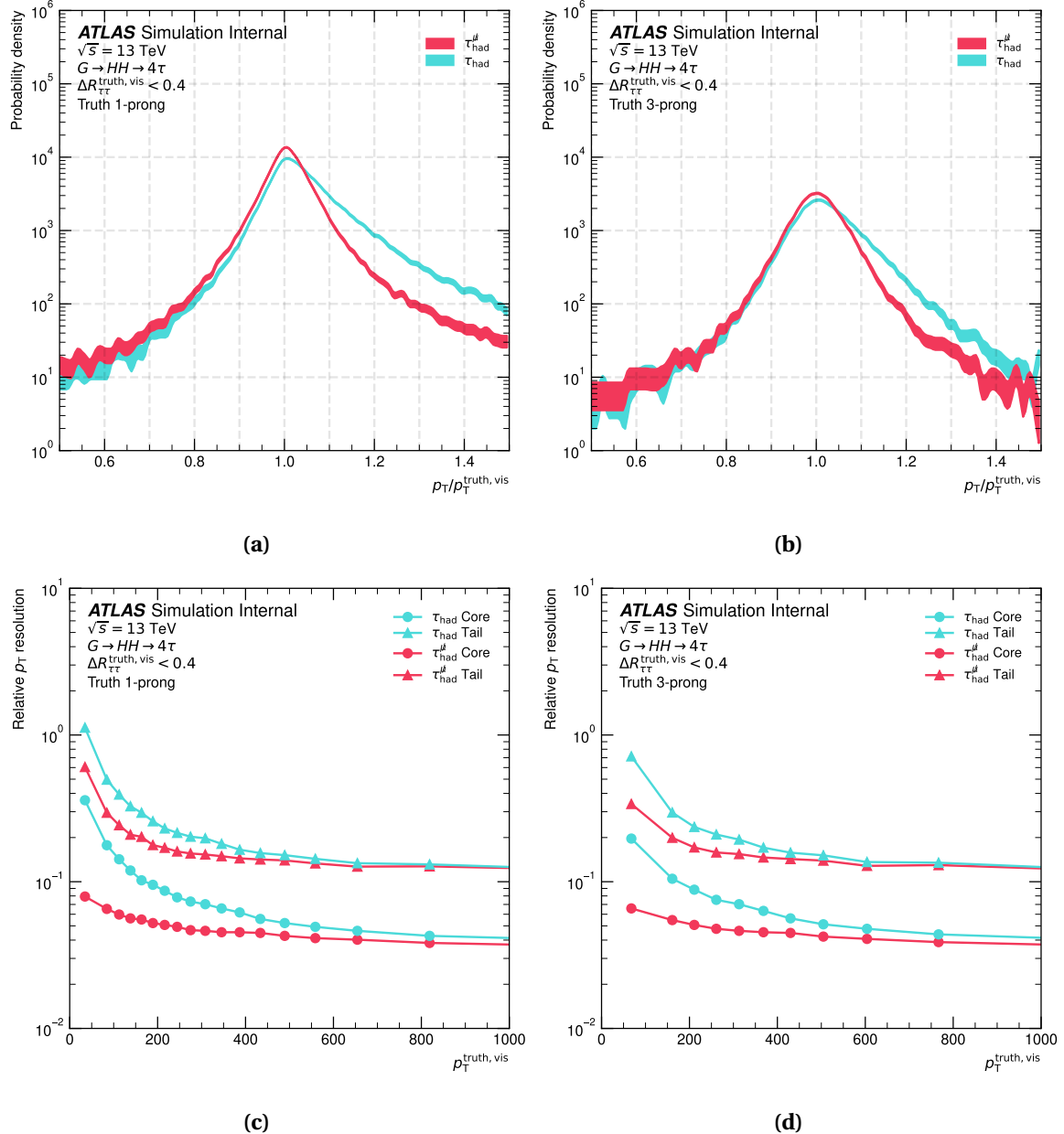


Fig. 5.8 (a) (b): the distributions of the calibrated transverse energy residuals for $\tau_{\text{had-vis}}$ with (red) and without (blue) muon removal. **(c) (d):** the relative core (68%) and tail (95%) $\tau_{\text{had-vis}}$ E_T resolutions as functions of $\tau_{\text{had-vis}}$ E_T^{truth} . The left plots show the 1-prong case and the right plots show the 3-prong case.

bottom or top quarks semi-leptonic decay. In addition, a reconstructed muon is required to be found inside the τ_{seed} jet. The τ_{had} candidates in which no muon is present are not considered in Figure 5.9, as identical TauID results would be expected for these cases.

The background rejection power decreases slightly in the 3-prong case. After the removal of the muon within the τ_{seed} in the case of background events, the TauID algorithm finds it more challenging to reject a semi-leptonic heavy-flavour jet. The 1-prong background rejection power increases slightly in the low p_{T} region after removal of the muon due to two competing phenomena. The muon being removed is often the only charged track found inside the τ_{seed} jet. Thus, the number of reconstructed 1-prong τ_{seed} jets decreases significantly. For the remaining reconstructed 1-prong τ_{seed} jets, the background rejection performance does suffer from the removal of the muon.

The signal efficiency observed in the $G \rightarrow HH \rightarrow 4\tau$ samples, and background rejection power observed in the $t\bar{t}$ sample are combined to form the ROC curves, which are defined as the background rejection factor as a function of the signal efficiency. In addition to the same reconstruction level selections as the background τ_{seed} jets discussed previously, the signal τ_{seed} jets are also required to be truth-matched to the $\tau_{\mu}\tau_{\text{had}}$ pairs. To minimise the bias introduced by the misalignment of the signal and background momentum spectra, the background events are re-weighted so that the p_{T} distribution of the background samples matches the signal sample. The ROC curves illustrating the performance with and without muon removal are shown in Figure 5.10. An order-of-magnitude performance gain is seen across the spectrum in both 1-prong and 3-prong curves when muon removal is applied.

To demonstrate the performance of the τ_{had}^{μ} method in reconstructing and identifying di- τ systems within the $G \rightarrow HH \rightarrow 4\tau$ process, Figure 5.11 presents the combined τ_{had} reconstruction and identification efficiencies as a function of the truth-level Graviton mass. The efficiencies shown correspond to the identification of individual di- τ systems

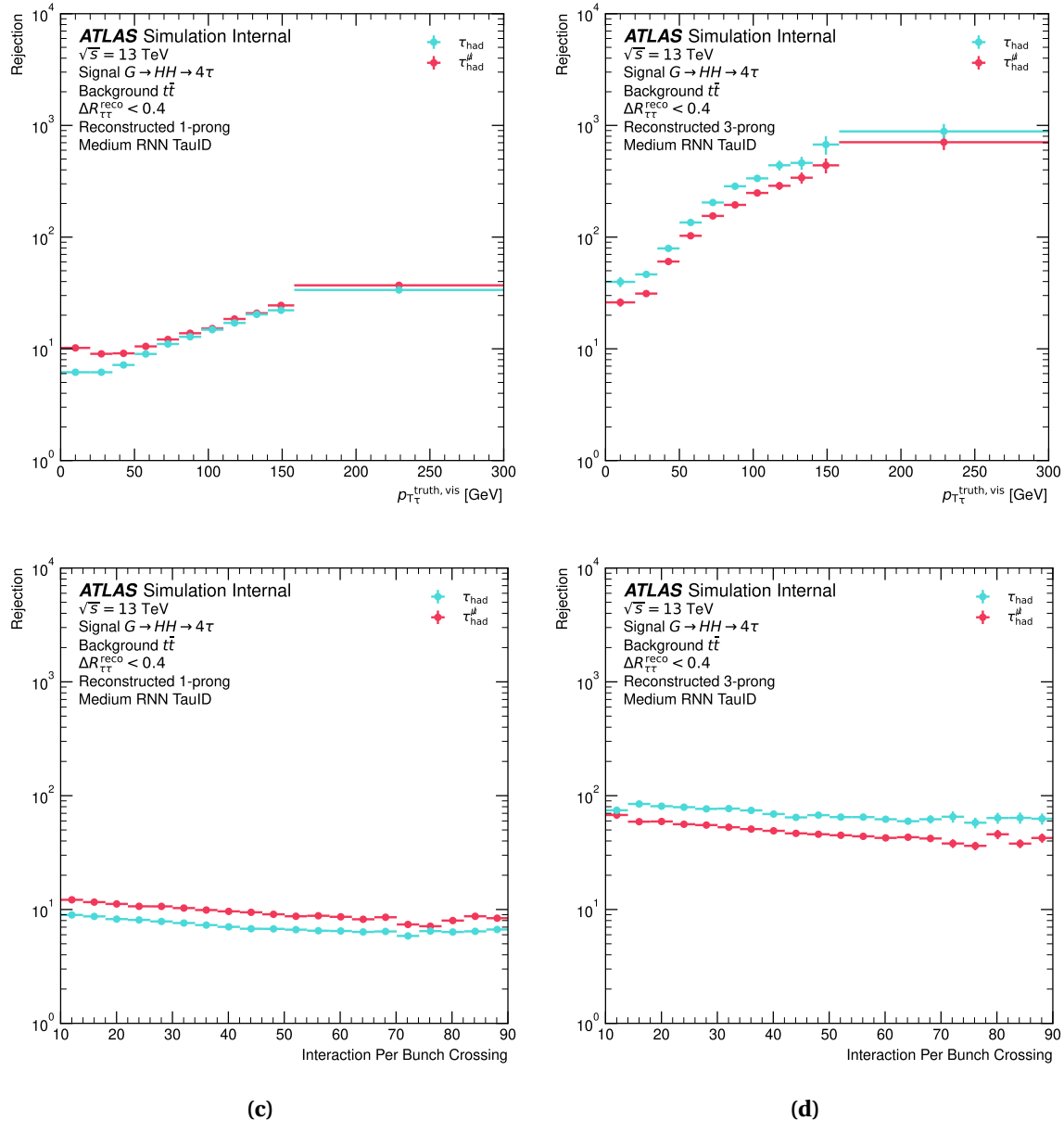


Fig. 5.9 The signal rejection ratios for τ_{seed} jets reconstructed from jets originating from semi-muonic bottom decays in $t\bar{t}$ events at medium TauID working point, as functions of the reconstructed p_T (a) (b), and pile-up (c) (d). The left panel shows the reconstructed 1-prong case, the right panel shows the 3-prong case.

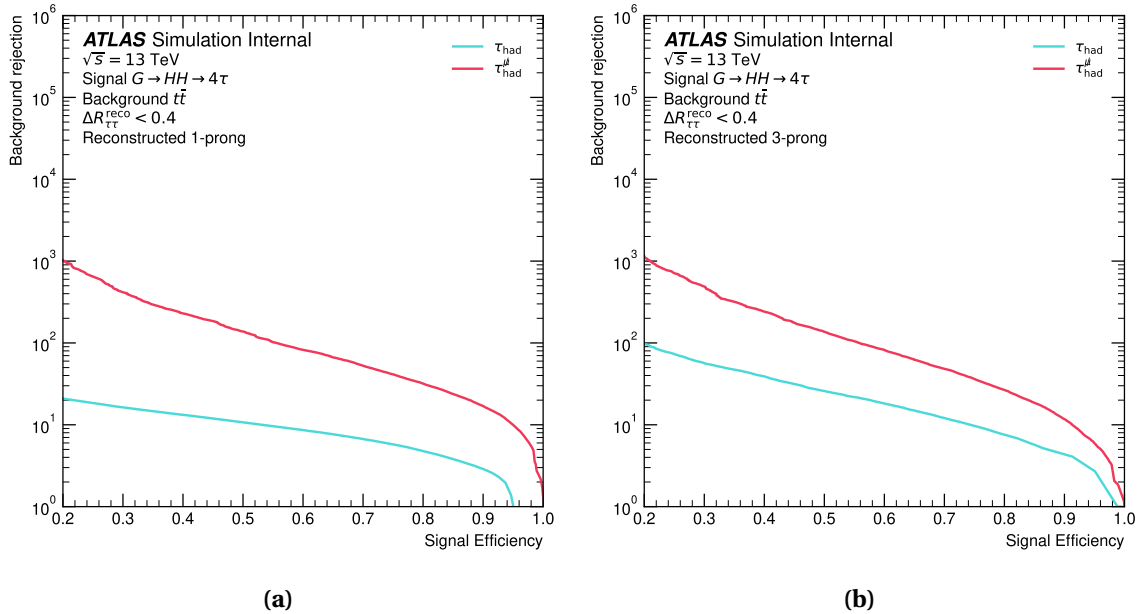


Fig. 5.10 The receiver operating characteristic (ROC) curves with and without muon removal. (a) shows the reconstructed 1-prong case, (b) shows the 3-prong case.

originating from Higgs boson decays. Compared to the standard ATLAS TauID, the τ_{had}^{μ} method demonstrates a complete recovery in the identification efficiency for both 1-prong and 3-prong τ_{had} decays for high-mass $G \rightarrow HH \rightarrow 4\tau$ samples.

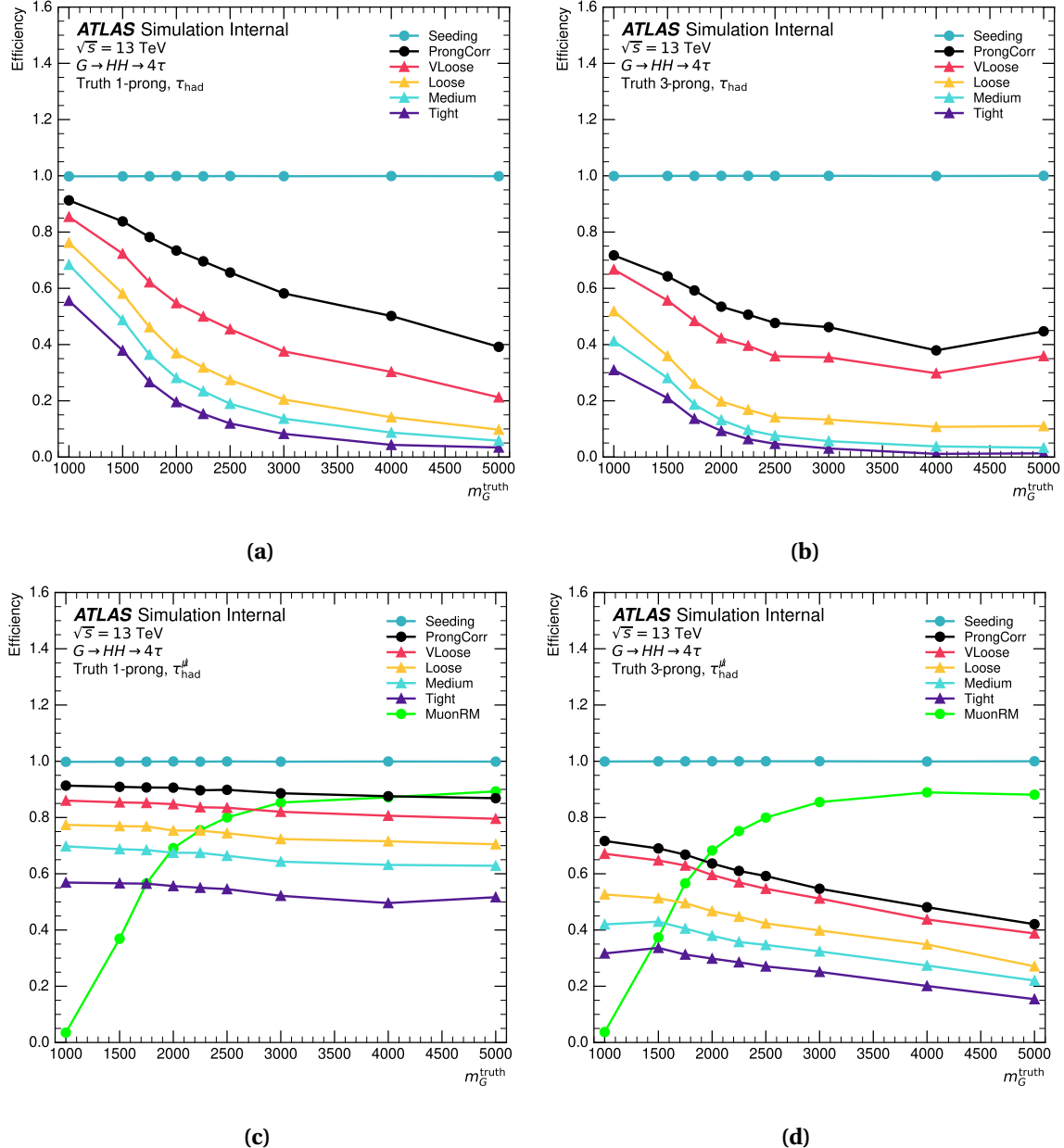


Fig. 5.11 The signal efficiencies of the TauID working points, as a function of the truth-level Graviton mass, m_G^{truth} , for truth 1-prong (a) and 3-prong (b) τ_{had} with the standard ATLAS TauID; and for truth 1-prong (c) and 3-prong (d) τ_{had} with the τ_{had}^μ method. The efficiencies shown correspond to the identification of individual di- τ systems originating from Higgs boson decays. The “Seeding” lines indicate the efficiency of a truth-level τ_{had} being reconstructed as τ_{seed} . The “ProngCorr” line shows the efficiency of a truth-level τ_{had} being reconstructed with the correct number of associated charged-particle tracks. The “MuonRM” lines show the efficiency of a muon being removed inside the τ_{seed} .

5.4 Validation of the τ_{had}^{μ} method in the $Z \rightarrow \tau_{\mu}\tau_{\text{had}}$ channel

5.4.1 The collinear assumptions and event reconstruction

The τ_{had}^{μ} method was developed for searches like high-mass BSM physics, such as the $G \rightarrow HH$ process, as described in Section 5.3. However, it is useful to test its performance considering a SM process. The Drell-Yan production of a Z boson in association with high- p_T jets from QCD initial-state radiation is considered as benchmark process.

The detector signature of the boosted $Z \rightarrow \tau_{\mu}\tau_{\text{had}}$ process includes one hadronically decaying τ and a muon, in association with significant missing transverse momentum ($E_{\text{T}}^{\text{miss}}$) from the neutrinos produced in the two τ decays. In this case, the hadronically decaying τ and the muon are likely to fall within the same τ_{seed} jet. In well measured events, the vector sum of the transverse momenta of the three neutrinos dominates the measured $E_{\text{T}}^{\text{miss}}$, which in azimuth direction should lie between the observed muon and the τ_{had} . Also, on average, the $E_{\text{T}}^{\text{miss}}$ should be closer in azimuth to the muon, because the leptonic decay produces two neutrinos and the hadronic decay only one.

Without incorporating $E_{\text{T}}^{\text{miss}}$, reconstructing the Z invariant mass is not possible. However, it is possible to approximate the momenta of the neutrinos with the collinear assumptions [134] as follows:

- the transverse momenta of the three neutrinos dominate the measured $E_{\text{T}}^{\text{miss}}$, and other contributions are negligible;
- each τ lepton is sufficiently boosted such that the neutrino (or pair of neutrinos) produced in its decay is collinear with its visible decay products ².

²In events in which the $E_{\text{T}}^{\text{miss}}$ lies outside the azimuthal angle between the visible decay products of the tau leptons (e.g., due to detector resolution), the $E_{\text{T}}^{\text{miss}}$ is projected onto the direction of the nearest visible decay, and the neutrino momentum associated with the other tau lepton is set to zero. Furthermore, events for which collinear reconstruction is not possible, i.e., with $E_{\text{T}}^{\text{miss}}$ deviating by more than 90° from the muon or the τ_{had}^{μ} in $\Delta\phi$, are discarded.

Together with the momenta of the visible decay products, this procedure allows the momenta of the two tau leptons, and hence the momentum, transverse momentum ($p_{T\mu-\text{had}}^{\text{col}}$), and mass ($m_{\mu-\text{had}}^{\text{col}}$) of the system produced by the decay of the Z boson, to be reconstructed. The jets recoiling against the Z boson are reconstructed using the anti- k_t algorithm with a radius parameter of 0.4, which operates on topological clusters calibrated to the EM scale [81].

5.4.2 Event-selection

Candidate events are required to be triggered by an un-prescaled single-muon trigger or an un-prescaled E_T^{miss} trigger. The thresholds of the p_T required to fire each trigger vary for different data-taking periods. For the single muon trigger, the p_T requirement for triggers with object isolation requirement ranges from 20-26 GeV, while the p_T threshold for non-isolated muons remains constant at 50 GeV. The E_T^{miss} triggers have a p_T threshold of 70 GeV for the 2015 data-taking period and remain constant at 110 GeV for the rest of Run 2. Approximately 97% of $Z \rightarrow \tau_\mu\tau_{\text{had}}$ MC events that pass the final signal selection criteria pass the trigger selection. For the signal-region (SR) selection, events passing the trigger requirements are required to have at least one muon-removal τ_{had} object with $p_T > 15$ GeV and a RNN TauID score > 0.1 , excluding pseudorapidity ranges $1.37 < |\eta| < 1.52$ and $|\eta| > 2.5$. This selection implies that at least one reconstructed muon passing “Medium” ID is inside the cone of the selected τ_{had}^μ . An additional $p_T > 10$ GeV requirement on the corresponding muon is imposed. In this study, the overlap removal (OLR) between muons and τ_{had} candidates is turned off. The default overlap removal algorithm as described in Ref. [135] would remove the τ_{had}^μ candidates if the muon removal method is successful. To suppress background from events containing heavy flavour jets, events are vetoed if they contain any jet that satisfies the DL1d based b -tagging algorithm at an 85% efficiency working point [89]. The invariant mass, $m_{\mu-\text{had}}^{\text{vis}}$, of the visible $\tau_\mu\tau_{\text{had}}$ system is required to

satisfy $m_{\mu-\text{had}}^{\text{vis}} > 5 \text{ GeV}$. The signed $\Delta\phi$ between the muon and $E_{\text{T}}^{\text{miss}}$ ($\Delta\phi_{\mu-E_{\text{T}}^{\text{miss}}}^{\text{signed}}$) is required to be $-0.1 < \Delta\phi_{\mu-E_{\text{T}}^{\text{miss}}}^{\text{signed}} < 0.4$. The sign of $\Delta\phi_{\mu-E_{\text{T}}^{\text{miss}}}^{\text{signed}}$ is determined by the direction of the τ_{had} . If the $E_{\text{T}}^{\text{miss}}$ is inside the opening angle of the muon and the τ_{had} or if the $E_{\text{T}}^{\text{miss}}$ is outside the opening angle but closer to the muon, then the sign is positive; otherwise, it is negative. Since the focus of the analysis is the boosted $Z \rightarrow \tau_{\mu}\tau_{\text{had}}$ process, a loose requirement $m_{\mu-\text{had}}^{\text{col}} > 40 \text{ GeV}$, and a requirement $p_{\text{T}\mu-\text{had}}^{\text{col}} > 250 \text{ GeV}$ are applied. To study the QCD multijets background contributions not described by the MC, a control-region (CR) is defined with the same selection requirements as the SR, except that the muon and τ_{had}^{μ} have the same charge, and there is no requirement on $\Delta\phi_{\mu-E_{\text{T}}^{\text{miss}}}^{\text{signed}}$ or number of jets passing the b -tagging requirement. Table 5.1 summarizes the event-selection requirements for SR and CR.

Table 5.1 Summary of event-selection requirements

Object	Signal-Region Selection	Control-Region Selection
τ_{had}^{μ}	$0 < \eta < 1.37$ or $1.52 < \eta < 2.5$ Jet RNN score > 0.1 $p_{\text{T}} > 15 \text{ GeV}$ 1 or 3 charged tracks	$0 < \eta < 1.37$ or $1.52 < \eta < 2.5$ Jet RNN score > 0.1 $p_{\text{T}} > 15 \text{ GeV}$ 1 or 3 charged tracks
μ	$p_{\text{T}} > 10 \text{ GeV}$ “Medium” ID	$p_{\text{T}} > 10 \text{ GeV}$ “Medium” ID
$\tau_{\mu}\tau_{\text{had}}$ system	$m_{\mu-\text{had}}^{\text{vis}} > 5 \text{ GeV}$ $-0.1 < \Delta\phi_{\mu-E_{\text{T}}^{\text{miss}}}^{\text{signed}} < 0.4$ $m_{\mu-\text{had}}^{\text{col}} > 40 \text{ GeV}$ $p_{\text{T}\mu-\text{had}}^{\text{col}} > 250 \text{ GeV}$ no b -tag jet at 85% efficiency working point Opposite Sign muon and τ_{had}^{μ}	$m_{\mu-\text{had}}^{\text{vis}} > 5 \text{ GeV}$ $m_{\mu-\text{had}}^{\text{col}} > 40 \text{ GeV}$ $p_{\text{T}\mu-\text{had}}^{\text{col}} > 250 \text{ GeV}$ Same Sign muon and τ_{had}^{μ}

Figures 5.12–5.17 illustrate the distributions of selected variables in the SR and CR. As shown in Figure 5.14, the data and MC predictions agree well for $m_{\mu-\text{had}}^{\text{col}} > 40 \text{ GeV}$ in both the SR and CR, indicating that QCD processes not modelled by the MC simulations contribute negligibly to the background in the selected signal sample. The collinear mass reconstruction effectively reconstructs the di-tau system mass, as seen in the peak corresponding to the Z boson mass in Figure 5.14(a). The shape of the $m_{\mu-\text{had}}^{\text{col}}$ distribution for signal Drell-Yan events is very different from that seen in inclusive production, with a

much larger fraction of the signal events in the region $40 < m_{\mu-\text{had}}^{\text{col}} < 70$ GeV relative to that at the Z boson peak. This is a result of the sharply falling distribution in Z boson p_T for Drell-Yan production, coupled with the fact that the opening angle of boosted $\tau_\mu \tau_{\text{had}}$ systems decreases with decreasing $m_{\mu-\text{had}}^{\text{col}}$. Due to the the $m_{\mu-\text{had}}^{\text{col}} > 40$ GeV requirement, the number of events with $p_{T\mu-\text{had}}^{\text{col}}$ below 250 GeV is very low. This highlights the fact that the τ_{had}^μ reconstruction picks up τ_{had} only with a sufficiently high boost. An excess of data compared to the MC prediction is observed in the $p_T < 35$ GeV region within the SR. Further investigation has identified this discrepancy as a result of mis-modelling of the τ_{had} kinematics in the $Z \rightarrow \tau\tau$ MC simulation [136].

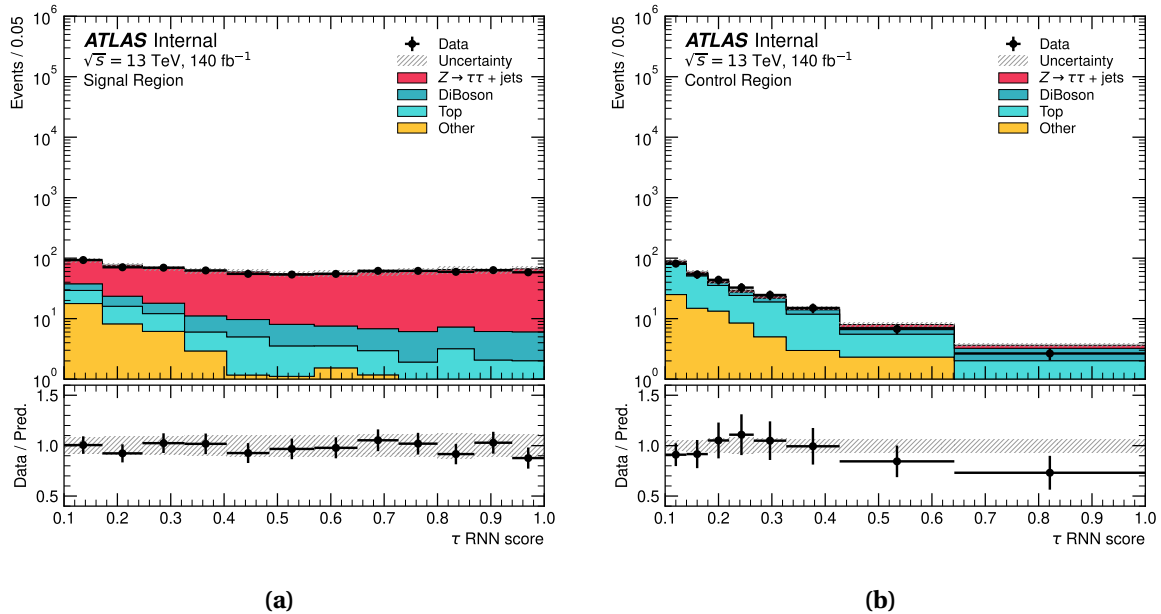


Fig. 5.12 The distribution of the RNN jet score for τ_{had}^μ : (a) in the SR and, (b) in the CR. “Top” represents the predicted contributions from the SM $t\bar{t}$, single-top, and tW processes. “DiBoson” indicates the contributions from WW , WZ , and ZZ processes. “Other” includes the contributions from the $Z \rightarrow ll + \text{jets}$ and $W + \text{jets}$ background processes. “ $Z \rightarrow \tau\tau + \text{jets}$ ” represents the contributions from the signal process. The uncertainties shown include both statistical and systematic uncertainties.

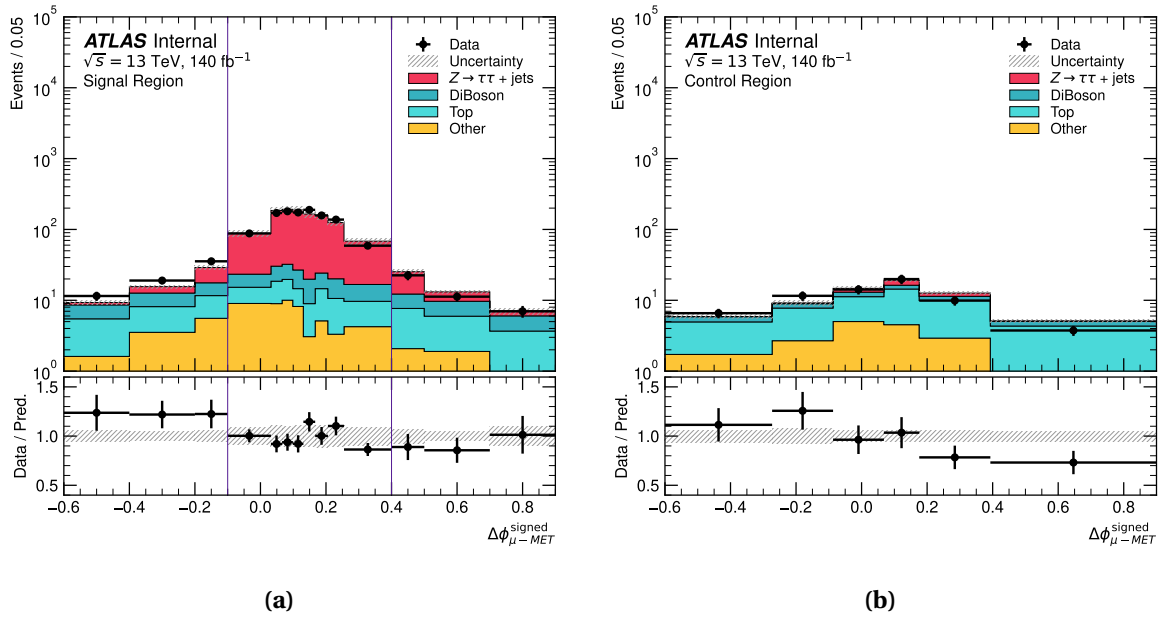


Fig. 5.13 The distribution of $\Delta\phi_{\mu-E_{\text{T}}^{\text{miss}}}^{\text{signed}}$ with all other event-selection criteria applied in the SR is shown in (a); the straight lines indicate the positions of the selection requirements. The same distribution in the CR is shown in (b). “Top” represents the predicted contributions from the SM $t\bar{t}$, single-top, and tW processes. “DiBoson” indicates the contributions from WW , WZ , and ZZ processes. “Other” includes the contributions from the $Z \rightarrow ll + \text{jets}$ and $W + \text{jets}$ background processes. “ $Z \rightarrow \tau\tau + \text{jets}$ ” represents the contributions from the signal process. The uncertainties shown include both statistical and systematic uncertainties.

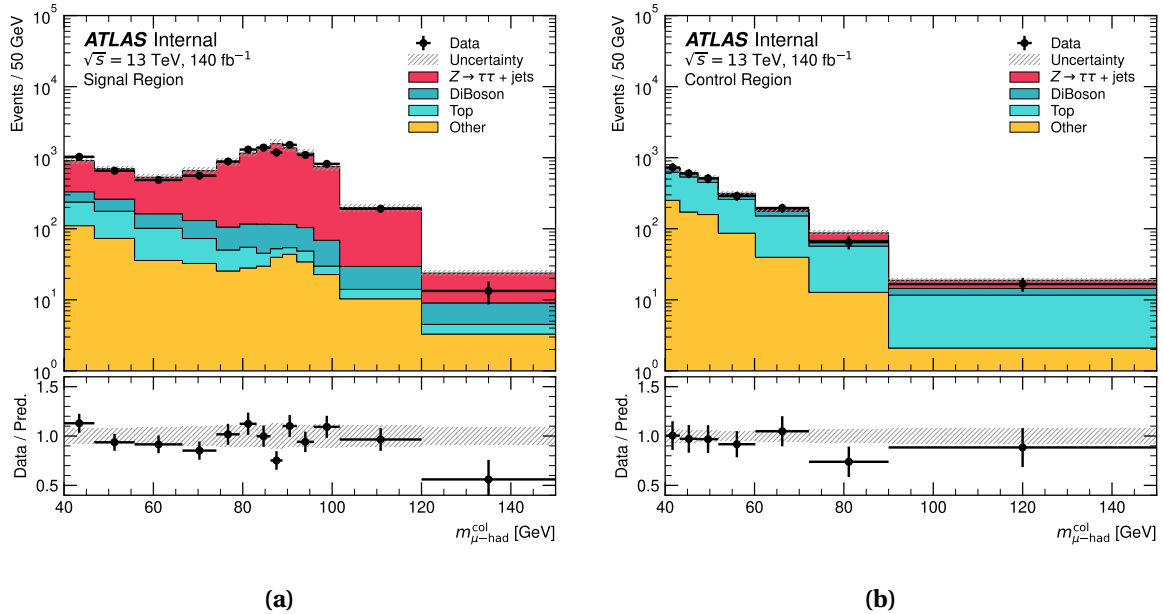


Fig. 5.14 The distribution of the $m_{\mu\text{-had}}^{\text{col}}$: (a) in the SR, and, (b) in the CR. “Top” represents the predicted contributions from the SM $t\bar{t}$, single-top, and tW processes. “DiBoson” indicates the contributions from WW , WZ , and ZZ processes. “Other” includes the contributions from the $Z \rightarrow ll + \text{jets}$ and $W + \text{jets}$ background processes. “ $Z \rightarrow \tau\tau + \text{jets}$ ” represents the contributions from the signal process. The uncertainties shown include both statistical and systematic uncertainties.

5.4.3 Systematic uncertainties

The dominant source of systematic uncertainty in the comparison between the observed and expected yields in the SR is the modelling of the cross-section for Z boson production. As discussed in Section 5.2, a +10% correction is applied to the predicted numbers for $Z \rightarrow \tau\tau$ events, with the full size of this correction quoted as a systematic uncertainty.

The most significant sources of experimental systematic uncertainties are TauID and tau energy scale (4%), jet energy scale and resolution (2%), E_T^{miss} (2%) [137], and luminosity (0.8%) [124].

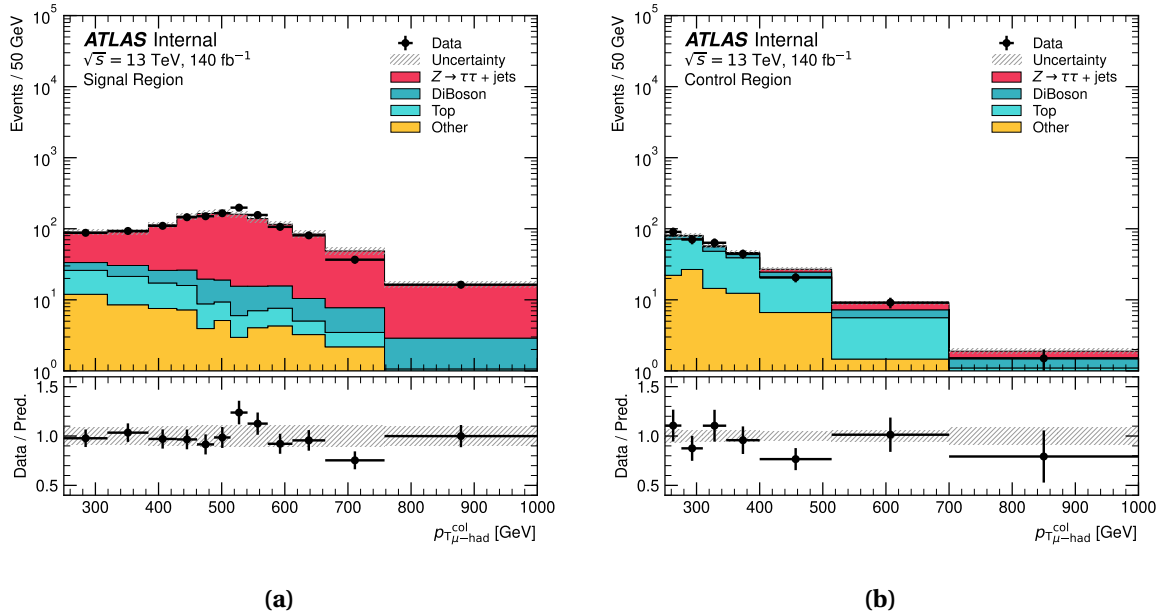


Fig. 5.15 The distribution of the $p_{T\mu-\text{had}}^{\text{col}}$: (a) in the SR, and, (b) in the CR. “Top” represents the predicted contributions from the SM $t\bar{t}$, single-top, and tW processes. “DiBoson” indicates the contributions from WW , WZ , and ZZ processes. “Other” includes the contributions from the $Z \rightarrow ll + \text{jets}$ and $W + \text{jets}$ background processes. “ $Z \rightarrow \tau\tau + \text{jets}$ ” represents the contributions from the signal process. The uncertainties shown include both statistical and systematic uncertainties.

5.5 Results

In order to understand the performance improvement comparing to the standard ATLAS τ_{had} reconstruction and identification, Figure 5.18 shows comparisons between the data and MC predictions for $m_{\mu-\text{had}}^{\text{col}}$ distributions corresponding to various signal selections; Figure 5.18a shows the SR defined in Section 5.4.2; Figure 5.18b shows the sample SR^{std} , which uses the standard ATLAS τ_{had} candidates; without the muon removal, but otherwise corresponds to the same event-selection as SR; Figure 5.18c shows the sample SR_{tight} , which imposes an additional “tight” RNN TauID requirement on the τ_{had}^{μ} candidates, but otherwise corresponds to the SR selection; Figure 5.18d shows the sample $\text{SR}_{\text{tight}}^{\text{std}}$, which imposes an additional “tight” RNN TauID requirement and uses the standard τ_{had} , without muon removal.

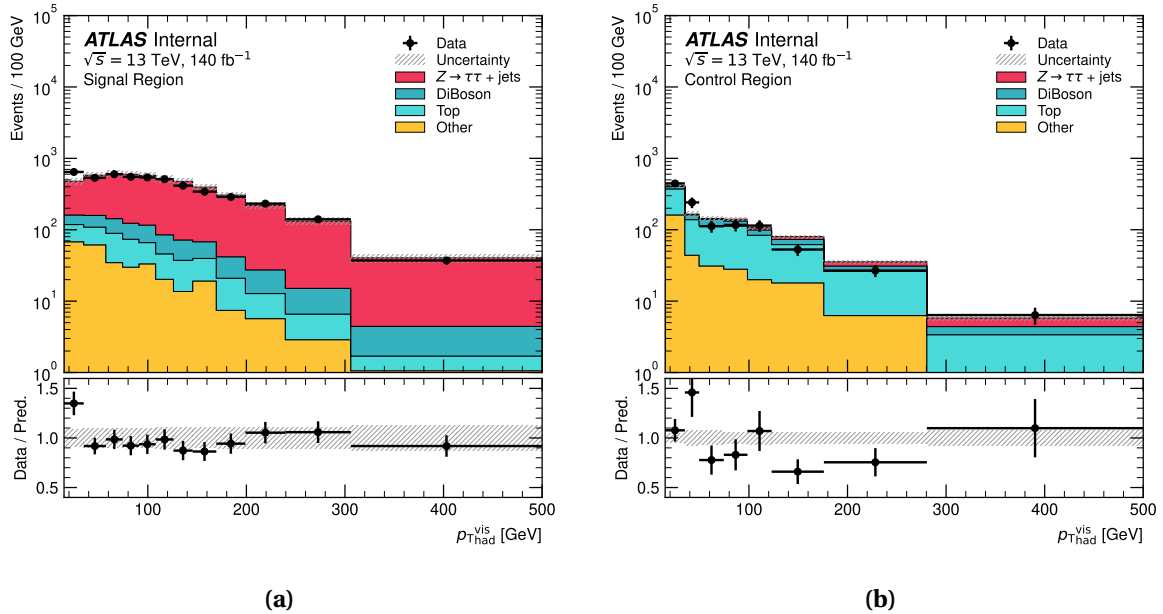


Fig. 5.16 The distribution of the p_{T} of the τ_{had}^N : (a) in the SR and, (b) in the CR. “Top” represents the predicted contributions from the SM $t\bar{t}$, single-top, and tW processes. “DiBoson” indicates the contributions from WW , WZ , and ZZ processes. “Other” includes the contributions from the $Z \rightarrow ll + \text{jets}$ and $W + \text{jets}$ background processes. “ $Z \rightarrow \tau\tau + \text{jets}$ ” represents the contributions from the signal process. The uncertainties shown include both statistical and systematic uncertainties.

Table 5.2 shows the event yields corresponding to the various signal selections defined previously, and the CR. The number of events observed in the ATLAS Run 2 data are given, as well as the SM-predicted contributions from signal and background processes.

Compared with the standard ATLAS TauID, the τ_{had}^N achieves around three times more signal events in the SR, while maintaining a similar number of background events. In the SR_{tight} region, the number of signal events is four times higher than using the nominal $\tau_{\text{had}}^{\text{std}}$, again while maintaining a similar number of background events. Subtracting the expected background yield in the SR of 230 ± 5 events gives a measured yield for $Z \rightarrow \tau_\mu\tau_{\text{had}}$ of 925 ± 34 events. This can be compared to the expected yield for $Z \rightarrow \tau_\mu\tau_{\text{had}}$ of 958 ± 8 (stat.) ± 115 (syst.) events. Adding all sources of statistical and systematic uncertainty results in a total uncertainty of 12%. The ratio between the background-subtracted data and the expected signal yields is 0.97 ± 0.12 .

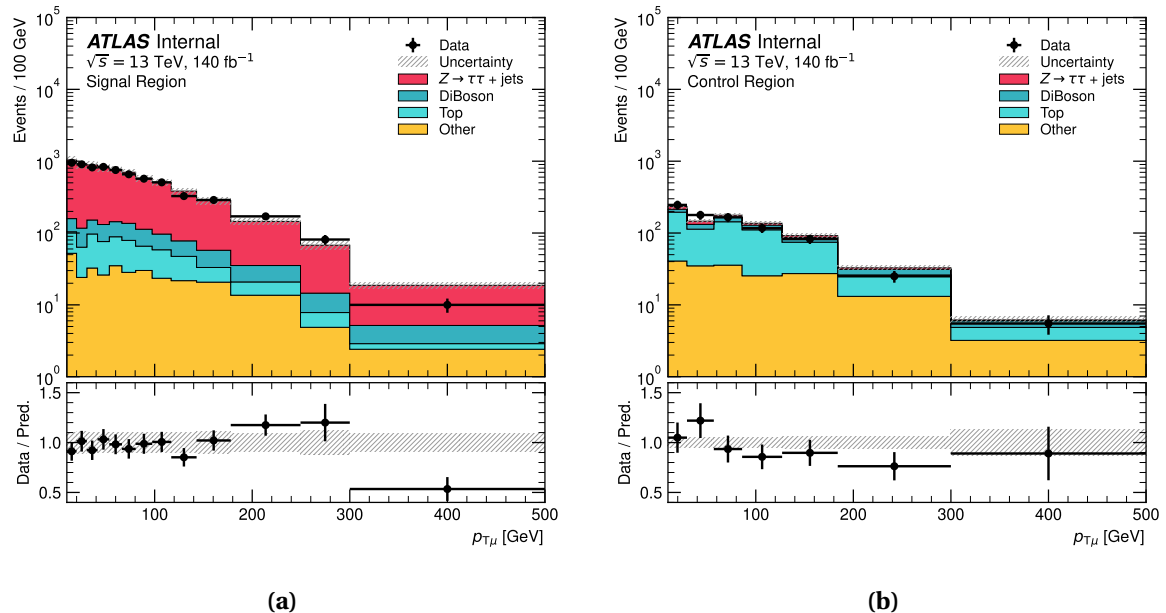


Fig. 5.17 The distribution of the p_T of the muon removed from the τ_h^{μ} : (a) in the SR and, (b) in the CR. “Top” represents the predicted contributions from the SM $t\bar{t}$, single-top, and tW processes. “DiBoson” indicates the contributions from WW , WZ , and ZZ processes. “Other” includes the contributions from the $Z \rightarrow ll + \text{jets}$ and $W + \text{jets}$ background processes. “ $Z \rightarrow \tau\tau + \text{jets}$ ” represents the contributions from the signal process. The uncertainties shown include both statistical and systematic uncertainties.

Table 5.2 Event yields in different event-selections, as defined in the text. SR, SR_{tight} and CR are with the τ_{had}^{μ} method, while SR^{std} and SR_{tight}^{std} are with the standard ATLAS TauID. The uncertainties quoted are statistical only. The $Z \rightarrow \tau\tau$ contribution is scaled by +10% to account for the difference between the MC prediction and the data.

	SR	SR^{std}	SR_{tight}	$\text{SR}_{\text{tight}}^{\text{std}}$	CR
Data	1155 ± 34	616 ± 25	705 ± 27	210 ± 14	286 ± 17
MC total	1188 ± 10	574 ± 8	733 ± 7	223 ± 4	302 ± 7
$Z \rightarrow \tau\tau$	958 ± 8	339 ± 4	646 ± 6	124 ± 2	20 ± 1
Di-boson	93 ± 1	37 ± 1	51 ± 1	15 ± 0	39 ± 1
Top	70 ± 3	153 ± 5	26 ± 2	67 ± 3	165 ± 5
Other	66 ± 4	45 ± 4	10 ± 2	17 ± 2	78 ± 4

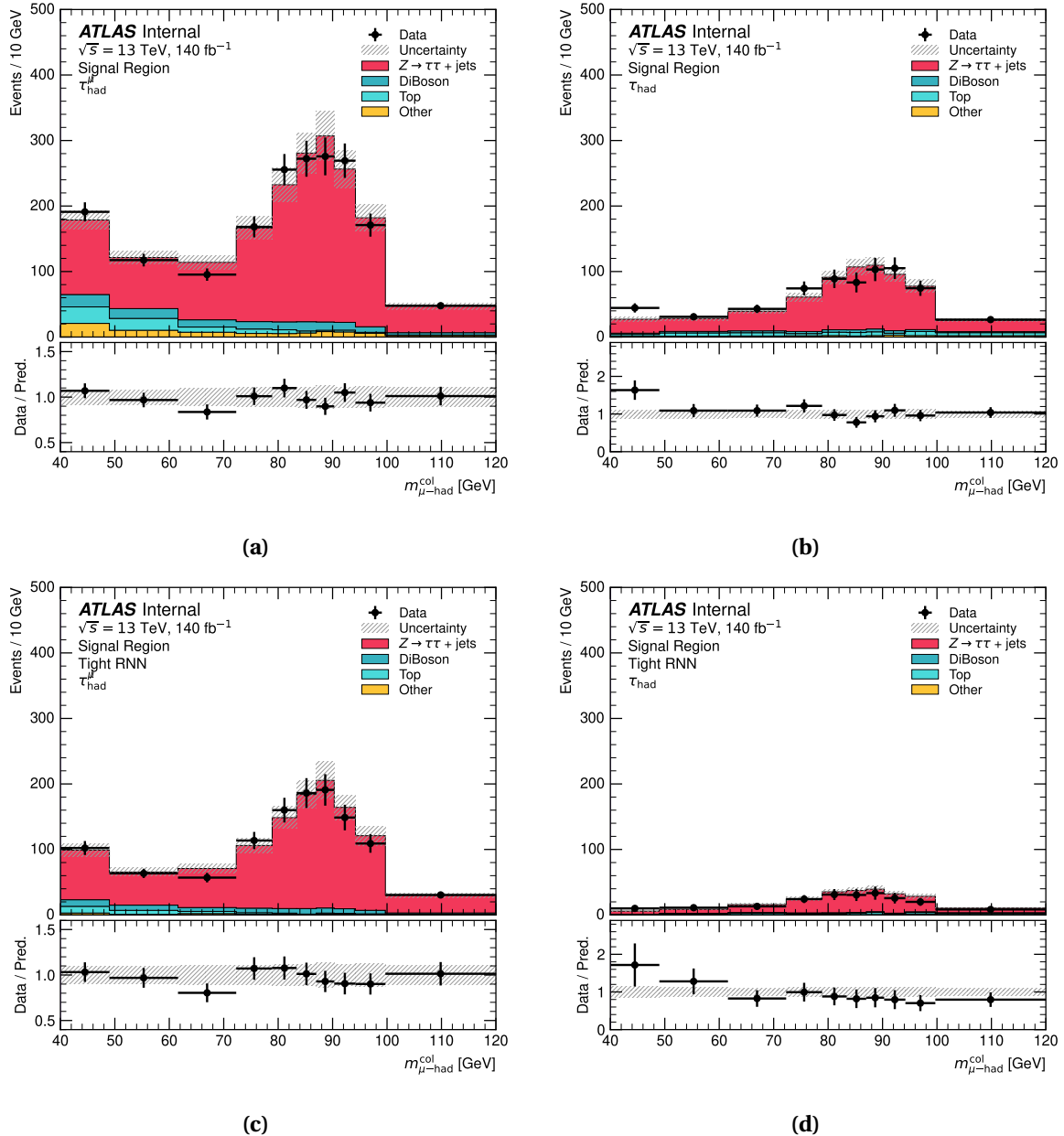


Fig. 5.18 The distributions of $m_{\mu-\text{had}}^{\text{col}}$ corresponding to the various signal selections defined in the text: (a) SR, (b) SR^{std}, (c) SR_{tight}, and (d) SR_{tight}^{std}. SR, SR_{tight} and CR are with the τ_{had}^μ method, while SR^{std} and SR_{tight}^{std} are with the standard ATLAS TauID.

5.6 Summary and conclusion

In this chapter, the case of a highly boosted pair of τ leptons is considered, in which one τ decays produce a muon and the other τ decays hadronically, with the visible decay products reconstructed within a single τ_{seed} jet. In such cases, the standard ATLAS TauID for hadronically decaying τ leptons fails due to the presence of the nearby muon.

The development of a muon-removal procedure using samples of high-mass $G \rightarrow HH \rightarrow 4\tau$ events is described. This τ_{had}^{μ} method recovers the τ_{had} reconstruction and identification efficiencies to the level expected for isolated τ_{had} decays for all TauID working points. The measurement precision for the kinematic properties of the visible τ_{had} system is similarly recovered. The τ_{had}^{μ} objects are benchmarked by selecting a sample of highly boosted $Z \rightarrow \tau_{\mu}\tau_{\text{had}}$ final states using the complete Run 2 dataset recorded by the ATLAS detector. Good agreement is found between data and MC predictions in both the signal $Z \rightarrow \tau_{\mu}\tau_{\text{had}}$ region and in a control-region in which the muon and τ_{had} candidate have same-sign charges. The comparison of rates in the signal region gives a ratio between the background-subtracted data and the expected signal yields of 0.97 ± 0.12 .

The results presented in this chapter demonstrate the effectiveness of the τ_{had}^{μ} objects in enhancing the signal sensitivity of the boosted $\tau_{\mu}\tau_{\text{had}}$ channel. The observed good agreement between the data and the SM theory predictions in the signal region reaffirms the robustness of the newly developed object.

Chapter 6

The electron-removal method for boosted $\tau_e \tau_{\text{had}}$ reconstruction

6.1 Introduction

Similar to the $\tau_\mu \tau_{\text{had}}$ channel, if an electron lies within the τ_{seed} jet, the standard TauReco and TauID algorithm is not able to reconstruct and identify the τ_{had} . Figure 6.1 shows the combined reconstruction and identification efficiency as a function of the truth-level $\Delta R_{\tau\tau}^{\text{truth},\text{vis}}$. The efficiency of the TauReco and TauID algorithms drop significantly when the $\Delta R_{\tau\tau}^{\text{truth},\text{vis}}$ is less than 0.4, as the electron begin to merge with the τ_{seed} jet. As a result, the possibility of reconstructing the correct number of τ_{had} tracks is significantly reduced, and the τ_{had} identification efficiency drops significantly in all the WPs. Having demonstrated the success of the τ_{had}^μ , we proposed a similar method for the $\tau_e \tau_{\text{had}}$ channel, the electron-removal τ_{had} (τ_{had}^ℓ).

The τ_{had}^ℓ reconstruction is however much more challenging than the τ_{had}^μ , technically and physically. The electron is not a minimum ionising particle (MIP) like the muon. Its energy deposition in the calorimeter makes it much more complicated to remove. The electron showers in the calorimeter, depositing most of its energy in the EM calorimeter. In

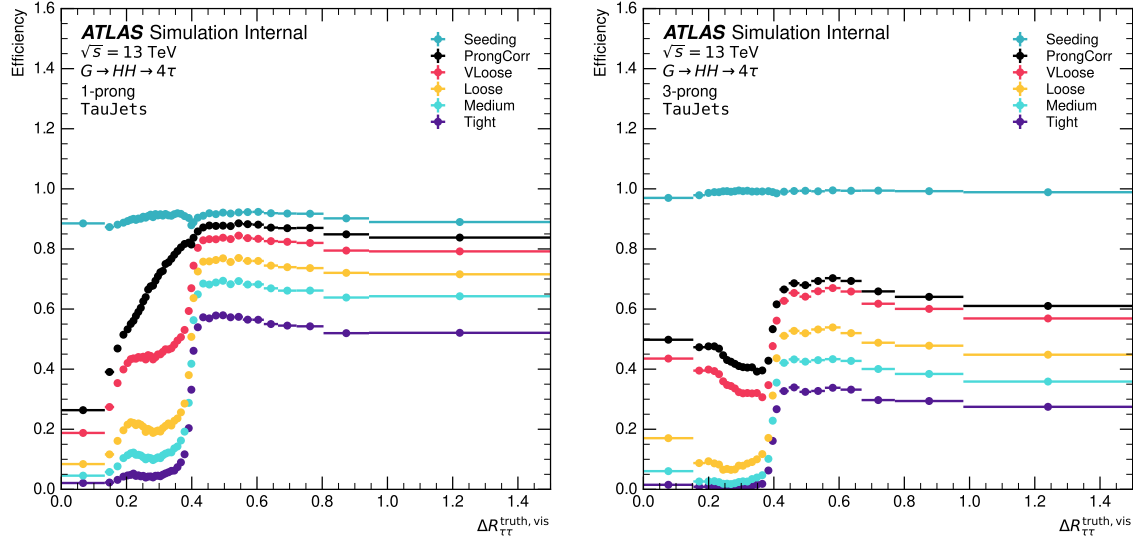


Fig. 6.1 The combined reconstruction and identification efficiency of the standard TauReco and TauID as a function of the truth-level $\Delta R_{\tau\tau}^{\text{truth}, \text{vis}}$. The efficiency is shown for the different working points of the TauID algorithm. In addition, the “Reco” and “ProngCorr” efficiencies are shown, which are the efficiency of the τ_{had} being seeded, and the efficiency of the TauRec algorithm to reconstruct the correct number of tracks in the τ_{had} , respectively.

very highly boosted cases, the electron can also deposit significant energy in the hadronic calorimeter. In the context of the τ_{had}^k , the electron cluster can merge with the τ_{had} clusters, making the separation of the clusters difficult. The presence of the electron in the τ_{seed} jet can also drag the barycentre of the τ_{had} to the direction of the electron. Simply removing the electron from the τ_{seed} jet results in a τ_{had} with a shifted axis, with some of the τ_{had} decay products being outside the core-cone of the τ_{seed} jet. This problem severely affects the efficacy of a simple electron-removal method.

In Section 6.2, we present an accretive method to reconstruct the τ_{had}^k in the presence of an electron. We also show that the accretive τ_{had}^k can be reconstructed with high efficiency in the region where the $\Delta R_{\tau\tau}^{\text{truth}, \text{vis}} > 0.2$. The energy and spatial resolution of the τ_{had}^k are presented in Section 6.3. An initial benchmark of the τ_{had}^k in the $Z \rightarrow \tau_e \tau_{\text{had}}$ channel is presented in Section 6.4. The summary and outlook of the τ_{had}^k reconstruction is presented in Section 6.5.

6.2 Accretive τ_{had}^k reconstruction method

For the development of τ_{had}^k , the $G \rightarrow HH \rightarrow 4\tau$ MC samples as described in Chapter 5 are used. However, instead of utilising the full mass range of the $G \rightarrow HH \rightarrow 4\tau$ samples, only the $m_G = 1500$ GeV sample is considered due to limitations in resources for custom ATLAS MC production. This sample is chosen because it covers the $\Delta R_{\tau\tau}^{\text{truth}}$ range from 0.1 to 0.6, which represents the most comprehensive region for τ_{had}^k reconstruction. The accretive τ_{had}^k reconstruction is a six-step process for every event:

1. The first step is to identify the electrons that satisfy the MediumLH WP, without isolation requirements.
2. The second step is to remove the tracks and calorimeter clusters associated with the electrons from the event.
3. Thirdly, using the remaining LCTopo clusters and tracks, the τ_{seed} jets are re-clustered with the anti- k_t algorithm with $R = 0.4$.
4. In the fourth step, re-clustered electron-free τ_{seed} jets with $\Delta R_{\tau\tau}^{\text{reco}} > 0.6$ to any identified electron are removed from the event, as they should not be affected by the electron.
5. Then, the electron-free track and cluster collections are supplied to the TauRec algorithm, which reconstructs the τ_{had}^k candidates from the remaining τ_{seed} jets.
6. Finally, the τ_{had}^k candidates are identified using the standard TauID algorithm.

Figure 6.2 shows the TauID efficiency of the accretive τ_{had}^k reconstruction method as a function of the truth-level $\Delta R_{\tau\tau}^{\text{truth,vis}}$. Compared to more than 90% MediumLH efficiency for isolated electrons at high p_T [72], the “ElecRM” efficiency is significantly lower, at around 70% in $\Delta R_{\tau\tau}^{\text{truth,vis}} > 0.2$ region. Below this threshold, the electron ID efficiency

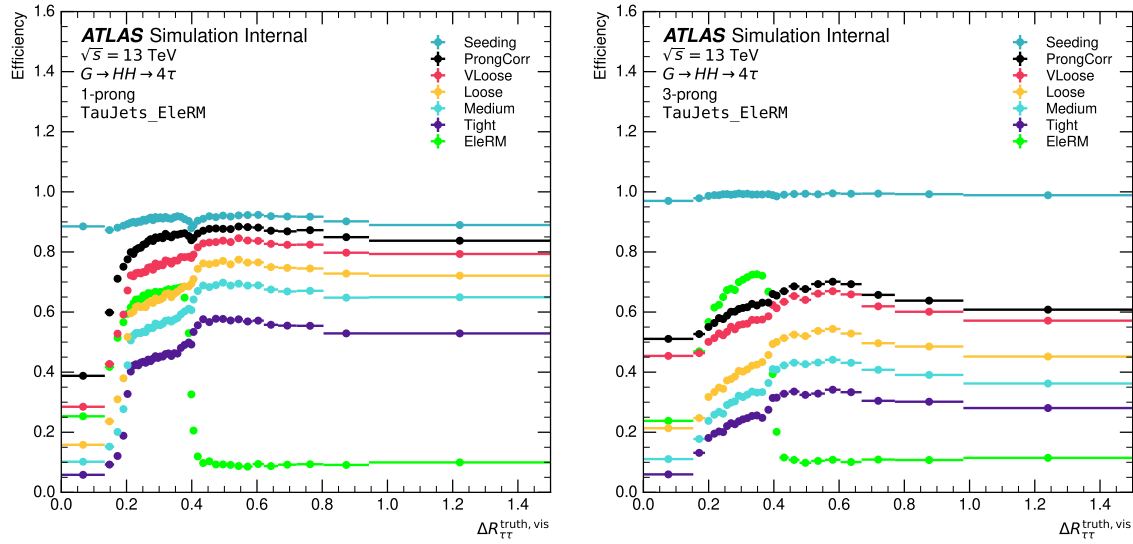


Fig. 6.2 The combined reconstruction and identification efficiency of the accretive τ_{had}^k reconstruction method as a function of the truth $\Delta R_{\tau\tau}^{\text{truth},\text{vis}}$. The efficiency is shown for every working points of the TauID algorithm. In addition, the “Reco”, “ElecRM”, and “ProngCorr” efficiencies are shown, which is the efficiency of the τ_{had} being seeded, the efficiency of the electron-removal, and the efficiency of the TauRec algorithm reconstructing the correct number of tracks, respectively.

drops significantly, as the electron and τ_{had} clusters start to merge. The TauID efficiency of the τ_{had}^k is significantly higher than the standard TauID algorithm in this region, but not as high as the TauID efficiency for isolated τ_{had} candidates.

If we only consider the case where the overlapping electron is identified and removed, the performance as functions of truth-level $\Delta R_{\tau\tau}^{\text{truth},\text{vis}}$, $p_T^{\text{truth},\text{vis}}$, and $|\eta|^{\text{truth},\text{vis}}$ are shown in Figure 6.3. In such cases, the TauID efficiency in various WPs in the $\Delta R_{\tau\tau}^{\text{truth},\text{vis}} > 0.2$ region are completely recovered. The “ProngCorr” efficiency is also recovered to more than 90% in the $\Delta R_{\tau\tau}^{\text{truth},\text{vis}} > 0.2$ region for 1-prong τ_{had}^k . The “ProngCorr” efficiency reaches 80% for 3-prong τ_{had}^k at low- p_T . In 3-prong case, higher track multiplicity makes it more challenging to reconstruct τ_{had} , especially in high p_T region. When the electron is identified and removed, the TauID efficiency behaves similarly to the standard TauID algorithm and the muon-removal method. The similarity shows that the accretive τ_{had}^k objects can be treated as isolated τ_{had} objects. In all cases, the electron-removal, TauRec,

and TauID efficiencies drops significantly in the $\Delta R_{\tau\tau}^{\text{truth},\text{vis}} < 0.2$ region. As the electron and τ_{had} clusters start to merge in this region, both the identification of the electron and the reconstruction of the τ_{had} becomes more challenging.

This method is much more challenging technically compared to the case for τ_{had}^{μ} , due to the limitations of the event-level thinning in the ATLAS xAOD Event Data Model (EDM). TauRec algorithms rely on the individual calorimeter cell information to function. After the ATLAS Tier-0 reconstruction, the calorimeter cell information is discarded unless they are associated with a reconstructed standard τ_{had} candidates. The τ_{had}^{ℓ} objects contains different clusters than the standard τ_{had} objects, in which the cells are not preserved in the xAOD. As a result, the τ_{had}^{ℓ} reconstruction is not possible in the standard ATLAS xAOD EDM. It can only be performed in the ATLAS Tier-0 reconstruction. The τ_{had}^{ℓ} objects originate from a different set of τ_{seed} jets, meaning that unlike the τ_{had}^{μ} , there is no direct equivalent in the standard τ_{had} collection. To save Tier-0 CPU usage and xAOD storage, only the τ_{had}^{ℓ} objects that are within $\Delta R_{\tau\tau}^{\text{truth},\text{vis}} < 0.6$ are saved in the xAOD.

6.3 Energy and spatial resolution of the τ_{had}^{ℓ}

Having demonstrated the TauID efficiency of the τ_{had}^{ℓ} , we now turn our attention to the energy and spatial resolution of the τ_{had}^{ℓ} . The relative energy resolution ($\frac{p_T^{\text{reco}}}{p_T^{\text{truth}}}$) of the τ_{had}^{ℓ} is shown in Figure 6.4. The spatial resolution of the τ_{had}^{ℓ} in terms of the difference in the truth and reconstructed ϕ and η are shown in Figure 6.5. The τ_{had}^{ℓ} objects show significantly better energy and spatial resolution than the standard τ_{had} objects. Before the electron-removal, the τ_{had} objects have a significant upper tail in the energy resolution, from the electron calorimeter deposit. The energy resolution of τ_{had}^{ℓ} objects is much improved. Order-of-magnitude improvements are observed in both 1- and 3-prong cases in energy residuals. For the spatial resolution, without the electron dragging on the τ_{seed}

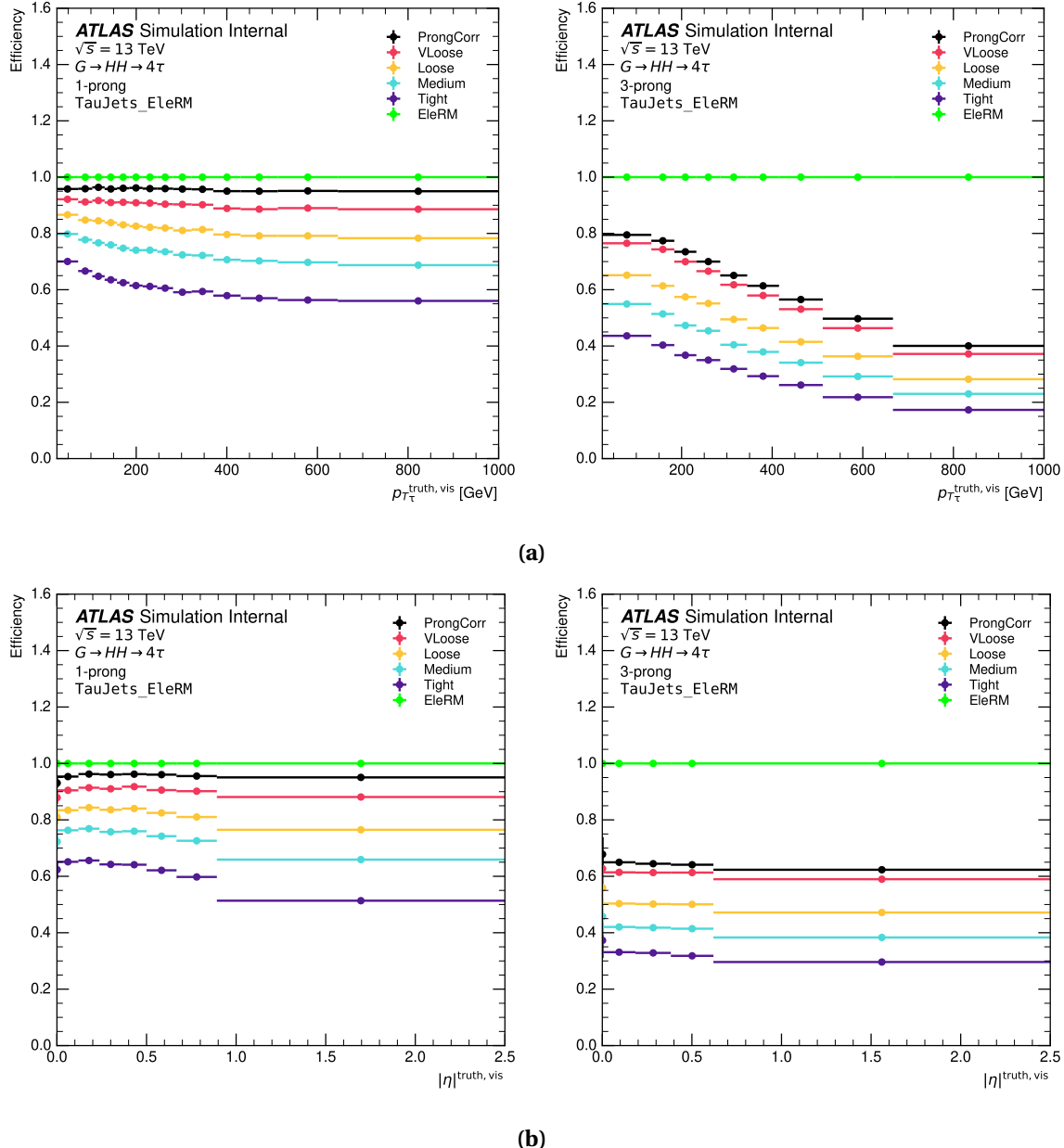


Fig. 6.3 The efficiency of the accretive τ_{had}^k reconstruction method as a function of the truth-level $p_{T\tau}^{\text{truth},\text{vis}}$ (a), and $|\eta|^{\text{truth},\text{vis}}$ (b), where the electron is identified and removed. The efficiency is shown for the different working points of the TauID algorithm for 1-prong and 3-prong. In addition, the “ElecRM”, and “ProngCorr” efficiencies are the efficiency of the electron-removal, and the efficiency of the TauRec algorithm to reconstruct the correct number of tracks in the τ_{had} , respectively.

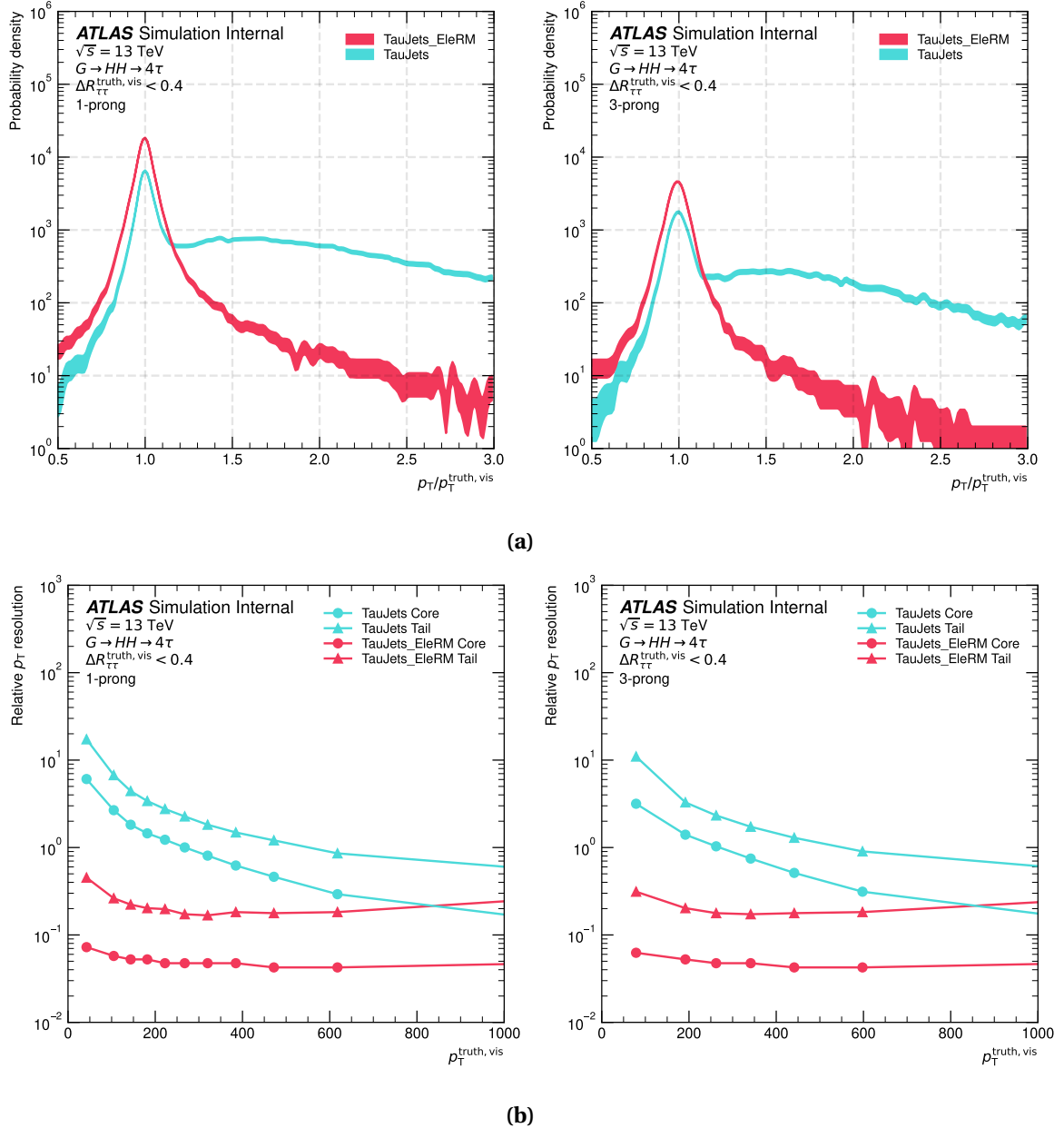


Fig. 6.4 The distributions of the calibrated transverse energy residuals for $\tau_{\text{had-vis}}$ with τ_{had}^k (red) and τ_{had} (blue) are shown in (a). The relative core (68%) and tail (95%) $\tau_{\text{had-vis}}$ p_T resolutions as functions of $p_T^{\text{truth, vis}}$ are shown in (b). The left plots show the 1-prong case and the right plots show the 3-prong case.

jet barycentre, the τ_{had}^k objects have a order-of-magnitude smaller ϕ and η tails and significantly higher peaks, compared to the standard τ_{had} objects.

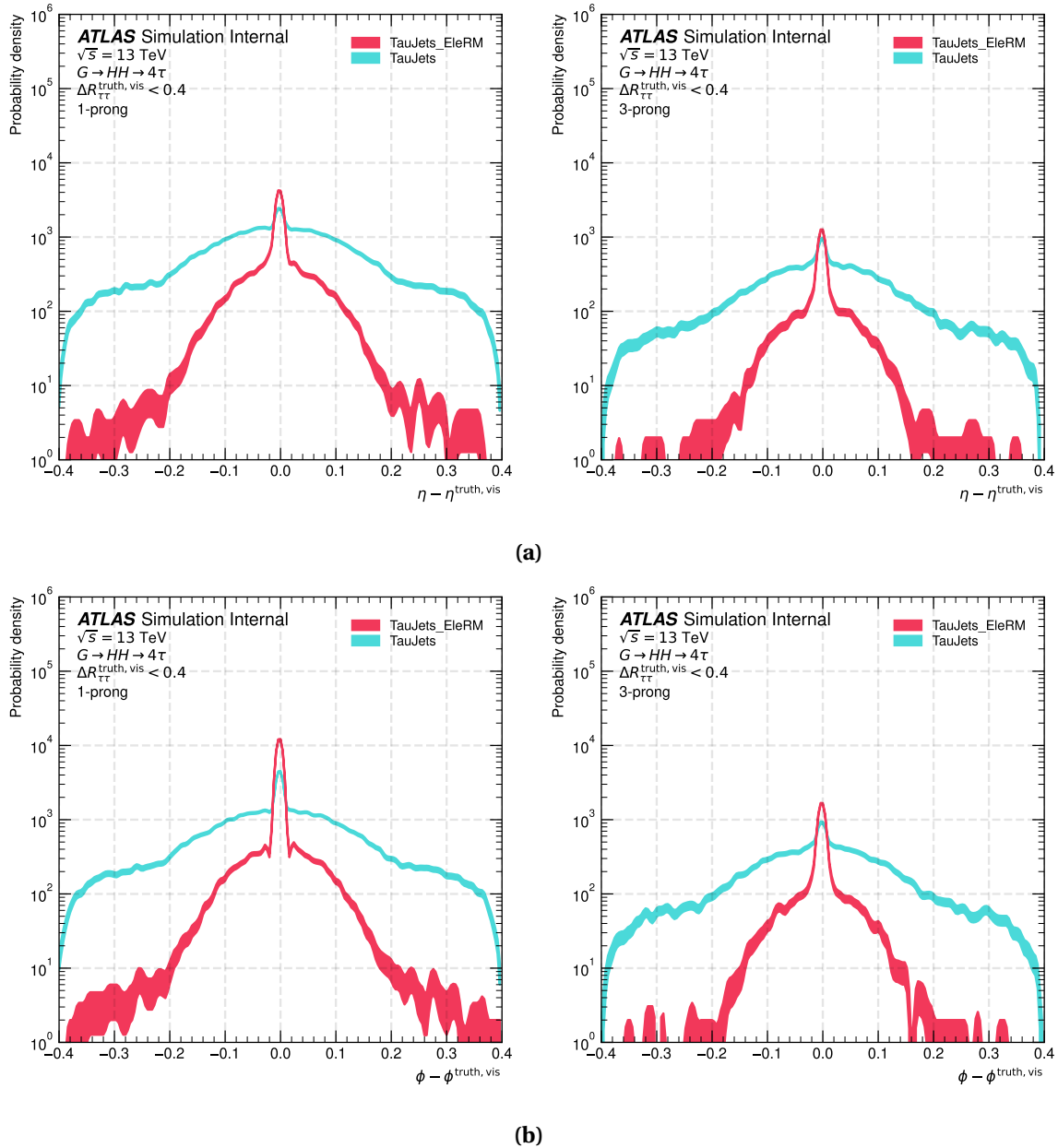


Fig. 6.5 The distributions of the ϕ (a) and η (b) residuals for $\tau_{\text{had-vis}}$ with τ_{had}^k (red) and τ_{had} (blue) are shown. The left plots show the 1-prong case and the right plots show the 3-prong case.

6.4 Benchmark of the τ_{had}^k in the $Z \rightarrow \tau_e \tau_{\text{had}}$ channel

Since the reconstruction of τ_{had}^k objects runs on the ATLAS Tier-0 reconstruction, they have only become available in the ATLAS 2024 data collection. Thanks to the exceptional 2024 operation of LHC and ATLAS, at the time of writing, ATLAS has collected a large

amount of data in 2024 that corresponds to an integrated luminosity of 91 fb^{-1} . For now, the benchmark of the τ_{had}^{ℓ} in the $Z \rightarrow \tau_e \tau_{\text{had}}$ channel is performed with the data currently available. Not all the data collected is suitable for physics analysis, but the "Good Run List" (GRL) [69] is not available at the time of writing. From the previous Run-3 operations [75], we estimate that around 85 fb^{-1} of the data collected is suitable for physics analysis. A complete Run-3 reprocessing of the 2022-2023 data is scheduled for the fourth-quarter of 2024, which will include the reconstruction of τ_{had}^{ℓ} objects. At the end of 2024, we will have the τ_{had}^{ℓ} objects in the full Run-3 data, corresponding to a projected integrated luminosity of around 160 fb^{-1} .

The τ_{had}^{ℓ} has been scheduled for the ATLAS MC samples for 2024 data-taking conditions. Unfortunately, at the time of writing, no MC sample that contain τ_{had}^{ℓ} is available due to previously unforeseen delays in the MC validation and production. In the coming years, MC samples for the 2022 and 2023 data-taking conditions will be reprocessed with the τ_{had}^{ℓ} objects included.

6.4.1 Event-selection

The event-selection and the $\tau_e \tau_{\text{had}}$ collinear reconstruction in the $Z \rightarrow \tau_e \tau_{\text{had}}$ channel is very similar to the τ_{had}^{μ} benchmark, with the τ_{had}^{μ} replaced by the τ_{had}^{ℓ} . Exceptions include the trigger requirements, the slightly tighter jet RNN score requirements, and a loose electron-veto RNN requirement. event-selection requirements in the $Z \rightarrow \tau_e \tau_{\text{had}}$ channel are summarised in Table 6.1. In addition to these selections, the τ_{had}^{ℓ} in the SR are required to have opposite charge to the electron. The τ_{had}^{ℓ} in the CR is required to have same charge to the electron. The fraction of the selected events that pass the specified triggers is 80%. The actual trigger efficiency is by definition lower than this value, which is significantly lower than the 97% observed in the $\tau_{\mu} \tau_{\text{had}}$ benchmark SR. The $E_{\text{T}}^{\text{miss}}$ trigger efficiency is

Table 6.1 Summary of event-selection requirements for the $Z \rightarrow \tau_e \tau_{\text{had}}$ channel.

Object	Selection
Triggers	HLT_xe65_cell_xe90_pfopufit_L1XE50
	HLT_e26_lhtight_ivarloose_L1eEM26M
	HLT_e60_lhmedium_L1eEM26M
	HLT_e140_lhloose_L1eEM26M
τ_{had}^k	$0 < \eta < 1.37$ or $1.52 < \eta < 2.5$
	Jet RNN score > 0.15
	e-veto RNN score > 0.05
e	$p_T > 15 \text{ GeV}$
	$p_T > 10 \text{ GeV}$
	“MediumLH” ID
$\tau_e \tau_{\text{had}}$ system	$\Delta R(e, \tau_{\text{had}}^k) < 0.4$
	$-0.1 < \Delta\phi_{e-E_T^{\text{miss}}}^{\text{signed}} < 0.4$
	$m_{e-\text{had}}^{\text{col}} > 40 \text{ GeV}$
	$p_{T e-\text{had}}^{\text{col}} > 250 \text{ GeV}$
no b-tag jet at 85% efficiency working point	

considerably lower compared to the $Z \rightarrow \tau_\mu \tau_{\text{had}}$ benchmark, which is expected due to the calorimeter deposit from the electron.

6.4.2 Results

Without MC samples, the exact composition of the events in the analysis regions is not known. Instead, we rely on kinematic distributions, TauID distributions, and event yields in the SR and CR to understand the background level and signal purity in the $Z \rightarrow \tau_e \tau_{\text{had}}$ channel. From the τ_{had}^μ benchmark, we know that the highly boosted $Z \rightarrow \tau_\mu \tau_{\text{had}}$ channel is very clean, with a high purity of $\tau_\mu \tau_{\text{had}}$ events and minimal background. We shall demonstrate below that the τ_{had}^k benchmark in the $Z \rightarrow \tau_e \tau_{\text{had}}$ channel is expected to show similar traits in the highly boosted $Z \rightarrow \tau_e \tau_{\text{had}}$ channel, given the similar characteristics found during the τ_{had}^k and τ_{had}^μ developments.

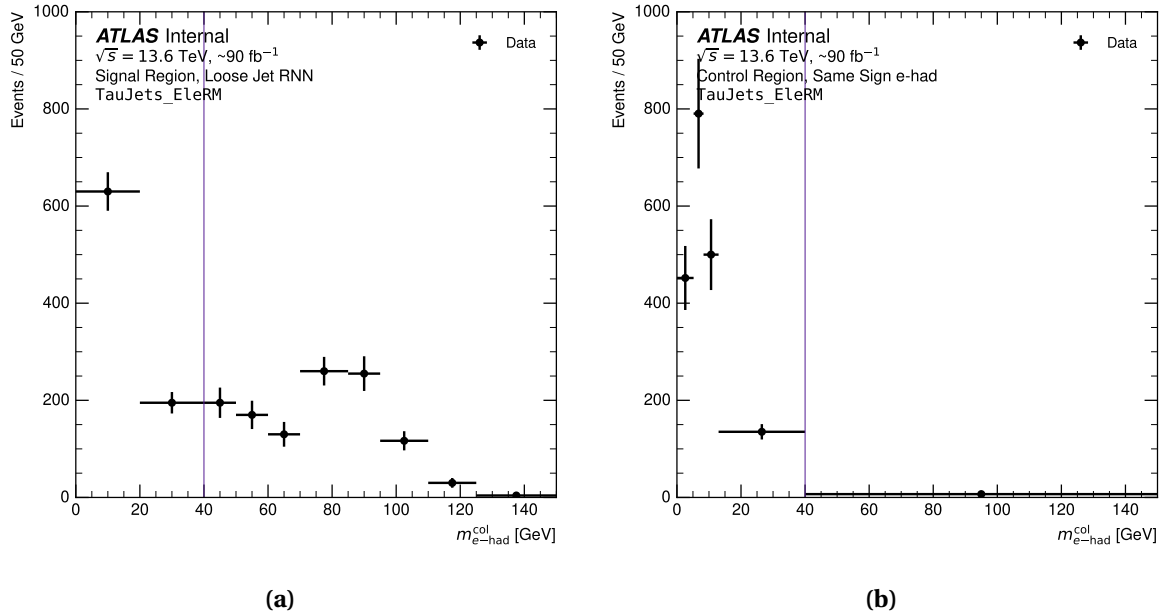


Fig. 6.6 The distribution of the $m_{e-\text{had}}^{\text{col}}$: (a) in the SR, and, (b) in the CR. All requirement criteria are applied, except the requirement on the variable being plotted. The vertical line indicates the event-selection requirement on this variable.

The $\tau_e \tau_{\text{had}}$ collinear mass ($m_{e-\text{had}}^{\text{col}}$), transverse momentum ($p_{T e-\text{had}}^{\text{col}}$), the τ_{had}^k TauID RNN score, and TauID eveto score distributions are shown in Figure 6.6-6.9, respectively. The SR distributions provide an estimation of the combined signal and background level, whereas the CR distributions give an estimation of the background level.

It is encouraging to see that the distribution of $m_{e-\text{had}}^{\text{col}}$ has the same shape as the $m_{\mu-\text{had}}^{\text{col}}$ in the $Z \rightarrow \tau_\mu \tau_{\text{had}}$ channel, featuring a peak at the Z boson mass and a shoulder in the low-mass region. The shape of the $m_{e-\text{had}}^{\text{col}}$ distribution for signal Drell-Yan events seen in Figure 6.6 is very different from that seen in inclusive production, with a much larger fraction of the signal events in the region $40 < m_{e-\text{had}}^{\text{col}} < 70 \text{ GeV}$ relative to that at the Z boson peak. This is a result of the sharply falling distribution in Z boson p_T for Drell-Yan production, coupled with the fact that the opening angle of boosted $\tau_e \tau_{\text{had}}$ systems decreases with decreasing $m_{e-\text{had}}^{\text{col}}$. The $p_{T e-\text{had}}^{\text{col}}$ distribution in the SR shows a peak at a transverse momentum of around 450 GeV, also consistent with the $p_{T \mu-\text{had}}^{\text{col}}$ distribution in the $Z \rightarrow \tau_\mu \tau_{\text{had}}$ channel. The jet RNN distribution in the SR is statistically

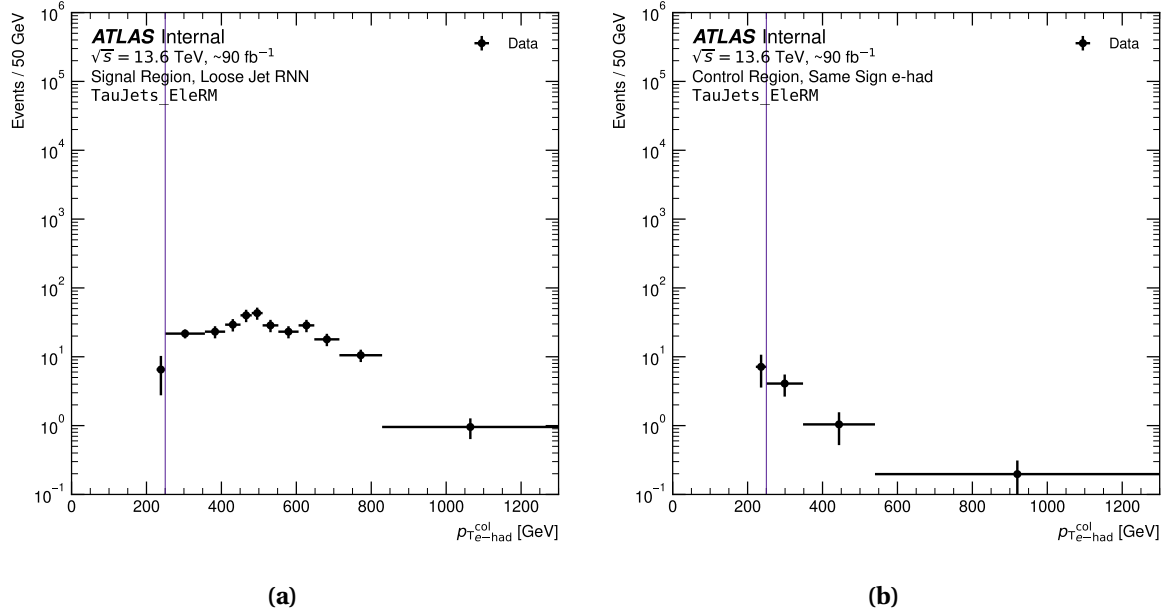


Fig. 6.7 The distribution of the $p_{\text{Te-had}}^{\text{col}}$: (a) in the SR, and, (b) in the CR. All requirement criteria are applied, except the requirement on the variable being plotted. The vertical line indicates the event-selection requirement on this variable.

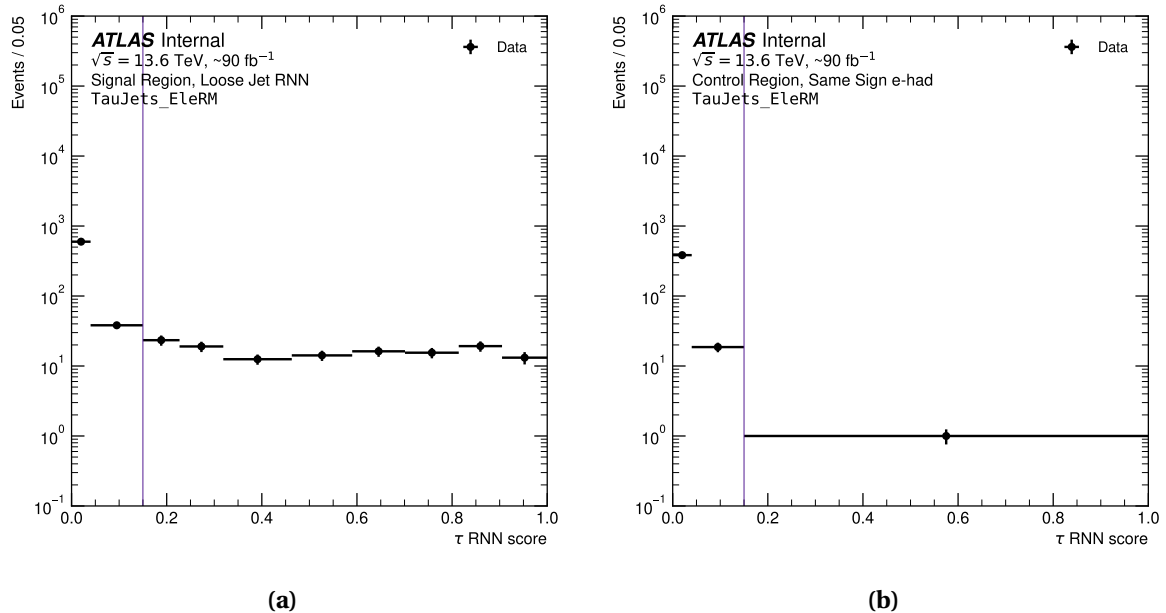


Fig. 6.8 The distribution of the TauID RNN score: (a) in the SR, and, (b) in the CR. All requirement criteria are applied, except the requirement on the variable being plotted. The vertical line indicates the event-selection requirement on this variable.

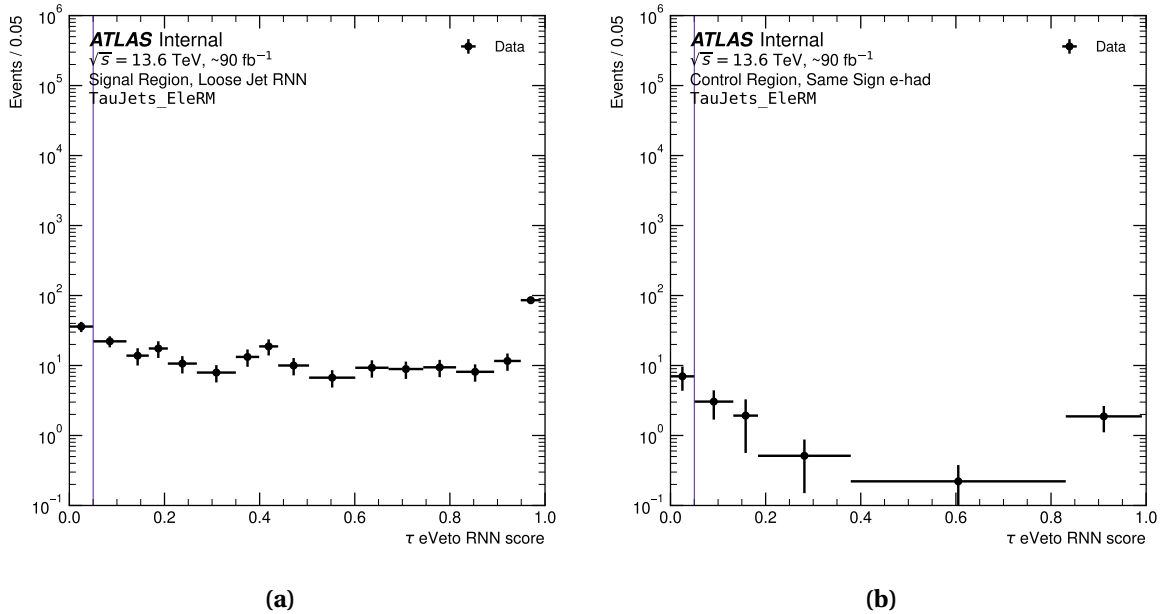


Fig. 6.9 The distribution of the TauID e-veto RNN score: (a) in the SR, and, (b) in the CR. All requirement criteria are applied, except the requirement on the variable being plotted. The vertical line indicates the event-selection requirement on this variable.

consistent with a flat distribution, in the higher RNN score region, indicating a high signal purity in the SR. An increase in the event yield at the low RNN score region is observed in the SR, indicating a non-negligible background contribution. This is in line with the CR jet RNN distribution. The electron-veto RNN distribution shows a bump in the low-score region, indicating a non-negligible contribution from electron background.

Figure 6.10 shows comparisons between the event yield for $m_{e-\text{had}}^{\text{col}}$ distributions corresponding to various SR definitions, each mirroring the τ_{had}^{ℓ} benchmark. Figure 6.10a shows the nominal SR. Figure 6.10b shows the sample SR^{std}. Figure 6.10c shows the sample SR_{tight}. Figure 6.10d shows the sample SR_{tight}^{std}.

The event yields in the various SR and CR are shown in Table 6.2. Without MC samples, the signal and background levels in the SR can only be estimated using the TauID efficiency and the event yields in the CR. To estimate the signal and background levels in the SR, we make the following assumptions:

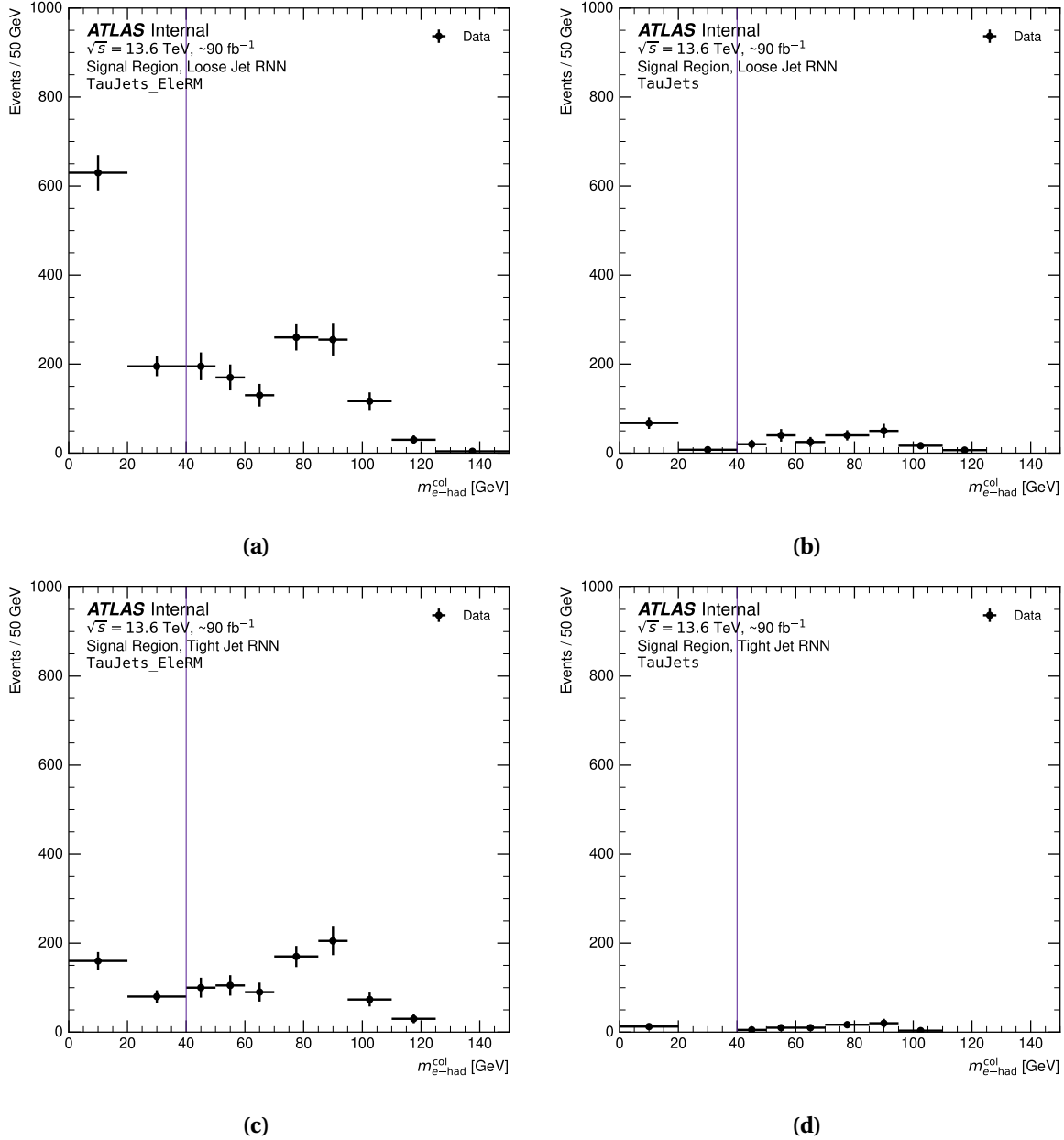


Fig. 6.10 The distribution of the $m_{e-\text{had}}^{\text{col}}$ in the SR: (a) nominal SR, (b) SR^{std}, (c) SR_{tight}, and, (d) SR_{tight}^{std}. SR, SR_{tight} and CR are with the τ_{had}^e method, while SR^{std} and SR_{tight}^{std} are with the standard ATLAS TauID.

- The TauID efficiency in the SR is the same as the TauID efficiency observed when flattening the RNN score.

Table 6.2 Event yields in SR and CR. SR, SR_{tight} , SR^{std} , and $\text{SR}_{\text{tight}}^{\text{std}}$ are defined mirroring the τ_{had}^{μ} benchmark. CR, CR_{tight} , CR^{std} , and $\text{CR}_{\text{tight}}^{\text{std}}$ are defined by requiring the same charge electron- τ_{had} in the SR, SR_{tight} , SR^{std} , and $\text{SR}_{\text{tight}}^{\text{std}}$, respectively. SR, SR_{tight} and CR are with the τ_{had}^{ℓ} method, while SR^{std} and $\text{SR}_{\text{tight}}^{\text{std}}$ are with the standard ATLAS TauID. The uncertainties quoted are statistical only.

	SR	SR_{tight}	SR^{std}	$\text{SR}_{\text{tight}}^{\text{std}}$
Data	274 ± 17	182 ± 13	46 ± 7	15 ± 4
	CR	CR_{tight}	CR^{std}	$\text{CR}_{\text{tight}}^{\text{std}}$
Data	15 ± 4	5 ± 2	3 ± 2	1 ± 1

- The increase in TauID background rejection power when moving from the Loose to Tight WP is the same in both the SR and CR.
- The $Z \rightarrow \tau_e \tau_{\text{had}}$ signal contribution is negligible in the CR.

"

Based on these assumptions, the signal and background levels in the SR can be estimated using the following equations:

$$\begin{aligned} n_{\text{data}}^{\text{SR}} &= 85\% \times n_{\text{sig}}^{\text{all}} + n_{\text{bkg}}^{\text{SR}}, \\ n_{\text{data}}^{\text{SRtight}} &= 60\% \times n_{\text{sig}}^{\text{all}} + n_{\text{bkg}}^{\text{SRtight}}, \end{aligned} \quad (6.1)$$

where:

- $n_{\text{data}}^{\text{SR}}$ is the number of data events in the SR,
- $n_{\text{data}}^{\text{SRtight}}$ is the number of data events in the SR_{tight} ,
- $n_{\text{sig}}^{\text{all}}$ is the estimated total number of signal events in the SR, before the application of the selection requirement on tau RNN score.
- $n_{\text{bkg}}^{\text{SR}}$ is the estimated number of background events in the SR,
- $n_{\text{bkg}}^{\text{SRtight}}$ is the estimated number of background events in the SR_{tight} .

The ratio of background events between the SR and SR_{tight} can be estimated from the ratio of data events in the CR and CR_{tight}:

$$\frac{n_{\text{bkg}}^{\text{SRtight}}}{n_{\text{bkg}}^{\text{SR}}} = \frac{n_{\text{data}}^{\text{CRtight}}}{n_{\text{data}}^{\text{CR}}}, \quad (6.2)$$

where:

- $n_{\text{data}}^{\text{CR}}$ is the number of data events in the CR,
- $n_{\text{data}}^{\text{CRtight}}$ is the number of data events in the CR_{tight}.

By solving these equations, the estimated number of background events in the SR is $n_{\text{bkg}}^{\text{SR}} = 31^{+57}_{-31}$, and the estimated number of signal events in the SR is $n_{\text{sig}}^{\text{SR}} = 243^{+31}_{-57}$. Similarly, the estimated number of signal events in the SR_{tight} is $n_{\text{sig}}^{\text{SRtight}} = 172^{+10}_{-19}$, and the estimated number of background events in the SR_{tight} is $n_{\text{bkg}}^{\text{SRtight}} = 10^{+19}_{-10}$. Repeating the same process for the SR^{std} and SR_{tight}^{std} regions yields signal estimations of zero events in both regions, indicating that the assumptions above may not hold in SR^{std} and SR_{tight}^{std}, or that these regions are background-dominated. The estimated signal purity in the SR is $88\%^{+12\%}_{-20\%}$, and in the SR_{tight} it is $95\%^{+5\%}_{-11\%}$. All quoted uncertainties are statistical only.

The τ_{had}^k objects show a significant improvement in signal yield compared to the standard τ_{had} objects; the background-inclusive yield is six times higher in the SR and 12 times higher in the SR_{tight}. Compared with the τ_{had}^μ benchmark, the τ_{had}^k benchmark exhibits a similar level of signal purity but a lower signal yield. Normalising to unit luminosity, the τ_{had}^μ benchmark yields 6.8 ± 0.8 (syst. + stat.) events per fb^{-1} in the SR, while the τ_{had}^k benchmark yields $2.7^{+0.3}_{-0.6}$ events per fb^{-1} in the SR. This corresponds to $40\%^{+6\%}_{-10\%}$ of the τ_{had}^μ benchmark yield.

The difference in signal yield is entirely expected. The τ_{had}^k algorithm has a lower reconstruction and identification efficiency (roughly 70% of that of the τ_{had}^μ objects); the trigger efficiency is lower (less than 80% of the τ_{had}^μ benchmark); the TauID requirements

are tighter (90% of the τ_{had}^μ benchmark); The Z boson production cross-section increases by 5% with the centre of mass energy change from 13 TeV to 13.6 TeV is expected (105%). Combining these factors, the expected SR signal yield should be around 53% of the τ_{had}^μ benchmark, which is higher than the observed $40\%^{+6\%}_{-10\%}$. The difference can be attributed to the systematic uncertainties in the TauID efficiency, the trigger efficiency, and the Z boson production cross-section.

6.5 Summary and outlook

In this chapter, we have considered the case of a highly boosted pair of τ leptons, where one τ decays to produce an electron and the other τ decays hadronically. In such cases, the visible decay products are reconstructed within a single τ_{seed} jet.

We have described the development of an electron-removal procedure using samples of high-mass $G \rightarrow HH \rightarrow 4\tau$ events. We have demonstrated that this τ_{had}^ℓ method recovers the τ_{had} identification efficiency back to the level expected for isolated τ_{had} decays for all TauID working points when the electron is properly removed. The measurement precision for the kinematic properties of the visible τ_{had} system is similarly recovered. We have benchmarked the τ_{had}^ℓ objects by selecting a sample of highly boosted $Z \rightarrow \tau_e \tau_{\text{had}}$ final states using the partial 90 fb^{-1} Run 3 dataset recorded by the ATLAS detector in 2024 at a centre-of-mass energy of 13.6 TeV.

We found that the τ_{had}^ℓ objects have a significant improvement in the $\tau_e \tau_{\text{had}}$ reconstruction efficiency, with an event yield of 274 ± 17 in the SR — six times higher than the standard τ_{had} objects, and 12 times higher if the SR_{tight} is considered. The signal purity in the SR is estimated to be $88\%^{+12\%}_{-20\%}$, and in the SR_{tight} it is estimated to be $95\%^{+5\%}_{-11\%}$, comparable to the τ_{had}^μ benchmark. The limited event yields in the CR highlight the success in suppressing background contributions.

This study, together with the τ_{had}^{μ} benchmark, demonstrates that the lepton-removal τ_{had} reconstruction is ready for physics analysis at the ATLAS experiment. These lepton-removal objects lay the foundation for future searches for high-mass BSM resonances in the $\tau_{\text{lep}} \tau_{\text{had}}$ channel. They also open up exciting opportunities for exploring other new physics phenomena at the ATLAS experiment.

Chapter 7

A search for the Graviton in the $HH \rightarrow b\bar{b}\tau_\mu\tau_{\text{had}}$ channel

7.1 Introduction

The Graviton is a spin-2 particle that mediates the gravitational force. In addition to the RS model, the Graviton is also predicted by other models such as string theory. The search for gravity in LHC boils down to a search for an undiscovered BSM heavy spin-2 particle (G). This type of search is sensitive to a broad range of other BSM theory, such as the Supersymmetry (SUSY) model, Two-Higgs Doublet Model (2HDM), the Composite Higgs Models (CHM), etc., which predict the existence of spin-0 heavy scalar particles (X) that couple with the SM Higgs boson. Fig 7.1 shows the Feynman diagram of the gluon–gluon production of the X and G . These production processes are predicted to have the largest cross-section at the LHC, should they exist. The predicted cross-section of the $pp \rightarrow G \rightarrow HH$ production at the LHC centre of mass energies of 13 TeV and 13.6 TeV as functions of the G mass are shown in Fig 7.2.

After the discovery of the Higgs boson, such searches have been performed extensively by ATLAS and CMS collaborations using Run-1 and Run-2 data, but no evidence of new

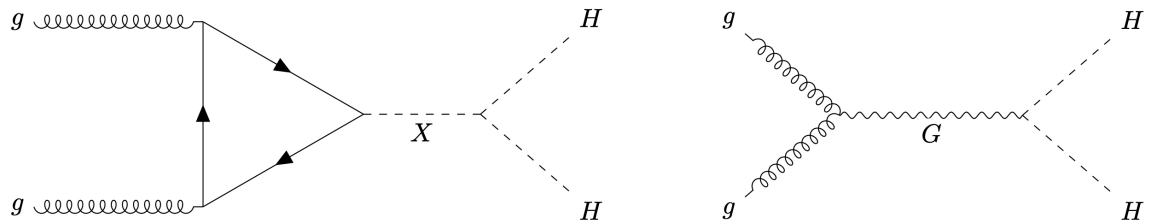


Fig. 7.1 Feynman diagram of the gluon–gluon production of the X and G .

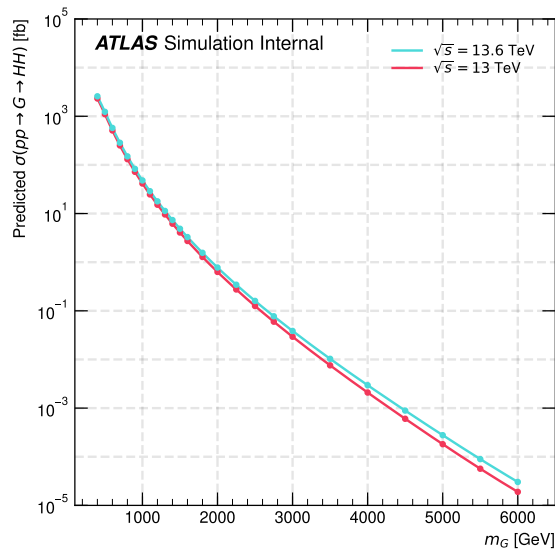


Fig. 7.2 Predicted cross-section of the $pp \rightarrow G \rightarrow HH$ production at the LHC centre of mass energy of 13 TeV and 13.6 TeV.

heavy particles has been found yet. In the $G/X \rightarrow HH$ channel, CMS published the combination [138] of the $HH \rightarrow b\bar{b}b\bar{b}$ [139], $HH \rightarrow b\bar{b}\tau\tau$ [140], $HH \rightarrow b\bar{b}\gamma\gamma$ [141], $HH \rightarrow b\bar{b}W^+W^-$ [142, 143], and $HH \rightarrow 4W/2W2\tau/4\tau \rightarrow 2l$ [144] searches using the full Run-2 data in 2024. Prior to this, ATLAS published the Run-2 combination [145] of the resonant $HH \rightarrow b\bar{b}b\bar{b}$ [146], $HH \rightarrow b\bar{b}\gamma\gamma$ [147], and $HH \rightarrow b\bar{b}\tau\tau$ [148] searches in 2023, as well as a dedicated search for the highly boosted di-Higgs production in the $HH \rightarrow b\bar{b}\tau_{\text{had}}\tau_{\text{had}}$ channel using the boosted $\tau_{\text{had}}\tau_{\text{had}}$ tagger [149]. Table 7.1 summarises the latest expected

Table 7.1 Summary of the expected and observed 95% CL limits on the production cross-section of the di-higgs ($\sigma(G/X \rightarrow HH)$) set by ATLAS and CMS. Limits are given in fb. The numbers inside and outside the brackets are the observed and the expected limits respectively.

Mass	Channel	CMS		ATLAS	
		$\sigma(X \rightarrow HH)$	$\sigma(G \rightarrow HH)$	$\sigma(X \rightarrow HH)$	$\sigma(G \rightarrow HH)$
1 TeV	Combined	5 (3)	3 (2)	6 (10)	N/A
	$HH \rightarrow b\bar{b}b\bar{b}$	7 (5)	3 (3)	8 (7)	8 (9)
	$HH \rightarrow b\bar{b}\tau\tau$	40 (22)	1 (1)	10 (30)	N/A
	$HH \rightarrow b\bar{b}\gamma\gamma$	10 (5)	7 (3)	50 (50)	N/A
2 TeV	Combined	0.6 (0.5)	0.4 (0.3)	2 (3)	N/A
	$HH \rightarrow b\bar{b}b\bar{b}$	0.7 (0.7)	0.4 (0.4)	2 (3)	2 (3)
	$HH \rightarrow b\bar{b}\tau\tau$	140 (140)	N/A	40 (50)	N/A
	$HH \rightarrow b\bar{b}\gamma\gamma$	2 (2)	2 (1)	N/A	N/A
3 TeV	Combined	0.5 (0.5)	0.2 (0.2)	1 (1)	N/A
	$HH \rightarrow b\bar{b}b\bar{b}$	0.5 (0.5)	0.2 (0.2)	1 (1)	1 (1)
	$HH \rightarrow b\bar{b}\tau\tau$	1400 (1400)	N/A	50 (50)	N/A
	$HH \rightarrow b\bar{b}\gamma\gamma$	1 (1)	1.0 (0.8)	N/A	N/A
4 TeV	Combined	0.3 (0.3)	N/A	1 (3)	N/A
	$HH \rightarrow b\bar{b}b\bar{b}$	0.4 (0.4)	N/A	1 (3)	1 (2)
	$HH \rightarrow b\bar{b}\tau\tau$	N/A	N/A	N/A	N/A
	$HH \rightarrow b\bar{b}\gamma\gamma$	1 (1)	0.8 (0.7)	N/A	N/A
5 TeV	Combined	0.2 (0.3)	N/A	1 (1)	N/A
	$HH \rightarrow b\bar{b}b\bar{b}$	0.3 (0.3)	N/A	1 (1)	1 (1)
	$HH \rightarrow b\bar{b}\tau\tau$	N/A	N/A	N/A	N/A
	$HH \rightarrow b\bar{b}\gamma\gamma$	1 (1)	N/A	N/A	N/A

and observed 95% CL limits on the production cross-section of the di-Higgs ($\sigma(pp \rightarrow G \rightarrow$

$HH)$) set by ATLAS and CMS at 1 to 5 TeV mass points. For both ATLAS and CMS, the $HH \rightarrow b\bar{b}b\bar{b}$ channel is the most sensitive channel for the heavy resonance search in $G/X \rightarrow HH$ channels. This channel has the highest branching ratio, and both collaborations have the most mature reconstruction techniques tagging highly boosted $b\bar{b}$ system [150, 151]. CMS has been taking the lead in the search in the $HH \rightarrow b\bar{b}b\bar{b}$ and $HH \rightarrow b\bar{b}\gamma\gamma$ channel. On the other hand, ATLAS currently leads the search in the $HH \rightarrow b\bar{b}\tau\tau$ channel, thanks to the boosted $\tau_{had}\tau_{had}$ tagger. Compared to the predicted cross-sections, the upper limits set by ATLAS and CMS collaborations have strongly excluded the existence of the Graviton in the mass lower than 2 TeV. However, above 2 TeV, the limits set by the both collaborations are still far higher than the predictions.

We choose the muon-removal τ_{had} reconstruction (τ_{had}^μ) as the boosted $\tau_\mu\tau_{had}$ tagger [136, 152]. The aim of such alternative reconstruction is to improve the τ_{had} reconstruction and identification efficiency in the boosted $\tau_\mu\tau_{had}$ channel, as discussed in Chapter 5. In the meantime, the ATLAS boosted $b\bar{b}$ tagger incorporated graph neural networks (GNN) [92] to significantly improve the boosted $b\bar{b}$ tagging (GN2x). In this chapter, we will present the search for the Graviton in the $HH \rightarrow b\bar{b}\tau_\mu\tau_{had}$ channel with the 140 fb^{-1} ATLAS Run-2 data. Using the τ_{had}^μ tagger and the newly developed GN2x boosted $b\bar{b}$ tagger [92], this analysis achieves the best sensitivity in the $HH \rightarrow b\bar{b}\tau\tau$ channel to date. The expected 95% CL limits on $\sigma(pp \rightarrow G \rightarrow HH)$ for masses in the range 2-5 TeV are ten-times lower than the previous ATLAS search in the $HH \rightarrow b\bar{b}\tau\tau$ channel, more than 100 times lower than the expected limits set by the CMS collaboration in the same channel.

Section 7.2 describes the data and MC samples used in the analysis. Section 7.3 describes the signal-region event-selection Section 7.5 describes the systematic uncertainties considered in this analysis. Section 7.6 describes the statistical analysis and limit setting. Section 7.7 presents the results of the analysis and discusses the future prospects.

7.2 Data and MC

Full ATLAS Run-2 data was used in this analysis. The data collected at $\sqrt{s} = 13$ TeV corresponds to an integrated luminosity of 140 fb^{-1} . For this analysis, the prediction for the SM contributions are from the same MC samples as those used for the τ_{had}^{μ} benchmark analysis detailed in Chapter 5, with the exception of the addition of the SM Higgs and di-Higgs samples.

Higgs boson production via gluon–gluon fusion (ggF) was simulated at next-to-next-to-leading-order (NNLO) accuracy in QCD using POWHEG BOX v2 [112–114, 153, 154]. The simulation achieved NNLO accuracy for arbitrary inclusive $gg \rightarrow H$ observables by re-weighting the Higgs boson rapidity spectrum in HJ-MINLO [155–157] to that of HNNLO [158]. The PDF4LHC15NNLO PDF set [159] and the AZNLO tune [160] of PYTHIA 8 [117] were used. The gluon–gluon fusion prediction from the Monte Carlo samples was normalised to the next-to-next-to-next-to-leading-order cross-section in QCD plus electroweak corrections at NLO [161–171]. The normalisation of all Higgs boson samples accounts for the decay branching ratio calculated with HDECAY [172–174] and PROPHCY4F [175–177].

Higgs boson production via vector-boson fusion was simulated with POWHEG BOX v2 [112–114, 178] and interfaced with PYTHIA 8 [117] for parton shower and non-perturbative effects, with parameters set according to the AZNLO tune [160]. The POWHEG prediction is accurate to next-to-leading order (NLO) and uses the PDF4LHC15NLO PDF set [159]. It was tuned to match calculations with effects due to finite heavy-quark masses and soft-gluon resummation up to NNLL. The Monte Carlo prediction was normalised to an approximate-NNLO QCD cross-section with NLO electroweak corrections [179–181]. The normalisation of all Higgs boson samples accounts for the decay branching ratio calculated with HDECAY [172–174] and PROPHECY4F [175–177].

Higgs boson production in association with a vector boson was simulated using POWHEG BOX v2 [112–114, 178] and interfaced with PYTHIA 8 [117] for parton shower and non-perturbative effects. The POWHEG prediction is accurate to next-to-leading order for VH boson plus one-jet production. The loop-induced $gg \rightarrow ZH$ process was generated separately at leading order. The PDF4LHC15NLO PDF set [159] and the AZNLO tune [160] of PYTHIA 8 [117] were used. The Monte Carlo prediction was normalised to cross-sections calculated at NNLO in QCD with NLO electroweak corrections for $q\bar{q}/qg \rightarrow VH$ and at NLO and next-to-leading-logarithm accuracy in QCD for $gg \rightarrow ZH$ [182–188]. The normalisation of all Higgs boson samples accounts for the decay branching ratio calculated with HDECAY [172–174] and PROPHECY4F [175–177].

The ggF production of the SM Higgs boson pairs, with one Higgs boson decaying into $b\bar{b}$ and the other one to $\tau^+\tau^-$ is generated with the Powheg Box v2 generator at NLO with finite top-quark mass, and using the PDF4LHC15NLO PDFset. Parton shower and hadronisation are simulated using PYTHIA 8.244 [117] with the A14 tune and the NNPDF2.3LO [119] PDF set.

The $G \rightarrow HH \rightarrow b\bar{b}\tau\tau$ signal samples are generated with the same setup as the $G \rightarrow HH \rightarrow 4\tau$ samples in the τ_{had}^μ development, detailed in Chapter 5. To enhance the statistics, the Higgs bosons in the signal $G \rightarrow HH \rightarrow b\bar{b}\tau\tau$ samples are forced to decay to a pair of b -quarks or a pair of τ -leptons, in equal branching fractions. To calculate the effective cross-sections for the $G \rightarrow HH$ production, a scale factor of

$$\frac{\text{BR}_{\text{SM}}(HH \rightarrow b\bar{b}\tau\tau)}{\text{BR}_{\text{Gen}}(HH \rightarrow b\bar{b}\tau\tau)} = \frac{0.073}{0.5} = 0.146$$

was applied to the generator reported cross-sections, where $\text{BR}_{\text{SM}}(HH \rightarrow b\bar{b}\tau\tau) = 0.073$ is the SM branching ratio of the $HH \rightarrow b\bar{b}\tau\tau$ decay, and $\text{BR}_{\text{Gen}}(HH \rightarrow b\bar{b}\tau\tau) = 0.5$ is the generator-enhanced branching ratio for the same process.

7.3 Event-selection

Table 7.2 Summary of signal region event-selection criteria. SR events pass at least one trigger listed below. A control region is defined in which events fail any one or more of the cuts marked with *, while passing every other selection. For better CR statistics, the lower bound of $m_{\tau\tau}^{\text{col}}$ and m_{bb} is relaxed to 60 GeV for CR. “fatjet” refers to the large-radius jet clustered with the anti- k_t algorithm with $R = 1.0$.

Object	Selection
Triggers	lowest un-prescaled single muon triggers lowest un-prescaled E_T^{miss} triggers
τ_{had}^μ	$0 < \eta < 1.37$ or $1.52 < \eta < 2.5$ "VeryLoose" RNN jet WP $p_T > 20 \text{ GeV}$
Removed μ	Found inside the τ_{had}^μ $p_T > 10 \text{ GeV}$ "Medium" ID WP
bb system	fatjet GN2x score > -5.0 fatjet passes "QCD1.55%" WP * $90 < m_{bb} < 160 \text{ GeV}$ $p_{T\text{bb}} > 250 \text{ GeV}$ $\Delta R_{\text{fj-jet}} < 0.03$ *
$\tau_\mu \tau_{\text{had}}$ system	Opposite sign μ and τ_{had}^μ * $m_{\tau\tau}^{\text{vis}} > 5 \text{ GeV}$ $-0.1 < \Delta\phi_{\mu-\text{MET}}^{\text{signed}} < 0.4$ $m_{\tau\tau}^{\text{col}} > 90 \text{ GeV}$ $p_{T\tau\tau}^{\text{col}} > 250 \text{ GeV}$
Event level cut	$ \Delta\phi_{\text{bb}-\tau\tau} > \pi/2$

The event-selection criteria are summarised in Table 7.2. Recorded events are required to satisfy the same triggers as the τ_{had}^μ benchmark analysis detailed in Chapter 5. The signal-region events are required to have at least one τ_{had}^μ candidate with $p_T > 20 \text{ GeV}$ and pseudorapidity satisfying $0 < |\eta| < 1.37$ or $1.52 < |\eta| < 2.5$. A “VeryLoose” RNN jet WP is applied to the τ_{had}^μ candidate. The removed muon is required to have $p_T > 10 \text{ GeV}$ and to pass the “Medium” ID WP. The fatjet is required to have a GN2x score greater than -5.0 and to pass the “QCD1.55%” GN2x WP [92]. The invariant mass of the $b\bar{b}$ system,

Table 7.3 Event yields in the SR and CR regions. The uncertainties are statistical only. The signal yields are shown with fixed cross-sections $\sigma(pp \rightarrow G \rightarrow HH) = 1 \text{ fb}$.

	SR	CR
Data	1 ± 1	219 ± 15
SM MC total	0.71 ± 0.09	205 ± 2
jets + $Z \rightarrow \tau\tau$	0.19 ± 0.05	114 ± 1
diBoson	0.11 ± 0.02	16.1 ± 0.4
Top	0.12 ± 0.03	46 ± 2
Higgs	0.12 ± 0.07	11 ± 1
Others	0.168 ± 0.005	18 ± 2
$G(2 \text{ TeV}) \rightarrow HH$	0.515 ± 0.002	0.178 ± 0.001
$G(3 \text{ TeV}) \rightarrow HH$	0.712 ± 0.002	0.173 ± 0.001
$G(4 \text{ TeV}) \rightarrow HH$	0.748 ± 0.002	0.196 ± 0.001
$G(5 \text{ TeV}) \rightarrow HH$	0.728 ± 0.002	0.218 ± 0.001

m_{bb} , is required to be between 90 and 160 GeV, and the p_T of the $b\bar{b}$ system, p_{Tbb} , is required to be greater than 250 GeV. The ΔR separation between the fatjet and the closest standard-radius jet, $\Delta R_{\text{fj-jet}}$, is required to be less than 0.03. The $\tau_\mu\tau_{\text{had}}$ system is required to consist of an oppositely charged muon and τ_{had}^μ candidate, and the visible mass of the $\tau_\mu\tau_{\text{had}}$ system, $m_{\tau\tau}^{\text{vis}}$, is required to be greater than 5 GeV. The signed angular separation in the transverse plane between the muon and the E_T^{miss} , $\Delta\phi_{\mu-\text{MET}}^{\text{signed}}$, is required to be between -0.1 and 0.4 . The invariant mass of the $\tau_\mu\tau_{\text{had}}$ system, $m_{\tau\tau}^{\text{col}}$, is required to be greater than 90 GeV, and the p_T of the $\tau_\mu\tau_{\text{had}}$ system, $p_{T\tau\tau}^{\text{col}}$, is required to be greater than 250 GeV. At the event level, the absolute angular separation in ϕ between the $b\bar{b}$ system and the $\tau_\mu\tau_{\text{had}}$ system, $|\Delta\phi_{bb-\tau\tau}|$, is required to be greater than $\pi/2$. For the CR, the lower bounds of $m_{\tau\tau}^{\text{col}}$ and m_{bb} are relaxed to 60 GeV to increase the statistics. Events that fail any one or more of the GN2x requirements, the opposite-sign muon and τ_{had}^μ requirement, or the $\Delta R_{\text{fj-jet}}$ requirement, while passing all other selections, are defined as belonging to the CR.

7.3.1 m_{bb} and $m_{\tau\tau}^{col}$ cuts optimisation

The m_{bb} and $m_{\tau\tau}^{col}$ distributions are two powerful discriminants for the $G \rightarrow HH$ signal. To maximise the sensitivity of the analysis, the cut values on the m_{bb} and $m_{\tau\tau}^{col}$ distributions are determined at pre-selection level. All other event-selection criteria are applied except for the m_{bb} and $m_{\tau\tau}^{col}$ cuts during the optimisation. The signal and background efficiencies and the significance (Z) for different cut values on the m_{bb} and $m_{\tau\tau}^{col}$ distributions are shown in Figure 7.3. Due to the low number of expected events, the p-value is calculated using an interpolated Poisson cumulative distribution function (CDF). Then, Z is derived from the p-value using $Z = \Phi^{-1}(1 - p)$, where Φ is the CDF of the standard normal distribution. The optimal cut values are chosen to maintain high signal efficiencies and high significance. The values of the optimal cuts are chosen to be looser than the values that maximise Z , as m_{bb} and $m_{\tau\tau}^{col}$ are not the most powerful discriminants for the $G \rightarrow HH$ signal. The $m_{bb\tau\tau}^{col}$ distribution provides better separation between the signal and background, especially for the high-mass signals.

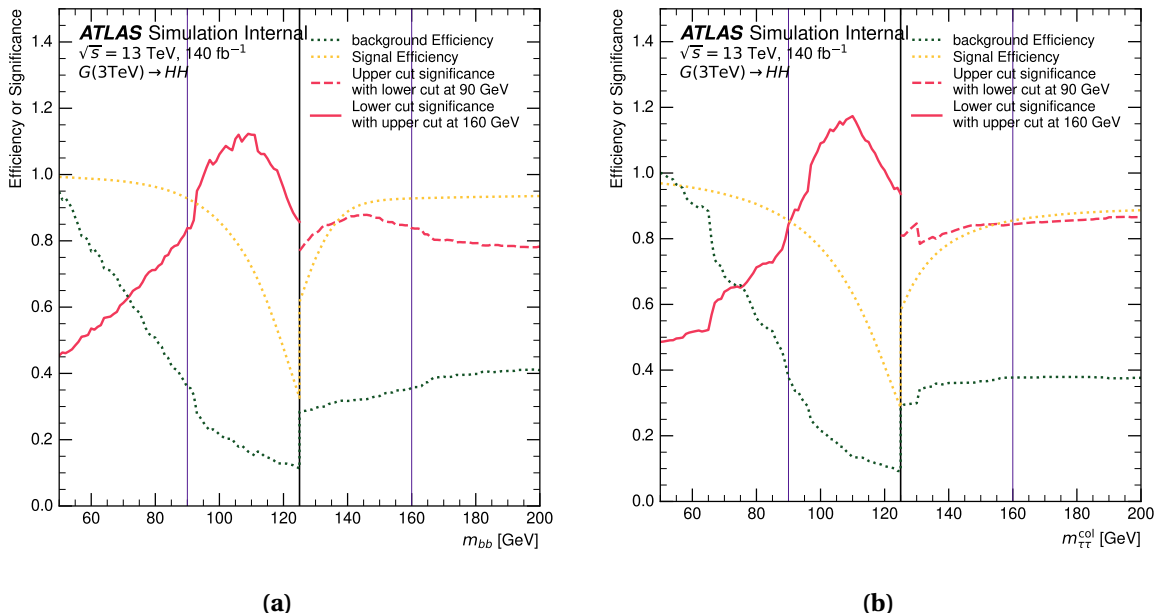


Fig. 7.3 The G 3 TeV signal efficiency, background efficiency, and the significance for different cut values on the m_{bb} (a), and $m_{\tau\tau}^{col}$ (b) distributions.

7.4 Results

Figures 7.4 to 7.14 show the distributions of various variables in the SR and CR. “ $Z \rightarrow \tau\tau + \text{jets}$ ” refers to the contributions of the $Z \rightarrow \tau\tau + \text{jets}$ processes. “Top” refers to the contributions of the SM top quark processes, including $t\bar{t}$ and single top. “VV/VH/HH” refers to the contributions of the SM diboson, VH , and HH processes. “Higgs” refers to the contributions of the SM Higgs boson processes, including ggF and VBF productions. “Other” refers to the contributions of the remaining SM processes, including $W + \text{jets}$ and $Z \rightarrow ll + \text{jets}$. The signal processes shown in these plots are normalised to the expected 95% confidence level (CL) limits of the $\sigma(pp \rightarrow G \rightarrow HH)$. For variables used in the event-selection, these plots display the distributions after all other event-selections have been applied, except for the variable itself. The event yields in the SR and CR regions are presented in Table 7.3. Good agreement between data and MC simulation is observed in the CR, indicating that the MC prediction is reliable in this region. It also suggests negligible QCD background contamination in both the CR and SR. Figure 7.4 shows the distribution of $|\Delta\phi_{bb-\tau\tau}|$ between the two b -jets and the two τ -leptons. Figure 7.5 displays the distribution of the $\Delta\phi_{\mu-\text{MET}}^{\text{signed}}$ variable. The sign of $\Delta\phi_{\mu-\text{MET}}^{\text{signed}}$ is defined to be positive if the E_T^{miss} is on the same side as the τ_had^μ candidate, and negative otherwise. Figure 7.6 illustrates the $\Delta R_{\text{fj-jet}}$ distributions. This variable is utilised to reject events exhibiting significant activity in the periphery of the fatjet, which often indicates the presence of gluon-induced heavy-flavour jets. Figure 7.7 shows the distribution of the GN2x_{fj} variable, which is the output of the GN2x tagger. The WP chosen for this analysis is the “QCD1.55%” WP, corresponding to a signal efficiency of 85%. Figures 7.8 and 7.9 present the distributions of m_{bb} and p_{Tbb} of the two b -jets derived from the fatjet. Figures 7.10 and 7.11 show the distributions of $m_{\tau\tau}^{\text{col}}$ and $p_{T\tau\tau}^{\text{col}}$ of the two τ -leptons reconstructed with the collinear approximation [136, 152], incorporating the E_T^{miss} . The p_{Tbb} and $p_{T\tau\tau}^{\text{col}}$ of Standard Model (SM) backgrounds fall sharply with increasing p_T , while the signal

processes peak at $\frac{1}{2}m_G$. The signal m_{bb} and $m_{\tau\tau}^{\text{col}}$ distributions exhibit a clear peak at m_H . SM “VV/VH/HH” processes show broad distributions in the m_{bb} and $m_{\tau\tau}^{\text{col}}$ spectra from m_Z to m_H . The contribution from top quark processes is clearly visible in the m_{bb} around 175 GeV. A clear peak at m_Z is observed in the $m_{\tau\tau}^{\text{col}}$ distribution from the $Z \rightarrow \tau\tau + \text{jets}$ processes, indicating that the $Z + \text{heavy flavour jets}$ processes are well modelled in the high- p_T region. Other SM processes display falling distributions in the m_{bb} and $m_{\tau\tau}^{\text{col}}$ spectra. Figure 7.12 shows the distribution of the $m_{bb\tau\tau}^{\text{col}}$ variable, which is the invariant mass of the $b\bar{b}$ system and the two τ -leptons. This variable reconstructs the di-Higgs mass in the signal process. Non-resonant SM processes exhibit falling distributions in the $m_{bb\tau\tau}^{\text{col}}$ spectra, while the signal processes show a clear peak at m_G . The lower tails of the $m_{bb\tau\tau}^{\text{col}}$ distributions from high-mass signals indicate poor detector resolution in the high-mass region. Figure 7.13 presents the distribution of the p_T of the muon found inside the τ_{had}^μ (p_T^μ). Figure 7.14 displays the distribution of the TauID jet RNN score (RNN_τ) of the τ_{had}^μ candidate. Figure 7.15 shows the distribution of the product of the $\tau_\mu\tau_{\text{had}}$ charges.

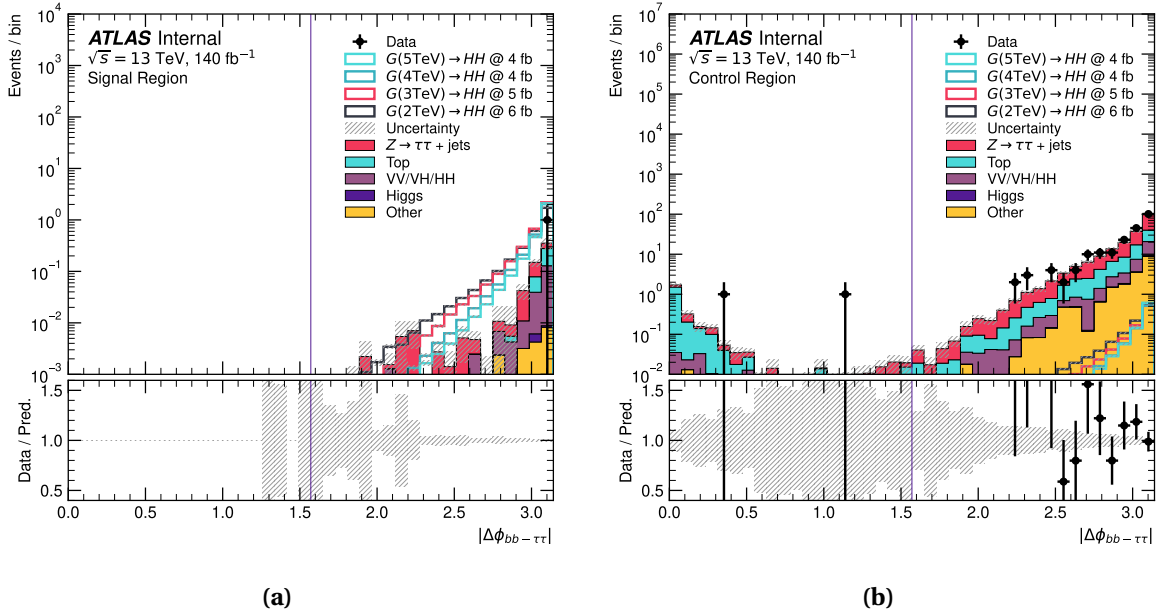


Fig. 7.4 The distribution of the $|\Delta\phi_{bb-\tau\tau}|$ in the SR (a), and CR (b).

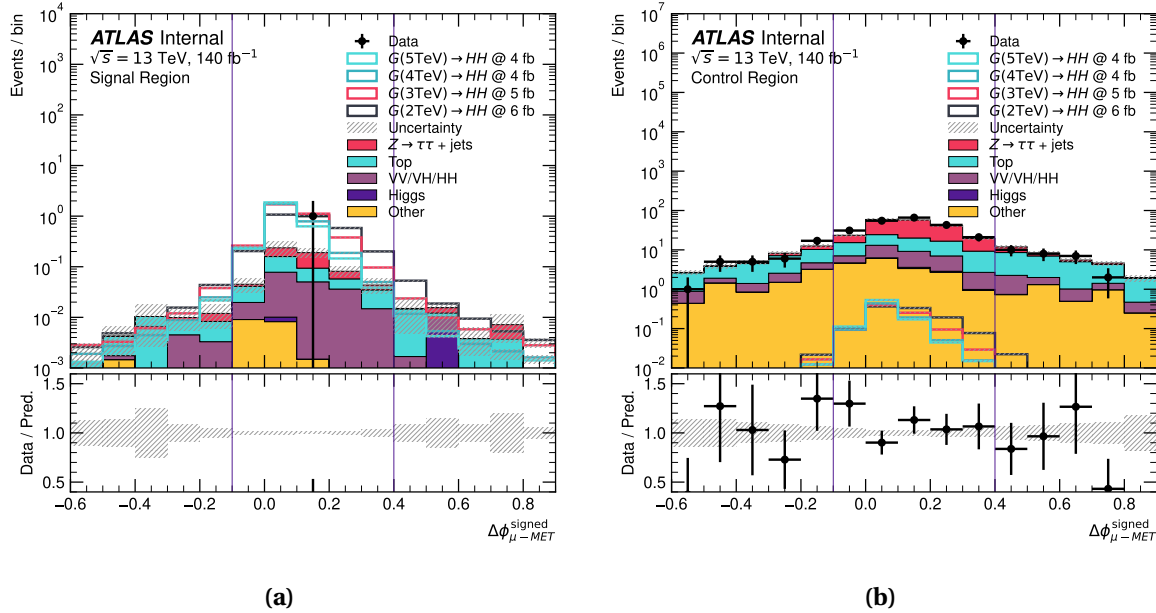


Fig. 7.5 The distribution of the $\Delta\phi_{\mu-\text{MET}}^{\text{signed}}$ in the SR (a), and CR (b).

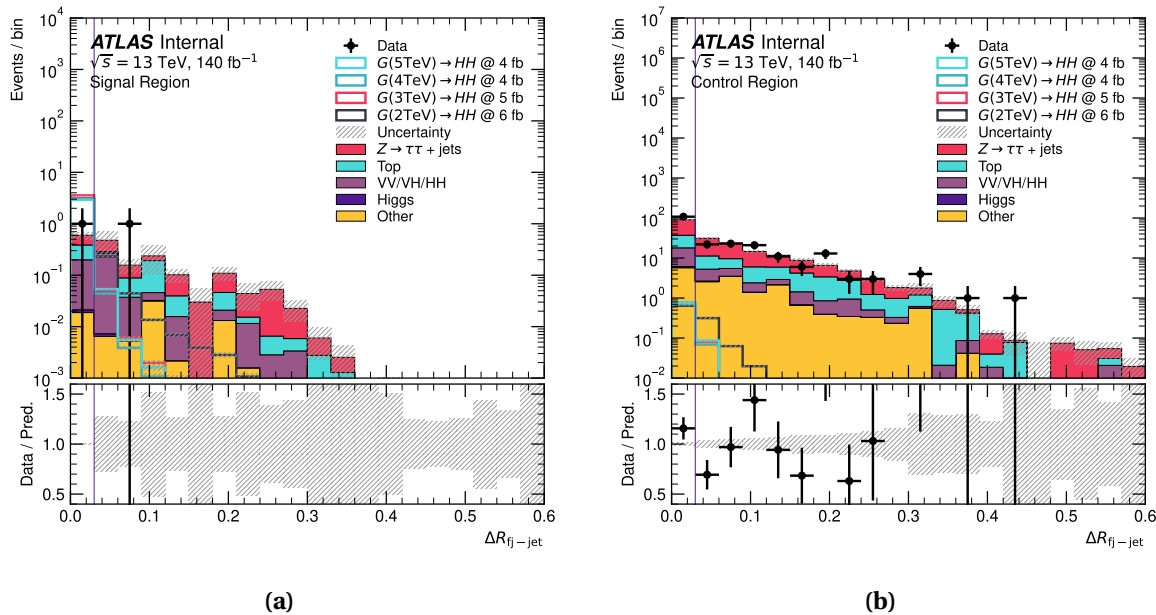


Fig. 7.6 The distribution of the $\Delta R_{fj-\text{jet}}$ in the SR (a), and CR (b).

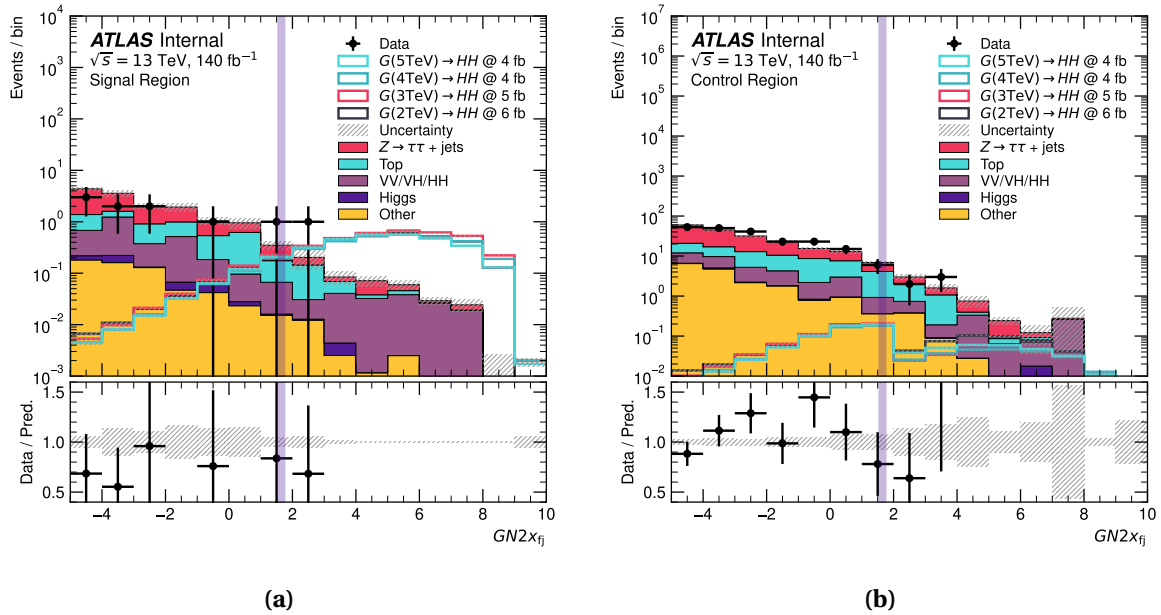


Fig. 7.7 The distribution of the $GN2x_{fj}$ in the SR (a), and CR (b). The translucent band indicates the cut value of “QCD1.55%” $GN2x$ WP, ranging from 1.6 to 1.7 in the region where the fatjet mass is between 90 and 160 GeV.

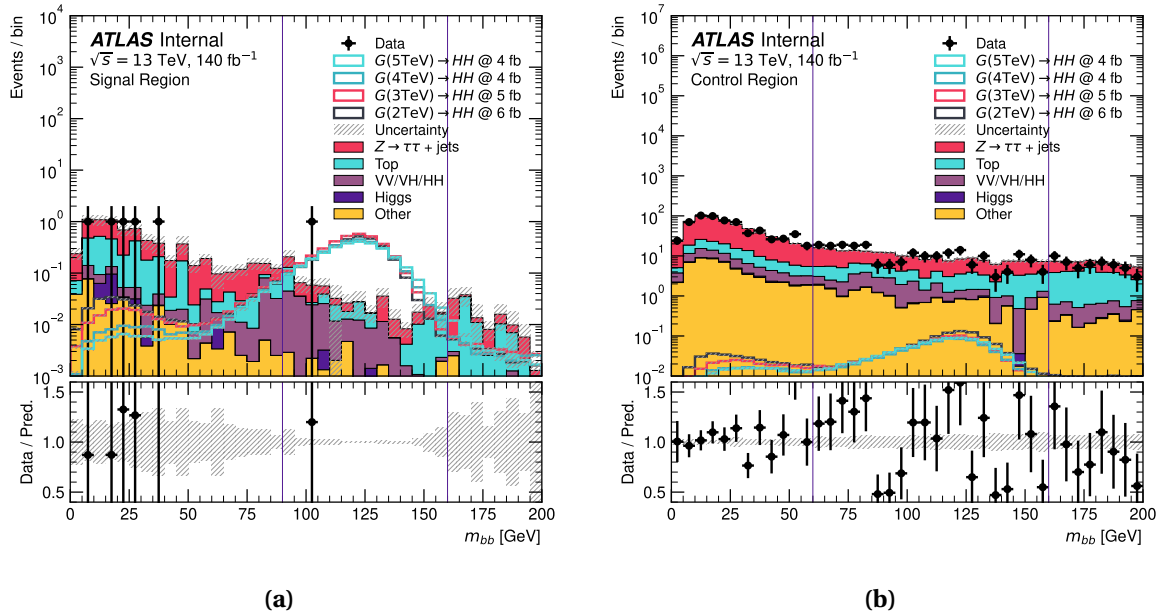


Fig. 7.8 The distribution of the m_{bb} in the SR (a), and CR (b).

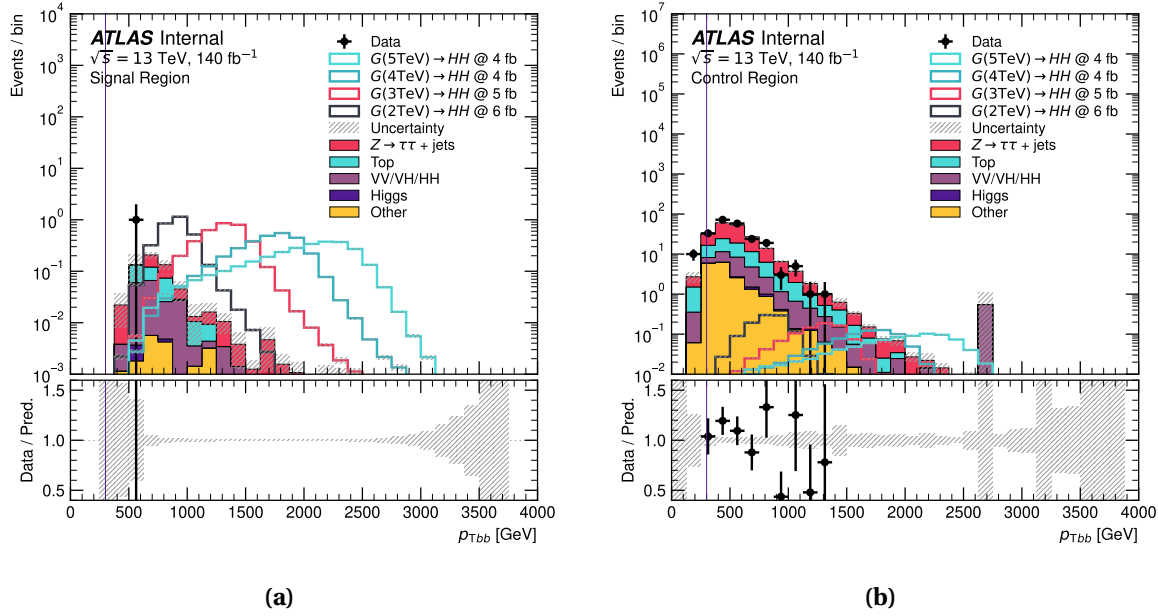


Fig. 7.9 The distribution of the p_{Tbb} in the SR (a), and CR (b). The p_{Tbb} distribution extends to lower values in the CR than in the SR due to the relaxed $m_{\tau\tau}^{col}$ and m_{bb} requirements. This is because lower values of $m_{\tau\tau}^{col}$ and m_{bb} in the CR allow di- τ and $b\bar{b}$ systems at lower p_T to be produced whilst still satisfying the condition $\Delta R < 0.4$.

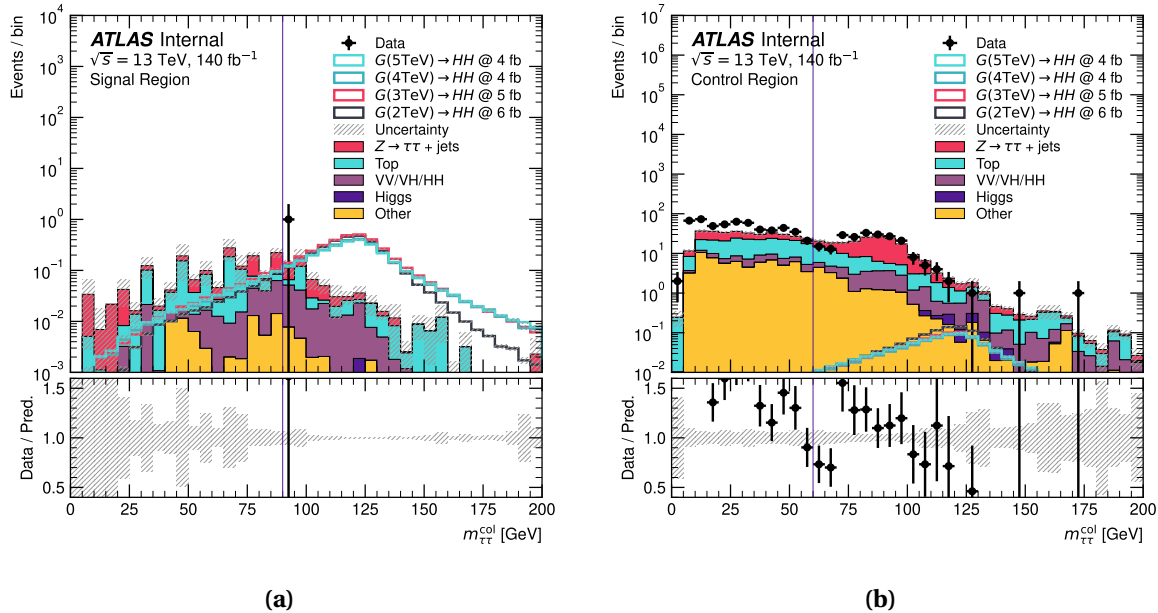


Fig. 7.10 The distribution of the $m_{\tau\tau}^{col}$ in the SR (a), and CR (b).

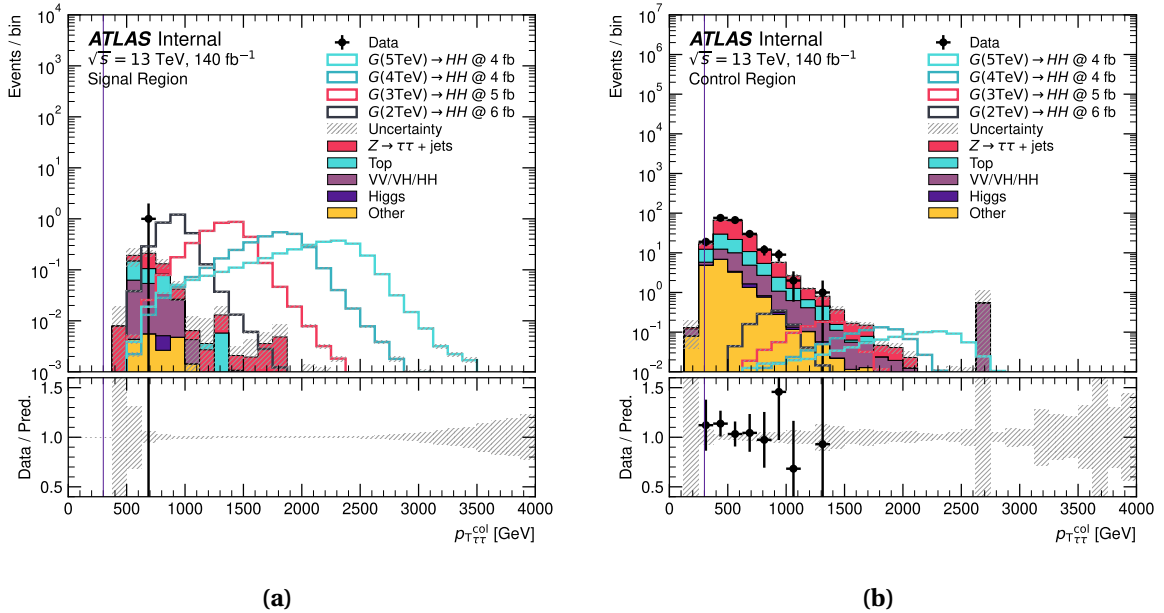


Fig. 7.11 The distribution of the $p_{T\tau\tau}^{\text{col}}$ in the SR (a), and CR (b). The $p_{T\tau\tau}^{\text{col}}$ distribution extends to lower values in the CR than in the SR due to the relaxed $m_{\tau\tau}^{\text{col}}$ and m_{bb} requirements. This is because lower values of $m_{\tau\tau}^{\text{col}}$ and m_{bb} in the CR allow di- τ and $b\bar{b}$ systems at lower p_T to be produced whilst still satisfying the condition $\Delta R < 0.4$.

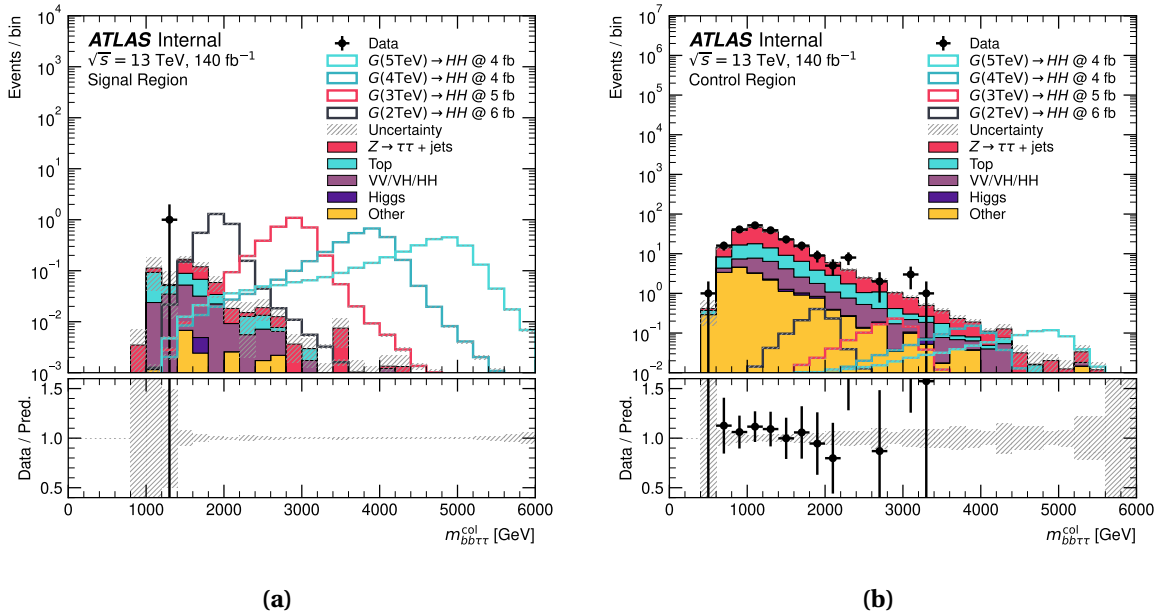


Fig. 7.12 The distribution of the $m_{bb\tau\tau}^{\text{col}}$ in the SR (a), and CR (b). The $m_{bb\tau\tau}^{\text{col}}$ distribution extends to lower values in the CR than in the SR due to the relaxed $m_{\tau\tau}^{\text{col}}$ and m_{bb} requirements. This is because lower values of $m_{\tau\tau}^{\text{col}}$ and m_{bb} in the CR allow di- τ and $b\bar{b}$ systems at lower p_T to be produced whilst still satisfying the condition $\Delta R < 0.4$.

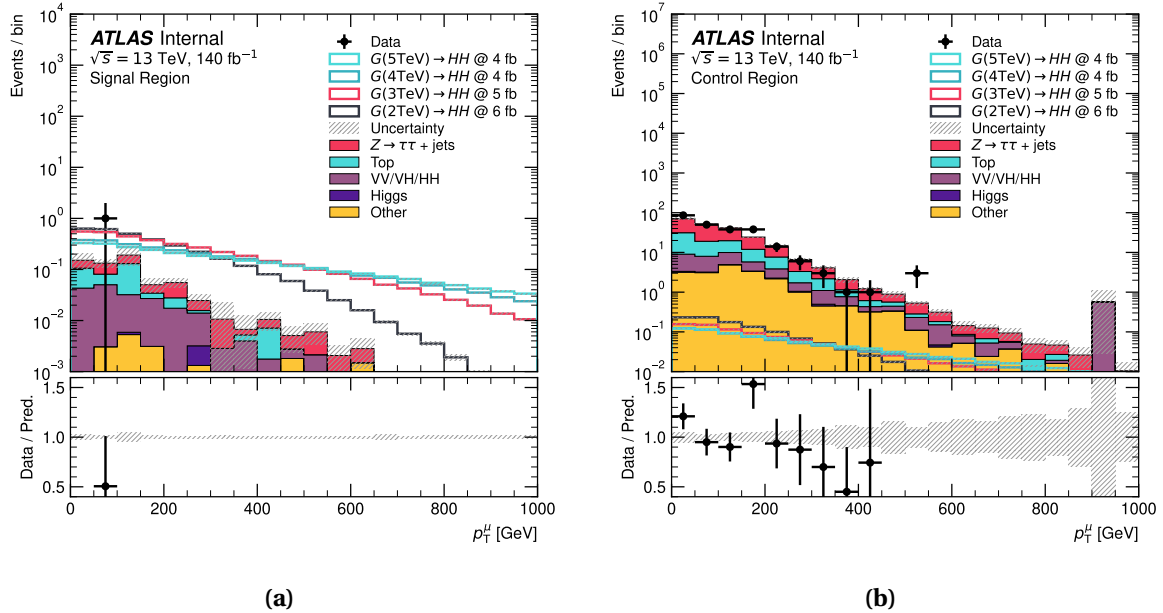


Fig. 7.13 The distribution of the p_T^μ in the SR (a), and CR (b).

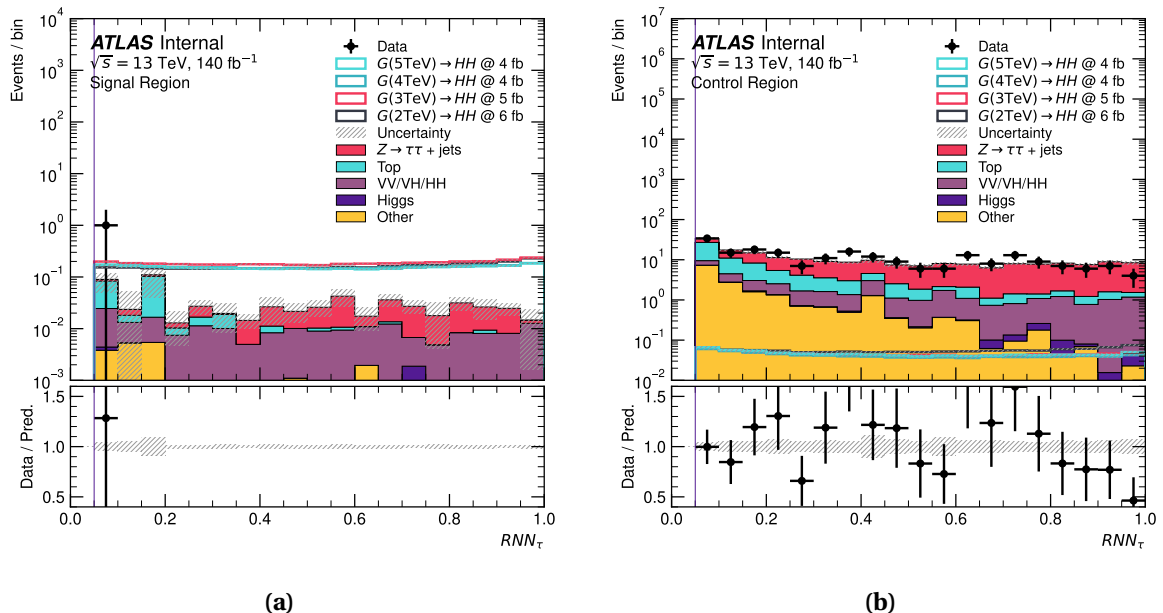


Fig. 7.14 The distribution of the RNN_τ in the SR (a), and CR (b).

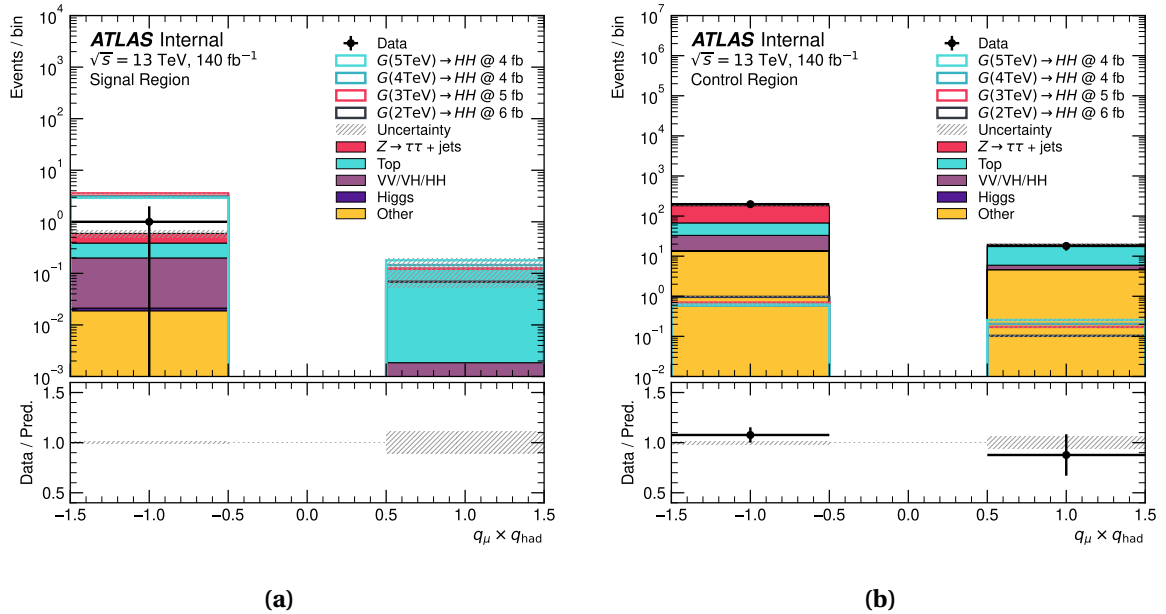


Fig. 7.15 The distribution of the product of the $\tau\tau$ charges in the SR (a), and CR (b).

7.5 Systematic uncertainties

As a conservative estimation, the following systematic uncertainties are considered:

- Jet energy scale and resolution, tau energy scale and resolution, E_T^{miss} and other experimental uncertainties (20%): These uncertainties can shift the reconstructed $m_{bb\tau\tau}^{\text{col}}$ spectrum by altering the measured energies and momenta of jets, τ leptons, and the missing transverse energy. A 20% overall uncertainty is used here as a placeholder, guided by typical variations observed in similar analyses at this stage of development. In a more detailed study, each of these sources would be evaluated separately through systematic variations of calibration constants, comparison to data-driven control samples, and application of smearing and scaling factors, then combined into a total systematic uncertainty following standard procedures.
- Theoretical uncertainties in the background cross sections, luminosity, and other parameters (50%): The theoretical cross section calculations for background processes come with an intrinsic uncertainty, which can be further affected by PDF

variations, scale variations, and higher-order corrections. We also include here uncertainties on the integrated luminosity measurement. In this preliminary search, we assign a large 50% systematic uncertainty to cover these effects conservatively. As the analysis matures, these uncertainties would typically be reduced using more accurate theoretical predictions and improved luminosity calibrations.

- Theoretical uncertainties in the signal modelling, GN2x identification efficiency ($^{+15\%}_{-20\%}$), τ_{had}^μ reconstruction and identification efficiency (12%), and other parameters (20%): For the signal process, uncertainties arise from theoretical cross section calculations and parton shower modeling, which affect the predicted event rates and kinematics. Additional uncertainties stem from experimental efficiencies—for instance, the GN2x x_{bb} tagger performance and the τ_{had}^μ reconstruction and identification efficiency. Although each of these sources could in principle be evaluated separately through specialized studies (using tag-and-probe methods or dedicated control regions), we have here grouped them into a single combined uncertainty. We assign a conservative 20% overall normalization uncertainty to account for possible deviations in the modeling and reconstruction, while specifically quoting the GN2x identification efficiency uncertainty as $^{+15\%}_{-20\%}$ and the τ -ID uncertainty as 12%. In the future, once the GN2x tagger calibration is fully validated, these uncertainties can be refined and broken down more precisely.

The final SM background yield in the signal region (SR) is 0.7 ± 0.1 (stat.) ± 0.3 (syst.). Again, these systematic uncertainties are intentionally chosen to be conservative “placeholder” values. Our preliminary investigations indicate that the largest systematic uncertainty will come from the new GN2x x_{bb} tagger, which is still under development and not yet fully calibrated. Once its performance is characterised in more detail, we expect to revisit and refine the individual systematic sources—jet and tau energy scales, cross-section normalizations, tagger efficiencies, etc. using the standard suite of techniques. At that

point, each source of uncertainty can be quantified more rigorously, substantially reducing the overall uncertainty on both the background prediction and the signal acceptance.

7.6 Interpretation

A statistical model is used to interpret the results, performing a binned likelihood fit to the data. The likelihood model is constructed with the `pyhf` package [189]. Given the low number of events in the signal-region, the asymptotic approximation in the likelihood model is not reliable. Instead, the five-bin SR $m_{bb\tau\tau}^{\text{col}}$ histogram is used as the probability density function (PDF) for the signal and background. Using this PDF, we generate 10000 toy-based experiments with and without signal contributions to estimate the empirical CL_{s+b} and CL_b [190] distributions, respectively. From these distributions, the expected 95% CL limits on $\sigma(pp \rightarrow G \rightarrow HH)$ are calculated based on the 95th percentile of the empirical CL_s distribution. The limits obtained using the asymptotic approximation are included to illustrate the disagreement between the two methods in the low-statistics regime. The expected 95% CL limits on $\sigma(pp \rightarrow G \rightarrow HH)$ at various mass points are shown in Figure 7.16. The expected limits are shown as the dotted black line. The $\pm 1\sigma$ and $\pm 2\sigma$ bands are depicted as shaded regions around the expected limits. The black solid lines show the observed limits. The expected and observed upper limits, as well as the predicted cross-sections, are presented in Table 7.4.

Table 7.4 The expected and observed 95% CL limits on the $\sigma(G \rightarrow HH)$ on various mass points.

Mass [GeV]	-2σ [fb]	-1σ [fb]	Exp. [fb]	$+1\sigma$ [fb]	$+2\sigma$ [fb]	Observed [fb]
2000	4.6	5.5	6.1	8.9	13.2	5.8
3000	3.0	4.3	4.5	4.9	6.8	4.0
4000	3.5	3.7	4.0	4.7	6.1	3.8
5000	3.2	3.6	4.0	4.9	6.0	4.0

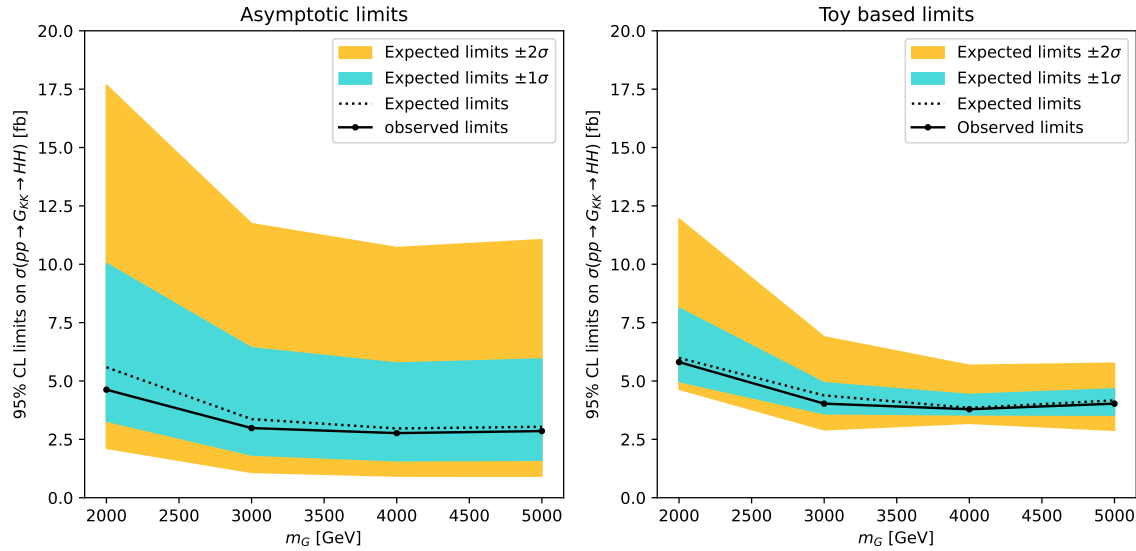


Fig. 7.16 The expected 95% CL limits on the $\sigma(pp \rightarrow G \rightarrow HH)$ on various mass points. The expected limits are shown as the dotted line. The $\pm 1\sigma$ and $\pm 2\sigma$ bands are shown as the shaded regions around the expected limits. The marked solid lines show the observed limits.

7.7 Conclusion

In this analysis, we have conducted an investigation into the $G \rightarrow HH \rightarrow b\bar{b}\tau\tau$ process using the full ATLAS Run-2 dataset, collected at $\sqrt{s} = 13$ TeV with an integrated luminosity of 140 fb^{-1} . The search benefits from advancements in the ATLAS Combined Performance, particularly the GNN-based $b\bar{b}$ -jet tagging algorithm and the muon-removal technique for τ_{had} identification. The event-selection was optimised to enhance signal sensitivity while maintaining a near zero background level.

Our results demonstrate good agreement between the data and the MC simulations in the CR, indicating negligible QCD background contamination in the SR. Statistical and systematic uncertainties were evaluated and incorporated into the final upper limits.

The 95% CL limits on $\sigma(pp \rightarrow G \rightarrow HH)$ are derived for mass points ranging from 2 to 5 TeV. Notably, the limits from this search are more than ten times better than the previous ATLAS search in the $b\bar{b}\tau\tau$ channel. For instance, at a resonance mass of 3000 GeV, we obtained a limit of 3.8 fb, compared to the previous limit of approximately 55 fb in the

$HH \rightarrow b\bar{b}\tau_{\text{had}}\tau_{\text{had}}$ channel. However, our limits are less stringent than those obtained in the $b\bar{b}b\bar{b}$ channel, primarily due to the lower branching ratio of the $HH \rightarrow b\bar{b}\tau_{\mu}\tau_{\text{had}}$ process. With the two lepton removal reconstruction methods, boosted di-tau systems can now be reconstructed for all three channels — $\tau_{\mu}\tau_{\text{had}}$, $\tau_e\tau_{\text{had}}$ and $\tau_{\text{had}}\tau_{\text{had}}$. These algorithm advancements could position ATLAS to approach the 1 fb limits set by the $HH \rightarrow b\bar{b}b\bar{b}$ channel with all three sub-channels, especially considering the significantly lower background in the $HH \rightarrow b\bar{b}\tau\tau$ final state.

Chapter 8

Conclusion

In this thesis, we have explored multiple facets of tau lepton reconstruction and identification within the ATLAS detector framework, as well as conducted a detailed search for the Graviton in the $bb\tau\tau$ decay channel.

The muon-removal method developed for the boosted $\tau_\mu\tau_{\text{had}}$ reconstruction has demonstrated significant improvements in the identification efficiency of hadronically decaying taus in the presence of a nearby muon. This method recovers the τ_{had} identification efficiency to levels expected for isolated τ_{had} decays across all TauID working points, ensuring that the measurement precision for the kinematic properties of the visible τ_{had} system is maintained. This advancement was validated through benchmarking with a highly boosted $Z \rightarrow \tau_\mu\tau_{\text{had}}$ sample from the complete Run-2 dataset recorded by the ATLAS detector. The results showed good agreement between data and Monte Carlo simulations, highlighting the robustness of the method.

The electron-removal method for boosted $\tau_e\tau_{\text{had}}$ reconstruction similarly displayed significant improvements. This method accurately reconstructs the visible decay products within a single τ_{seed} jet, addressing challenges posed by the presence of nearby electrons. This advancement enhances the signal yield, and in the mean time suppresses

the background contamination. The method's effectiveness was benchmarked using the $Z \rightarrow \tau_e \tau_{\text{had}}$ channel.

In our search for the Graviton in the $bb\tau\tau$ channel, we utilised the full ATLAS Run-2 dataset, collected at $\sqrt{s} = 13$ TeV with an integrated luminosity of 140 fb^{-1} . This search benefited from the advancements in ATLAS combined performance, particularly the GNN-based bb -jet tagging algorithm and the muon-removal technique for τ_{had} identification. Our results showed good agreement between data and Monte Carlo simulations in the control region, indicating negligible QCD background contamination in the signal region. Statistical and systematic uncertainties were evaluated and incorporated into the upper limits.

The expected 95% confidence level (CL) upper limits on the $\sigma(pp \rightarrow G \rightarrow HH)$ were derived for mass points ranging from 2 to 5 TeV. The limits obtained from this analysis significantly outperformed previous ATLAS searches in the $bb\tau\tau$ channel. For instance, at a resonance mass of 3000 GeV, we achieved a limit of 3.8 fb , compared to the previous limit of approximately 55 fb in the $HH \rightarrow b\bar{b}\tau_{\text{had}}\tau_{\text{had}}$ channel. Despite the 20-times lower $HH \rightarrow b\bar{b}\tau_{\mu}\tau_{\text{had}}$ branching ratio, our limits were only 5-times less stringent than those obtained in the $HH \rightarrow b\bar{b}b\bar{b}$ channel. This highlights the performance of the muon-removal technique in the τ_{had} identification, and the success of this analysis in suppressing the SM background contamination.

In conclusion, the advancements in tau lepton reconstruction presented in this thesis open up a new final state in the search for new physics phenomena. The results of the Graviton search in the $bb\tau\tau$ channel demonstrate the potential of these advancements to significantly enhance the discovery potential of the ATLAS experiment in the highly boosted di- τ channel.

References

- [1] R. L. Workman et al., *Review of particle physics*, PTEP **2022** (2022) 083C01 (cit. on pp. 1, 5, 37).
- [2] M. K. Gaillard, P. D. Grannis and F. J. Sciulli, *The standard model of particle physics*, Rev. Mod. Phys. **71** (2 1999) S96 (cit. on pp. 1, 5).
- [3] L. Evans and P. Bryant, *LHC Machine*, JINST **3** (2008) S08001 (cit. on pp. 1, 35, 93).
- [4] S. Carlip, D.-W. Chiou, W.-T. Ni and R. Woodard, *Quantum gravity: A brief history of ideas and some prospects*, International Journal of Modern Physics D **24** (2015) 1530028, ISSN: 1793-6594, URL: <http://dx.doi.org/10.1142/S0218271815300281> (cit. on p. 2).
- [5] L. Randall and R. Sundrum, *Large mass hierarchy from a small extra dimension*, Phys. Rev. Lett. **83** (1999) 3370 (cit. on pp. 5, 26, 92).
- [6] A. L. Fitzpatrick, J. Kaplan, L. Randall and L.-T. Wang, *Searching for the Kaluza-Klein graviton in bulk RS models*, JHEP **09** (2007) 013, arXiv: [hep-ph/0701150](https://arxiv.org/abs/hep-ph/0701150) (cit. on p. 5).
- [7] H. Davoudiasl and T. G. Rizzo, *Bulk physics at a graviton factory*, Physics Letters B **512** (2001) 100, ISSN: 0370-2693, URL: [http://dx.doi.org/10.1016/S0370-2693\(01\)00704-3](http://dx.doi.org/10.1016/S0370-2693(01)00704-3) (cit. on p. 5).
- [8] *A new map of all the particles and forces*, 2020, URL: <https://www.quantamagazine.org/a-new-map-of-the-standard-model-of-particle-physics-20201022/> (cit. on p. 7).
- [9] ATLAS Collaboration, *Determination of the strong coupling constant from transverse energy-energy correlations in multijet events at $\sqrt{s} = 13$ TeV with the ATLAS detector*, JHEP **07** (2023) 085, arXiv: [2301.09351 \[hep-ex\]](https://arxiv.org/abs/2301.09351) (cit. on p. 18).
- [10] L. Nanni, *Fermi's theory of beta decay: a first attempt at electroweak unification*, Advanced Studies in Theoretical Physics **13** (2019) 281, ISSN: 1313-1311, URL: <http://dx.doi.org/10.12988/astp.2019.8939> (cit. on p. 18).
- [11] J. Goldstone, A. Salam and S. Weinberg, *Broken Symmetries*, Phys. Rev. **127** (3 1962) 965, URL: <https://link.aps.org/doi/10.1103/PhysRev.127.965> (cit. on p. 18).
- [12] L. Di Lella and C. Rubbia, *The Discovery of the W and Z Particles*, Adv. Ser. Direct. High Energy Phys. **23** (2015) 137 (cit. on p. 18).

- [13] C. S. Wu, E. Ambler, R. W. Hayward, D. D. Hoppes and R. P. Hudson, *Experimental Test of Parity Conservation in Beta Decay*, *Phys. Rev.* **105** (4 1957) 1413, URL: <https://link.aps.org/doi/10.1103/PhysRev.105.1413> (cit. on p. 20).
- [14] N. Arkani-Hamed, S. Dimopoulos and G. Dvali, *The hierarchy problem and new dimensions at a millimeter*, *Physics Letters B* **429** (1998) 263, ISSN: 0370-2693, URL: [http://dx.doi.org/10.1016/S0370-2693\(98\)00466-3](http://dx.doi.org/10.1016/S0370-2693(98)00466-3) (cit. on pp. 26, 27).
- [15] J. Overduin and P. Wesson, *Kaluza-Klein gravity*, *Physics Reports* **283** (1997) 303, ISSN: 0370-1573, URL: [http://dx.doi.org/10.1016/S0370-1573\(96\)00046-4](http://dx.doi.org/10.1016/S0370-1573(96)00046-4) (cit. on p. 26).
- [16] *Exploring new physics*, 2020, URL: <https://w3.lnf.infn.it/research/theoretical-physics/enp> (visited on 28/04/2020) (cit. on p. 29).
- [17] NNPDF Collaboration, *The path to proton structure at one-percent accuracy*, *The European Physical Journal C* **82** (2022), ISSN: 1434-6052 (cit. on p. 31).
- [18] NNPDF Collaboration, *Photons in the proton: implications for the LHC*, (2024), arXiv: [2401.08749 \[hep-ph\]](https://arxiv.org/abs/2401.08749) (cit. on p. 31).
- [19] NNPDF Collaboration, *The path to N^3 LO parton distributions*, (2024), arXiv: [2402.18635 \[hep-ph\]](https://arxiv.org/abs/2402.18635) (cit. on p. 31).
- [20] NNPDF Collaboration, *Evidence for intrinsic charm quarks in the proton*, *Nature* **608** (2022) 483, ISSN: 1476-4687 (cit. on p. 32).
- [21] *CERN's accelerator complex*, 2022, URL: <https://home.cern/science/accelerators/accelerator-complex> (cit. on p. 34).
- [22] *Synchro-Cyclotron division, SC: divisional reports - 1952*, (), URL: <https://cds.cern.ch/record/1606751> (cit. on p. 33).
- [23] J. B. Adams, *The CERN proton synchrotron*, *Nature* **185** (1960) 568, ISSN: 1476-4687, URL: <https://doi.org/10.1038/185568a0> (cit. on p. 33).
- [24] N. Doble, L. Gatignon, K. Hübner and E. Wilson, *The Super Proton Synchrotron (SPS): a tale of two lives*, *Adv. Ser. Direct. High Energy Phys.* **27** (2017) 135, URL: <https://cds.cern.ch/record/2312568> (cit. on p. 33).
- [25] H. Schopper, *LEP: The lord of the collider rings at CERN 1980-2000: The making, operation and legacy of the world's largest scientific instrument*, 2009, ISBN: 978-3-540-89300-4 (cit. on p. 34).
- [26] J. Alcaraz et al., *Precision electroweak measurements and constraints on the Standard Model*, (2007), arXiv: [0712.0929 \[hep-ex\]](https://arxiv.org/abs/0712.0929) (cit. on p. 34).
- [27] ATLAS Collaboration, *The ATLAS Experiment at the CERN Large Hadron Collider*, *JINST* **3** (2008) S08003 (cit. on pp. 35, 40).
- [28] CMS Collaboration, *The CMS Experiment at the CERN LHC*, *JINST* **3** (2008) S08004 (cit. on p. 35).

- [29] LHCb Collaboration, *The LHCb detector at the LHC*, JINST **3** (2008) S08005 (cit. on p. 35).
- [30] ALICE Collaboration, *The ALICE experiment at the CERN LHC*, JINST **3** (2008) S08002 (cit. on p. 35).
- [31] TOTEM Collaboration, *The TOTEM experiment at the CERN Large Hadron Collider*, Journal of Instrumentation **3** (2008) S08007, URL: <https://dx.doi.org/10.1088/1748-0221/3/08/S08007> (cit. on p. 35).
- [32] ATLAS Collaboration, *Observation of a new particle in the search for the Standard Model Higgs boson with the ATLAS detector at the LHC*, Phys. Lett. B **716** (2012) 1, arXiv: [1207.7214 \[hep-ex\]](https://arxiv.org/abs/1207.7214) (cit. on p. 36).
- [33] CMS Collaboration, *Observation of a new boson at a mass of 125 GeV with the CMS experiment at the LHC*, Phys. Lett. B **716** (2012) 30, arXiv: [1207.7235 \[hep-ex\]](https://arxiv.org/abs/1207.7235) (cit. on p. 36).
- [34] G. Arduini et al., *LHC Upgrades in preparation of Run 3*, Journal of Instrumentation **19** (2024) P05061, URL: <https://dx.doi.org/10.1088/1748-0221/19/05/P05061> (cit. on p. 37).
- [35] A.-L. Perrot et al., *The second long shutdown of the LHC and its injectors: feedback from the accelerator coordination and engineering group*, JACoW IPAC **2022** (2022) 2052, URL: <https://cds.cern.ch/record/2845779> (cit. on p. 38).
- [36] A. Brodeur, D. Gray, A. Islam and S. Bhuiyan, *A literature review of the economics of COVID-19*, Journal of Economic Surveys **35** (2021) 1007, eprint: <https://onlinelibrary.wiley.com/doi/pdf/10.1111/joes.12423> (cit. on p. 38).
- [37] G. Apollinari, O. Brüning, T. Nakamoto and L. Rossi, *High Luminosity Large Hadron Collider HL-LHC*, en, 2015, URL: <https://cds.cern.ch/record/2120673> (cit. on p. 38).
- [38] M. Benedikt, A. Blondel, P. Janot, M. Mangano and F. Zimmermann, *Future Circular Colliders succeeding the LHC*, Nature Physics **16** (2020) 402, ISSN: 1745-2481, URL: <https://doi.org/10.1038/s41567-020-0856-2> (cit. on p. 39).
- [39] ATLAS Collaboration, *The ATLAS Experiment at the CERN Large Hadron Collider: A Description of the Detector Configuration for Run 3*, (2023), arXiv: [2305.16623 \[physics.ins-det\]](https://arxiv.org/abs/2305.16623) (cit. on pp. 41, 44, 47, 49, 52, 55).
- [40] ATLAS Collaboration, *ATLAS: Letter of Intent for a General-Purpose pp Experiment at the Large Hadron Collider at CERN*, CERN-LHCC-92-004; LHCC-I-2, 1992, URL: <https://cds.cern.ch/record/291061> (cit. on p. 40).
- [41] ATLAS Collaboration, *ATLAS: Technical Proposal for a General-Purpose pp Experiment at the Large Hadron Collider at CERN*, CERN-LHCC-94-043; LHCC-P-2, 1994, URL: <https://cds.cern.ch/record/290968> (cit. on p. 40).
- [42] ATLAS Collaboration, *Measurement of the centrality dependence of the charged particle pseudorapidity distribution in lead–lead collisions at $\sqrt{s_{NN}} = 2.76$ TeV with the ATLAS detector*, Phys. Lett. B **710** (2012) 363, arXiv: [1108.6027 \[hep-ex\]](https://arxiv.org/abs/1108.6027) (cit. on p. 42).

- [43] ATLAS Collaboration, *ATLAS New Small Wheel: Technical Design Report*, ATLAS-TDR-020; CERN-LHCC-2013-006, 2013,
URL: <https://cds.cern.ch/record/1552862> (cit. on pp. 42, 50).
- [44] ATLAS Collaboration, *ATLAS Liquid Argon Calorimeter Phase-I Upgrade: Technical Design Report*, ATLAS-TDR-022; CERN-LHCC-2013-017, 2013,
URL: <https://cds.cern.ch/record/1602230> (cit. on pp. 42, 48).
- [45] ATLAS Collaboration, *ATLAS TDAQ System Phase-I Upgrade: Technical Design Report*, ATLAS-TDR-023; CERN-LHCC-2013-018, 2013,
URL: <https://cds.cern.ch/record/1602235> (cit. on pp. 42, 56).
- [46] ATLAS Collaboration, *ATLAS Forward Proton Phase-I Upgrade: Technical Design Report*, ATLAS-TDR-024; CERN-LHCC-2015-009, 2015,
URL: <https://cds.cern.ch/record/2017378> (cit. on p. 42).
- [47] ATLAS Collaboration, *ATLAS Phase-II Upgrade Scoping Document*, CERN-LHCC-2015-020, LHCC-G-166, 2015,
URL: <https://cds.cern.ch/record/2055248> (cit. on p. 42).
- [48] ATLAS Collaboration, *ATLAS Inner Tracker Strip Detector: Technical Design Report*, ATLAS-TDR-025; CERN-LHCC-2017-005, 2017,
URL: <https://cds.cern.ch/record/2257755> (cit. on p. 42).
- [49] ATLAS Collaboration, *ATLAS Muon Spectrometer Phase-II Upgrade: Technical Design Report*, ATLAS-TDR-026; CERN-LHCC-2017-017, 2017,
URL: <https://cds.cern.ch/record/2285580> (cit. on p. 42).
- [50] ATLAS Collaboration, *ATLAS LAr Calorimeter Phase-II Upgrade: Technical Design Report*, ATLAS-TDR-027; CERN-LHCC-2017-018, 2017,
URL: <https://cds.cern.ch/record/2285582> (cit. on p. 42).
- [51] ATLAS Collaboration, *ATLAS Tile Calorimeter Phase-II Upgrade: Technical Design Report*, ATLAS-TDR-028; CERN-LHCC-2017-019, 2017,
URL: <https://cds.cern.ch/record/2285583> (cit. on p. 42).
- [52] ATLAS Collaboration, *ATLAS TDAQ Phase-II Upgrade: Technical Design Report*, ATLAS-TDR-029; CERN-LHCC-2017-020, 2017,
URL: <https://cds.cern.ch/record/2285584> (cit. on p. 42).
- [53] ATLAS Collaboration, *ATLAS Inner Tracker Pixel Detector: Technical Design Report*, ATLAS-TDR-030; CERN-LHCC-2017-021, 2017,
URL: <https://cds.cern.ch/record/2285585> (cit. on p. 42).
- [54] ATLAS Collaboration, *A High-Granularity Timing Detector for the ATLAS Phase-II Upgrade: Technical Design Report*, ATLAS-TDR-031; CERN-LHCC-2020-007, 2020,
URL: <https://cds.cern.ch/record/2719855> (cit. on p. 42).
- [55] ATLAS Collaboration, *The ATLAS Inner Detector commissioning and calibration*, Eur. Phys. J. C **70** (2010) 787, arXiv: [1004.5293 \[hep-ex\]](https://arxiv.org/abs/1004.5293) (cit. on p. 44).

- [56] ATLAS Collaboration, *Operation and performance of the ATLAS semiconductor tracker*, JINST **9** (2014) P08009, arXiv: [1404.7473 \[hep-ex\]](https://arxiv.org/abs/1404.7473) (cit. on p. 44).
- [57] ATLAS Collaboration, *Performance of the ATLAS Transition Radiation Tracker in Run 1 of the LHC: tracker properties*, JINST **12** (2017) P05002, arXiv: [1702.06473 \[hep-ex\]](https://arxiv.org/abs/1702.06473) (cit. on pp. 44, 45).
- [58] ATLAS Collaboration, *ATLAS Magnet System: Magnet Project Technical Design Report, Volume 1*, ATLAS-TDR-6; CERN-LHCC-97-018, 1997, URL: <https://cds.cern.ch/record/338080> (cit. on p. 45).
- [59] ATLAS Collaboration, *ATLAS Pixel Detector: Technical Design Report*, ATLAS-TDR-11; CERN-LHCC-98-013, 1998, URL: <https://cds.cern.ch/record/381263> (cit. on p. 45).
- [60] B. Abbott et al., *Production and integration of the ATLAS Insertable B-Layer*, JINST **13** (2018) T05008, arXiv: [1803.00844 \[physics.ins-det\]](https://arxiv.org/abs/1803.00844) (cit. on p. 45).
- [61] ATLAS Collaboration, *Operation and performance of the ATLAS semiconductor tracker in LHC Run 2*, JINST **17** (2022) P01013, arXiv: [2109.02591 \[physics.ins-det\]](https://arxiv.org/abs/2109.02591) (cit. on p. 45).
- [62] ATLAS Collaboration, *Performance of the ATLAS track reconstruction algorithms in dense environments in LHC Run 2*, Eur. Phys. J. C **77** (2017) 673, arXiv: [1704.07983 \[hep-ex\]](https://arxiv.org/abs/1704.07983) (cit. on p. 46).
- [63] ATLAS Collaboration, *ATLAS Liquid Argon Calorimeter: Technical Design Report*, ATLAS-TDR-2; CERN-LHCC-96-041, 1996, URL: <https://cds.cern.ch/record/331061> (cit. on p. 46).
- [64] ATLAS Collaboration, *ATLAS Tile Calorimeter: Technical Design Report*, ATLAS-TDR-3; CERN-LHCC-96-042, 1996, URL: <https://cds.cern.ch/record/331062> (cit. on p. 46).
- [65] ATLAS Collaboration, *ATLAS Muon Spectrometer: Technical Design Report*, ATLAS-TDR-10; CERN-LHCC-97-022, CERN, 1997, URL: <https://cds.cern.ch/record/331068> (cit. on p. 49).
- [66] ATLAS Collaboration, *Studies of the muon momentum calibration and performance of the ATLAS detector with pp collisions at $\sqrt{s} = 13$ TeV*, Eur. Phys. J. C **83** (2023) 686, arXiv: [2212.07338 \[hep-ex\]](https://arxiv.org/abs/2212.07338) (cit. on pp. 52, 74).
- [67] ATLAS Collaboration, *ATLAS Forward Detectors for Measurement of Elastic Scattering and Luminosity: Technical Design Report*, ATLAS-TDR-18; CERN-LHCC-2008-004, 2008, URL: <https://cds.cern.ch/record/1095847> (cit. on p. 51).
- [68] G. Avoni et al., *The new LUCID-2 detector for luminosity measurement and monitoring in ATLAS*, JINST **13** (2018) P07017 (cit. on p. 53).
- [69] ATLAS Collaboration, *ATLAS data quality operations and performance for 2015–2018 data-taking*, JINST **15** (2020) P04003, arXiv: [1911.04632 \[physics.ins-det\]](https://arxiv.org/abs/1911.04632) (cit. on pp. 54, 129).

- [70] ATLAS Collaboration, *ATLAS High-Level Trigger, Data Acquisition and Controls: Technical Design Report*, ATLAS-TDR-16; CERN-LHCC-2003-022, 2003, URL: <https://cds.cern.ch/record/616089> (cit. on p. 54).
- [71] ATLAS Collaboration, *Electron and photon performance measurements with the ATLAS detector using the 2015–2017 LHC proton–proton collision data*, JINST **14** (2019) P12006, arXiv: [1908.00005 \[hep-ex\]](https://arxiv.org/abs/1908.00005) (cit. on p. 57).
- [72] ATLAS Collaboration, *Electron and photon efficiencies in LHC Run 2 with the ATLAS experiment*, (2023), arXiv: [2308.13362 \[hep-ex\]](https://arxiv.org/abs/2308.13362) (cit. on pp. 57, 58, 123).
- [73] ATLAS Collaboration, *Electron and photon energy calibration with the ATLAS detector using LHC Run 2 data*, JINST **19** (2023) P02009, arXiv: [2309.05471 \[hep-ex\]](https://arxiv.org/abs/2309.05471) (cit. on p. 58).
- [74] ATLAS Collaboration, *Identification of electrons using a deep neural network in the ATLAS experiment*, ATL-PHYS-PUB-2022-022, 2022, URL: <https://cds.cern.ch/record/2803878> (cit. on p. 59).
- [75] ATLAS Collaboration, *Preliminary analysis of the luminosity calibration of the ATLAS 13.6 TeV data recorded in 2022*, ATL-DAPR-PUB-2023-001, 2023, URL: <https://cds.cern.ch/record/2853525> (cit. on pp. 59, 129).
- [76] ATLAS Collaboration, *Jet reconstruction and performance using particle flow with the ATLAS Detector*, Eur. Phys. J. C **77** (2017) 466, arXiv: [1703.10485 \[hep-ex\]](https://arxiv.org/abs/1703.10485) (cit. on p. 61).
- [77] M. Cacciari, G. P. Salam and G. Soyez, *The anti- k_t jet clustering algorithm*, JHEP **04** (2008) 063, arXiv: [0802.1189 \[hep-ph\]](https://arxiv.org/abs/0802.1189) (cit. on p. 61).
- [78] ATLAS Collaboration, *Simultaneous energy and mass calibration of large-radius jets with the ATLAS detector using a deep neural network*, (2023), arXiv: [2311.08885 \[hep-ex\]](https://arxiv.org/abs/2311.08885) (cit. on pp. 61, 65).
- [79] ATLAS Collaboration, *Topological cell clustering in the ATLAS calorimeters and its performance in LHC Run 1*, Eur. Phys. J. C **77** (2017) 490, arXiv: [1603.02934 \[hep-ex\]](https://arxiv.org/abs/1603.02934) (cit. on p. 61).
- [80] ATLAS Collaboration, *Improving topological cluster reconstruction using calorimeter cell timing in ATLAS*, Eur. Phys. J. C **84** (2023) 455, arXiv: [2310.16497 \[physics.ins-det\]](https://arxiv.org/abs/2310.16497) (cit. on p. 61).
- [81] ATLAS Collaboration, *Jet energy scale and resolution measured in proton–proton collisions at $\sqrt{s} = 13$ TeV with the ATLAS detector*, Eur. Phys. J. C **81** (2021) 689, arXiv: [2007.02645 \[hep-ex\]](https://arxiv.org/abs/2007.02645) (cit. on pp. 62, 63, 110).
- [82] ATLAS Collaboration, *New techniques for jet calibration with the ATLAS detector*, Eur. Phys. J. C **83** (2023) 761, arXiv: [2303.17312 \[hep-ex\]](https://arxiv.org/abs/2303.17312) (cit. on p. 63).
- [83] ATLAS Collaboration, *Performance of top-quark and W-boson tagging with ATLAS in Run 2 of the LHC*, Eur. Phys. J. C **79** (2019) 375, arXiv: [1808.07858 \[hep-ex\]](https://arxiv.org/abs/1808.07858) (cit. on p. 64).

- [84] ATLAS Collaboration, *In situ calibration of large-radius jet energy and mass in 13 TeV proton–proton collisions with the ATLAS detector*, *Eur. Phys. J. C* **79** (2019) 135, arXiv: 1807.09477 [hep-ex] (cit. on p. 64).
- [85] ATLAS Collaboration, *Optimisation of large-radius jet reconstruction for the ATLAS detector in 13 TeV proton–proton collisions*, *Eur. Phys. J. C* **81** (2021) 334, arXiv: 2009.04986 [hep-ex] (cit. on p. 64).
- [86] ATLAS Collaboration, *Constituent-level pile-up mitigation techniques in ATLAS*, ATLAS-CONF-2017-065, 2017, URL: <https://cds.cern.ch/record/2281055> (cit. on p. 64).
- [87] ATLAS Collaboration, *The performance of missing transverse momentum reconstruction and its significance with the ATLAS detector using 140fb^{-1} of $\sqrt{s} = 13\text{TeV}$ pp collisions*, (2024), arXiv: 2402.05858 [hep-ex] (cit. on pp. 65, 67).
- [88] *Overlap Removal Tools*, 2017, URL: https://indico.cern.ch/event/631313/contributions/2683959/attachments/1518878/2373377/Farrell_ORTools_ftaghbb.pdf (cit. on p. 66).
- [89] ATLAS Collaboration, *ATLAS flavour-tagging algorithms for the LHC Run 2 pp collision dataset*, *Eur. Phys. J. C* **83** (2023) 681, arXiv: 2211.16345 [physics.data-an] (cit. on pp. 67, 71, 110).
- [90] ATLAS Collaboration, *Graph Neural Network Jet Flavour Tagging with the ATLAS Detector*, ATL-PHYS-PUB-2022-027, 2022, URL: <https://cds.cern.ch/record/2811135> (cit. on pp. 67, 69, 70).
- [91] ATLAS Collaboration, *Identification of Boosted Higgs Bosons Decaying Into $b\bar{b}$ With Neural Networks and Variable Radius Subjets in ATLAS*, ATL-PHYS-PUB-2020-019, 2020, URL: <https://cds.cern.ch/record/2724739> (cit. on p. 67).
- [92] ATLAS Collaboration, *Transformer Neural Networks for Identifying Boosted Higgs Bosons decaying into $b\bar{b}$ and $c\bar{c}$ in ATLAS*, ATL-PHYS-PUB-2023-021, 2023, URL: <https://cds.cern.ch/record/2866601> (cit. on pp. 67, 69, 70, 72, 142, 145).
- [93] ATLAS Collaboration, *Optimisation and performance studies of the ATLAS b -tagging algorithms for the 2017-18 LHC run*, ATL-PHYS-PUB-2017-013, 2017, URL: <https://cds.cern.ch/record/2273281> (cit. on p. 68).
- [94] ATLAS Collaboration, *Secondary vertex finding for jet flavour identification with the ATLAS detector*, ATL-PHYS-PUB-2017-011, 2017, URL: <https://cds.cern.ch/record/2270366> (cit. on p. 68).
- [95] ATLAS Collaboration, *Topological b -hadron decay reconstruction and identification of b -jets with the JetFitter package in the ATLAS experiment at the LHC*, ATL-PHYS-PUB-2018-025, 2018, URL: <https://cds.cern.ch/record/2645405> (cit. on p. 68).
- [96] S. Shleifer, J. Weston and M. Ott, *NormFormer: improved transformer pretraining with extra normalization*, 2021, arXiv: 2110.09456 [cs.CL], URL: <https://arxiv.org/abs/2110.09456> (cit. on p. 71).

- [97] J. L. Ba, J. R. Kiros and G. E. Hinton, *Layer normalization*, 2016, arXiv: [1607.06450 \[stat.ML\]](https://arxiv.org/abs/1607.06450), URL: <https://arxiv.org/abs/1607.06450> (cit. on p. 71).
- [98] ATLAS Collaboration, *Muon reconstruction and identification efficiency in ATLAS using the full Run 2 pp collision data set at $\sqrt{s} = 13 \text{ TeV}$* , *Eur. Phys. J. C* **81** (2021) 578, arXiv: [2012.00578 \[hep-ex\]](https://arxiv.org/abs/2012.00578) (cit. on pp. 72–74, 91, 97).
- [99] ATLAS Collaboration, *Reconstruction, Identification, and Calibration of hadronically decaying tau leptons with the ATLAS detector for the LHC Run 3 and reprocessed Run 2 data*, ATL-PHYS-PUB-2022-044, 2022, URL: <https://cds.cern.ch/record/2827111> (cit. on pp. 77, 79, 83–85, 87, 177).
- [100] ATLAS Collaboration, *Cut-based Identification of Hadronic τ Decays in Early ATLAS Data*, ATL-PHYS-PUB-2010-001, 2010, URL: <https://cds.cern.ch/record/1233743> (cit. on p. 77).
- [101] ATLAS Collaboration, *Identification and energy calibration of hadronically decaying tau leptons with the ATLAS experiment in pp collisions at $\sqrt{s} = 8 \text{ TeV}$* , *Eur. Phys. J. C* **75** (2015) 303, arXiv: [1412.7086 \[hep-ex\]](https://arxiv.org/abs/1412.7086) (cit. on p. 77).
- [102] R. M. Schmidt, *Recurrent Neural Networks (RNNs): a gentle introduction and overview*, 2019, arXiv: [1912.05911 \[cs.LG\]](https://arxiv.org/abs/1912.05911), URL: <https://arxiv.org/abs/1912.05911> (cit. on p. 81).
- [103] F. Chollet et al., *Keras*, 2015, URL: <https://keras.io> (cit. on p. 81).
- [104] Martín Abadi et al., *TensorFlow: large-scale machine learning on heterogeneous systems*, Software available from tensorflow.org, 2015, URL: <https://www.tensorflow.org/> (cit. on p. 81).
- [105] M. Zaheer et al., *Deep sets*, 2018, arXiv: [1703.06114 \[cs.LG\]](https://arxiv.org/abs/1703.06114), URL: <https://arxiv.org/abs/1703.06114> (cit. on p. 83).
- [106] A. Mao, M. Mohri and Y. Zhong, *Cross-entropy loss functions: theoretical analysis and applications*, 2023, arXiv: [2304.07288 \[cs.LG\]](https://arxiv.org/abs/2304.07288), URL: <https://arxiv.org/abs/2304.07288> (cit. on p. 86).
- [107] S. Ruder, *An overview of gradient descent optimization algorithms*, arXiv preprint arXiv:1609.04747 (2016) (cit. on p. 86).
- [108] ATLAS Collaboration, *Measurement of the tau lepton reconstruction and identification performance in the ATLAS experiment using pp collisions at $\sqrt{s} = 13 \text{ TeV}$* , ATLAS-CONF-2017-029, 2017, URL: <https://cds.cern.ch/record/2261772> (cit. on p. 90).
- [109] ATLAS Collaboration, *Reconstruction and identification of boosted di- τ systems in a search for Higgs boson pairs using 13 TeV proton–proton collision data in ATLAS*, ATLAS-CONF-2020-012, 2020, URL: <https://cds.cern.ch/record/2719518> (cit. on p. 91).

- [110] J. Alwall et al., *The automated computation of tree-level and next-to-leading order differential cross sections, and their matching to parton shower simulations*, *JHEP* **07** (2014) 079, arXiv: 1405.0301 [hep-ph] (cit. on p. 93).
- [111] S. Frixione, G. Ridolfi and P. Nason, *A positive-weight next-to-leading-order Monte Carlo for heavy flavour hadroproduction*, *JHEP* **09** (2007) 126, arXiv: 0707.3088 [hep-ph] (cit. on p. 93).
- [112] P. Nason, *A new method for combining NLO QCD with shower Monte Carlo algorithms*, *JHEP* **11** (2004) 040, arXiv: hep-ph/0409146 (cit. on pp. 93–95, 143, 144).
- [113] S. Frixione, P. Nason and C. Oleari, *Matching NLO QCD computations with parton shower simulations: the POWHEG method*, *JHEP* **11** (2007) 070, arXiv: 0709.2092 [hep-ph] (cit. on pp. 93–95, 143, 144).
- [114] S. Alioli, P. Nason, C. Oleari and E. Re, *A general framework for implementing NLO calculations in shower Monte Carlo programs: the POWHEG BOX*, *JHEP* **06** (2010) 043, arXiv: 1002.2581 [hep-ph] (cit. on pp. 93–95, 143, 144).
- [115] NNPDF Collaboration, R. D. Ball et al., *Parton distributions for the LHC run II*, *JHEP* **04** (2015) 040, arXiv: 1410.8849 [hep-ph] (cit. on pp. 93–95).
- [116] ATLAS Collaboration, *Studies on top-quark Monte Carlo modelling for Top2016*, ATL-PHYS-PUB-2016-020, 2016, URL: <https://cds.cern.ch/record/2216168> (cit. on p. 93).
- [117] T. Sjöstrand et al., *An introduction to PYTHIA 8.2*, *Comput. Phys. Commun.* **191** (2015) 159, arXiv: 1410.3012 [hep-ph] (cit. on pp. 93, 95, 143, 144).
- [118] ATLAS Collaboration, *ATLAS Pythia 8 tunes to 7 TeV data*, ATL-PHYS-PUB-2014-021, 2014, URL: <https://cds.cern.ch/record/1966419> (cit. on pp. 93, 95).
- [119] NNPDF Collaboration, R. D. Ball et al., *Parton distributions with LHC data*, *Nucl. Phys. B* **867** (2013) 244, arXiv: 1207.1303 [hep-ph] (cit. on pp. 93, 95, 144).
- [120] D. J. Lange, *The EvtGen particle decay simulation package*, *Nucl. Instrum. Meth. A* **462** (2001) 152 (cit. on pp. 93, 94).
- [121] ATLAS Collaboration, *The Pythia 8 A3 tune description of ATLAS minimum bias and inelastic measurements incorporating the Donnachie–Landshoff diffractive model*, ATL-PHYS-PUB-2016-017, 2016, URL: <https://cds.cern.ch/record/2206965> (cit. on p. 93).
- [122] A. D. Martin, W. J. Stirling, R. S. Thorne and G. Watt, *Parton distributions for the LHC*, *Eur. Phys. J. C* **63** (2009) 189, arXiv: 0901.0002 [hep-ph] (cit. on p. 93).
- [123] S. Agostinelli et al., *GEANT4 – a simulation toolkit*, *Nucl. Instrum. Meth. A* **506** (2003) 250 (cit. on p. 93).
- [124] ATLAS Collaboration, *Luminosity determination in pp collisions at $\sqrt{s} = 13$ TeV using the ATLAS detector at the LHC*, *Eur. Phys. J. C* **83** (2023) 982, arXiv: 2212.09379 [hep-ex] (cit. on pp. 93, 114).

- [125] E. Bothmann et al., *Event generation with Sherpa 2.2*, *SciPost Phys.* **7** (2019) 034, arXiv: [1905.09127 \[hep-ph\]](#) (cit. on p. 94).
- [126] S. Höche, F. Krauss, S. Schumann and F. Siegert, *QCD matrix elements and truncated showers*, *JHEP* **05** (2009) 053, arXiv: [0903.1219 \[hep-ph\]](#) (cit. on p. 94).
- [127] ATLAS Collaboration, *Measurement of the transverse momentum distribution of Drell–Yan lepton pairs in proton–proton collisions at $\sqrt{s} = 13$ TeV with the ATLAS detector*, *Eur. Phys. J. C* **80** (2020) 616, arXiv: [1912.02844 \[hep-ex\]](#) (cit. on p. 94).
- [128] ATLAS Collaboration, *Modelling and computational improvements to the simulation of single vector-boson plus jet processes for the ATLAS experiment*, *JHEP* **08** (2022) 089, arXiv: [2112.09588 \[hep-ex\]](#) (cit. on p. 94).
- [129] R. Frederix, E. Re and P. Torrielli, *Single-top t-channel hadroproduction in the four-flavour scheme with POWHEG and aMC@NLO*, *JHEP* **09** (2012) 130, arXiv: [1207.5391 \[hep-ph\]](#) (cit. on p. 94).
- [130] E. Re, *Single-top W t-channel production matched with parton showers using the POWHEG method*, *Eur. Phys. J. C* **71** (2011) 1547, arXiv: [1009.2450 \[hep-ph\]](#) (cit. on p. 95).
- [131] S. Frixione, E. Laenen, P. Motylinski, C. White and B. R. Webber, *Single-top hadroproduction in association with a W boson*, *JHEP* **07** (2008) 029, arXiv: [0805.3067 \[hep-ph\]](#) (cit. on p. 95).
- [132] ATLAS Collaboration, *Identification of hadronic tau lepton decays using neural networks in the ATLAS experiment*, ATL-PHYS-PUB-2019-033, 2019, URL: <https://cds.cern.ch/record/2688062> (cit. on p. 99).
- [133] ATLAS Collaboration, *Reconstruction of hadronic decay products of tau leptons with the ATLAS experiment*, *Eur. Phys. J. C* **76** (2016) 295, arXiv: [1512.05955 \[hep-ex\]](#) (cit. on p. 100).
- [134] R. Ellis, I. Hinchliffe, M. Soldate and J. Van Der Bij, *Higgs decay to $\tau^+\tau^-$ A possible signature of intermediate mass Higgs bosons at high energy hadron colliders*, *Nuclear Physics B* **297** (1988) 221, ISSN: 0550-3213, URL: <https://www.sciencedirect.com/science/article/pii/0550321388900193> (cit. on p. 109).
- [135] ATLAS Collaboration, *Measurements of Higgs boson production cross-sections in the $H \rightarrow \tau^+\tau^-$ decay channel in pp collisions at $\sqrt{s} = 13$ TeV with the ATLAS detector*, *JHEP* **08** (2022) 175, arXiv: [2201.08269 \[hep-ex\]](#) (cit. on p. 110).
- [136] Q. Dong and T. Wyatt, *Identification of hadronic τ lepton decays in the boosted $\tau_{\text{had}}\tau_\mu$ pair using muon removal technique in the ATLAS experiment*, tech. rep., CERN, 2024, URL: <https://cds.cern.ch/record/2899443> (cit. on pp. 112, 142, 148).
- [137] D. Baron, *Tau lepton universality test in the vector boson fusion topology using the ATLAS detector at the LHC*, Presented 12 Dec 2023, Manchester U., 2024, chap. 6, URL: <https://cds.cern.ch/record/2887993> (cit. on p. 114).

- [138] CMS Collaboration, *Searches for Higgs boson production through decays of heavy resonances*, (2024), arXiv: [2403.16926 \[hep-ex\]](#) (cit. on p. 141).
- [139] CMS Collaboration, *Search for a massive scalar resonance decaying to a light scalar and a Higgs boson in the four b quarks final state with boosted topology*, *Phys. Lett. B* **842** (2023) 137392, arXiv: [2204.12413 \[hep-ex\]](#) (cit. on p. 141).
- [140] CMS Collaboration, *Search for a heavy Higgs boson decaying into two lighter Higgs bosons in the $\tau\tau bb$ final state at 13 TeV*, *JHEP* **11** (2021) 057, arXiv: [2106.10361 \[hep-ex\]](#) (cit. on p. 141).
- [141] CMS Collaboration, *Search for a new resonance decaying into two spin-0 bosons in a final state with two photons and two bottom quarks in proton–proton collisions at $\sqrt{s} = 13$ TeV*, (2023), arXiv: [2310.01643 \[hep-ex\]](#) (cit. on p. 141).
- [142] CMS Collaboration, *Search for Higgs boson pair production in the $b\bar{b}W^+W^-$ decay mode in proton–proton collisions at $\sqrt{s} = 13$ TeV*, (2024), arXiv: [2403.09430 \[hep-ex\]](#) (cit. on p. 141).
- [143] CMS Collaboration, *Search for heavy resonances decaying to a pair of Lorentz-boosted Higgs bosons in final states with leptons and a bottom quark pair at $\sqrt{s} = 13$ TeV*, *JHEP* **05** (2022) 005, arXiv: [2112.03161 \[hep-ex\]](#) (cit. on p. 141).
- [144] CMS Collaboration, *Search for Higgs boson pairs decaying to WW^*WW^* , $WW^*\tau\tau$, and $\tau\tau\tau\tau$ in proton–proton collisions at $\sqrt{s} = 13$ TeV*, *JHEP* **07** (2023) 095, arXiv: [2206.10268 \[hep-ex\]](#) (cit. on p. 141).
- [145] ATLAS Collaboration, *Combination of searches for resonant Higgs boson pair production using pp collisions at $\sqrt{s} = 13$ TeV with the ATLAS detector*, (2023), arXiv: [2311.15956 \[hep-ex\]](#) (cit. on p. 141).
- [146] ATLAS Collaboration, *Search for resonant pair production of Higgs bosons in the $b\bar{b}b\bar{b}$ final state using pp collisions at $\sqrt{s} = 13$ TeV with the ATLAS detector*, *Phys. Rev. D* **105** (2022) 092002, arXiv: [2202.07288 \[hep-ex\]](#) (cit. on p. 141).
- [147] ATLAS Collaboration, *Search for Higgs boson pair production in the two bottom quarks plus two photons final state in pp collisions at $\sqrt{s} = 13$ TeV with the ATLAS detector*, *Phys. Rev. D* **106** (2022) 052001, arXiv: [2112.11876 \[hep-ex\]](#) (cit. on p. 141).
- [148] ATLAS Collaboration, *Search for resonant and non-resonant Higgs boson pair production in the $b\bar{b}\tau^+\tau^-$ decay channel using 13 TeV pp collision data from the ATLAS detector*, *JHEP* **07** (2023) 040, arXiv: [2209.10910 \[hep-ex\]](#) (cit. on p. 141).
- [149] ATLAS Collaboration, *Reconstruction and identification of boosted di- τ systems in a search for Higgs boson pairs using 13 TeV proton–proton collision data in ATLAS*, *JHEP* **11** (2020) 163, arXiv: [2007.14811 \[hep-ex\]](#) (cit. on p. 141).
- [150] ATLAS Collaboration, *Identification of boosted Higgs bosons decaying into b-quark pairs with the ATLAS detector at 13 TeV*, *Eur. Phys. J. C* **79** (2019) 836, arXiv: [1906.11005 \[hep-ex\]](#) (cit. on p. 142).

- [151] *Identification of highly Lorentz-boosted heavy particles using graph neural networks and new mass decorrelation techniques*, (2020), URL: <https://cds.cern.ch/record/2707946> (cit. on p. 142).
- [152] Q. Dong and T. Wyatt, *A benchmark for the re-reconstructed hadronic τ objects with overlapping muon signatures removed with the ATLAS detector*, tech. rep., CERN, 2024, URL: <https://cds.cern.ch/record/2890038> (cit. on pp. 142, 148).
- [153] K. Hamilton, P. Nason, E. Re and G. Zanderighi, *NNLOPS simulation of Higgs boson production*, JHEP **10** (2013) 222, arXiv: [1309.0017 \[hep-ph\]](https://arxiv.org/abs/1309.0017) (cit. on p. 143).
- [154] K. Hamilton, P. Nason and G. Zanderighi, *Finite quark-mass effects in the NNLOPS POWHEG+MiNLO Higgs generator*, JHEP **05** (2015) 140, arXiv: [1501.04637 \[hep-ph\]](https://arxiv.org/abs/1501.04637) (cit. on p. 143).
- [155] K. Hamilton, P. Nason and G. Zanderighi, *MINLO: multi-scale improved NLO*, JHEP **10** (2012) 155, arXiv: [1206.3572 \[hep-ph\]](https://arxiv.org/abs/1206.3572) (cit. on p. 143).
- [156] J. M. Campbell et al., *NLO Higgs boson production plus one and two jets using the POWHEG BOX, MadGraph4 and MCFM*, JHEP **07** (2012) 092, arXiv: [1202.5475 \[hep-ph\]](https://arxiv.org/abs/1202.5475) (cit. on p. 143).
- [157] K. Hamilton, P. Nason, C. Oleari and G. Zanderighi, *Merging $H/W/Z + 0$ and 1 jet at NLO with no merging scale: a path to parton shower + NNLO matching*, JHEP **05** (2013) 082, arXiv: [1212.4504 \[hep-ph\]](https://arxiv.org/abs/1212.4504) (cit. on p. 143).
- [158] S. Catani and M. Grazzini, *Next-to-Next-to-Leading-Order Subtraction Formalism in Hadron Collisions and its Application to Higgs-Boson Production at the Large Hadron Collider*, Phys. Rev. Lett. **98** (2007) 222002, arXiv: [hep-ph/0703012 \[hep-ph\]](https://arxiv.org/abs/hep-ph/0703012) (cit. on p. 143).
- [159] J. Butterworth et al., *PDF4LHC recommendations for LHC Run II*, J. Phys. G **43** (2016) 023001, arXiv: [1510.03865 \[hep-ph\]](https://arxiv.org/abs/1510.03865) (cit. on pp. 143, 144).
- [160] ATLAS Collaboration, *Measurement of the Z/γ^* boson transverse momentum distribution in pp collisions at $\sqrt{s} = 7$ TeV with the ATLAS detector*, JHEP **09** (2014) 145, arXiv: [1406.3660 \[hep-ex\]](https://arxiv.org/abs/1406.3660) (cit. on pp. 143, 144).
- [161] D. de Florian et al., *Handbook of LHC Higgs Cross Sections: 4. Deciphering the Nature of the Higgs Sector*, (2017), arXiv: [1610.07922 \[hep-ph\]](https://arxiv.org/abs/1610.07922) (cit. on p. 143).
- [162] C. Anastasiou et al., *High precision determination of the gluon fusion Higgs boson cross-section at the LHC*, JHEP **05** (2016) 058, arXiv: [1602.00695 \[hep-ph\]](https://arxiv.org/abs/1602.00695) (cit. on p. 143).
- [163] C. Anastasiou, C. Duhr, F. Dulat, F. Herzog and B. Mistlberger, *Higgs Boson Gluon-Fusion Production in QCD at Three Loops*, Phys. Rev. Lett. **114** (2015) 212001, arXiv: [1503.06056 \[hep-ph\]](https://arxiv.org/abs/1503.06056) (cit. on p. 143).
- [164] F. Dulat, A. Lazopoulos and B. Mistlberger, *iHixs 2 – Inclusive Higgs cross sections*, Comput. Phys. Commun. **233** (2018) 243, arXiv: [1802.00827 \[hep-ph\]](https://arxiv.org/abs/1802.00827) (cit. on p. 143).
- [165] R. V. Harlander and K. J. Ozeren, *Finite top mass effects for hadronic Higgs production at next-to-next-to-leading order*, JHEP **11** (2009) 088, arXiv: [0909.3420 \[hep-ph\]](https://arxiv.org/abs/0909.3420) (cit. on p. 143).

- [166] R. V. Harlander and K. J. Ozeren, *Top mass effects in Higgs production at next-to-next-to-leading order QCD: Virtual corrections*, *Phys. Lett. B* **679** (2009) 467, arXiv: 0907.2997 [hep-ph] (cit. on p. 143).
- [167] R. V. Harlander, H. Mantler, S. Marzani and K. J. Ozeren, *Higgs production in gluon fusion at next-to-next-to-leading order QCD for finite top mass*, *Eur. Phys. J. C* **66** (2010) 359, arXiv: 0912.2104 [hep-ph] (cit. on p. 143).
- [168] A. Pak, M. Rogal and M. Steinhauser, *Finite top quark mass effects in NNLO Higgs boson production at LHC*, *JHEP* **02** (2010) 025, arXiv: 0911.4662 [hep-ph] (cit. on p. 143).
- [169] S. Actis, G. Passarino, C. Sturm and S. Uccirati, *NLO electroweak corrections to Higgs boson production at hadron colliders*, *Phys. Lett. B* **670** (2008) 12, arXiv: 0809.1301 [hep-ph] (cit. on p. 143).
- [170] S. Actis, G. Passarino, C. Sturm and S. Uccirati, *NNLO computational techniques: The cases $H \rightarrow \gamma\gamma$ and $H \rightarrow gg$* , *Nucl. Phys. B* **811** (2009) 182, arXiv: 0809.3667 [hep-ph] (cit. on p. 143).
- [171] M. Bonetti, K. Melnikov and L. Tancredi, *Higher order corrections to mixed QCD-EW contributions to Higgs boson production in gluon fusion*, *Phys. Rev. D* **97** (2018) 056017, arXiv: 1801.10403 [hep-ph] (cit. on p. 143), Erratum: *Phys. Rev. D* **97** (2018) 099906(E).
- [172] A. Djouadi, J. Kalinowski and M. Spira, *HDECAY: a program for Higgs boson decays in the Standard Model and its supersymmetric extension*, *Comput. Phys. Commun.* **108** (1998) 56, arXiv: hep-ph/9704448 (cit. on pp. 143, 144).
- [173] M. Spira, *QCD Effects in Higgs Physics*, *Fortsch. Phys.* **46** (1998) 203, arXiv: hep-ph/9705337 (cit. on pp. 143, 144).
- [174] A. Djouadi, M. M. Mühlleitner and M. Spira, *Decays of Supersymmetric Particles: the Program SUSY-HIT (SUspect-SdecaY-Hdecay-InTerface)*, *Acta Phys. Polon. B* **38** (2007) 635, arXiv: hep-ph/0609292 (cit. on pp. 143, 144).
- [175] A. Bredenstein, A. Denner, S. Dittmaier and M. M. Weber, *Radiative corrections to the semileptonic and hadronic Higgs-boson decays $H \rightarrow WW/ZZ \rightarrow 4$ fermions*, *JHEP* **02** (2007) 080, arXiv: hep-ph/0611234 (cit. on pp. 143, 144).
- [176] A. Bredenstein, A. Denner, S. Dittmaier and M. M. Weber, *Precise predictions for the Higgs-boson decay $H \rightarrow WW/ZZ \rightarrow 4$ leptons*, *Phys. Rev. D* **74** (2006) 013004, arXiv: hep-ph/0604011 [hep-ph] (cit. on pp. 143, 144).
- [177] A. Bredenstein, A. Denner, S. Dittmaier and M. M. Weber, *Precision calculations for the Higgs decays $H \rightarrow ZZ/WW \rightarrow 4$ leptons*, *Nucl. Phys. Proc. Suppl.* **160** (2006) 131, arXiv: hep-ph/0607060 [hep-ph] (cit. on pp. 143, 144).
- [178] P. Nason and C. Oleari, *NLO Higgs boson production via vector-boson fusion matched with shower in POWHEG*, *JHEP* **02** (2010) 037, arXiv: 0911.5299 [hep-ph] (cit. on pp. 143, 144).

- [179] M. Ciccolini, A. Denner and S. Dittmaier,
Strong and Electroweak Corrections to the Production of a Higgs Boson + 2 Jets via Weak Interactions at the Large Hadron Collider, *Phys. Rev. Lett.* **99** (2007) 161803, arXiv: [0707.0381 \[hep-ph\]](#) (cit. on p. 143).
- [180] M. Ciccolini, A. Denner and S. Dittmaier, *Electroweak and QCD corrections to Higgs production via vector-boson fusion at the CERN LHC*, *Phys. Rev. D* **77** (2008) 013002, arXiv: [0710.4749 \[hep-ph\]](#) (cit. on p. 143).
- [181] P. Bolzoni, F. Maltoni, S.-O. Moch and M. Zaro, *Higgs Boson Production via Vector-Boson Fusion at Next-to-Next-to-Leading Order in QCD*, *Phys. Rev. Lett.* **105** (2010) 011801, arXiv: [1003.4451 \[hep-ph\]](#) (cit. on p. 143).
- [182] M. L. Ciccolini, S. Dittmaier and M. Krämer, *Electroweak radiative corrections to associated WH and ZH production at hadron colliders*, *Phys. Rev. D* **68** (2003) 073003, arXiv: [hep-ph/0306234 \[hep-ph\]](#) (cit. on p. 144).
- [183] O. Brein, A. Djouadi and R. Harlander,
NNLO QCD corrections to the Higgs-strahlung processes at hadron colliders, *Phys. Lett. B* **579** (2004) 149, arXiv: [hep-ph/0307206](#) (cit. on p. 144).
- [184] O. Brein, R. V. Harlander, M. Wiesemann and T. Zirke,
Top-quark mediated effects in hadronic Higgs-Strahlung, *Eur. Phys. J. C* **72** (2012) 1868, arXiv: [1111.0761 \[hep-ph\]](#) (cit. on p. 144).
- [185] L. Altenkamp, S. Dittmaier, R. V. Harlander, H. Rzehak and T. J. E. Zirke,
Gluon-induced Higgs-strahlung at next-to-leading order QCD, *JHEP* **02** (2013) 078, arXiv: [1211.5015 \[hep-ph\]](#) (cit. on p. 144).
- [186] A. Denner, S. Dittmaier, S. Kallweit and A. Mück,
HAWK 2.0: A Monte Carlo program for Higgs production in vector-boson fusion and Higgs strahlung at hadron colliders, *Comput. Phys. Commun.* **195** (2015) 161, arXiv: [1412.5390 \[hep-ph\]](#) (cit. on p. 144).
- [187] O. Brein, R. V. Harlander and T. J. E. Zirke,
vh@nnlo – Higgs Strahlung at hadron colliders, *Comput. Phys. Commun.* **184** (2013) 998, arXiv: [1210.5347 \[hep-ph\]](#) (cit. on p. 144).
- [188] R. V. Harlander, A. Kulesza, V. Theeuwes and T. Zirke,
Soft gluon resummation for gluon-induced Higgs Strahlung, *JHEP* **11** (2014) 082, arXiv: [1410.0217 \[hep-ph\]](#) (cit. on p. 144).
- [189] L. Heinrich, M. Feickert, G. Stark and K. Cranmer,
pyhf: pure-Python implementation of HistFactory statistical models, *Journal of Open Source Software* **6** (2021) 2823 (cit. on p. 157).
- [190] A. L. Read, *Presentation of search results: the CL_S technique*, *J. Phys. G* **28** (2002) 2693 (cit. on p. 157).

Appendix A

Investigation for truth 3-prong τ_{had} reconstructed as 2-prong

Introduction

The reconstruction efficiency of the particle-level 3-prong τ_{had} decreases with increasing p_{T} of the τ_{had} , particularly in the high-mass region of this analysis. When the 3-prong τ_{had} is not correctly reconstructed, it is most often reconstructed as a 2-prong τ_{had} , typically due to the failure to identify one of the charged pions. For visible p_{T} of the τ_{had} around 1 TeV, the probability of correctly reconstructing a 3-prong τ_{had} can be as low as 45% [99], as reported in Chapter 5. In such cases, the probability of it being reconstructed as a 2-prong τ_{had} (3-to-2p migration) is approximately 30%, while the probability of being reconstructed as a 1-prong (3-to-1p migration) τ_{had} is around 15%. The remaining probability is attributed to reconstruction as a 4-prong (3-to-4 migration) or 0-prong (3-to-0 migration) τ_{had} , both of which are negligible compared to other types of migration.

From the perspective of this analysis, the 3-to-1p migration is not problematic, as reconstructed 1-prong τ_{had} s are included in the signal region (SR). Likewise, the 3-to-4 and 3-to-0 migrations are not concerning, as these rarely occur. By including reconstructed

2-prong τ_{had} s in the SR, the signal acceptance for the high-mass $G \rightarrow HH$ signal can potentially increase by 10%. However, the background composition must be carefully analysed to ensure that the inclusion of 2-prong τ_{had} s does not significantly increase background contamination.

Event-selections

Table A.1 shows the event yields in the SR_{2p} and CR_{2p} regions. The selection on the charge of the muon and τ_{had} is loosened to $q_\mu \times q_{\tau_{\text{had}}} \leq 0$, as the charge of the 2-prong τ_{had} can only be 0 or ± 2 . The prongness selection is set to 2-prong, ensuring that these regions are orthogonal to the SR and CR regions in the main analysis. The TauID jet RNN score cut moves up from 0.05 to 0.15 to suppress the top background contamination. All other selection criteria for the SR_{2p} and CR_{2p} regions remain identical to those used in the SR and CR regions of the main analysis.

The same set of distributions as shown in the main text is presented in Figures A.1 to A.12. Good agreement between data and MC is observed across these distributions in CR_{2p}, indicating that the 2-prong τ_{had} selection is also well-modelled in the MC simulation.

Results

As expected, the signal efficiency in the SR_{2p} is roughly 10% of the signal efficiency in the main analysis for $G(3 - 5 \text{ TeV})$. The SR_{2p} signal yield for $G(2 \text{ TeV})$ is roughly 7% of the signal yield in the SR, indicating that the 3-to-2 migration is less prominent for the lower $p_T \tau_{\text{had}}$. The SM MC predicted 0.11 events in the SR_{2p}, the composition of which is different from the nominal SR, with the $t\bar{t}$ being the dominant background. Other major backgrounds appeared in the nominal SR, such as $Z \rightarrow \tau\tau$ and diBoson, are sources of genuine $\tau_\mu\tau_{\text{had}}$, which are suppressed by the 2-prong τ_{had} selection in the SR_{2p}. In

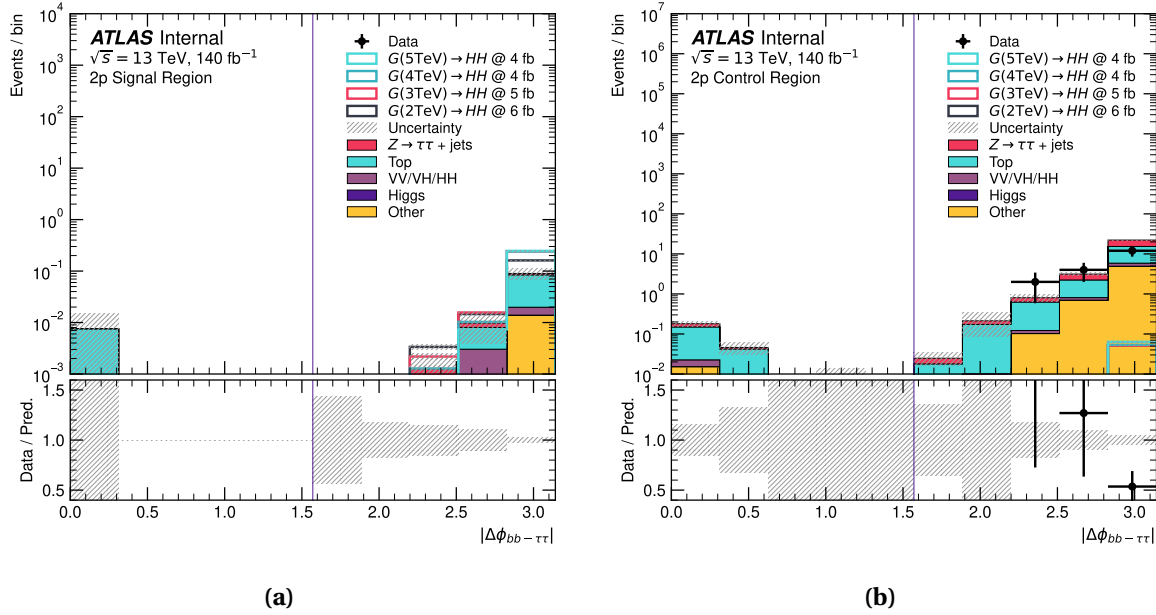


Fig. A.1 The distribution of the $|\Delta\phi_{bb-\tau\tau}|$ in the SR (a), and CR (b).

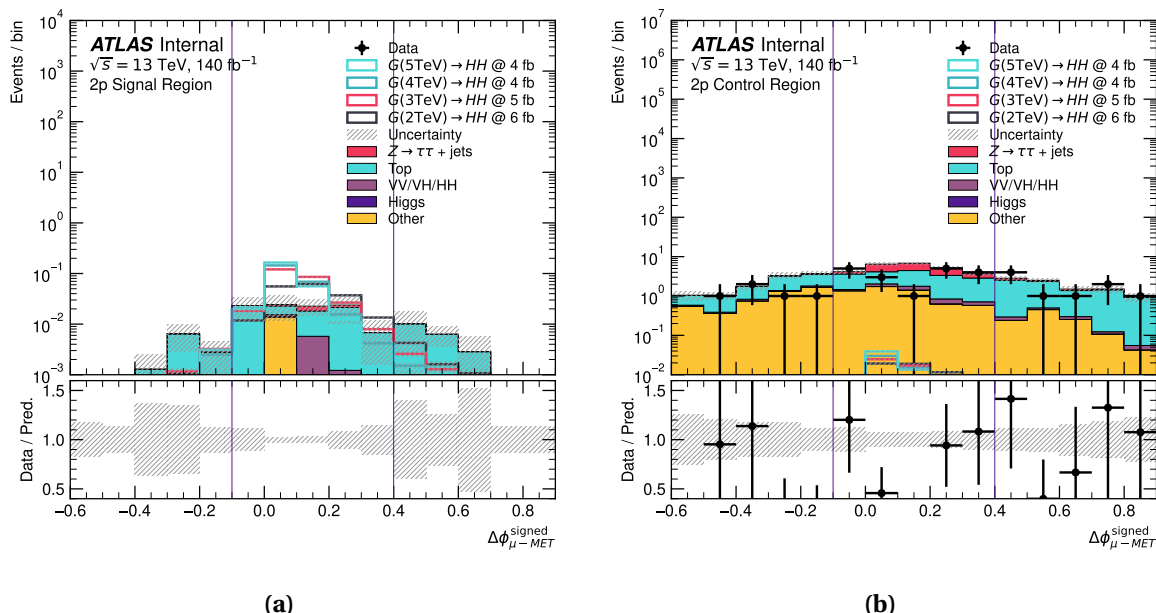


Fig. A.2 The distribution of the $\Delta\phi_{\mu-MET}^{signed}$ in the SR (a), and CR (b).

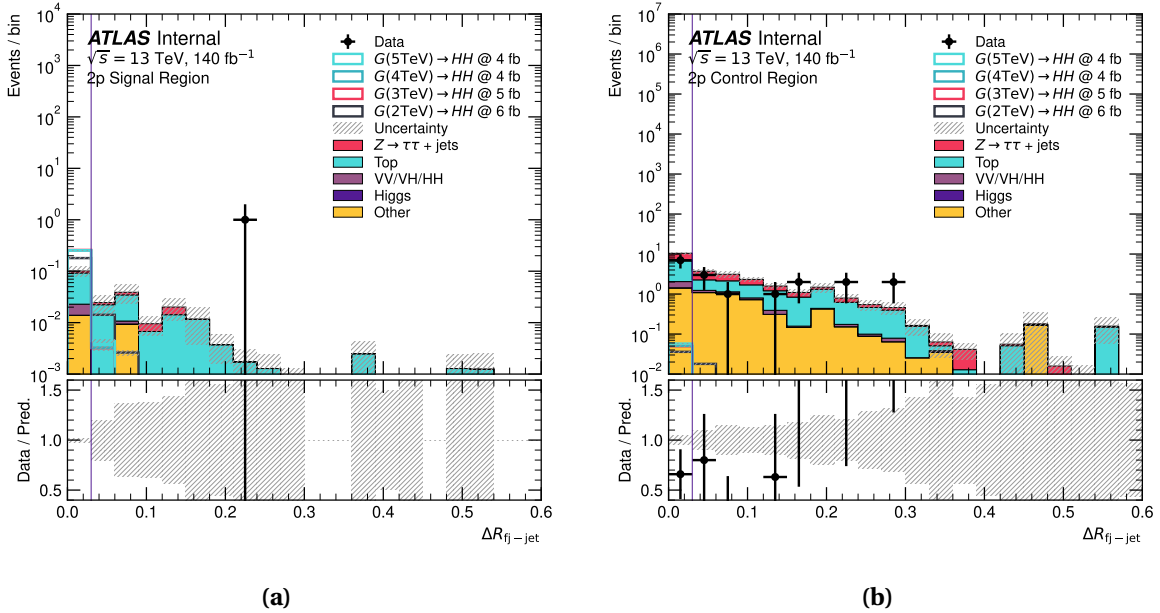


Fig. A.3 The distribution of the $\Delta R_{\text{fj-jet}}$ in the SR (**a**), and CR (**b**).

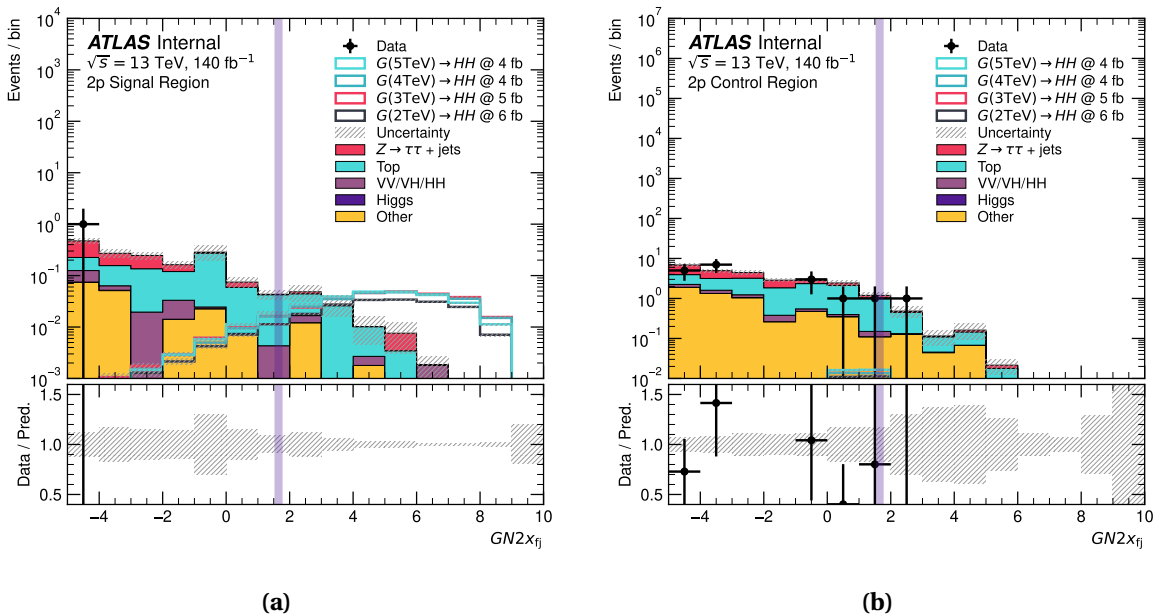


Fig. A.4 The distribution of the GN2x_{fj} in the SR (a), and CR (b). The translucent band indicates the cut value of “QCD1.55%” GN2x WP, ranging from 1.6 to 1.7 in the region where the fatjet mass is between 90 and 160 GeV.

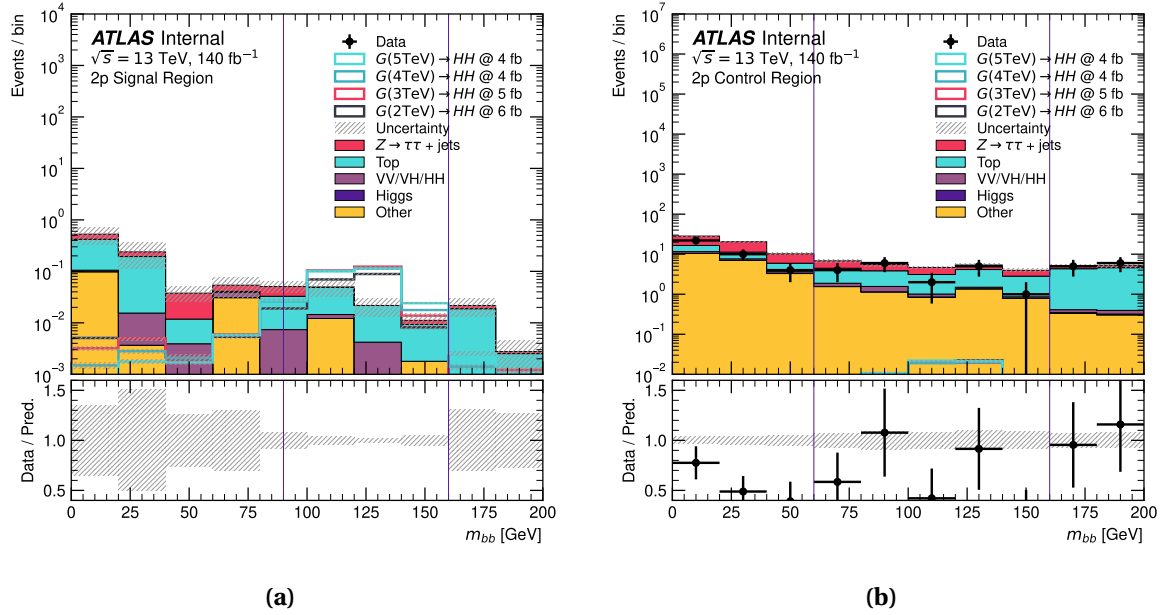


Fig. A.5 The distribution of the m_{bb} in the SR (a), and CR (b).

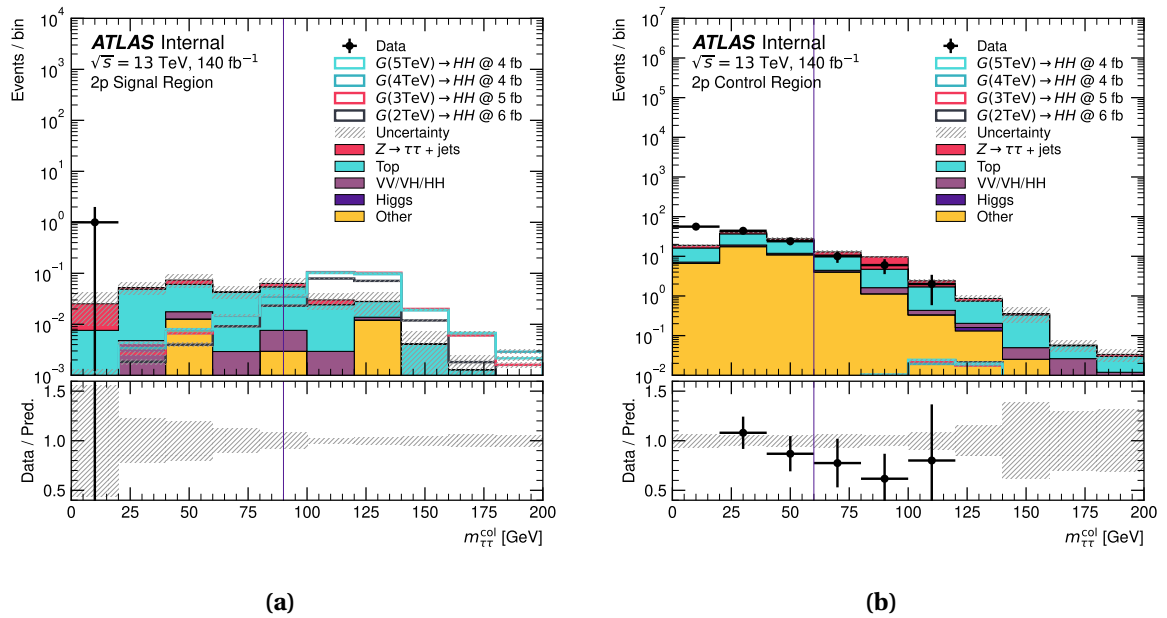


Fig. A.6 The distribution of the m_{tt}^{col} in the SR (a), and CR (b).

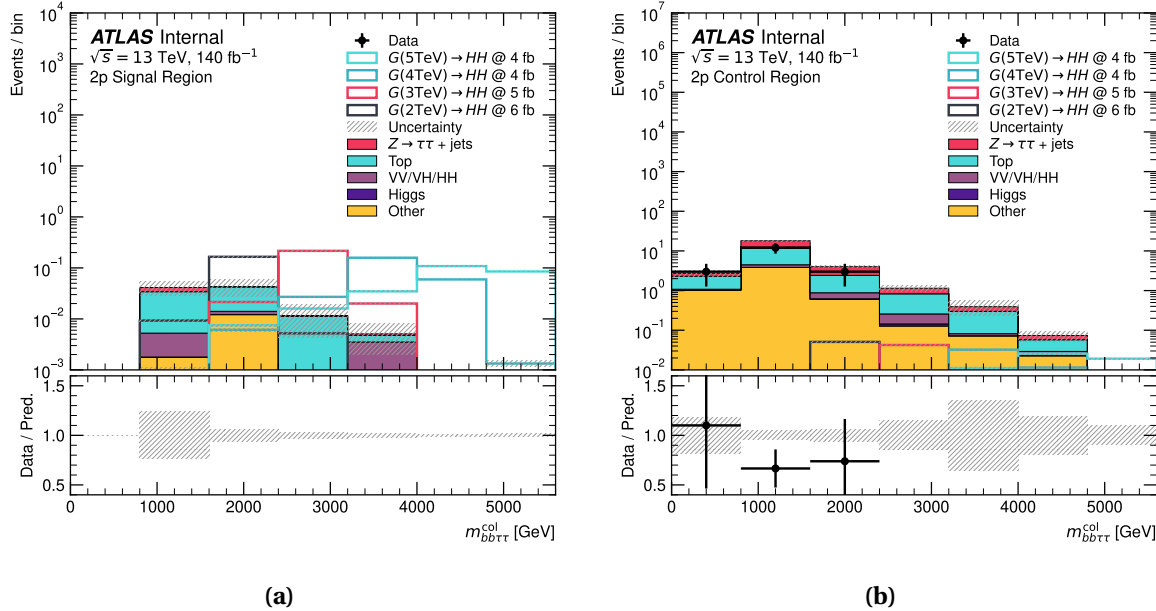


Fig. A.7 The distribution of the $m_{bb\tau\tau}^{\text{col}}$ in the SR (a), and CR (b). The $m_{bb\tau\tau}^{\text{col}}$ distribution extends to lower values in the CR than in the SR due to the relaxed $m_{\tau\tau}^{\text{col}}$ and m_{bb} requirements. This is because lower values of $m_{\tau\tau}^{\text{col}}$ and m_{bb} in the CR allow di- τ and $b\bar{b}$ systems at lower p_T to be produced whilst still satisfying the condition $\Delta R < 0.4$.

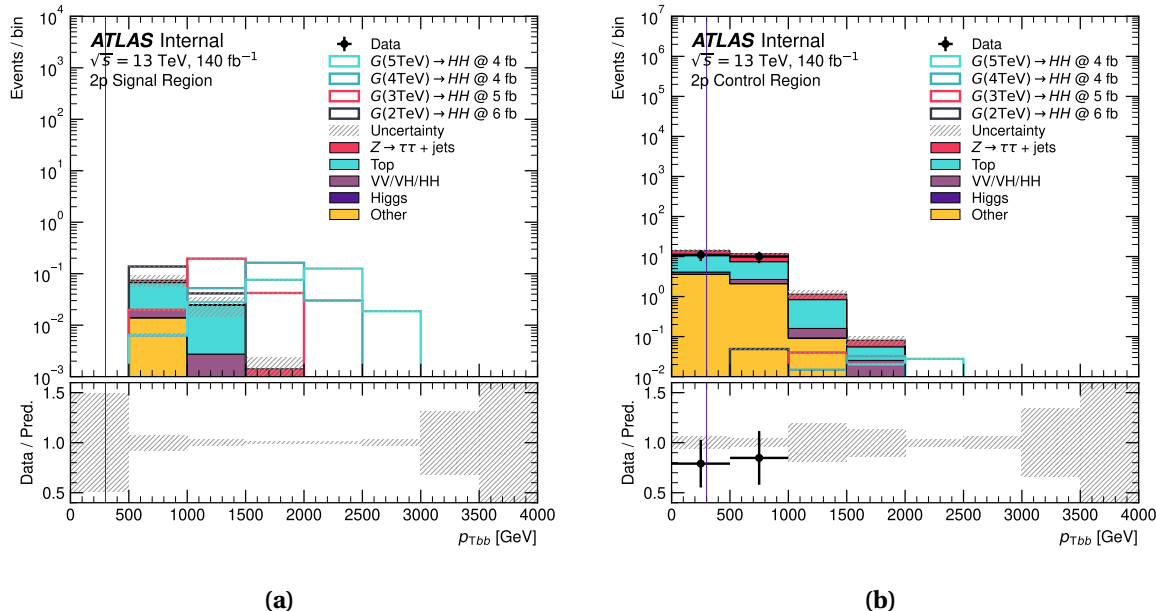


Fig. A.8 The distribution of the p_{Tbb} in the SR (a), and CR (b). The p_{Tbb} distribution extends to lower values in the CR than in the SR due to the relaxed $m_{\tau\tau}^{\text{col}}$ and m_{bb} requirements. This is because lower values of $m_{\tau\tau}^{\text{col}}$ and m_{bb} in the CR allow di- τ and $b\bar{b}$ systems at lower p_{T} to be produced whilst still satisfying the condition $\Delta R < 0.4$.

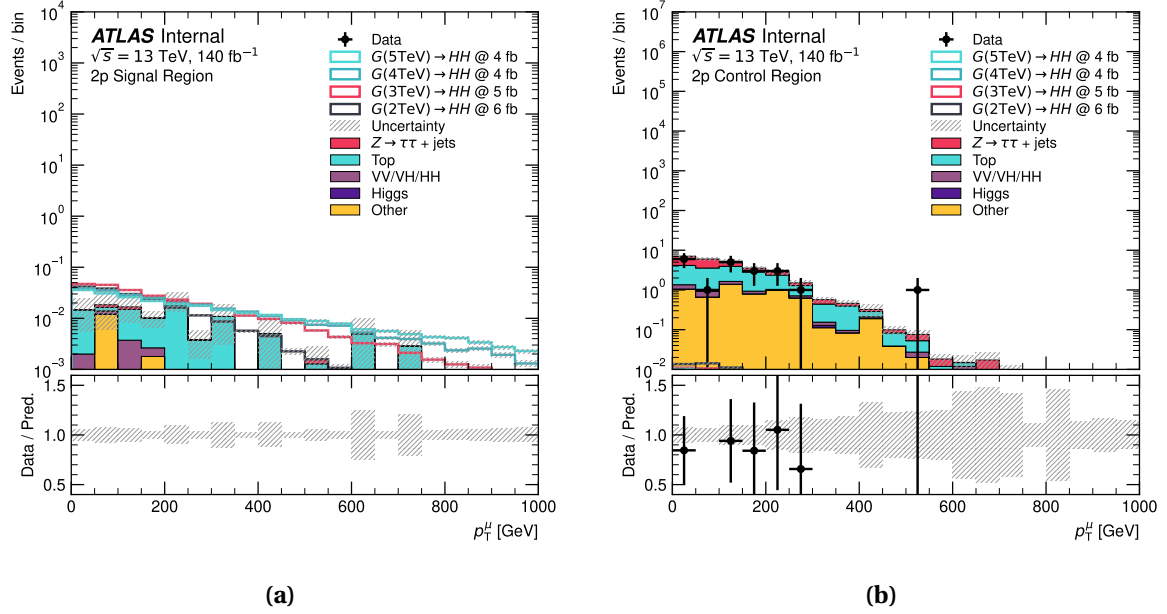


Fig. A.9 The distribution of the p_T^μ in the SR (a), and CR (b).

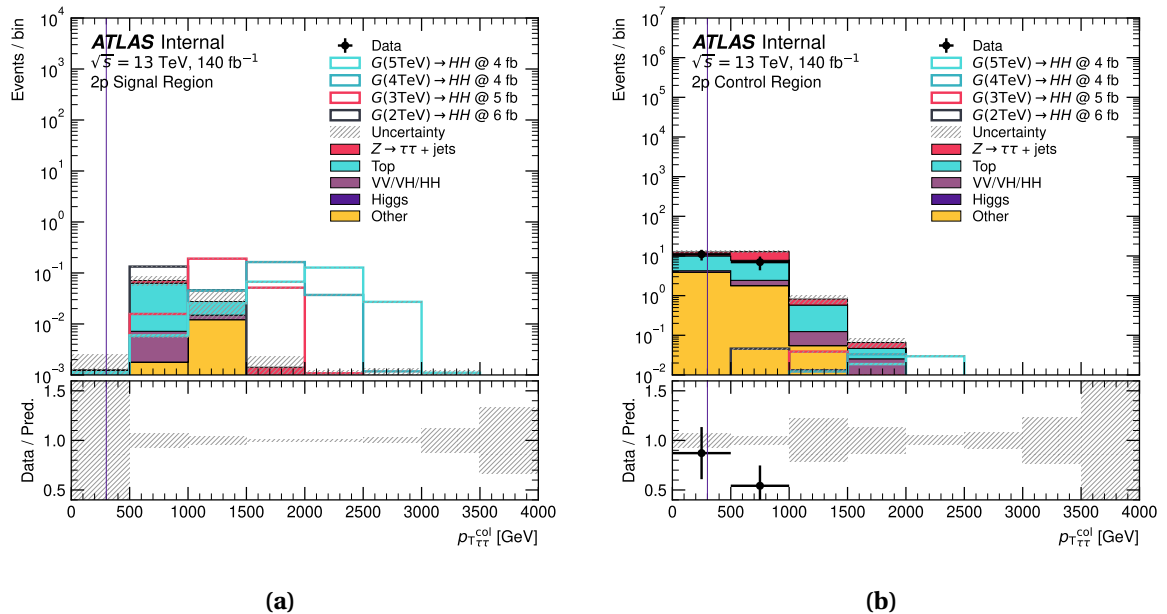


Fig. A.10 The distribution of the $p_{T\tau\tau}^{col}$ in the SR (a), and CR (b). The $p_{T\tau\tau}^{col}$ distribution extends to lower values in the CR than in the SR due to the relaxed $m_{\tau\tau}^{col}$ and m_{bb} requirements. This is because lower values of $m_{\tau\tau}^{col}$ and m_{bb} in the CR allow di- τ and $b\bar{b}$ systems at lower p_T to be produced whilst still satisfying the condition $\Delta R < 0.4$.

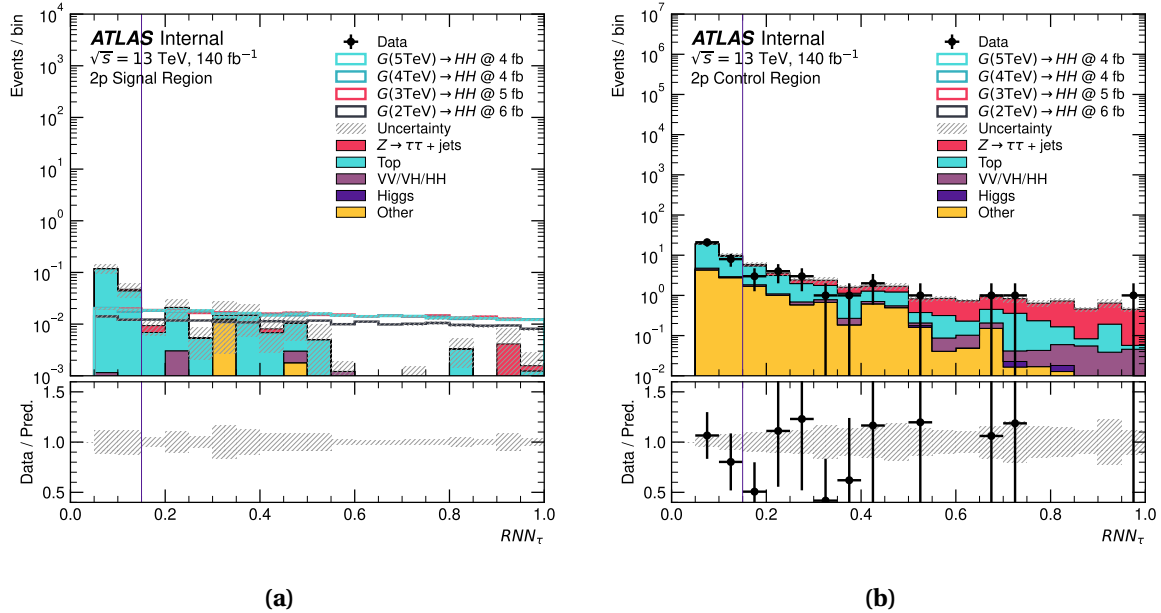


Fig. A.11 The distribution of the RNN_τ in the SR (a), and CR (b).

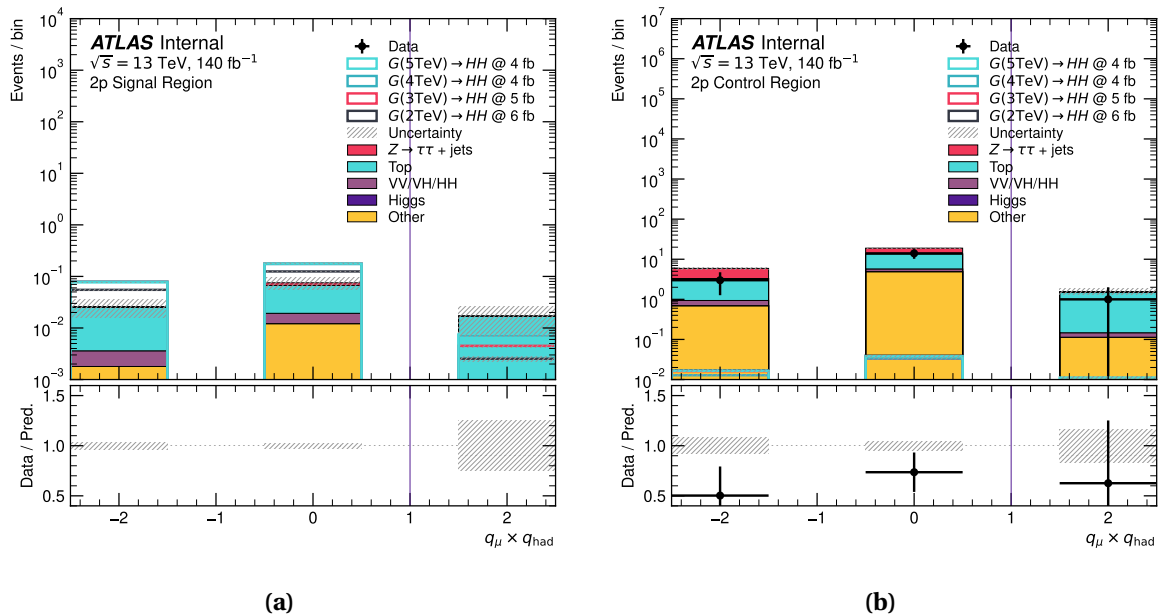


Fig. A.12 The distribution of the product of the $\tau\tau$ charges in the SR (a), and CR (b).

Table A.1 Event yields in the SR 2p and CR 2p regions. Apart from the different selection criteria for prongness and charge, the SR 2p and CR 2p regions are identical to the SR and CR regions in the main analysis. The uncertainties are statistical only. The signal yields are shown with fixed cross-sections $\sigma(pp \rightarrow G \rightarrow HH) = 1 \text{ fb}$.

	SR 2p	CR 2p
Data	0	47 ± 7
SM MC total	0.11	46 ± 3
jets + $Z \rightarrow \tau\tau$	0.01	6.3 ± 0.3
diBoson	0.01	1.5 ± 0.1
Top	0.10	31 ± 1
Higgs	0.00	0.03 ± 0.02
Others	0.01	7 ± 2
$G(2 \text{ TeV}) \rightarrow HH$	0.0343	0.0114
$G(3 \text{ TeV}) \rightarrow HH$	0.0598	0.0129
$G(4 \text{ TeV}) \rightarrow HH$	0.0725	0.0162
$G(5 \text{ TeV}) \rightarrow HH$	0.0731	0.0188

the CR_{2p} , genuine $\tau_\mu \tau_{\text{had}}$ backgrounds are also suppressed for the same reason, the $t\bar{t}$ contribution is promoted to be the dominant background.

Discussion

In exchange of the 10% signal acceptance increase, the SR_{2p} region see a 10% increase in the background contamination. We required a slightly tighter τ_{had} jet RNN score cut, which has the effect that the background contamination is reduced significantly, without sacrificing much signal acceptance. Given that the SR and SR_{2p} regions are essentially background-free, and the fact that this analysis is heavily bottle-necked by the signal yield, the increase in the background contamination is acceptable.

This analysis is the first in ATLAS to use the 2-prong τ_{had} in the signal region. With the 10% increase in signal acceptance, the sensitivity of this analysis is expected improve roughly linearly with the increase in signal acceptance. The expected upper-limits, incorporating the SR_{2p} contributions, are shown in Table A.2. The Brazil band plots are

shown in Figure A.13. The limits are obtained with a 10-bin counting experiment, with the 2-prong analysis concatenated to the main analysis.

Table A.2 The expected and observed 95% CL limits on the $\sigma(G \rightarrow HH)$ on various mass points. Limits are obtained with the 2-prong analysis concatenated to the main analysis.

Mass [GeV]	-2σ [fb]	-1σ [fb]	Exp. [fb]	$+1\sigma$ [fb]	$+2\sigma$ [fb]	Observed [fb]
2000	4.3	5.1	5.7	8.0	11.9	5.4
3000	2.9	3.5	4.1	4.7	6.5	3.8
4000	3.1	3.2	3.6	4.1	5.3	3.5
5000	2.9	3.4	3.8	4.3	5.4	3.8

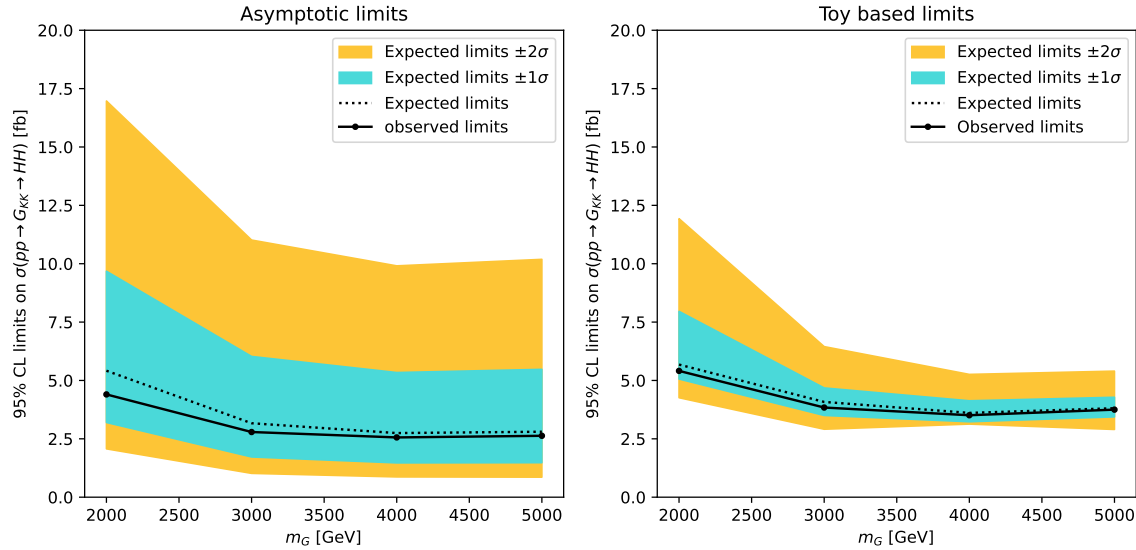


Fig. A.13 The expected and observed 95% CL limits on the $\sigma(G \rightarrow HH)$ on various mass points. Limits are obtained with the 2-prong analysis concatenated to the main analysis.